



DGK Veröffentlichungen der DGK
Ausschuss Geodäsie der Bayerischen Akademie der Wissenschaften

Reihe C

Dissertationen

Heft Nr. 779

David Becker

**Advanced Calibration Methods
for Strapdown Airborne Gravimetry**

München 2016

Verlag der Bayerischen Akademie der Wissenschaften

ISSN 0065-5325

ISBN 978-3-7696-5191-1

Diese Arbeit ist gleichzeitig veröffentlicht in:
Schriftenreihe Fachrichtung Geodäsie der Technischen Universität Darmstadt
ISBN 978-3-935631-40-2, Nr. 51, Darmstadt 2016



DGK Veröffentlichungen der DGK

Ausschuss Geodäsie der Bayerischen Akademie der Wissenschaften

Reihe C

Dissertationen

Heft Nr. 779

Advanced Calibration Methods for Strapdown Airborne Gravimetry

Vom Fachbereich Bau- und Umweltingenieurwissenschaften
der Technischen Universität Darmstadt
zur Erlangung des akademischen Grades eines
Doktor-Ingenieurs (Dr.-Ing.)
genehmigte Dissertation

vorgelegt von

Dipl.-Inform. David Becker, M.Sc.

aus Usingen

München 2016

Verlag der Bayerischen Akademie der Wissenschaften

ISSN 0065-5325

ISBN 978-3-7696-5191-1

Diese Arbeit ist gleichzeitig veröffentlicht in:
Schriftenreihe der Fachrichtung Geodäsie der Technischen Universität Darmstadt
ISBN 978-3-935631-40-2, Nr. 51, Darmstadt 2016

Adresse der DGK:



Ausschuss Geodäsie der Bayerischen Akademie der Wissenschaften (DGK)

Alfons-Goppel-Straße 11 • D – 80 539 München

Telefon +49 – 89 – 23 031 1113 • Telefax +49 – 89 – 23 031 - 1283 / - 1100

e-mail post@dgk.badw.de • <http://www.dgk.badw.de>

Referent: Prof. Dr.-Ing. Matthias Becker

Prof. Dr. René Forsberg

Tag der Einreichung: 15.06.2016

Tag der mündlichen Prüfung: 01.09.2016

Diese Dissertation ist auf dem Server der DGK unter <<http://dgk.badw.de/>>
sowie auf dem Server der TU Darmstadt unter <<http://tuprints.ulb.tu-darmstadt.de/5691/>>
elektronisch publiziert

© 2016 Bayerische Akademie der Wissenschaften, München

Alle Rechte vorbehalten. Ohne Genehmigung der Herausgeber ist es auch nicht gestattet,
die Veröffentlichung oder Teile daraus auf photomechanischem Wege (Photokopie, Mikrokopie) zu vervielfältigen

ISSN 0065-5325

ISBN 978-3-7696-5191-1

Acknowledgements

I sincerely want to thank my supervisor, *Prof. Dr.-Ing. Matthias Becker*, for his continuous and profound support and guidance over the past five years. I also want to thank my colleague *Dr.-Ing. Stefan Leinen*, for his constant support and many fruitful discussions, and also for providing valuable suggestions for this thesis.

I want to thank the colleagues at DTU Space for a successful cooperation over the past three years. The investigations presented in this thesis heavily rely on the availability of airborne gravity data sets, which were acquired in the scope of this cooperation. In particular, thanks to *Prof. Dr. René Forsberg*, *Dr. Arne Vestergaard Olesen*, *Dr. J. Emil Nielsen*, and *Tim Jensen*, for many helpful ideas, suggestions, and fruitful discussions.

Also, I want to express my gratitude to iMAR Navigation, for the outstanding support over the last years. In particular, I want to thank *Dr.-Ing. Edgar v. Hinüber* for granting me access to the professional calibration facilities at iMAR. Also, thanks to *Markus Petry* for his valuable suggestions and assistance regarding the sensor calibrations.

I want to thank my colleagues at the chair of Physical and Satellite Geodesy (PSG) for a constructive and friendly work environment.

The Chile aerogravity campaign was carried out in cooperation with the Instituto Geográfico Militar, Chile, and the US National Geospatial-Intelligence Agency (NGA). The Malaysia aerogravity campaigns were financed by the Department of Survey and Mapping Malaysia (JUPEM). The Mozambique/Malawi aerogravity campaign was financed by NGA. The PolarGap aerogravity campaign was financed by the European Space Agency (ESA), and carried out in cooperation with the British Antarctic Survey (BAS), and the Norwegian Polar Institute (NPI). All campaigns were carried out in cooperation with the Danish National Space Institute at the Technical University of Denmark (DTU Space).

Zusammenfassung

Als Fluggravimetrie wird die Vermessung des Schwerefeldes der Erde bezeichnet, wobei als mobile Messplattform ein Flugzeug zum Einsatz kommt. Für solche Messungen existieren in der Praxis zwei verschiedene Typen von Messinstrumenten: 1. Mechanische Federgravimeter, welche während des Fluges mit Hilfe einer geregelten kardanischen Aufhängung in einer konstanten Orientierung gehalten werden, welche entlang der vertikalen Lotlinie des Schwerefeldes ausgerichtet ist; 2. Fest mit dem Flugzeugkörper verbundene Inertiale Messsysteme (IMU), welche je eine Triade von Akzelerometern und Messkreiseln beinhalten. Letztere Systeme sind üblicherweise für Navigationsanwendungen konzipiert, sie bieten aber auch für gravimetrische Messungen viele praktische Vorteile gegenüber den etablierteren, kardanisch aufgehängten Federgravimetern. Insbesondere sind hier der erheblich geringere Platz- und Energiebedarf zu nennen, der autonome Betrieb des Instruments im Flug, die geringere Empfindlichkeit gegenüber Turbulenzen, sowie die erheblich geringeren Anschaffungskosten.

Die vorliegende Arbeit stellt einen Beitrag zur IMU-basierten Fluggravimetrie dar. Die in der Praxis größte Fehlerquelle bei solchen Messungen sind nicht-kompensierte Driften der Akzelerometer. Es wird zunächst theoretisch, sowie anhand von Simulationen gezeigt, dass solche Sensordriften in der Praxis nicht von der zu bestimmenden Schwere trennbar sind. Hierauf aufbauend werden verschiedene Kalibriermethoden entwickelt, welche die im Flug auftretenden Driften reduzieren sollen. Vorrangig sind hier temperaturabhängige Effekte zu nennen. Die untersuchten Kalibriermethoden werden anhand von Realdaten von fünf Fluggravimetrie-Kampagnen evaluiert. Hierfür werden zunächst die gängigen Evaluationsmethoden zusammengefasst und diskutiert. Für die IMU-basierten Schweremessungen wird schließlich eine Genauigkeit von etwa $1 \cdot 10^{-5} \text{ m/s}^2$ nachgewiesen, welche gleichwertig oder sogar höher ist als die unter vergleichbaren Bedingungen erzielbare Genauigkeit von mechanischen Federgravimetern, welche in der Praxis nach wie vor die Standardinstrumentierung darstellen.

Abstract

Airborne gravimetry is the determination of the Earth's gravity field, using aircraft as mobile measurement platforms. For such measurements, there exist two predominant types of instrumentation: 1. Mechanical spring gravimeters, which are mounted on a gimbaled platform in order to maintain a constant sensor orientation during the flight, aligned with the local vertical of the gravity field; 2. aircraft body-fixed 'strap-down' Inertial Measurement Units (IMU), containing each one sensor triad of accelerometers and gyroscopes. While IMUs are commonly designed for navigation applications, they also turn out to have several practical advantages also for gravimetric applications, compared to the more established platform-stabilised spring-gravimeters. In particular advantageous are the lower space and energy consumption, the autonomous operation during the flights, the lower sensitivity to turbulence, and the considerably lower acquisition costs.

This thesis is a contribution to the improvement of kinematic, IMU-based gravimetry (denoted as *strapdown gravimetry*). In practice, the predominant source of errors of such systems arises from uncompensated accelerometer drifts. It is shown theoretically, and based on simulations as well, that such drifts are in practice inseparable from the gravity signal which is to be determined. Based on this finding, several accelerometer calibration methods are developed, aiming at the reduction of in-flight accelerometer drifts. In particular, thermal effects are shown to be the predominant error source. The proposed calibration methods are evaluated on real data, taken from five different airborne gravity campaigns. The common airborne gravimetry evaluation methods are summarised and discussed. An IMU-based gravity measurement accuracy of approximately $1 \cdot 10^{-5} \text{ m/s}^2$ is verified, being equal or even superior compared to the achievable accuracy of mechanical spring-gravimeters under comparable conditions, which are still the predominant instrumentation for airborne gravimetry.

Contents

Notation	v
List of Symbols	vii
1 Introduction	1
1.1 The Earth's gravity field	1
1.2 Gravimetry	2
1.2.1 Terrestrial gravimetry	3
1.2.2 Satellite gravimetry	3
1.2.3 Shipborne and airborne gravimetry	4
1.2.4 Strapdown and stable-platform gravimetry	5
1.3 Applications	7
1.3.1 Geoid determination	7
1.3.2 Geophysical applications	9
1.4 Thesis outline	9
2 State of the art	11
2.1 Stable-platform airborne gravimetry	11
2.2 Strapdown gravimetry	12
2.3 IMU calibration methods	15
2.4 GNSS processing	17
3 An Integrated IMU/GNSS Strapdown Gravimetry System	19
3.1 Extended Kalman filter	20
3.1.1 Modelling IMU measurements as control	21
3.1.2 Error state space formulation	22
3.2 Strapdown Gravimetry System Design	22
3.2.1 Coordinate frames	22
3.2.2 Normal gravity and gravity disturbance	23
3.2.3 System state	23
3.2.4 Navigation equations	24
3.2.5 Sensor biases	26
3.2.6 Modelling the along-track gravity disturbance as a stochastic process	27
3.2.7 Summary	28
3.3 Measurement updates	28
3.4 Navigation update	30
3.5 Gravity reductions	31
3.5.1 Global gravity model reductions	31
3.5.2 Topographic reductions	32
3.5.3 Modified system state	32
3.6 Optimal smoothing	34

4	System analysis	35
4.1	Observability	35
4.1.1	Structure graph analysis	35
4.1.2	Algebraic analysis	40
4.1.3	Scenarios and examples	41
4.2	Estimability	44
4.2.1	Definition	44
4.2.2	Simulated flight trajectories	45
4.2.3	Real data example	48
4.3	Implications for SAG	50
5	Error propagation analysis	55
5.1	Methodology	55
5.2	Systematic errors	59
5.2.1	Discretisation error	59
5.2.2	IMU timestamp error	60
5.2.3	Lever arm error	61
5.2.4	Sensor misalignments	62
5.2.5	Initial alignment error	65
5.2.6	Accelerometer errors	66
5.2.7	Gyroscope errors	66
5.3	Stochastic sensor errors	69
5.3.1	IMU sensor noise	69
5.3.2	GNSS coordinate observation noise	69
5.4	Summary	72
6	Calibration methods for strapdown gravimetry	75
6.1	iMAR RQH-1003 functional system design	76
6.2	Honeywell QA-2000 sensor characteristics	77
6.3	Manufacturer calibrations	80
6.4	Thermal calibration of the vertical accelerometer	80
6.4.1	Warm-up calibration	81
6.4.2	Temperature oven calibration	83
6.5	Parametric error models	85
6.5.1	Bias, scale factor, cross-coupling (BSC)	85
6.5.2	Bias, two scale factors, cross-coupling (BSSC)	91
6.5.3	Discussion	94
6.6	Extended sample-based error models	95
6.6.1	A sample-based TRP calibration for strapdown airborne gravimetry	96
6.7	Comparisons of the calibration results	104
7	Quality assessment	107
7.1	Internal quality assessment	107
7.1.1	Cross-over residuals	107
7.1.2	Repeated lines or line segments	113
7.1.3	Error of closure	113
7.2	Comparisons against external reference data	114
7.2.1	Inter-system comparison	114
7.2.2	Global Earth gravity models	114
7.2.3	Topographic gravity effect	116
7.2.4	Ground control points	116
7.3	A Turbulence Metric	117

8 Results	121
8.1 Chile (2013)	124
8.1.1 Cross-over analysis	126
8.1.2 Errors of closure	127
8.1.3 Comparison against LCR	128
8.1.4 High-frequency comparison against topographic effect	131
8.1.5 Comparison against GGM05C	133
8.2 Malaysia (2014 and 2015)	135
8.2.1 Cross-over analysis: Scalar gravity	135
8.2.2 Cross-over analysis: Deflections of the Vertical	138
8.2.3 Comparison against GGM05C	138
8.3 Northern Mozambique and Malawi (2015)	143
8.3.1 Cross-over analysis	143
8.3.2 Comparison against GGM05C	145
8.4 PolarGap campaign, Antarctica (2015/2016)	148
8.4.1 Heading initialisation without gyro-compassing	150
8.4.2 Cross-over analysis	151
8.5 Effect of turbulence	151
8.6 Summary	153
9 Conclusions	155
10 Outlook	159
References	161
List of Acronyms	167
Appendix	169
A Detailed campaign information	169
A.1 Attitude characteristics	169
A.2 Measurement lines	169

Notation

\mathbf{a}	a vector
\mathbf{a}^b	a vector a , given in the b -frame
\mathbf{C}_q^p	Direction-cosine matrix, $\mathbf{a}^p = \mathbf{C}_q^p \mathbf{a}^q$
\mathbf{A}	a matrix
$\mathbf{0}$	zero matrix
\mathbf{I}	identity matrix
ω	a scalar rotation rate
$\boldsymbol{\omega}_{bc}^a$	Rotation rate vector of the c -frame w.r.t. the b -frame, given in the a -frame.
$\begin{pmatrix} \mathbf{A} & \mathbf{B} \\ \mathbf{C} & \mathbf{D} \end{pmatrix}$	a block matrix, consisting of four sub-matrices
$\text{diag}(\mathbf{a})$	diagonal matrix, with elements taken from \mathbf{a}
$\text{dim}(\mathbf{a})$	the number of elements (the dimension) of \mathbf{a}
$ A $	the number of elements of a set A
$ \mathbf{a} $ or $\ \mathbf{a}\ _2$	Euclidean norm of a vector
a	a scalar, $a = \mathbf{a} $
$\mathbf{a}^T, \mathbf{A}^T$	transposed vector or matrix
\mathbf{A}^{-1}	inverse of a matrix
$\mathbf{a} \times \mathbf{b}$	cross product
$\mathbf{q}_1 \bullet \mathbf{q}_2$	quaternion multiplication
$[\mathbf{a} \times]$	cross product-forming matrix, $[\mathbf{a} \times] \mathbf{b} = \mathbf{a} \times \mathbf{b}$
$\boldsymbol{\Omega} = [\boldsymbol{\omega} \times]$	Skew-symmetric matrix of a rotation vector
$\left. \frac{\partial f}{\partial x} \right _a$	the partial derivative of f with respect to x , evaluated at a
$\dot{a}, \ddot{a}, \dddot{a}, \dots$	time-derivatives of a quantity a
$\overset{(n)}{a}$	n -th time-derivative of a quantity a
a	a measured quantity
\tilde{a}	a true quantity ¹
\hat{a}	an estimated quantity ¹
\bar{a}	a smoothed quantity ¹
a_{sim}	a simulated quantity

¹For readability, accents are only used, if the type of quantity is not clear from the context.



List of Symbols

Coordinate frames (Sect. 3.2.1)

i	The inertial frame.
e	The Earth-centred Earth-fixed frame.
n	The North-East-Down navigation frame.
b	The Front-Right-Down body-fixed frame.
\mathbf{a}^q	A vector \mathbf{a} , expressed in a frame q .
a^N	North component of a vector \mathbf{a}^n
a^E	East component of a vector \mathbf{a}^n
a^D	Down component of a vector \mathbf{a}^n

General

σ	a standard deviation
μ	a mean value
φ	Ellipsoidal latitude
λ	Ellipsoidal longitude
h	Ellipsoidal height
R^N	Ellipsoidal radius of curvature along Meridian
R^E	Ellipsoidal radius of curvature along the transverse
ω_e	Scalar Earth rotation rate
$\boldsymbol{\omega}_{ie}$	Earth rotation rate vector
$\boldsymbol{\omega}_{en}$	Transport rate (due to vehicle motion in a curvilinear frame)
$\boldsymbol{\omega}_{nb}$	Rotation rate of the vehicle w.r.t. the n -frame
\mathbf{f}	the specific force acting on the b frame w.r.t. the i -frame
\mathbf{r}	vehicle position
$\mathbf{v} = \dot{\mathbf{r}}$	vehicle velocity w.r.t. the e -frame
$\mathbf{a} = \ddot{\mathbf{r}}$	vehicle acceleration w.r.t. the e -frame
$\boldsymbol{\psi}$	vehicle orientation w.r.t. the n -frame
\mathbf{b}_a	3-D vector of accelerometer biases
\mathbf{b}_ω	3-D vector of gyroscope biases
l	Lever arm (eccentricity of an aiding sensor)
\mathbf{q}	Quaternion vector (4-D)
$\text{Rot}_a(\alpha)$	A rotation by α around the a -axis (3×3 -Matrix)

Gravity potential, gravity, and geodetic reference system

\mathbf{g}	the Earth's gravity
$d\mathbf{g}$	Gravity disturbance vector
dg	Gravity disturbance
ξ, η	Components of the deflection of the vertical
$\Delta\mathbf{g}$	Gravity anomaly
N	Geoid height (or: geoidal undulation)
W	the Earth's geopotential

C	Geopotential Cote
H	Orthometric height
γ	normal gravity vector
γ	normal gravity
γ_0	normal gravity on the ellipsoid
a	semi-major axis of the ellipsoid
e	eccentricity of the ellipsoid

Kalman filter and smoother

\mathbf{a}_k	a quantity \mathbf{a} , given at time epoch k
\mathbf{x}	system state
$\delta\mathbf{x}_k$	error state
\mathbf{u}_k	control vector
n	number of system states: $n = \dim(\mathbf{x})$
N	total number of IMU epochs
\mathbf{P}	$n \times n$ Error covariance matrix
dt	IMU time-increment (reciprocal IMU data rate)
φ	System transition function
Φ	Linearised state transition model
\mathbf{F}	Linearised differential state transition model
\mathbf{B}	Linearised control-input matrix
\mathbf{w}^s	System noise
\mathbf{Q}	System noise covariance matrix
\mathbf{z}	vector of measurements
m	number of measurements: $m = \dim(\mathbf{z})$
\mathbf{w}^z	Measurement noise
\mathbf{R}	Measurement noise covariance matrix
\mathbf{h}	m -dimensional measurement function
\mathbf{H}	linearised measurement model ($m \times n$)
\mathbf{K}	Kalman gain matrix
\mathbf{i}	Innovation vector
\mathbf{S}	Innovation covariance matrix

Gravity evaluation

χ'	Cross-over differences of gravity estimates
χ	Cross-over differences of gravity <i>disturbance</i> estimates
Δh	Height difference of the two adjacent lines at a cross-over point
ρ	Cross-over residual correction factor

Chapter 1

Introduction

One of the major tasks of physical geodesy is the determination of the Earth's gravity field, and its potential W (*Hofmann-Wellenhof and Moritz, 2006; Torge and Müller, 2012*). The most important reference surface for geodetic height systems is the *geoid*, being the equipotential surface $W = W_0 = \text{const}$ for a predefined reference potential W_0 . This reference potential is commonly associated with the mean sea level.

The definition of this surface is intuitive in the absence of topography above sea level, however the equipotential surface continues below the landmasses. Therefore, the geoid can be thought of as the mean sea level of an imaginative global ocean, continuing below the continents. The value of the geopotential on the geoid (*Moritz, 1980*)

$$W_0 \approx 62.636 \cdot 10^6 \text{ m}^2/\text{s}^2 = 62.636 \text{ MJ/kg} \quad (1.1)$$

may be interpreted as the energy which is required to move a unit mass located on the geoid to infinity, or equally, the energy performed by the Earth's gravity field to move a unit mass from infinity to the geoid. The geopotential $W(x, y, z)$ is a scalar field, assigning a scalar value to each coordinate triple (x, y, z) of a Cartesian earth-fixed coordinate frame.

1.1 The Earth's gravity field

The vector of gravity \mathbf{g} is defined as the gradient of the geopotential,

$$\mathbf{g} = \text{grad } W = \left(\frac{\partial W}{\partial x} \quad \frac{\partial W}{\partial y} \quad \frac{\partial W}{\partial z} \right)^T. \quad (1.2)$$

Thus, the gravity field $\mathbf{g} = \mathbf{g}(x, y, z)$ is a vector field, assigning a vector to each coordinate triple. The magnitude $g = |\mathbf{g}|$ is called *scalar gravity*.

The common unit for gravity used in the geodetic literature is *Gal*, which is not contained in the SI standard. It is defined as $1 \text{ Gal} = 1 \cdot 10^{-2} \text{ m/s}^2$. The units $1 \text{ mGal} = 1 \cdot 10^{-5} \text{ m/s}^2$ and $1 \mu\text{Gal} = 1 \cdot 10^{-8} \text{ m/s}^2$ will be used throughout the text as well.

Several concepts exist on how to derive the geometrical shape of the geoid based on gravity measurements. For this, a geodetic reference system is used, commonly defining an oblate, rotating spheroid (also denoted as rotating *ellipsoid of revolution*), approximating the shape of the geoid, and rotating at the Earth's rotation rate ω_e (*Moritz, 1980*). The surface of the ellipsoid is at the same time an equipotential surface of its gravity potential, called the *normal gravity potential* U . On the ellipsoid, it is defined as $U = U_0 = W_0$. The normal potential U can easily be computed for any point on or above the ellipsoid (*Torge and Müller, 2012*). As for the actual gravity potential, the *normal gravity vector* $\boldsymbol{\gamma}$ is defined as the gradient of the normal potential: $\boldsymbol{\gamma} = \text{grad}(U)$.

The actual geodetic quantities are then reduced to differences with respect to this reference system: The shape of the geoid can be defined by the vertical distance N between the geoid and the ellipsoid surface. N is called *geoid height*, or *geoidal undulation*. The *gravity disturbance* is defined as the difference between the actual gravity at a point P , and the normal gravity at the same point: $d\mathbf{g} = \mathbf{g}_P - \boldsymbol{\gamma}_P$. Further, the *gravity anomaly* is defined as the difference between the gravity at a point P , and the normal gravity at a point Q above or below P , with $W_P = U_Q$: $\Delta\mathbf{g} = \mathbf{g}_P - \boldsymbol{\gamma}_Q$. A fundamental functional relationship between these quantities was formulated by Stokes using a surface integral:

$$N_P = \frac{R}{4\pi\gamma_0} \iint_{\sigma} \Delta g S(\psi) d\sigma, \quad (1.3)$$

with Earth radius R , the spherical distance ψ between the point P and the running integration point, and *Stokes' function* (Hofmann-Wellenhof and Moritz, 2006)

$$S(\psi) = \frac{1}{\sin(\psi/2)} - 6 \sin \frac{\psi}{2} + 1 - 5 \cos \psi - 3 \cos \psi \ln\left(\sin \frac{\psi}{2} + \sin^2 \frac{\psi}{2}\right). \quad (1.4)$$

Eq. 1.3 shows, that the knowledge of the gravity field (Δg) also allows the determination of the shape of the geoid, N . The practical use of knowing N will be discussed later in this chapter. For details on the derivation of Eq. 1.3, the reader is referred to standard literature on physical geodesy, as Hofmann-Wellenhof and Moritz (2006); Torge and Müller (2012).

Similar as for the scalar gravity, the direction of the local gravity vector at any point P can be expressed with respect to the direction of the normal gravity vector at the same point. Expressing the vectors in a local North-East-Down coordinate frame, and with the assumptions, that $g^{\text{North}} \ll g^{\text{Down}}$ and $g^{\text{East}} \ll g^{\text{Down}}$, the angular *deflection of the vertical* (DoV) can be defined by its two components

$$\xi = -\frac{dg^{\text{North}}}{g} = -\frac{g^{\text{North}} - \gamma^{\text{North}}}{g}, \quad \text{and} \quad (1.5)$$

$$\eta = -\frac{dg^{\text{East}}}{g} = -\frac{g^{\text{East}}}{g}, \quad (1.6)$$

because $\gamma^{\text{East}} = 0$ due to the radial symmetry of the ellipsoid of revolution (spheroid). Note, that ξ increases when (hypothetically) introducing attracting masses in the South, and η increases when adding masses in the West. With these definitions, the angular components of the deflection of the vertical can be transformed into horizontal gravity components, and vice versa.

1.2 Gravimetry

While today there is no practical way of directly measuring the geopotential W with reasonable accuracy, the gravity \mathbf{g} can be determined either

- by measuring the force that is acting on a proof mass, or
- by measuring accelerations (second derivative of observed positions) of a test body being in free fall in a vacuum.

These are the main concepts of *gravimeters*.

Depending on the instrument design and the type of the measured effect, gravimeters may be limited to *scalar gravimetry*, i.e. the determination of $g = |\mathbf{g}|$. In contrast, vector gravimetry allows the determination of the full 3-D gravity vector \mathbf{g} (or equivalently, g , ξ , and η).

Another distinction is commonly made with respect to the requirement of a reference gravity value:

- *Relative* gravimetry is the determination of gravity with respect to a known reference gravity value. In other words, relative gravimetry can only determine gravity *differences* between two points.
- *Absolute* gravimetry is the direct determination of gravity, without any external information.

This thesis is primarily concerned with *relative vector gravimetry*.

There are three principal *modi operandi* for the gravity determination using a gravimeter, given by the type of the measurement platform. These different modes of gravimetry are briefly introduced in the following sections.

1.2.1 Terrestrial gravimetry

Terrestrial gravimetry is the determination of gravity on the Earth's surface: The terrestrial gravimeter is statically standing on the ground without any movement during the measurement. Terrestrial gravimetry enables the gravity determination at high accuracy (typically tens of μGal or better), and high spatial resolution, as there is no lower bound on the spacing between the measurement points. However, measurements can be difficult or even impossible in areas of rugged terrain or water. In addition, performing terrestrial gravimetry for larger areas can be very costly, because the static measurements are time- and labour-consuming. The points have to be accessed on ground, e.g. using land vehicles or helicopters.

Historically, terrestrial gravimetry was the only *modus operandi*. Until today, many countries maintain or extend dense terrestrial gravity point networks, serving as the main data source for the determination of national height reference surfaces, also referred to as *local* geoids.

Especially for large countries and remote areas, the use of terrestrial gravimetry for the establishment of a national height system is too costly and time-consuming. Instead, a relatively sparse network of terrestrial gravity points is combined with airborne, shipborne, or satellite gravity data.

1.2.2 Satellite gravimetry

With the launch of the Challenging Minisatellite Payload (CHAMP) mission (2000-2010), gravity observations from space became available by observing the orbital deviations of this satellite. Until today, two more satellite missions were established, the Gravity Recovery And Climate Experiment (GRACE, 2002), and the Gravity field and steady-state Ocean Circulation Explorer (GOCE, 2009).

The GRACE mission consists of two low-Earth-orbiting satellites on the same orbits, which can determine their mutual distance with very high precision, also denoted as satellite-to-satellite tracking (SST). Variations of this mutual distance arise from local variations of the gravitational attraction of the Earth. Therefore, the distance variations allow the deduction of gravity.

In addition to gravity, GOCE also provides measurements of the gravity gradient tensor $\text{grad } \mathbf{g} = \text{grad}(\text{grad } W)$, consisting of five independent gradients (*Torge and Müller, 2012*):

$$W_{xx} = \frac{\partial^2 W}{\partial x^2}, \quad (1.7)$$

$$W_{yy} = \frac{\partial^2 W}{\partial y^2}, \quad (1.8)$$

$$W_{xy} = W_{yx} = \frac{\partial^2 W}{\partial x \partial y}, \quad (1.9)$$

$$W_{xz} = W_{zx} = \frac{\partial^2 W}{\partial x \partial z}, \quad \text{and} \quad (1.10)$$

$$W_{yz} = W_{zy} = \frac{\partial^2 W}{\partial y \partial z}. \quad (1.11)$$

With higher altitudes, the attenuation of the Earth's gravity field limits the spatial resolution of the gravity determination (*Torge, 1989*). Satellite gravimetry orbits are chosen as low as possible to limit this effect, e.g. GOCE was operated at an altitude of only 283.5 km, yielding a spatial resolution on the geoid of the order of 100 km (GRACE: 450 km to 500 km altitude, yielding a resolution of ≈ 150 km). More details will be provided in Sect. 7.2.2.

Satellite missions have greatly contributed to global gravity models (GGM), and also enabled new methods of global Earth system research in the fields of oceanography, glaciology, and geophysics. However, the limited spatial resolution does not allow a satellite-only determination of local geoids at a sufficient resolution.

1.2.3 Shipborne and airborne gravimetry

Shipborne and airborne gravimetry is today's most important link between terrestrial and satellite gravimetry in terms of resolution and coverage. In the most common set-up, a ship, or a fixed-wing aircraft, is equipped with a sea or air gravimeter, which is designed for kinematic measurements, in combination with a geodetic GNSS receiver. Table 1.1 shows the typical parameters of airborne gravimetry and its products.

In the kinematic set-up, a gravimeter can not directly measure gravity, but only the superposition of gravity and vehicle accelerations $\ddot{\mathbf{r}}^i$, which cannot be avoided in practice. This superposition is called *specific force* \mathbf{f} . In an inertial coordinate frame i , it is defined as (*Jekeli, 2001*)

$$\mathbf{f}^i = \ddot{\mathbf{r}}^i - \mathbf{g}^i. \quad (1.12)$$

This definition is intuitive, as gravity can not be distinguished from an acceleration in the *opposite* direction. In particular, $\mathbf{f}^i = \mathbf{0}$ during a free fall in a vacuum.

For the application of kinematic gravimetry, Eq. 1.12 is transformed into

$$\mathbf{g}^i = \ddot{\mathbf{r}}^i - \mathbf{f}^i. \quad (1.13)$$

While \mathbf{f} is measured by the gravimeter, the vehicle accelerations $\ddot{\mathbf{r}}^i$ have to be determined by an aiding sensor, as e.g. GNSS. When expressing Eq. 1.12 in an Earth-fixed, i.e. rotated coordinate system, centrifugal, Coriolis, and Euler forces have to be accounted for (*Britting, 1971*). The Euler term can be neglected under the assumption of a constant Earth's rotation rate vector.

It is just briefly mentioned here, that the third possible transformation of Eq. 1.12 is commonly used for inertial positioning (or: inertial navigation). Assuming the gravity is known, the vehicle accelerations can be computed using:

$$\ddot{\mathbf{r}}^i = \mathbf{f}^i + \mathbf{g}^i. \quad (1.14)$$

flight altitude	500 m to 4000 m above topography
aircraft speed	50 m/s to 100 m/s
flight line spacing	2 km to 40 km
resolution	3 km to 7 km half wavelength
accuracy level	1 mGal to 3 mGal

Table 1.1: Typical parameters of airborne gravimetry

The acceleration vector is then integrated twice (utilising initial values for velocity and position), allowing a continuous kinematic positioning.

There are two fundamental types of gravimeters for the use in shipborne or airborne gravimetry, differing by the way the instrument is mounted to the vehicle body (also referred to as *mechanisation*). Throughout the text, the following terminology will be used:

1. A *platform-stabilised gravimeter* is mounted on a mechanically stabilised platform, which maintains the orientation of the sensor's sensitive axis aligned with the local vertical of the gravity field. For this, at least two degrees of freedom are required for the platform steering, implemented in practice by a combination of gyroscopes and torque motors running in a feedback loop. Equally, the term *platform-stabilised gravimetry* denotes the gravity determination using a platform-stabilised gravimeter.
2. A *strapdown gravimeter* is firmly connected (*strapped down*) to the vehicle body. Due to the time-variable orientations of the vehicle during the measurement, a full triad of orthogonal accelerometers is generally required. The orientation of the accelerometer triad is computed using angular rate measurements of a triad of gyroscopes. This allows an analytical determination of the measured specific force with respect to a superordinate coordinate frame (as a local North-East-Down coordinate frame, or any other Earth-fixed frame). This approach is therefore sometimes referred to as an *analytical platform* mechanisation. Instead of the term *strapdown gravimeter*, the term *strapdown inertial measurement unit* (IMU) is used interchangeably throughout the text. While a *strapdown IMU* is the more general term for a strapdown inertial sensor with three accelerometers and three gyroscopes, the term *strapdown gravimeter* is used if a device (usually consisting of the same set of six inertial sensors) was *specifically* designed for the application of gravity determination. The process of gravity determination with a strapdown IMU is denoted as *strapdown gravimetry*.

The general term *airborne gravimetry*, *kinematic gravimetry*, or just *gravimetry* will be used in the text, if a certain statement is independent of the choice of the sensor mechanisation.

As of today, kinematic gravimetry is only available as *relative* gravimetry: The gravity measurements are tied to a reference gravity point, which is typically situated at the port, or at the airport. It is just noted here, that there are emerging technologies, which may allow an accurate *absolute* gravity determination in kinematic mode in the future, based on cold-atom interferometry (*Bidel et al.*, 2013; *Zahzam et al.*, 2016).

1.2.4 Strapdown and stable-platform gravimetry

This section provides a motivation for strapdown gravimetry, in contrast to the more established stable-platform approach.

¹The long-term stability is regarded to be poor with respect to the typical goal of airborne gravimetry: A gravity determination at the 1 mGal level. It is noted again, that this sensor was actually not designed for the gravity determination.

	iMAR RQH-1003	LaCoste & Romberg S-type
Mechanisation	strapdown	2-axis stabilised platform
Principle	3-D quartz accelerometer	1-D zero-length spring
Classifications	relative gravimetry	relative gravimetry
	vector gravimetry	scalar gravimetry
Weight	12.5 kg	80 kg (including rack)
Dimensions	20 x 20 x 35 cm	70 x 55 x 65 cm (rack)
In-flight operator required?	no	yes
Power consumption	< 40 Watts	< 300 Watts
Thermal stabilisation	no	yes
Long-term stability	poor ¹	excellent
Robustness against turbulence	very good	poor
In-operation altitude changes?	yes	limited

Table 1.2: Comparison of a LaCoste & Romberg S-type gravimeter, against a iMAR RQH-1003 navigation grade strapdown IMU, in the context of airborne gravimetry. A photograph of the two devices is shown in Fig. 1.1.

Platform-stabilised systems are relatively heavy and space consuming. Including the required devices for the power supply, and including the instrument rack with the gimbaled platform (incl. torque motors), a typical platform stabilised system has a total weight of the order of 50 kg to 150 kg. A navigation grade strapdown IMU is available today with less than 10 kg of weight, and a tendency of further weight reductions can be observed.

Since the mechanical spring of the classical systems is very sensitive to temperature changes, the internal sensor temperature is usually stabilised using a temperature feedback loop. This is an important basis for the well-known long-term stability of these devices, on the other hand increasing the energy consumption. In addition, the torque motors for the platform stabilisation usually show a significant energy consumption. Platform-stabilised systems with peak power requirements of 300 to 500 Watts are known to the author. A strapdown IMU has usually a considerably lower energy consumption, of the order of tens of Watts. In practice, the low energy consumption enables a self-sufficient operation of an IMU, as it can run for hours on a medium size battery. (For example, the iMAR RQH-1003 system can run for approximately four hours on a 12 V/12 Ah battery.)

Usually, stabilised-platform systems require an on-board operator during the measurements, in particular for unlocking and locking the very sensitive mechanical spring after take-off and before landing, respectively. Conversely, a strapdown IMU can operate autonomously, no operator is required on board the vehicle.

Lastly, it needs to be mentioned that the consumer market for platform-stabilised systems is very small, leading to higher prices. A state-of-the-art stabilised-platform system can cost 500,000 US-dollars and more, while a standard off-the-shelf navigation-grade strapdown IMU, as it is investigated in the scope of this thesis, is available from approximately 150,000 US-dollars.

Tab. 1.2 shows a comparison of two typical representatives of the two classes of devices. (Gravity results from these two devices will be evaluated in Chap. 8.) A visual comparison is provided in Fig. 1.1.

The poor long-term stability of an off-the-shelf strapdown IMU is the most limiting factor for strapdown gravimetry. Many examples can be found in the literature, showing that this is a general issue when using navigation-grade strapdown IMU's for gravimetry (cf. Sect. 2.2). In the scope of this thesis, IMU calibration methods are being developed and evaluated, with

the main goal of increasing the long-term stability of the sensors, thereby enabling stand-alone strapdown gravimetry at the 1 mGal accuracy level.



Figure 1.1: An iMAR RQH-1003 strapdown IMU (left), and a LaCoste & Romberg S-type sea/air gravimeter on a 2-axis stabilised platform (right). This set-up photograph was taken inside a KingAir BeechCraft 350 fixed-wing aircraft. The main characteristics of the two sensors are shown in Tab. 1.2.

1.3 Applications

1.3.1 Geoid determination

Most national height-system definitions are based on the gravity potential. These definitions comply with the intuitive understanding of a height: that there is no water flow between any two points of equal height (assuming the absence of tides and friction). Therefore, the most straight-forward 'height' definition is the use of the gravity potential itself. This is the concept of the *geopotential cote*, being the geopotential difference with respect to a reference value W_{P_0} at a reference point P_0 :

$$C_P = W_{P_0} - W_P. \quad (1.15)$$

For a better intuition, this quantity (given in m^2/s^2) may be transformed into units of length (metres) by dividing it by some pre-defined constant gravity value.

As mentioned above, the geopotential, and thus the geopotential cote can not be measured directly in practice. However, geopotential *differences* can be determined using a combination of levelled height differences dn , and gravity measurements g along the path from P_0 to P :

$$C_P = W_{P_0} - W_P = \int_{P_0}^P g \, dn. \quad (1.16)$$

In practice, the reference point P_0 is typically located at an oceanic coast, if a mean sea level is used for the definition the reference height (height zero).

There are different height definitions in practice, differing by the type of gravity that is used for the transformation of the cote into a height. Only *orthometric* heights are introduced here as an example: The orthometric height H_P at point P is defined as the vertical distance between the geoid and P , measured along the local plumb line going through P . Based on the geopotential cote, the orthometric height is defined as

$$H_P = \frac{C_P}{\bar{g}}, \quad (1.17)$$

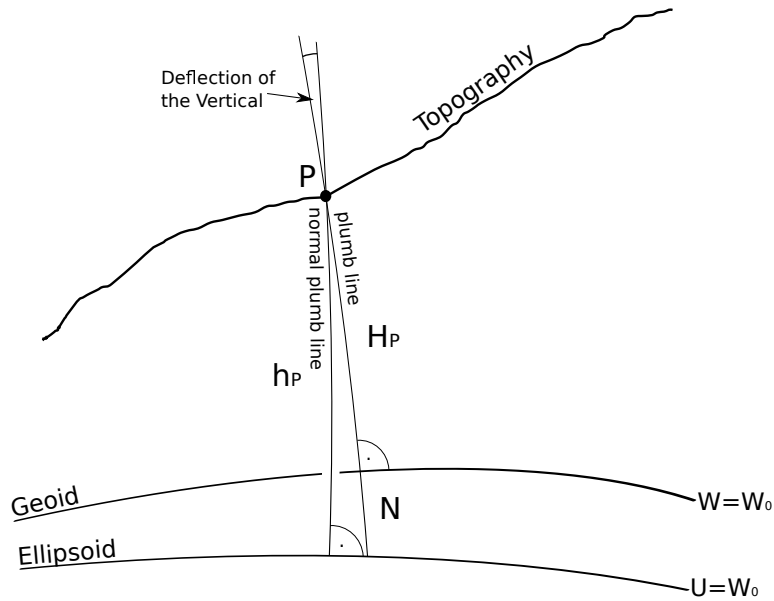


Figure 1.2: Fundamental relation between geoid, ellipsoid, orthometric height H_P of a point P , ellipsoidal height h_P , and geoid height N .

where \bar{g} denotes the mean gravity along the plumb line from P to the geoid. In practice, \bar{g} has to be approximated, based on assumptions regarding the density of the topographic masses. For details on the different height definitions, the reader is referred to *Hofmann-Wellenhof and Moritz (2006)* or *Torge and Müller (2012)*.

Today, levelling over large distances can be facilitated by using high-precision differential GNSS, at an accuracy level of few centimetres, being sufficient for many practical applications. This yields enormous savings in terms of surveying costs and time. However, it is evident from Eq. 1.17, that for the determination of orthometric heights, also gravity measurements are required, being a costly factor in practice.

Therefore, it appears desirable, to measure point heights *only* using GNSS. However, GNSS by itself only provides purely geometric, Earth-fixed coordinates. The property of zero water flow between two points of equal heights is not fulfilled.

However, knowing the shape of the geoid, expressed here by means of the geoid height N , relaxes the requirement of gravity measurements for the determination of orthometric heights. For this, the ellipsoidal height h_P is defined as the distance between the point P and the ellipsoid (as defined by a geodetic reference system), measured along the local *normal* plumb line. Since both the shape of the normal plumb lines and the surface of the ellipsoid are known exactly, h_P can be directly computed from GNSS measurements. The relationship between h_P , and the orthometric height H_P is then given as

$$H_P \approx h_P - N. \quad (1.18)$$

This fundamental equation is illustrated in Fig. 1.2. It indicates the enormous benefit of knowing the geometry of the geoid, N : GNSS-derived ellipsoidal heights h can directly be transformed into orthometric heights H , relaxing the requirement of both levelling *and* in-field gravity measurements. This is today's most important geodetic application of airborne gravimetry: The determination of a local geoid model from airborne gravity measurements (potentially in combination with available terrestrial gravity data), allowing the establishment of national height systems.

1.3.2 Geophysical applications

The knowledge of sub-surface density distributions is an important information for geophysical investigations. However, in particular the determination of the sub-surface materials and densities can be very costly in practice, requiring boreholes of considerable depth.

The most important geophysical application of gravity data is the determination of the sub-surface density distribution (*gravity inversion*). While the knowledge of the density distribution would allow the unambiguous computation of gravity anomalies, the inverse transformation is ambiguous, requiring additional geophysical models and constraints (*Oldenburg, 1974; Boulanger and Chouteau, 2001*). Other data sources, as magnetic, seismic, or electric data, are commonly used in combination with gravity data for the inversion, helping to resolve ambiguities based on assumptions on the material properties (*Li and Oldenburg, 1998*).

Some examples which are relevant in practice are:

- The determination of ice cap thicknesses. Based on assumptions on the density of the bedrock density in combination with the known density of ice, the gravity data can provide estimates for the height of the bedrock surface. A practical example can be found in *Fretwell et al. (2013)*.
- The determination of the geometry of fault lines / tectonics, and its changes over time.
- The determination of other time-variable sub-surface mass movements.
- The gravity inversion can be used for mineral exploration. In particular, oil has a relatively small density compared to rock, allowing the gravimetric discovery of oil resources (*Lelièvre et al., 2012*).

1.4 Thesis outline

This thesis is a contribution towards improving the accuracy of strapdown airborne gravimetry systems. The focus is set on strapdown gravimetry for geodetic applications.

Chap. 2 provides an overview of the state of the art of airborne gravimetry, and strapdown gravimetry in particular. Other authors consistently report a poor long-term stability for strapdown gravimetry, when using an off-the-shelf navigation-grade strapdown IMU. Such long-term instabilities prevent a stand-alone use of such devices for geodetic applications. Further, several publications on IMU calibration methods are introduced, serving as a basis for the parametric calibration methods investigated in this thesis.

The one-step error-state space Extended Kalman filter algorithm for the strapdown gravimetry system is introduced in Chap. 3. The non-linear navigation equations are shown, and the linearised system model and observation models are being deduced. The chapter introduces the modelling of gravity as a Gauss-Markov process. A Kalman smoother is applied to the outputs of the Extended Kalman Filter (EKF).

Chap. 4 provides an analysis of the strapdown gravimetry system. Based on an observability analysis, it is shown, 1. why the determination of the horizontal gravity components is difficult, and 2. why non-linear accelerometer drifts can not be removed from the estimated gravity in practice. A *quantitative* insight into the system is given by an estimability analysis. In particular, it is investigated *how much* observations of certain type and accuracy can contribute to the gravity determination. It is also shown, how aircraft manoeuvres comprising accelerations can positively affect the strapdown gravity determination in theory. Some practical conclusions are drawn from the analyses.

A comprehensive error propagation analysis is presented in Chap. 5. The analysis is based on realistic simulations of aerogravity flights. A variety of systematic errors are investigated,

as time-stamping errors, discretisation errors, GNSS-antenna lever arm errors, and also systematic inertial sensor errors, as biases, scale factors, cross-couplings and misalignments. The findings are complemented by a brief analysis of stochastic inertial sensor errors, as accelerometer and gyroscope noise, gradual stochastic accelerometer drifts, and GNSS coordinate noise. These error propagation simulations can be shown to support the qualitative conclusions drawn in Chap. 4.

Chap. 6 discusses a variety of IMU calibration methods, with an emphasis on long-term accelerometer errors. Among the discussed calibration methods are

1. sample-based models: look-up tables of sensor errors in a predefined state-space, and
2. the more established parametric approaches, calibrating biases, scale factors, and sensor misalignments based on sensor observations in different orientations.

The feasibility of an in-field calibration is briefly discussed for the individual methods. The discussed calibration methods are implemented for an iMAR RQH-1003 navigation-grade strapdown IMU.

As a preparation for the real-data evaluations presented in Chap. 8, a summary of established airborne gravimetry evaluation methods is provided in Chap. 7. Some of the methods, as cross-over residuals and repeated line residuals, are discussed in more depth. Practical recommendations on how to apply these methods are being deduced.

Chap. 8 presents real-data examples of strapdown airborne gravimetry. Measurements from five different airborne gravity campaigns are evaluated, in particular analysing the benefits of the individual calibration methods shown in Chap. 6. The evaluation includes cross-over analyses, an inter-system comparison against stable-platform gravity data, and comparisons against a global gravity model (GGM). The invariance of the strapdown gravity quality against turbulence is shown.

The thesis is concluded with a summary of the central findings, and an outlook.

Chapter 2

State of the art

The first section of this chapter provides an overview of stable-platform airborne gravimetry, which as of today is the predominant method of airborne gravity determination for geodetic applications. The second section gives an overview of publications on strapdown gravimetry, identifying the long-term instability of the sensor as the main limitation of this approach. The third section deals with IMU calibration methods in general, followed by a brief section on GNSS processing in view of airborne gravimetry.

2.1 Stable-platform airborne gravimetry

After kinematic gravimetry systems for the use in underwater gravimetry had already been investigated since the early 1950s, the first test of airborne gravimetry was published in 1960 using a stabilised-platform spring gravimeter (*Nettleton et al.*, 1960). The measuring principle can be explained as follows: A mechanical spring is attached to a horizontal beam, both being in a high-viscosity fluid to dampen mechanical vibration and shocks. A so-called zero-length spring is being used (*LaCoste*, 1988). The tension of the spring is automatically adjusted in a feedback control circuit, such that the beam approximately maintains its horizontal alignment. The output of the sensor is given as a combination of the beam velocity (it is an underdamped system), and the applied spring tension. These quantities are then transformed into units of a specific force by using pre-calibrated look-up tables. In a kinematic set-up, this type of gravimeter requires a convergence time of typically 100s to 200s in order to provide results at the level of few mGal. This implies, that the maximum *spatial* resolution of the gravity measurements is limited mainly by the aircraft speed, where lower speeds yield a higher spatial resolution.

In practice, the platform stabilisation is subject to inaccuracies coming from latencies of the feedback-circuit, and drifts of the gyroscopes. Auxiliary, horizontally aligned accelerometers are used for computationally reducing such errors. In fact, a proper design of platform tilt corrections could be shown to be crucial for accurate stable-platform gravimetry (*LaCoste*, 1967; *Olesen*, 2002).

Aircraft accelerations $\ddot{\mathbf{r}}$ have to be removed from the measured specific force (cf. Sec. 1.2.3). Before global navigation satellite systems (GNSS) became available in the 1990s, the aircraft accelerations had to be measured using radar altimetry in combination with high-resolution terrain models.

Airborne gravimetry experienced a significant rise when the Global Positioning System (GPS) became available in the 1990s. The second derivatives of aircraft GPS positions could be used to determine the aircraft accelerations $\ddot{\mathbf{r}}$ more accurately and more easily compared to radar altimetry. Since then, the combination of a platform-stabilised spring gravimeter and GPS has been the predominant method for airborne gravity determination, with reported accuracies of 1 mGal to 4 mGal at a spatial resolution of several kilometres (typically 3 km

to 10 km half-wavelength, depending on the aircraft speed). An overview of the platform-stabilised gravity data acquisition, and its use for the local geoid determination, can be found in *Forsberg and Olesen (2010)*. More results from stabilised-platform airborne gravimetry campaigns can be found in *Brozena (1992)*; *Brozena et al. (1997)*; *Bastos et al. (1998)*; *Forsberg et al. (2001)*; *Studinger et al. (2008)*.

2.2 Strapdown gravimetry

In parallel to the development and rise of platform-stabilised gravimeters, *Schwarz (1983)* already formulated the potential of using inertial measurement units (IMU) for geodetic positioning and gravity field determination. In particular, an IMU with three orthogonal accelerometers enables the determination of the full 3-D gravity vector (*vector gravimetry*). *Forsberg et al. (1986)* was able to show, that accuracies of 1-2 arc seconds are possible for the deflections of the vertical (DoV), and 2.5 mGal to 4 mGal for the (vertical) gravity anomalies. Mainly due to the difficulties of determining the vehicle accelerations $\ddot{\mathbf{r}}$, these measurements were done in a semi-kinematic set-up: The vehicle (truck and helicopter) was parked in regular intervals to enable the gravity determination, by ensuring $\ddot{\mathbf{r}} = 0$, i.e. the specific force measurements could directly be used as gravity measurements, using $\mathbf{f} = -\mathbf{g}$. Exploiting such knowledge of static phases of the vehicle motion (*zero-velocity observations*) is still relevant for state-of-the-art navigation systems. Further, *Forsberg et al. (1986)* show the importance of using optimal smoothers for such a gravimetry system. The quality of the original (non-smoothed) real-time gravity estimates was shown to be worse by a factor of 3 and more.

As for stabilised-platform gravimetry, the availability of accurate GPS signals enabled strapdown gravimetry in a relatively simple and efficient set-up. (However, compared to today's technology, it should be noted that the kinematic GPS data acquisition from an aircraft was still a challenging task at that time.) The work of *Schwarz et al. (1992)* investigates the requirements to strapdown airborne vector gravimetry, also in view of the GNSS signal quality. Based on accuracy requirements defined by the respective applications of vector gravity data, e.g. for geophysical and geodetic applications, technical requirements for the IMU and the GPS systems are deduced. A more comprehensive discussion of practical problems, as GPS errors, and IMU errors coming from aircraft vibration, is provided in *Schwarz and Wei (1995)*. Also, the ultimate accuracy goal of scalar airborne gravimetry was defined to be 1 mGal in this publication.

Based on simulations, *Jekeli (1994)* investigates which kind of a stochastic process best models the along-track gravity signal over time. Different Gauss-Markov processes are compared, showing that third- and fourth-order Gauss-Markov processes may serve as suitable models.

Also based on simulations, *Jekeli (1994)* analyses in more detail the particular challenges of vector gravimetry. It is stated, that the strong correlation between attitude instabilities and the errors of the estimated deflections makes the gyroscope sensor stability the main limiting factor for the determination of the DoV. For example, an attitude error of 1 arc seconds fully propagates into the DoV estimates (equivalent to ≈ 5 mGal), while the same attitude error is negligible for the vertical component ($\ll 1 \mu\text{Gal}$). Based on simulated data, *Jekeli (1994)* expects that the DoVs can be determined at the level of 3 mGal (0.63 arc seconds) for wavelengths shorter than 250 km, when using centimetre-level GPS updates in combination with high-precision ring-laser gyroscopes (assuming a gyroscope bias of $0.0006^\circ/h$ and an angular random walk of $0.00037^\circ/\sqrt{h}$). A similar conclusion was already drawn in *Jekeli (1992)* for kinematic IMU/GPS gravimetry using a balloon as platform.

The operability of a strapdown gravimetry system could be shown by *Wei and Schwarz (1998)*. The system consisted of a Honeywell LASEREV III strapdown IMU, with Honeywell GG1342 ring-laser gyroscopes, and Honeywell QA-2000 accelerometers. Differential GPS

(DGPS) coordinates are used for the determination of the aircraft accelerations. Using a repeated-line agreement as quality metric, an estimated overall standard deviation of approximately 2 mGal, and 3 mGal, could be shown for along-track low-pass filters using threshold frequencies of 1/120 Hz, and 1/90 Hz, respectively.

Two different gravity processing methods are compared in *Wei and Schwarz (1998)*: 1. Using the gyroscope measurements for a full strapdown navigation solution, taking into account the orientation of the sensor, and 2. only using the *absolute* specific force $f = |\mathbf{f}^s|$ measured by the accelerometer triad in the sensor coordinate frame s . The latter approach appears desirable for its simplicity, as no attitude information is required (it is therefore called a *rotation-invariant* system). However, the results presented in *Wei and Schwarz (1998)* show, that the full strapdown approach systematically yields better results. In the scope of this thesis, only the full strapdown approach is investigated. Compared to the repeated-line agreement, the residuals of upward-continued ground points were clearly larger (4 mGal to 5 mGal vs. 2 mGal to 3 mGal). The authors formulated the expectation, that the uncertainties involved with the spatial interpolation of the terrestrial gravity points, and their upward continuation to flight altitude can reach the level of several mGal, thereby questioning the usability of such ground points as a reliable reference.

Shortly after this first successful test of strapdown gravimetry, the same group was able to confirm the results of their LASEREV III based strapdown gravimetry system (*Glennie and Schwarz, 1999*). After removing a linear drift from the gravity estimates, a cross-over analysis showed overall residuals as low as 1.6 mGal. This emphasises the high potential of strapdown gravimetry. However, it needs to be mentioned here, that these precision values heavily depend on the removal of biases and linear drifts, which were computed individually for each of the lines. Drifts of 4 mGal to 5 mGal per 15 minutes flight line are reported (≈ 18 mGal/h). Also, the presented residual cross-over differences may be rather optimistic, coming from a relatively weak over-determination for the estimation of linear drift parameters. This will be discussed in more detail in Sect. 7.1.1. Since the assumption of *linear* drifts is not true in practice, long-term drifts may still reside in the gravity estimates after applying such a linear drift interpolation method, cf. *Becker et al. (2015b)*.

It is just noted here, that *Glennie and Schwarz (1999)* report an optimal low-pass filter cut-off frequency for their test flights between 1/90 Hz and 1/120 Hz. The iMAR RQH-1003 strapdown IMU, used for gravimetry tests in this thesis, shows a similar optimum low-pass frequency of approximately 1/90 Hz. *Lower* cut-off frequencies may allow better estimation results, if the actual along-track gravity does not contain such high-frequency component (promoted by lower flight speeds, and higher flight altitudes). Using *higher* low-pass threshold frequencies apparently introduces more noise than signal to the estimates, independent of the gravity field characteristics.

In *Kwon and Jekeli (2001)*, a so-called wavenumber correlation filter was introduced, extracting correlating parts of the individual gravity measurements of *repeated* flight tracks. Vertical gravity estimates at a precision level of 3 mGal to 4 mGal could be achieved on real data using a Honeywell LASEREV III IMU. The horizontal gravity components could be estimated at a precision of 6 mGal. For production-oriented campaigns, it should be noted though, that the repetition of all flight lines may be too costly in practice.

Kwon and Jekeli (2001) also analyse two different methods for modelling gravity: 1. *Not* modelling gravity at all, but using the Kalman-filtered accelerometer bias estimates as gravity estimates instead, and 2. adding gravity states to an IMU/GNSS navigation Kalman filter, explicitly modelling gravity as a third-order Gauss-Markov process. It is stated, that such an extension of the filter state yielded *worse* results compared to not modelling gravity at all. In this thesis, the extended state approach is still being used, because it conversely yielded *best* results after applying an optimal filter to the Kalman filter estimates, commonly referred to as *Kalman smoother*, or *RTS smoother* (*Rauch et al., 1965*).

Comparison results of the same LASEREV III strapdown IMU gravimetry system, and a platform-stabilised LaCoste & Romberg S-type sea/air gravimeter (LCR) are presented in *Glennie et al. (2000)*. The two sensors were flown side by side for a set of three test flights out of Greenland. For the first time, a direct comparison between stable-platform and strapdown gravimetry was published. Such a side-by-side comparison can be expected to be the *only* way of getting resilient comparison results, because each aerogravity flight shows different operation conditions, making the comparison among different flights or campaigns difficult. Such conditions are for example

- the weather conditions / turbulence,
- the flight altitude and flight speed,
- aircraft-specific effects (as the so-called *phugoid* motion or other vibrations, cf. *McRuer et al. (2014)*),
- the tropospheric and ionospheric activity hampering the GNSS signals,
- the GNSS satellite constellation,
- the characteristics of the *true* gravity signal, mainly depending on flight altitude and terrain type, or
- the type of filtering, and the type of the applied bias or drift removal, which itself may yield different results depending on the line lengths and/or the number of cross-over points per line (some details are discussed in *Becker et al. (2015b)*, and also in Chap. 7 of this thesis).

In addition to the inter-system comparison, *Glennie et al. (2000)* were able to verify the results based on shipborne gravity data, which was available along the flight tracks. The low flight altitude of only 300 m allowed the use of this data without the requirement of an upward continuation. For the LCR data processing, a low-pass filter with a cut-off frequency of 1/200 Hz was used. To ensure comparability, the LASEREV III system was filtered with the same parameters. Again, a linear drift had to be removed from the strapdown gravity estimates, documented to be as much as 0.01 mGal/s (equalling 36 mGal per hour). After low-pass filtering and drift removal for the strapdown data, both systems showed an agreement between 1.1 mGal and 4.4 mGal among the different flight lines. It is concluded in *Glennie et al. (2000)*, that strapdown gravimetry has a comparable potential for the gravity field determination with respect to the more established stable-platform systems (as LCR), except that the long wavelength stability of the strapdown sensors is relatively poor, preventing its stand-alone use for full-spectrum gravimetry. Instead, the authors expect that a *combination* of both types of sensors may be beneficial, augmenting the long-wavelength stability of the LCR system with the higher spatial resolution of a strapdown device.

Summing up, while a strapdown gravimetry system could be shown to have a similar or even superior quality in the short-wavelength spectrum compared to mechanical stable-platform spring gravimeters (*Glennie et al., 2000; Bruton, 2002*), its long-term instability prevents stand-alone strapdown gravimetry at the accuracy level of 1 mGal. It is expected by several authors, that such long-term drifts of the gravity estimates come from uncompensated drifts of the accelerometers. For an almost horizontal and non-accelerated flight, such accelerometer drifts are inseparable from along-track changes of the gravity signal, because *all* observations show an equal response to either an accelerometer bias change, or an along-track change of the gravity signal of the same direction and intensity (*Glennie and Schwarz, 1999; Kwon and Jekeli, 2001; Deurloo, 2011*). This inseparability will be discussed in more detail in Chap. 4, based on an observability analysis.

Most authors suggest the removal of constant biases or linear drifts for each of the individual flight lines, using a least-squares regression based on redundant or external measurements, as cross-over residuals (*Hwang et al. (2006)*; *Glennie and Schwarz (1999)*, and others), or global gravity models (*Bos et al., 2011*; *Deurloo, 2011*; *Ayres-Sampaio et al., 2015*), see also *Becker et al. (2015b)*. This thesis aims to show, that by using appropriate IMU calibration methods, *accuracies* at the 1 mGal-level can be reached using very similar off-the-shelf inertial sensors *without applying any bias or drift removal* to the gravity estimates.

In particular, *Bruton et al. (2001)* and *Bruton (2002)*, who faced similar drift rates using the same Honeywell LASEREV III system, expressed the expectation, that a relevant portion of these drifts may come from *thermal* effects. A side by side comparison is presented in *Bruton et al. (2001)* between the LASEREV III strapdown system, and an AIRGrav airborne gravimetry system. The latter is a *thermally stabilised* IMU, mounted on a three-axis stabilised platform. While the LASEREV III system showed drift rates between 0.013 mGal/km and 0.065 mGal/km (equivalent with 2.1 mGal/h to 10.5 mGal/h for the average flight speed of 45 m/s), the AIRGrav system showed rates between 0.0005 mGal/km and 0.003 mGal/km (0.1 mGal/h to 0.5 mGal/h). The findings presented in this thesis support this expectation of a thermal dependency, showing that similar drift rates of the iMAR RQH-1003 system of 3 mGal/h to 4 mGal/h can be reduced to only ≈ 0.3 mGal/h by applying a suitable thermal correction to the QA-2000 accelerometer measurements.

2.3 IMU calibration methods

There exists plenty of literature on the calibration of IMU's, and accelerometers and triads of accelerometers in particular. The main principles for the calibration of lower-grade, so-called *microelectromechanical systems* (MEMS) are mostly identical to those carried out on tactical-grade or navigation-grade devices.

A standard error model for a single accelerometer is the combination of bias and scale factor. Most of the sensor errors of a single accelerometer can typically be described using such a model. The reason for this can be found in the working principle of an accelerometer: A proof mass is maintained in some defined zero-position using a feedback loop. The force, that needs to be applied to maintain this zero position (e.g. by using an electromagnetic field, controlled by an electric current) is then proportional to the specific force that is acting on the proof mass (following Newtons Second Law of motion). Thus, there is a proportionality factor between the controlled quantity (as the electric current) and the specific force. An accelerometer *bias* can be interpreted as the force that needs to be applied to keep the proof-mass in its defined zero-position, if actually *no* specific force is acting on the proof mass (i.e., the accelerometer is in free fall). An accelerometer scale factor arises from errors of the proportionality factor, usually coming from inaccuracies of the electronic components (the quantisation and analogue-to-digital conversion of the applied quantity, or the actuator system maintaining the zero-position). Such errors can change over time, and also over different temperatures. While the long-term changes over months or years can usually not be predicted adequately, the temperature dependency shows a relatively good repeatability in general.

A thermal calibration of an accelerometer is the determination of any reproducible temperature dependencies of the sensor. The calibration principle is simple: The sensor is exposed to different temperatures, and the outputs are compared to a ground-truth reference value. Typical implementations are (*Bhatt et al., 2012*):

- The *soak* method: The sensor is given time to stabilise thermally, having a constant ambient temperature (the core temperature of the sensor is typically higher, due to its electrical energy consumption). The outputs are then recorded for several ambient temperatures, together with core temperature readings, if available.

- The *ramp* method: The sensor is exposed to a variable ambient temperature (e.g. a linear temperature increase over time). The sensor outputs, and the ambient or core temperature are recorded continuously.

The ramp method is not only a temperature calibration, but in fact also a temperature *gradient* calibration: It typically takes a significant amount of time for the sensor to thermally stabilise. For example, for a QA-2000 accelerometer mounted inside the iMAR RQH-1003 housing, it takes up to two hours for the internal sensor temperature to converge with less than 1 K difference w.r.t. the asymptotic temperature (after infinite time). Thus, changes of the ambient temperature yield changes in the accelerometer readings with considerable latency, depending on the physical characteristics of the involved materials, the temperature gradients, and the absolute temperature level.

The ramp method is still a useful method for the calibration of a warming-up phase of the sensor. For such specific *changes* of temperature (and potentially changes of the temperature gradient), it can be expected to yield better results than the soak method. Both methods are investigated in this thesis.

With respect to some external reference orientation of the accelerometer, two more parameters have to be taken into consideration: the two angular misalignments of the sensor's sensitive axis with respect to the predefined external orientation. These angular misalignments are sometimes denoted as hinge (-axis) and pendulum (-axis). Thermal dependencies of these parameters can also be observed in practice, potentially coming from thermal deformations of the IMU housing, or bends of the accelerometer suspension.

A strapdown IMU usually comprises three nominally orthogonal accelerometers. This yields a total of 12 parameters for a triad of accelerometers (three biases and scale factors, and a total of six misalignment angles).

Calibrations of this set of parameters (or a subset of these) are commonly based on the measurement of the local gravity in different IMU orientations (also referred to as *multi-position* methods). A good overview of such methods is shown in *El-Diasty and Pagiatakis (2008)*. The accelerometer readings for six static orientations (each of the three axes pointing up and down) is sufficient for the determination of the three biases, scale factors, and the three non-orthogonality angles (*cross-couplings*) of the triad. For high-precision calibrations, the exact 3-D gravity vector is required as an input. This requirement is seldom met in practice, because the deflections of the vertical are relatively difficult to determine in the field, compared to terrestrial *scalar* gravity measurements.

A novel method was introduced by *Shin and El-Sheimy (2002)*, relaxing the requirement of knowing the 3-D gravity vector. It is shown, that only using the absolute gravity measurements of the accelerometer triad $\tilde{\mathbf{f}} = |\tilde{\mathbf{f}}^s|$, and comparing it to the *scalar* ground truth gravity value, is sufficient for the determination of the nine aforementioned parameters. For this, however, each orientation of the IMU will only contribute a single condition equation to the non-linear system. Therefore, a set of nine orientations is required for a direct computation of the nine parameters without over-determination. Using a larger set of IMU orientations is suggested by several authors in order to enable a least-squares adjustment with a reasonable over-determination (*Shin and El-Sheimy, 2002; Skog and Händel, 2006; Batista et al., 2011*). A major advantage of this method is, that the actual orientation of the IMU does not need to be known. Therefore, such a calibration can be done in-field even for high-precision sensors, without using any professional calibration equipment (as a calibration turn table). This will be illustrated in more detail in Sect. 6.4.

It is just briefly noted here, that such a multi-position (or multi-orientation) calibration can be equally used for the determination of gyroscope errors. However, scale factors and cross-couplings can not be determined reasonably, when using the relatively weak Earth rotation rate as stimulus signal. This issue is addressed by *Syed et al. (2007)*, who propose a modified implementation based on a stronger stimulus signal, using a three-axis turn table.

Several authors (*Aggarwal et al.*, 2008b,a; *Yang et al.*, 2013) investigate *thermal* multi-position calibrations: For a set of different nominal ambient temperatures, the IMU is given time to thermally stabilise ('soak' approach). Then, the multi-position calibration as introduced above is repeated for each of these nominal temperatures. The individual parameter estimates, computed for the discrete, nominal temperatures, are then interpolated using a regression polynomial or a smoothing spline, yielding nine continuous parameter functions of temperature (for each of the nine parameters: biases, scale factors, and cross-couplings). This approach will be investigated in Sect. 6.5.1 for the iMAR RQH-1003 unit. Also, an extended parametric error model is investigated, using additional scale factors.

An important assumption for multi-position approaches in general is the constancy of the estimated parameters for the whole set of observations (among the different IMU orientations). Thus, the *ramp*-method introduced above is not applicable to a thermal multi-position calibration (or only with respective modifications), as thermal drifts occurring *within* a set of multi-position observations can not be avoided.

Chap. 6 will also investigate non-parametric, *sample-based* approaches, which are less established in the literature. After applying a standard calibration (bias, scale factor, cross-coupling), the residual sensor errors are collected in a look-up table. This look-up table is constructed for a larger set of samples in a predefined state space, for example accounting for temperature and IMU orientation.

2.4 GNSS processing

The focus of this thesis is set on the design and evaluation of strapdown IMU calibration methods for the use in strapdown gravimetry. Several authors state, that such IMU errors are the main limiting factor when aiming at more accurate strapdown airborne gravity estimates (and this expectation is supported by the findings presented in this thesis). It is just briefly noted here, that several authors also investigated methods for the accurate determination of aircraft accelerations from GNSS, for the application of strapdown gravimetry (*Jekeli and Garcia*, 1997; *Bruton et al.*, 2002; *Kreye and Hein*, 2003). In particular, *Jekeli and Garcia* (1997) show on real data, that an averaging of the GNSS-derived accelerations over 40 s is sufficient to gain estimates at the 1-mGal-level. By comparing this period to the typical strapdown gravimetry low-pass frequencies documented in the literature (typically 1/90 Hz or lower, cf. Sect. 2.2), it can be seen, that a state-of-the-art GNSS processing is presumably *not* the limiting factor for an IMU/GNSS strapdown gravimetry system. More details, including a spectral comparison of GNSS accelerations and accelerometer measurements, can be found in *Jekeli* (2001).

It is an open question, if, or how much airborne gravimetry in general can benefit from the new global navigation satellite systems becoming available (Beidou, Galileo). An analysis based on simulated observation data is presented in *Skaloud et al.* (2015). In the scope of this thesis, an integrated IMU/GNSS Kalman filter approach is being used. GNSS coordinate observations are introduced to the filter, which are computed in a pre-processing step using the commercial software Waypoint GrafNav 8.60 (*Novatel Inc.*, 2014). Introducing readily processed coordinates and velocities to an integrated IMU/GNSS filter is commonly referred to as a *loosely-coupled* IMU/GNSS integration. This thesis will use GNSS coordinates gained from GNSS precise point positioning (PPP) (*Kouba and Héroux*, 2001), as well as from two-frequency carrier phase-differential GNSS (PD-GNSS) (*Hunzinger*, 1997; *Hofmann-Wellenhof et al.*, 2012).

Chapter 3

An Integrated IMU/GNSS Strapdown Gravimetry System

In this chapter, a Kalman Filter is designed for the integration of IMU and GNSS observations. The Kalman Filter is a well-known *best linear unbiased estimator* (BLUE) for time-discrete linear systems. For non-linear systems, the *Extended Kalman Filter* (EKF, cf. *Gelb* (1974)) can be used, which is based on a first-order Taylor approximation of the system and measurement models. The EKF does not have the BLUE property in general, because of the errors resulting from the linearisation.

For strapdown gravimetry, there exist two common approaches for the processing of the IMU measurements in the literature:

- The cascaded approach, as used by *Glennie and Schwarz* (1999); *Glennie et al.* (2000); *Bruton* (2002) and others:
 1. A standard IMU/GNSS *navigation* algorithm, typically based on a Kalman Filter, is executed in order to determine the rotation matrix \mathbf{C}_b^n , transforming quantities between the local-level coordinate frame n , and the body-fixed IMU sensor frame s for each epoch. For details on such navigation filters, the reader is referred to *Groves* (2013); *Jekeli* (2001). The unmodelled along-track gravity changes may propagate into the attitude and accelerometer bias estimates. GNSS coordinates are introduced as measurements to the EKF, and sometimes velocity measurements as well. A Kalman smoother may be applied (cf. Sect. 3.6).
 2. Using an aiding sensor, aircraft accelerations $\ddot{\mathbf{r}}^n$ are computed separately, e.g. by computing the second derivatives of GNSS coordinates.
 3. The IMU specific force measurements \mathbf{f}^b are transformed into the navigation frame using $\mathbf{f}^n = \mathbf{C}_b^n \mathbf{f}^b$, where the rotation matrix \mathbf{C}_b^n is taken from the integrated IMU/GNSS navigation solution.
 4. The gravity \mathbf{g} is then essentially determined by applying a low-pass filter to the difference $\ddot{\mathbf{r}}^n - \mathbf{f}^n$ (cf. Eq. 1.13).
- The *one-step* approach uses a single Kalman filter, integrating *all* relevant measurements and quantities, in particular including system states for gravity. Commonly, a *Kalman smoother* or *RTS smoother* (*Rauch et al.*, 1965) is applied to the outputs of the EKF. This smoother is directly applied to the EKF outputs, not requiring any additional parameters. The one-step approach was introduced by *Schwarz and Wei* (1990), and used in similar form by *Kwon and Jekeli* (2001); *Tomé* (2002); *Deurloo* (2011); *Deurloo et al.* (2015); *Becker et al.* (2015b); *Ayres-Sampaio et al.* (2015). The one-step approach is also called *indirect* approach, because gravity estimates are actually derived from the comparison of *coordinates*, as will be shown later in this section (*Jekeli*, 2001).

In the scope of this thesis, only the one-step approach will be taken into consideration for the following reasons:

- No additional low-pass filter needs to be applied to the outputs of the EKF, simplifying the overall process. The smoothed EKF estimates automatically include higher frequency components of the gravity signal *to the extent to which they are estimable* (cf. Chap. 4).
- The one-step approach is regarded as the more rigorous one: Combining any available information in a *single* system model may enable an optimal estimation. Conversely, separating parts of the system, which are actually inseparable (as gravity and accelerometer biases, or the deflections of the vertical and attitude, cf. Sect. 4.1), may introduce unwanted smearing effects.
- Standard system analysis methods, as an observability analysis or an estimability analysis of the gravity states, can directly be applied to the system model of the one-step approach (cf. Chap. 4). Conversely, such methods are not directly applicable to the cascaded approach.

The well-known EKF equations are repeated in the following section for the sake of completeness, and also for the clarification of the used symbols in this thesis. For details on Kalman Filtering in general, the reader is referred to *Gelb (1974)*.

3.1 Extended Kalman filter

For an n -dimensional system state vector \mathbf{x}_{k-1} at time t_{k-1} , the state transition to the next epoch t_k is given as

$$\mathbf{x}_k = \boldsymbol{\varphi}(\mathbf{x}_{k-1}, \mathbf{u}_{k-1}, dt_{k-1}) + \mathbf{w}_{k-1}^s, \quad (3.1)$$

with control \mathbf{u} , time increment $dt_k = t_k - t_{k-1}$, the n -dimensional, non-linear state transition function $\boldsymbol{\varphi}$, and a vector of Gaussian white noise $\mathbf{w}^s \sim \mathcal{N}(\mathbf{0}, \mathbf{Q}_k)$, also called *system noise*. The linearised version of Eq. 3.1 can be defined using Jacobian matrices of partial derivatives as

$$\mathbf{x}_k = \boldsymbol{\Phi}_{k-1} \mathbf{x}_{k-1} + \mathbf{B}_{k-1} \mathbf{u}_{k-1} + \mathbf{w}_{k-1}^s, \quad \text{with} \quad (3.2)$$

$$\boldsymbol{\Phi}_{k-1} = \left. \frac{\partial \boldsymbol{\varphi}}{\partial \mathbf{x}} \right|_{\mathbf{x}_{k-1}} \quad (3.3)$$

$$\mathbf{B}_{k-1} = \left. \frac{\partial \boldsymbol{\varphi}}{\partial \mathbf{u}} \right|_{\mathbf{x}_{k-1}}. \quad (3.4)$$

For many applications, the system state change $\mathbf{x}_k - \mathbf{x}_{k-1}$ is proportional to the time increment dt_k , allowing a differential definition of the state transition function $\boldsymbol{\varphi}$, using

$$\boldsymbol{\varphi}(\mathbf{x}_{k-1}, \mathbf{u}_{k-1}, dt_{k-1}) = \mathbf{x}_{k-1} + \mathbf{f}(\mathbf{x}_{k-1}, \mathbf{u}_{k-1}) dt_{k-1}, \quad \text{and} \quad (3.5)$$

$$\boldsymbol{\Phi}_{k-1} = \mathbf{I} + \mathbf{F}_{k-1} dt_{k-1}, \quad \text{with} \quad (3.6)$$

$$\mathbf{F}_{k-1} = \left. \frac{\partial \mathbf{f}}{\partial \mathbf{x}} \right|_{\mathbf{x}_{k-1}}, \quad (3.7)$$

where \mathbf{I} denotes the $n \times n$ identity matrix.

External information is introduced to the EKF using the concept of *measurements*. The measurement model contains the functional, and the stochastic model of the measurements.

As for the system model, the measurement model can be defined in its general (non-linear) form, and its linearised equivalent as

$$\mathbf{z}_k = \mathbf{h}(\mathbf{x}_k) + \mathbf{w}_k^z, \quad \text{and} \quad (3.8)$$

$$\mathbf{z}_k = \mathbf{H}_k \mathbf{x}_k + \mathbf{w}_k^z, \quad \text{respectively,} \quad (3.9)$$

with measurements \mathbf{z} , measurement noise $\mathbf{w}^z \sim \mathcal{N}(\mathbf{0}, \mathbf{R}_k)$, and the Jacobian matrix of the partial derivatives

$$\mathbf{H}_k = \left. \frac{\partial \mathbf{h}}{\partial \mathbf{x}} \right|_{\mathbf{x}_k}. \quad (3.10)$$

Assuming m measurements at time epoch k ($\dim(\mathbf{z}_k) = m$), the matrix \mathbf{H}_k is of the dimension $m \times n$.

The system is initialized with \mathbf{x}_0 and its covariance matrix \mathbf{P}_0 . The KF (or EKF) is then based on two steps, carried out in each epoch: the prediction step (computing the state transition from t_{k-1} to t_k), and the measurement update, filtering the system state by means of a measurement \mathbf{z}_k (if a measurement is available). Predicted and filtered quantities are marked with superscripts $-$, and $+$, respectively.

The prediction step from t_{k-1} to t_k is based on the filtered state and covariance estimates of the previous epoch:

$$\hat{\mathbf{x}}_k^- = \boldsymbol{\varphi}(\hat{\mathbf{x}}_{k-1}^+, \mathbf{u}_{k-1}, dt_{k-1}) \quad (3.11)$$

$$\hat{\mathbf{P}}_k^- = \boldsymbol{\Phi}_{k-1} \hat{\mathbf{P}}_{k-1}^+ \boldsymbol{\Phi}_{k-1}^T + \mathbf{Q}_{k-1}. \quad (3.12)$$

Note, that the linearisation of $\boldsymbol{\varphi}$ is only used for the prediction of the covariance matrix \mathbf{P} , while the actual prediction of the system state can be evaluated exactly, using the non-linear transition function $\boldsymbol{\varphi}$.

The measurement update is given as

$$\hat{\mathbf{x}}_k^+ = \hat{\mathbf{x}}_k^- + \mathbf{K}_k \mathbf{i}_k \quad (3.13)$$

$$\hat{\mathbf{P}}_k^+ = \hat{\mathbf{P}}_k^- - \mathbf{K}_k \mathbf{S}_k \mathbf{K}_k^T, \quad \text{with} \quad (3.14)$$

$$\mathbf{i}_k = \mathbf{z}_k - \mathbf{h}(\hat{\mathbf{x}}_k^-) \quad (3.15)$$

$$\mathbf{S}_k = \mathbf{H}_k \hat{\mathbf{P}}_k^- \mathbf{H}_k^T + \mathbf{R}_k \quad (3.16)$$

$$\mathbf{K}_k = \hat{\mathbf{P}}_k^- \mathbf{H}_k^T \mathbf{S}_k^{-1}, \quad (3.17)$$

with innovation \mathbf{i} , innovation covariance matrix \mathbf{S} and Kalman gain matrix \mathbf{K} . The innovation \mathbf{i} can be regarded as the driving force of the Kalman Filter: It compares the actual measurement \mathbf{z}_k with a hypothetical measurement $\mathbf{h}(\hat{\mathbf{x}}_k^-)$, that would have been sensed by an error-free sensor, if the predicted system state was error-free.

Note: The quantities \mathbf{i} , \mathbf{S} and \mathbf{K} are *estimated* quantities, and even $\boldsymbol{\Phi}$, \mathbf{Q} , and \mathbf{R} may depend on the estimated system state $\hat{\mathbf{x}}$ itself for some applications. The respective accent ($\hat{\cdot}$) was omitted here for clarity.

3.1.1 Modelling IMU measurements as control

For efficiency reasons, the high-rate IMU measurements, accelerations and turn rates at 100 Hz or more, are not introduced to the EKF as *measurements* in the sense of the Kalman Filter definition, but as control \mathbf{u} instead. This can reduce the computational load drastically in practice, because the time-consuming matrix inversion \mathbf{S}^{-1} is not required at the high IMU data rate. Another advantage is, that the accelerations and turn rates do not have to be included in the system state, as it would be required in order to model the functional relationship expressed by the \mathbf{h} function (Eq. 3.8). The noise of the inertial sensors is then

accounted for in the system noise vector \mathbf{w}^s : the accelerometer noise maps into the velocity system noise, and the gyroscope noise maps into the attitude system noise (Groves, 2013).

Aiding information, as pre-processed GNSS coordinate and velocity observations, will be introduced to the EKF as measurements \mathbf{z} as introduced above, yielding innovations \mathbf{i} with respect to the predicted quantities (*loosely-coupled* integration).

The prediction of the system state covariance matrix \mathbf{P} (Eq. 3.12) can be done at a lower rate, e.g. only at 10 Hz or 1 Hz, without any significant impact on the state estimates (the system can be assumed to be linear for very short time periods), cf. Groves (2013).

3.1.2 Error state space formulation

For reasons of numerical stability, it is a common approach for integrated IMU/GNSS systems to use an error state space formulation of the Kalman filter. Here, the actual *system states*, position, velocity, attitude, and sensor error estimates, are maintained *outside* of the filter, while the filter's *error state* vector $\delta\hat{\mathbf{x}}$ is modelled as the difference between the estimated and the true quantities, i.e.

$$\delta\hat{\mathbf{x}} = \hat{\mathbf{x}} - \mathbf{x}. \quad (3.18)$$

An immediate consequence of the bias-free estimation is, that the *predicted* error state vanishes at all times, i.e. $\delta\hat{\mathbf{x}}^- = \mathbf{0}$. After each measurement update, the estimated error state vector $\delta\hat{\mathbf{x}}^+$ is applied externally to the system states, and has to be reset to zero afterwards. Therefore, in the error-state formulation, Eq. 3.11 has to be replaced by letting

$$\delta\hat{\mathbf{x}}_k^- = \mathbf{0}. \quad (3.19)$$

3.2 Strapdown Gravimetry System Design

The system design for the strapdown gravimetry system is based on an error state space EKF. First, the used coordinate frames need to be introduced. Then the system state \mathbf{x} is defined, followed by a brief deduction of the system and observation models.

3.2.1 Coordinate frames

First, the relevant coordinate frames are introduced. All coordinate frames used are right-handed and Cartesian, thus the definition of two of the three mutually perpendicular axes suffices to define the frame:

- The Earth-centred inertial frame, denoted with superscript i : Located in the Geocentre, with x^i pointing towards the vernal equinox, and z^i pointing towards the Earth's North Pole, as given by the ITRF 2008 frame (Altamimi et al., 2011).
- The Earth-centred and Earth-fixed frame, denoted with superscript e : Located in the Geocentre, with x^e pointing towards the intersection of the Greenwich meridian and the Earth's equatorial plane, and $z^e = z^i$.
- The navigation frame (sometimes called *local level* frame), denoted with superscript n : Located in the common intersection of the three sensitive accelerometer axes of the IMU, with x^n pointing towards North (as given by the ITRF 2008 frame), and z^n pointing downwards along the local tangent of the *normal* plumb line, and y^n pointing East. This frame is sometimes referred to as *North-East-Down* frame (*NED*). In the following, the components of any vector \mathbf{a}^n are therefore denoted as a^N , a^E , and a^D .

- The body-fixed frame, denoted with superscript b : Located at the same position as the n frame (see above), with x^b pointing to the *front* of the vehicle (based on any reasonable definition; aircraft: parallel to the fuselage axis), and z^b pointing downwards (e.g. perpendicular to the vehicle floor). Thus, y^b is pointing to the vehicle's *right* (aircraft: parallel to the wing-axis), completing the right-handed frame. Note in particular, that the body-fixed '*down*' is not collinear with the navigation-frame '*down*' in general, i.e. $z^n \neq z^b$. For better readability, the three axes will also be denoted by their intuitive direction with respect to the vehicle motion (Front-, Right-, and Down-Axis). When referring to the IMU sensors, which are aligned in these directions, also the notation X-, Y-, and Z-axis (or X-accelerometer etc.) is used.

Other authors add additional frames, e.g. an IMU sensor frame s , in addition to the body-fixed vehicle frame. In this thesis, only systems comprising a single IMU are analysed, therefore the body-fixed frame of the vehicle was *defined* here to be identical to the s frame without the loss of generality. Therefore, the s frame is omitted entirely in the scope of this thesis.

Note, that the position of the IMU, \mathbf{r} , is by definition zero in the navigation and body-fixed frames, $\mathbf{r}^n = \mathbf{r}^b = \mathbf{0}$. The IMU's position is given in the e frame as $\mathbf{r}^e = \begin{pmatrix} r_x^e & r_y^e & r_z^e \end{pmatrix}^T$, which can be also transformed into the more intuitive coordinate triple of ellipsoidal latitude φ , ellipsoidal longitude λ , and ellipsoidal height h . For all ellipsoidal quantities used in this thesis: normal gravity, the normal gravity gradient, and the definitions of North, East, and Down, the GRS80 ellipsoid definition is used (*Moritz, 1980*).

3.2.2 Normal gravity and gravity disturbance

For the definition of the system state, the gravity disturbance needs to be introduced first.

The gravity disturbance is defined as the 3-D vector of differences of the actual (true or observed) gravity \mathbf{g} , and the normal gravity vector $\boldsymbol{\gamma}$ at the same point (cf. Sect. 1.1). In the n -frame, this yields

$$d\mathbf{g}^n = \mathbf{g}^n - \boldsymbol{\gamma}^n = \begin{pmatrix} g^N \\ g^E \\ g^D \end{pmatrix} - \begin{pmatrix} 0 \\ 0 \\ \gamma \end{pmatrix}. \quad (3.20)$$

Note, that the horizontal components of $\boldsymbol{\gamma}$ are zero due to the ellipsoidal definition of the n -frame. The reference ellipsoid used in this thesis is the Geodetic Reference System 80 ellipsoid (GRS) (*Moritz, 1980*), yielding the following approximation for γ_0 on the ellipsoid, depending on the ellipsoidal latitude φ (*Torge and Müller, 2012*):

$$\begin{aligned} \gamma_0 = & \gamma_a (1 + 0.0052790414 \sin^2 \varphi + 2.32718 \cdot 10^{-5} \sin^4 \varphi \\ & + 1.262 \cdot 10^{-7} \sin^6 \varphi + 7 \cdot 10^{-10} \sin^8 \varphi) \end{aligned} \quad (3.21)$$

where $\gamma_a = 978\,032.677\,15$ mGal is the normal gravity on the equator. For a point at ellipsoidal height $h \geq 0$, the definition of normal gravity in the scope of this thesis is based on the following approximation:

$$\gamma = \gamma_0 - (0.30877 - 4.3 \cdot 10^{-4} \sin^2 \varphi)h + 7.2 \cdot 10^{-8} h^2 \text{ [mGal]}, \quad (3.22)$$

where h is given in metres (*Torge and Müller, 2012*).

3.2.3 System state

The design of the strapdown gravimetry system is very similar to that of integrated IMU/GNSS navigation systems, but with additional error states for the gravity disturbance

\mathbf{dg} . The basic 18-dimensional error state is given as

$$\delta \mathbf{x} = \left(\delta \mathbf{r}^n \quad \delta \mathbf{v}^n \quad \delta \boldsymbol{\psi}^n \quad \delta \mathbf{b}_a^b \quad \delta \mathbf{b}_\omega^b \quad \delta \mathbf{dg}^n \right)^T, \quad (3.23)$$

being the 3-D *errors* of position $\delta \mathbf{r}^n$, velocity $\delta \mathbf{v}^n$, attitude $\delta \boldsymbol{\psi}^n$, accelerometer biases $\delta \mathbf{b}_a^b$, gyroscope biases $\delta \mathbf{b}_\omega^b$, and the gravity disturbance $\delta \mathbf{dg}^n$. Note, that this state definition includes the three-dimensional gravity disturbance, with North, East, and Down components, thereby enabling *vector* gravimetry. The horizontal components, dg^{North} and dg^{East} , can be easily transformed into the angular *deflections of the vertical* (DoV), which are more common in geodesy:

$$\xi = -dg^N/g, \quad \text{and} \quad (3.24)$$

$$\eta = -dg^E/g, \quad (3.25)$$

given here in units of radians, with $g = |\mathbf{g}| \approx g^D$ (for a horizontal gravity disturbance of up to 100 mGal, the error of this approximation is less than $5 \mu\text{Gal}$, yielding a relative error for ξ and η of less than 10^{-8}).

3.2.4 Navigation equations

The navigation equations of the strapdown gravimetry system are presented here briefly. More detailed derivations of these equations can be found in the standard literature on IMU/GNSS integration, cf. *Groves* (2013); *Wendel* (2011); *Titterton and Weston* (2004); *Britting* (1971).

Position

For the differential equation of the position error, the curvilinearity of the coordinate frame definition needs to be taken into account. With $\delta \mathbf{r}^n = \left(\delta r^N \quad \delta r^E \quad \delta r^D \right)^T$ and $\mathbf{v}^n = \left(v^N \quad v^E \quad v^D \right)^T$, the first-order Taylor approximation yields

$$\delta \dot{r}^N = \frac{v^N}{R^N} \delta r^D + \delta v^N \quad (3.26)$$

$$\delta \dot{r}^E = \frac{v^E \tan \varphi}{R^N} \delta r^N + \frac{v^E}{R^E} \delta r^D + \delta v^E \quad (3.27)$$

$$\delta \dot{r}^D = \delta v^D, \quad (3.28)$$

where R^N and R^E denote the ellipsoidal radii of curvature, of the local meridian, and the transverse, respectively:

$$R^N = R_0^N + h = \frac{a(1-e^2)}{(1-e^2 \sin^2 \varphi)^{\frac{3}{2}}} + h \quad (3.29)$$

$$R^E = R_0^E + h = \frac{a}{\sqrt{1-e^2 \sin^2 \varphi}} + h \quad (3.30)$$

with semi-major axis a , and eccentricity e (according to the GRS80 ellipsoid definition), cf. *Torge and Müller* (2012).

The partial derivatives of the position error with respect to the relevant error states (position and velocity) are therefore given as

$$\mathbf{F}_{11} = \frac{\partial \dot{\mathbf{r}}^n}{\partial \mathbf{r}^n} = \begin{pmatrix} 0 & 0 & v^N/R^N \\ v^E \tan \varphi / R^N & 0 & v^E/R^E \\ 0 & 0 & 0 \end{pmatrix}, \quad \text{and} \quad (3.31)$$

$$\frac{\partial \dot{\mathbf{r}}^n}{\partial \mathbf{v}^n} = \mathbf{I} \quad (3.32)$$

Velocity

The fundamental relationship between gravity, specific force and aircraft acceleration (velocity change) was already introduced in Eq. 1.14. When transforming this equation from the inertial frame into the navigation frame (or any other frame which is fixed with respect to the rotating Earth), the Coriolis and centrifugal accelerations have to be accounted for (*Britting, 1971; Groves, 2013*). The Euler term is neglected here, because the assumption of a constant Earth rotation rate vector can be done for gravimetry at the 1 mGal level without the loss of precision. Note, that the centrifugal acceleration is already included in the normal gravity γ . With Eq. 3.20 this yields

$$\ddot{\mathbf{r}}^n = \dot{\mathbf{v}}^n = \mathbf{C}_b^n \mathbf{f}^b + \gamma^n + \mathbf{d}g^n - (2\boldsymbol{\omega}_{ie}^n + \boldsymbol{\omega}_{en}^n) \times \mathbf{v}^n, \quad (3.33)$$

with rotation matrix from the b -frame to the n -frame, \mathbf{C}_b^n , specific force \mathbf{f}^b (as measured by the three accelerometers of a strapdown IMU), the Earth rotation rate vector $\boldsymbol{\omega}_{ie}^n$, and the turn rate vector arising from the movement of the n -frame (fixed to the vehicle) along its curvilinear axes, $\boldsymbol{\omega}_{en}^n$ (also called *transport rate*), with

$$\boldsymbol{\omega}_{ie}^n = \omega_e \begin{pmatrix} \cos \varphi \\ 0 \\ -\sin \varphi \end{pmatrix}, \quad \text{and} \quad (3.34)$$

$$\boldsymbol{\omega}_{en}^n = \begin{pmatrix} v^E/R^E \\ -v^N/R^N \\ -v^E \tan \varphi/R^E \end{pmatrix}, \quad (3.35)$$

with the scalar Earth rotation rate $\omega_e = |\boldsymbol{\omega}_{ie}|$. Introducing the error states (cf. Eq.3.18), Eq. 3.33 can be transformed with $[\mathbf{a} \times] \mathbf{b} = -[\mathbf{b} \times] \mathbf{a}$ into

$$\begin{aligned} \delta \dot{\mathbf{v}}^n = & \mathbf{C}_b^n \delta \mathbf{f}^b - [\mathbf{C}_b^n \mathbf{f}^b \times] \delta \boldsymbol{\psi}^n + \delta \gamma^n + \delta \mathbf{d}g^n \\ & - [(2\boldsymbol{\omega}_{ie}^n + \boldsymbol{\omega}_{en}^n) \times] \delta \mathbf{v}^n + [\mathbf{v}^n \times] (2\delta \boldsymbol{\omega}_{ie}^n + \delta \boldsymbol{\omega}_{en}^n), \end{aligned} \quad (3.36)$$

where the error quantities are again denoted with a preceding δ . The normal gravity error $\delta \gamma^n$ obviously only depends on the position error. The Jacobian matrix of partial derivatives of γ^n can be approximated as

$$\frac{\partial \gamma^n}{\partial \mathbf{r}^n} \approx \begin{pmatrix} 0 & 0 & 0 \\ 0 & 0 & 0 \\ 0 & 0 & 0.3086 \text{ mGal/m} \end{pmatrix}, \quad (3.37)$$

where the change of normal gravity due to small *horizontal* position errors was neglected, being of the order of only $1 \mu\text{Gal/m}$. Having state-of-the-art two-frequency differential GNSS coordinates or PPP coordinates available, position errors of less than 10 cm can be expected.

Note, that for a practical implementation of Eq. 3.36, and also for the determination of the matrix \mathbf{F}_k at time t_k , of course only the estimated or measured quantities, $\hat{\mathbf{C}}_b^n$, $\hat{\mathbf{f}}^b$, $\hat{\mathbf{v}}^n$, $\hat{\boldsymbol{\omega}}_{ie}^n$, and $\hat{\boldsymbol{\omega}}_{en}^n$ are available. Again, the accents were omitted for readability.

The partial derivatives of Eq. 3.36 with respect to position, velocity and attitude errors are given as

$$\mathbf{F}_{21} = \frac{\partial \dot{\mathbf{v}}^n}{\partial \mathbf{r}^n} = \frac{\partial \gamma^n}{\partial \mathbf{r}^n} + [\mathbf{v}^n \times] (2 \frac{\partial \boldsymbol{\omega}_{ie}^n}{\partial \mathbf{r}^n} + \frac{\partial \boldsymbol{\omega}_{en}^n}{\partial \mathbf{r}^n}) \quad (3.38)$$

$$\mathbf{F}_{22} = \frac{\partial \dot{\mathbf{v}}^n}{\partial \mathbf{v}^n} = -[(2\boldsymbol{\omega}_{ie}^n + \boldsymbol{\omega}_{en}^n) \times] + [\mathbf{v}^n \times] \frac{\partial \boldsymbol{\omega}_{en}^n}{\partial \mathbf{v}^n} \quad (3.39)$$

$$\mathbf{F}_{23} = \frac{\partial \dot{\mathbf{v}}^n}{\partial \boldsymbol{\psi}^n} = -[\hat{\mathbf{C}}_b^n \hat{\mathbf{f}}^b \times]. \quad (3.40)$$

The term $\delta \mathbf{f}^b$ in Eq. 3.36 is closely related to the accelerometer biases:

$$\delta \mathbf{f}^b = -\delta \mathbf{b}_a^b + \text{sensor noise} \quad (3.41)$$

$$\implies \frac{\partial \dot{\mathbf{v}}^n}{\partial \mathbf{b}_a^b} = -\mathbf{C}_b^n. \quad (3.42)$$

Further, the functional relation between the differential velocity error and the gravity disturbance error is simply given as

$$\frac{\partial \dot{\mathbf{v}}^n}{\partial \mathbf{d}\mathbf{g}^n} = \mathbf{I}. \quad (3.43)$$

Attitude

The differential equation for the attitude is given in matrix form as

$$\dot{\mathbf{C}}_b^n = \mathbf{C}_b^n \left[\boldsymbol{\omega}_{nb}^b \times \right] = \mathbf{C}_b^n \left[(\boldsymbol{\omega}_{ib}^b - \boldsymbol{\omega}_{in}^b) \times \right], \quad (3.44)$$

where $\boldsymbol{\omega}_{ib}^b$ is the rotation rate of the vehicle with respect to the inertial frame, given in the body-fixed frame. This quantity is measured by the three gyroscopes of the IMU. Note, that $\boldsymbol{\omega}_{in} = \boldsymbol{\omega}_{ie} + \boldsymbol{\omega}_{en}$ (for any frame). With the assumption of small attitude errors $\delta \boldsymbol{\psi}^n$, a first-order Taylor approximation of Eq. 3.44 yields (after the transformation to vectors):

$$\delta \dot{\boldsymbol{\psi}}^n = -[\boldsymbol{\omega}_{in}^n \times] \delta \boldsymbol{\psi}^n - \delta \boldsymbol{\omega}_{in}^n + \mathbf{C}_b^n \delta \boldsymbol{\omega}_{ib}^b. \quad (3.45)$$

The partial derivatives with respect to the error states are thus given as

$$\mathbf{F}_{31} = \frac{\partial \dot{\boldsymbol{\psi}}^n}{\partial \mathbf{r}^n} = -\frac{\partial \boldsymbol{\omega}_{in}^n}{\partial \mathbf{r}^n} \quad (3.46)$$

$$\mathbf{F}_{32} = \frac{\partial \dot{\boldsymbol{\psi}}^n}{\partial \mathbf{v}^n} = -\frac{\partial \boldsymbol{\omega}_{en}^n}{\partial \mathbf{v}^n} \quad (3.47)$$

$$\mathbf{F}_{33} = \frac{\partial \dot{\boldsymbol{\psi}}^n}{\partial \boldsymbol{\psi}^n} = -[\boldsymbol{\omega}_{in}^n \times]. \quad (3.48)$$

Note, that $\partial \boldsymbol{\omega}_{in}^n / \partial \mathbf{v}^n = \partial \boldsymbol{\omega}_{en}^n / \partial \mathbf{v}^n$, because the Earth's rotation vector does not depend on \mathbf{v}^n . The term $\delta \boldsymbol{\omega}_{ib}^b$ in Eq. 3.45 is closely related to the gyroscope biases:

$$\delta \boldsymbol{\omega}_{ib}^b = -\delta \mathbf{b}_\omega^b + \text{sensor noise} \quad (3.49)$$

$$\implies \frac{\partial \dot{\boldsymbol{\psi}}^n}{\partial \mathbf{b}_\omega^b} = -\mathbf{C}_b^n \quad (3.50)$$

3.2.5 Sensor biases

The IMU sensor biases \mathbf{b}_a^b and \mathbf{b}_ω^b are modelled as first-order Gauss-Markov processes (Gelb, 1974). This is a common approach for IMU/GNSS integrated systems, however later in thesis it will be shown, that due to a limited observability also simpler models as random walk or even a random constant can be sufficient. With the process correlation time τ , the first-order Gauss-Markov correlation parameters for the accelerometer and gyroscope biases are given as

$$\beta_a^{1st} = 1/\tau_a, \text{ and} \quad (3.51)$$

$$\beta_\omega^{1st} = 1/\tau_\omega, \text{ respectively.} \quad (3.52)$$

In practice, τ_a and τ_ω can be determined from an autocorrelation analysis of static sensor recordings. However, in a kinematic set-up, the sensor errors can be expected to be higher, in particular during dynamic motion.

Assuming identical correlation parameters for the triads of identical IMU sensors, the differential equations for the sensor biases are given as

$$\delta \dot{\mathbf{b}}_a^b = -\beta_a^{1st} \delta \mathbf{b}_a^b \implies \frac{\partial \dot{\mathbf{b}}_a^b}{\partial \mathbf{b}_a^b} = -\beta_a^{1st} \mathbf{I}, \text{ and} \quad (3.53)$$

$$\delta \dot{\mathbf{b}}_\omega^b = -\beta_\omega^{1st} \delta \mathbf{b}_\omega^b \implies \frac{\partial \dot{\mathbf{b}}_\omega^b}{\partial \mathbf{b}_\omega^b} = -\beta_\omega^{1st} \mathbf{I}. \quad (3.54)$$

3.2.6 Modelling the along-track gravity disturbance as a stochastic process

The gravity disturbance (Eq. 3.20) can be seen as a time-variable quantity in the context of an EKF, because it changes along the vehicle trajectory, and thus *over time*. The definition of the signal characteristics however should be made in the *spatial* domain, as the actual gravity field does of course not depend on the choice of the aircraft speed. The parameters are then transformed into *per-time* quantities during the algorithm runtime by means of the current horizontal vehicle velocity (Deurloo, 2011):

$$v^{\text{hor}} = \sqrt{(v^N)^2 + (v^E)^2}. \quad (3.55)$$

It is a priori unclear, which kind of a stochastic process best models the signal characteristics of the gravity disturbance along a trajectory in the spatial domain. It was therefore analysed in *Jekeli (1994)* based on a real-data example, how good different processes are able to approximate the actual gravity signal. The best fits are provided by third-order or fourth-order Gauss-Markov models. It is just noted here, that Gauss-Markov processes of first and second orders were also tested in the scope of this thesis, providing a similar quality of the gravity estimates.

Even the rather simplistic model of a random walk process (being a first-order Gauss-Markov process with infinite correlation time) might be able to provide useful estimates, as was shown in *Ayres-Sampaio et al. (2015)*; *Deurloo et al. (2015)*; *Deurloo (2011)*.

Second- and higher order Gauss-Markov processes are based on time-derivatives of the modelled quantity. Therefore, the time-derivatives of the gravity disturbances down to $\mathbf{d}\dot{\mathbf{g}}$, $\mathbf{d}\ddot{\mathbf{g}}$, and $\mathbf{d}\dddot{\mathbf{g}}$ need to be introduced for the second-, third-, and fourth-order models, respectively. Using for example a fourth-order Gauss Markov process, the augmented error state is given as

$$\delta \mathbf{x} = \left(\delta \mathbf{r}^n \quad \delta \mathbf{v}^n \quad \delta \psi^n \quad \delta \mathbf{b}_a^b \quad \delta \mathbf{b}_\omega^b \quad \delta \mathbf{d}\mathbf{g}^n \quad \delta \mathbf{d}\dot{\mathbf{g}}^n \quad \delta \mathbf{d}\ddot{\mathbf{g}}^n \quad \delta \mathbf{d}\ddot{\mathbf{g}}^n \right)^T. \quad (3.56)$$

The functional relationship between the different time-derivatives of the gravity disturbance is simply given as

$$\frac{d}{dt}(\delta \mathbf{d}\mathbf{g}^n) = \delta \mathbf{d}\dot{\mathbf{g}}^n, \quad (3.57)$$

$$\frac{d}{dt}(\delta \mathbf{d}\dot{\mathbf{g}}^n) = \delta \mathbf{d}\ddot{\mathbf{g}}^n, \text{ and} \quad (3.58)$$

$$\frac{d}{dt}(\delta \mathbf{d}\ddot{\mathbf{g}}^n) = \delta \mathbf{d}\dddot{\mathbf{g}}^n. \quad (3.59)$$

$$(3.60)$$

The time-propagation of an m -th order Gauss-Markov process can be defined as

$$\begin{pmatrix} \delta \mathbf{d}\dot{\mathbf{g}} \\ \vdots \\ \delta \mathbf{d}\mathbf{g}^{(m)} \end{pmatrix} = \mathcal{G} \begin{pmatrix} \delta \mathbf{d}\mathbf{g} \\ \vdots \\ \delta \mathbf{d}\mathbf{g}^{(m-1)} \end{pmatrix}, \quad (3.61)$$

where \mathcal{G} is shown for orders up to $m = 4$ in Tab. 3.1.

order m	\mathcal{G}	system noise
1	$-\beta_{dg}^{1st} \mathbf{I}$	$2\beta_{dg}^{1st} \sigma_{dg}^2$
2	$\begin{pmatrix} \mathbf{0} & \mathbf{I} \\ -(\beta_{dg}^{2nd})^2 \mathbf{I} & -2\beta_{dg}^{2nd} \mathbf{I} \end{pmatrix}$	$4(\beta_{dg}^{2nd})^3 \sigma_{dg}^2$
3	$\begin{pmatrix} \mathbf{0} & \mathbf{I} & \mathbf{0} \\ \mathbf{0} & \mathbf{0} & \mathbf{I} \\ -(\beta_{dg}^{3rd})^3 \mathbf{I} & -3(\beta_{dg}^{3rd})^2 \mathbf{I} & -3\beta_{dg}^{3rd} \mathbf{I} \end{pmatrix}$	$\frac{16}{3}(\beta_{dg}^{3rd})^5 \sigma_{dg}^2$
4	$\begin{pmatrix} \mathbf{0} & \mathbf{I} & \mathbf{0} & \mathbf{0} \\ \mathbf{0} & \mathbf{0} & \mathbf{I} & \mathbf{0} \\ \mathbf{0} & \mathbf{0} & \mathbf{0} & \mathbf{I} \\ -(\beta_{dg}^{4th})^4 \mathbf{I} & -4(\beta_{dg}^{4th})^3 \mathbf{I} & -6(\beta_{dg}^{4th})^2 \mathbf{I} & -4\beta_{dg}^{4th} \mathbf{I} \end{pmatrix}$	$\frac{32}{5}(\beta_{dg}^{4th})^7 \sigma_{dg}^2$

Table 3.1: Functional state transition for the gravity disturbance state, when being modelled as a m -th order Gauss-Markov process (Gelb, 1974; Kwon and Jekeli, 2001).

3.2.7 Summary

The full linearised state transition matrix, assuming a first-order Gauss-Markov process for the gravity disturbance, is given as

$$\mathbf{F} = \begin{pmatrix} \mathbf{F}_{11} & \mathbf{I} & \mathbf{0} & \mathbf{0} & \mathbf{0} & \mathbf{0} \\ \mathbf{F}_{21} & \mathbf{F}_{22} & \mathbf{F}_{23} & -\mathbf{C}_b^n & \mathbf{0} & \mathbf{I} \\ \mathbf{F}_{31} & \mathbf{F}_{32} & \mathbf{F}_{33} & \mathbf{0} & -\mathbf{C}_b^n & \mathbf{0} \\ \mathbf{0} & \mathbf{0} & \mathbf{0} & -\beta_a^{1st} \mathbf{I} & \mathbf{0} & \mathbf{0} \\ \mathbf{0} & \mathbf{0} & \mathbf{0} & \mathbf{0} & -\beta_\omega^{1st} \mathbf{I} & \mathbf{0} \\ \mathbf{0} & \mathbf{0} & \mathbf{0} & \mathbf{0} & \mathbf{0} & -\beta_{dg}^{1st} \mathbf{I} \end{pmatrix} \quad (3.62)$$

For higher Gauss-Markov orders m , the sub-matrix in the lower right is replaced by the respective \mathcal{G} from Tab. 3.1, and \mathbf{F} is extended with additional columns and rows for the derivatives of δdg^n , filled with zero sub-matrices $\mathbf{0}$.

3.3 Measurement updates

The different observations are introduced to the system using their functional relation to the system state. For the error-state space definition of the filter, this is equivalent to the information, how system state errors propagate into observation offsets. With the observation noise vector $\mathbf{w}_k^z \sim \mathcal{N}(\mathbf{0}, \mathbf{R}_k)$ this leads to

$$\delta z_k = h(\delta \mathbf{x}_k) + \mathbf{w}_k^z. \quad (3.63)$$

As introduced above, the Kalman filter measurement update requires a *linear* functional relationship between the states and the observations, given by the Jacobian matrix \mathbf{H}_k . For each of the different observations relevant for strapdown gravimetry, both the general and the linearised observation functions will be provided in the following.

Note: The linearised measurement models \mathbf{H} are derived in this section for the basic system state of Eq. 3.23. When modelling the gravity disturbance as a Gauss-Markov process of higher order $m \geq 2$, $m - 1$ additional 3×3 zero matrices have to be appended to the \mathbf{H} matrices accordingly to account for the additional time-derivatives of the gravity disturbance (cf. Eq. 3.56).

Coordinate

The coordinate update is in practice the most important measurement update for strap-down gravimetry, as will be shown in Chap. 4. Coordinate measurements are in practice referenced to an eccentric sensor position (as a GNSS antenna). This eccentricity with respect to the IMU centre of observations (the intersection of the three accelerometers' sensitive axes) is commonly referred to as *lever arm*, denoted here as \mathbf{l} . It is assumed in the scope of this thesis to be a constant with respect to the body-fixed coordinate frame: $\mathbf{l}^b = \text{const}$. The general observation equation can be defined in the earth-fixed coordinate frame as

$$\mathbf{z}_r^e = \mathbf{r}^e + \mathbf{l}^e. \quad (3.64)$$

For the error-state definition of the Kalman filter, the observation equation may be transformed into the n -frame, leading to

$$\delta \mathbf{z}_r^n = \delta \mathbf{r}^n + \mathbf{C}_b^n \mathbf{l}^b. \quad (3.65)$$

The comparison of true quantities and estimated quantities leads to the linearised observation model

$$\delta \mathbf{z}_r = \mathbf{H}_r \delta \mathbf{x} + \mathbf{w}^z, \quad \text{with} \quad (3.66)$$

$$\mathbf{H}_r = \begin{pmatrix} \mathbf{I} & \mathbf{0} & -[\mathbf{C}_b^n \mathbf{l}^b \times] & \mathbf{0} & \mathbf{0} & \mathbf{0} \end{pmatrix}. \quad (3.67)$$

Velocity

For velocity observations, again a lever arm \mathbf{l}^b needs to be accounted for, if the velocity observation has an eccentric reference position (e.g. a GNSS antenna). It is intuitive, that a change of the orientation will yield different velocities at the IMU centre of observations, and at the eccentric reference position, respectively. The observation equation is given as

$$\mathbf{z}_v^n = \mathbf{v}^n + \mathbf{C}_b^n (\boldsymbol{\omega}_{eb}^b \times \mathbf{l}^b). \quad (3.68)$$

In practice, $\boldsymbol{\omega}_{ie}$ is very small compared to $\boldsymbol{\omega}_{eb}$. Using the approximation $\boldsymbol{\omega}_{eb}^b \approx \boldsymbol{\omega}_{ib}^b$ allows the use of the gyroscope measurements $\boldsymbol{\omega}_{ib}^b$, which simplifies the computation. The linearised model is then given in error-state space definition as

$$\delta \mathbf{z}_v = \mathbf{H}_v \delta \mathbf{x} + \mathbf{w}^z, \quad \text{with} \quad (3.69)$$

$$\mathbf{H}_v = \begin{pmatrix} \mathbf{0} & \mathbf{I} & -[\mathbf{C}_b^n \boldsymbol{\Omega}_{ib}^b \mathbf{l}^b \times] & \mathbf{0} & [\mathbf{C}_b^n \mathbf{l}^b \times] & \mathbf{0} \end{pmatrix}. \quad (3.70)$$

For details on this linearisation, see *Groves* (2013) or *Wendel* (2011).

Note: The functional relationship with the gyroscope bias errors $\partial \delta \mathbf{z}_v / \partial \delta \mathbf{b}_\omega = [\mathbf{C}_b^n \mathbf{l}^b \times]$ is negligible in practice, when using gyroscopes of higher grade, as fibre-optical gyroscopes or ring-laser gyroscopes.

Attitude

An attitude observation which is referenced to the body-fixed frame can be applied without accounting for an eccentricity: The eccentricity has no relevance, since the orientation of the body-fixed b frame with respect to the n -frame or the e -frame does not depend on where the observation takes place:

$$\mathbf{z}_\psi^n = \boldsymbol{\psi}^n. \quad (3.71)$$

For the available data sets in the scope of this thesis, no attitude observations were available. The linearised version is still provided here for the *simulated* observations used in Chap. 4. Independent of the used representation of the three-dimensional orientation (e.g. as direction-cosine matrix \mathbf{C}_b^n , or as quaternion), the Jacobian matrix is simply given as

$$\mathbf{H}_\psi = \begin{pmatrix} \mathbf{0} & \mathbf{0} & \mathbf{I} & \mathbf{0} & \mathbf{0} & \mathbf{0} \end{pmatrix}. \quad (3.72)$$

Gravity Disturbance

Introducing a gravity disturbance measurement may appear somewhat contradictory, because it is actually the gravity disturbance that shall be *determined* by the filter. Still, this type of observation has practical relevance: If the trajectory contains points of known gravity, this knowledge can be introduced to the filter as a measurement. For airborne gravimetry this is typically the case after returning to the initial parking position on the apron of an airport, where a terrestrial gravity measurement of relatively high accuracy (better than $100 \mu\text{Gal}$) is typically available (airborne gravimetry is usually *relative* gravimetry). It is assumed here, that the gravity disturbance observation is given in the n -frame and referenced to the IMU centre of observations. The observation model is then given as

$$\mathbf{z}_{dg}^n = d\mathbf{g}^n, \quad (3.73)$$

leading to the linearised functional relationship

$$\mathbf{H}_{dg} = \begin{pmatrix} \mathbf{0} & \mathbf{0} & \mathbf{0} & \mathbf{0} & \mathbf{0} & \mathbf{I} \end{pmatrix}. \quad (3.74)$$

Note: Each of the measurement updates discussed in this section may be applied equivalently, if only a subset of components of the 3-D measurement vectors are available (for example, if only the vertical component of the gravity disturbance is known).

3.4 Navigation update

In the navigation update, the time-discrete accelerations $\tilde{\mathbf{f}}^b$ and turn rates $\tilde{\omega}_{ib}^b$ measured by the IMU are used to update the current estimates of position, velocity, and attitude, from epoch $k-1$ to epoch k . The equations are given here in an algorithmic fashion, showing the relevant inputs for each of the quantities being computed. The attitude update is based on quaternions \mathbf{q}_b^n , being an equivalent representation of the direction-cosine matrix \mathbf{C}_b^n (details can be found in *Groves* (2013)). The quaternion of the last epoch $\mathbf{q}_{b,k-1}^n$ is assumed to be available.

$$\mathbf{g}_{k-1}^n = \boldsymbol{\gamma}^n(\varphi_{k-1}, h_{k-1}) + d\mathbf{g}_{k-1}^n \quad (3.75)$$

$$\boldsymbol{\omega}_{nb,k}^b = (\tilde{\omega}_{ib,k}^b - \mathbf{b}_{\omega,k-1}^b) - (\boldsymbol{\omega}_{ie}^n(\varphi_{k-1}) + \boldsymbol{\omega}_{en}^n(\varphi_{k-1}, h_{k-1}, \mathbf{v}_{k-1}^n)) \quad (3.76)$$

$$\Delta\boldsymbol{\psi} = \boldsymbol{\omega}_{nb,k}^b \cdot dt_k \quad (3.77)$$

$$\Delta\mathbf{q} = \begin{pmatrix} \cos(0.5 \cdot |\Delta\boldsymbol{\psi}|) \\ \sin(0.5 \cdot |\Delta\boldsymbol{\psi}|) \frac{\Delta\boldsymbol{\psi}}{|\Delta\boldsymbol{\psi}|} \end{pmatrix} \quad (3.78)$$

$$\mathbf{q}_{b,k}^n = \mathbf{q}_{b,k-1}^n \bullet \Delta\mathbf{q} \quad (3.79)$$

$$\mathbf{f}_k^n = \mathbf{C}_{b,k}^n(\tilde{\mathbf{f}}_{ib,k}^b - \mathbf{b}_{a,k-1}^b) \quad (3.80)$$

$$\mathbf{a}_{\text{Coriolis},k}^n = -(2\boldsymbol{\omega}_{ie}^n + \boldsymbol{\omega}_{en}^n) \times \mathbf{v}_{k-1}^n \quad (3.81)$$

$$\mathbf{v}_k^n = \mathbf{v}_{k-1}^n + (\mathbf{f}_k^n + \mathbf{g}_{k-1}^n + \mathbf{a}_{\text{Coriolis},k}^n) \cdot dt_k \quad (3.82)$$

$$\varphi_k = \varphi_{k-1} + 0.5 \cdot (v_{k-1}^N + v_k^N) \cdot dt_k / R_N \quad (3.83)$$

$$\lambda_k = \lambda_{k-1} + 0.5 \cdot (v_{k-1}^E + v_k^E) \cdot dt_k / (R_E \cos \varphi_k) \quad (3.84)$$

$$h_k = h_{k-1} - 0.5 \cdot (v_{k-1}^D + v_k^D) \cdot dt_k \quad (3.85)$$

Note, that these equations contain some approximations, e.g. the Coriolis force for epoch k is computed based on \mathbf{v}_{k-1} . Iterations can be implemented to circumvent the approximations,

however in practice no significant changes of the results could be observed. The change of the quantities (as normal gravity, Coriolis acceleration, velocity) between two time-epochs is usually very small due to the very short time increments of a strapdown IMU (10 ms or less).

The update of the attitude is shown here using quaternions. It is just noted here, that for high-dynamic motion, a more exact computation may be preferable. A more exact method, based on matrix exponentials of the matrix $[\Delta\boldsymbol{\psi}\times]$, can be found in *Groves* (2013). However, for the data sets introduced in Chap. 8, no significant effect on the state estimates could be observed.

The update of latitude φ , longitude λ , and ellipsoidal height h is done based on the average velocity in the time interval $[t_{k-1}, t_k]$ to account for accelerations, which are assumed to be constant during this time interval.

The estimates of the sensor biases \mathbf{b}_a^b and \mathbf{b}_ω^b , and the gravity disturbance $d\mathbf{g}^n$, remain unchanged in the scope of the navigation update: The last estimate is also the best prediction for the next epoch. These states can only be updated, if measurements are introduced to the filter. Therefore, $\mathbf{b}_{a,k-1}^b$, $\mathbf{b}_{\omega,k-1}^b$, and \mathbf{g}_{k-1}^n are used in the above equations for epoch k , and $\mathbf{g}_k^n = \mathbf{g}_{k-1}^n$, and so forth.

3.5 Gravity reductions

The estimation process can in general be supported, if additional (external) information on the stochastic process can be introduced to the filter. In addition to the basic concept of measurements in the sense of a Kalman filter, such external information may be introduced using *reductions* of the estimated signal.

One example of such a reduction has already been introduced by using the concept of gravity disturbances, being the *residual* gravity with respect to normal gravity. Thus, the gravity vector \mathbf{g} was split into the two components

$$\mathbf{g} = \boldsymbol{\gamma} + d\mathbf{g}. \quad (3.86)$$

The estimation of the gravity disturbance is easier compared to the estimation of gravity, because the majority of the signal dynamics due to altitude changes of the aircraft is removed from the signal, thereby allowing a more trajectory-independent modelling of the stochastic process. (Residual effects of altitude changes can be observed in the gravity disturbance to the extent, to which the normal gravity gradient deviates from the actual gravity gradient.) Also, the use of the much smaller gravity disturbances as system states may yield a higher numerical stability: Gravity disturbances are usually <100 mGal (<400 mGal) in regions with flat (high-mountain) topography, contributing only $<0.01\%$ ($<0.04\%$) to the actual gravity.

In the following, the concept of gravity reductions shall be pursued in more depth, using global gravity models (GGM) and topographic reductions.

3.5.1 Global gravity model reductions

Satellite-based global gravity models (GGM) may be applied as a long-wavelength gravity reduction for airborne gravimetry. The resolution of the satellite gravity models is typically limited to wavelengths of ≈ 100 km and more. The gravity reduction $d\mathbf{g}_{\text{GGM}}^n$ can be computed for the aircraft positions along a flight trajectory based on the GNSS positions. In practice, this computation can be done as a preprocessing step, before the execution of the EKF algorithm.

By applying a long-wavelength gravity reduction, the characteristics of the (residual) gravity disturbance can change significantly, yielding different correlation parameters β_{dg} for the Gauss-Markov processes. Fig. 3.1 shows a real-data example, taken from an aerogravity flight over the Chilean Andes. It can be seen, that the statistical properties of the data

signal change significantly after applying the GGM reduction (Fig. 3.1, bottom left). The correlation time τ , being the leftmost intersection of the autocorrelation function with the $1/e$ -line (Fig. 3.1), reduces from 30 min to 12 min, equivalent to a spatial correlation distance of approximately 180 km, and 70 km, respectively.

3.5.2 Topographic reductions

When doing airborne gravimetry above mountainous terrain, the biggest part of the observed gravity disturbances may arise from the effect of the topographic masses below. The spectral contribution very much depends on the characteristics of the terrain. In general, both short (>1 km) and long wavelengths (>100 km) can be found in the topographic effect.

With global digital terrain models (DTM) and bathymetry models being available (*Amante and Eakins, 2009; Becker et al., 2009*), the topographic effect $\mathbf{dg}_{\text{top}}^n$ can be computed along the vehicle trajectory. Note, that the topographic effect has to be computed at flight altitude. Details on the computation of $\mathbf{dg}_{\text{top}}^n$ can be found in *Forsberg and Tscherning (1981)* and *Heck and Seitz (2007)*. For the topographic reductions shown in this thesis, the software GRAVSOFTEC was used (*Tscherning et al., 1992*).

In general, it appears reasonable to combine both reductions, GGM *and* topography, because the long-wavelength Bouguer disturbances (after removing the topographic effect) will only be covered by the GGM, while short-wavelength effects can only be reduced based on the topographic effect. However, it is important in this case to artificially *limit* the topographic reduction to shorter wavelengths (e.g. < 100 km) by computing the topographic effect only for a DTM which is limited to such higher frequencies. In practice, a low resolution DTM may be subtracted from the original full-resolution DTM. The topographic effect is then computed based on this *residual terrain model* (RTM), see *Forsberg (1984)*. Fig. 3.1 shows the topographic reduction for wavelengths shorter than 110 km, being consistent with one degree in latitudinal direction, which is the resolution of the applied global gravity model reduction.

After applying both reductions, the residual gravity disturbance signal is smoother, *and* has lower amplitudes. The original absolute range of 230 mGal reduces to 65 mGal, and, as expected, the reduced gravity disturbance has almost zero mean (Fig. 3.1).

3.5.3 Modified system state

Instead of using the standard definition of the gravity disturbance (Eqs. 3.20 and 3.86), the *reduced gravity disturbance* \mathbf{dg}_r^n is defined as

$$\mathbf{dg}_r^n = \mathbf{g}^n - \boldsymbol{\gamma}^n - \mathbf{dg}_{\text{top}}^n - \mathbf{dg}_{\text{GGM}}^n = \mathbf{dg}^n - \mathbf{dg}_{\text{top}}^n - \mathbf{dg}_{\text{GGM}}^n. \quad (3.87)$$

Thus, in the system state (Eq. 3.23, or its augmented version, Eq. 3.56), \mathbf{dg}^n will be replaced by \mathbf{dg}_r^n . The navigation update (Eq. 3.75) needs to be changed accordingly:

$$\mathbf{g}^n = \boldsymbol{\gamma}^n + \mathbf{dg}_{\text{top}}^n + \mathbf{dg}_{\text{GGM}}^n + \mathbf{dg}_r^n \quad (3.88)$$

The same equation may be applied to the final estimates of the reduced gravity, $\hat{\mathbf{dg}}_r^n$, in order to *restore* the full gravity vector.

The overall process of applying gravity reductions in order to support the gravity estimation can be summarized as

1. *Remove* portions of the gravity \mathbf{g}^n by applying the gravity reductions.
2. *Compute* the residual gravity disturbances \mathbf{dg}_r^n (done here using an EKF and a Kalman smoother).

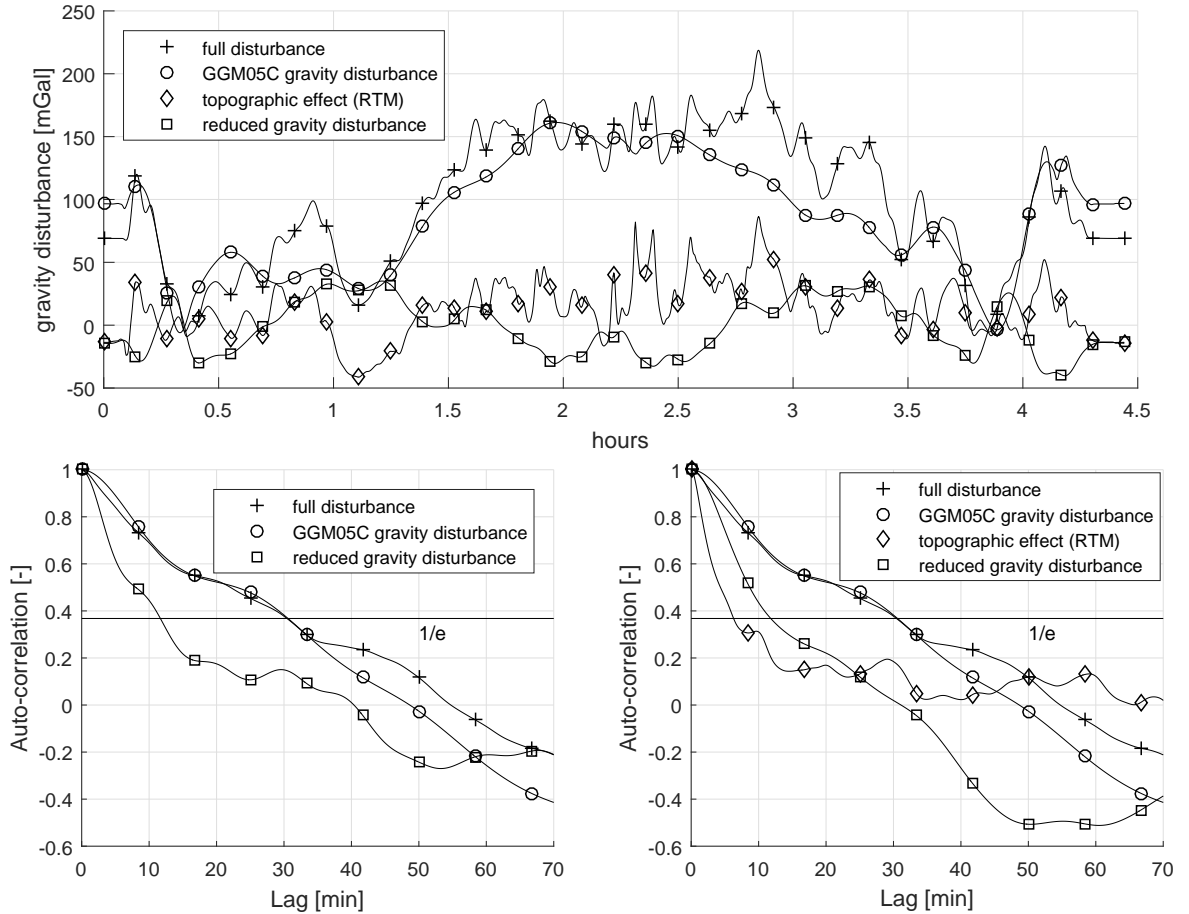


Figure 3.1: *Top:* Illustration of gravity disturbance and gravity reductions along a flight track (taken from flight 297 of the Chile campaign, cf. Chap. 8). *Bottom left:* Autocorrelation functions, if only the GGM reduction is applied. *Bottom right:* Autocorrelation functions, after applying both the GGM reduction and the topographic reduction. The GGM05C global gravity model (*Ries et al., 2016*) was evaluated to order and degree 360 at flight altitude. The topographic effect was computed for a residual terrain model (RTM) at flight altitude, for wavelengths shorter than one degree (≈ 110 km). The terrain information was taken from the SRTM15 Plus data set (including bathymetry), with a grid resolution of 15 arc seconds (*Becker et al., 2009*). For the computation of both reductions, the software GRAVSOFTE was used (*Tscherning et al., 1992*).

3. *Restore* the gravity \mathbf{g}^n by inversely applying the gravity reductions to $d\mathbf{g}_r^n$ (if required).

Thus, this method can be seen as a variant of the well-established *remove-compute-restore* technique, a tool which is commonly used for the geoid determination (*Forsberg and Tscherning, 1981*), to stabilise the downward continuation of surface gravity data to the geoid.

For the practical implementation of such gravity reductions, the actual reductions may be pre-computed in the n -frame, using pre-processed GNSS coordinates.

3.6 Optimal smoothing

An EKF can only use the information of the past epochs up to the current epoch t_k for the estimation of the current system state \mathbf{x}_k . (The information is actually stored inside \mathbf{x}_{k-1} and \mathbf{P}_{k-1} only, which however depend on \mathbf{x}_{k-2} and \mathbf{P}_{k-2} , and so forth.) Only the estimate of the final epoch t_N is based on the entire set of available information. This limitation is obvious for real-time applications. However, in airborne gravimetry, a real-time output of the estimates is usually not required. The state estimation at epoch t_k could be done by also looking at observations of future epochs.

An optimal smoother uses *all* available information for the estimation of the system state at *any* epoch. The Rauch-Tung-Striebel (RTS) smoother, also called *Kalman smoother*, is a very efficient algorithm, going *backwards* over the EKF estimates. In practice, results can be shown to improve significantly after applying the smoother. In particular, the gravity disturbance estimates, which require a considerable period of IMU and GNSS observations in order to converge to the mGal level (90s or more), show immense accuracy improvements by applying a smoother (*Forsberg et al., 1986*).

The RTS smoother is initialised using the EKF estimates of the last epoch: $\bar{\mathbf{x}}_N \equiv \mathbf{x}_N^+$ and $\bar{\mathbf{P}}_N \equiv \mathbf{P}_N^+$. The core RTS loop, going backward through the epochs, is then given as

$$\bar{\mathbf{x}}_k = \mathbf{x}_k^+ + \mathbf{C}_k(\bar{\mathbf{x}}_{k+1} - \mathbf{x}_{k+1}^-) \quad (3.89)$$

$$\bar{\mathbf{P}}_k = \mathbf{P}_k^+ + \mathbf{C}_k(\bar{\mathbf{P}}_{k+1} - \mathbf{P}_{k+1}^-)\mathbf{C}_k^T \quad (3.90)$$

$$\mathbf{C}_k = \mathbf{P}_k^+ \Phi_k^T (\mathbf{P}_{k+1}^-)^{-1}. \quad (3.91)$$

It can be seen, that the smoothed states $\bar{\mathbf{x}}_k$ are the combination of the a-posteriori state estimates, and an additional term introduced by the smoother.

When using an EKF in error state space formulation, Eq. 3.89 is given as

$$\delta\bar{\mathbf{x}}_k = \delta\mathbf{x}_k^+ + \mathbf{C}_k(\delta\bar{\mathbf{x}}_{k+1} - \delta\mathbf{x}_{k+1}^-). \quad (3.92)$$

The estimated a-posteriori errors $\delta\mathbf{x}_k^+$ were *already* applied to the (externally maintained) system state during the EKF runtime, which is crucial for limiting the linearisation errors. After the execution of the RTS-smoother, this portion of the smoothed $\delta\bar{\mathbf{x}}_k$ must not be applied *again* to the system state, but only the additional term introduced by the smoother in Eq. 3.92. The *residual* corrections, that need to be applied to the state estimates (position, velocity, a.s.f.), are therefore given as

$$\Delta\delta\bar{\mathbf{x}}_k = \delta\bar{\mathbf{x}}_k - \delta\mathbf{x}_k^+. \quad (3.93)$$

(The smoothed covariance estimates $\bar{\mathbf{P}}_k$ are valid without further modification.)

Chapter 4

System analysis

4.1 Observability

An observability analysis is carried out here for the IMU/GNSS integrated strapdown gravimetry system. In general, a system is called *observable*, if the observations (or measurements) introduced to the system enable the estimation of *all* system states.

An unobservable system can always be made observable by introducing additional observations. In particular, a system is always observable, if each of the states is being observed.

The original definition of observability is a binary measure. It is already noted here, that the 18-state strapdown gravimetry system, as introduced in Chap. 3 is *not* observable. Still, a deeper insight into this system can be obtained by a closer analysis of so-called *structure graphs*, and additionally by an algebraic analysis of the so-called *observation matrix*. Both concepts will be pursued in this section.

4.1.1 Structure graph analysis

Structure graphs enable an intuitive and visual observability analysis. Such a structure graph is generated using the following construction rules (*Dion et al.*, 2003):

1. For each system state, create a node in the graph.
2. For each observation (measurement), create an output node in the graph.
3. For each combination of two system states a and b (incl. $a = b$), add a directed edge from the a -node to the b -node, if $\partial \dot{b} / \partial a \neq 0$.
4. For each combination of system state a and observation z , add a directed edge from the a -node to the z -node, if $\partial z / \partial a \neq 0$.

Thus, the edges in the graph indicate non-zero elements in the \mathbf{F} matrix, and in the \mathbf{H} -matrices, respectively. Such a graph can only fully reflect the observability of a system, if these non-zero elements are linearly independent. Such a system is then called a *structured system* (*Dion et al.*, 2003). As will be shown later, the strapdown gravimetry system is *not* strictly a structured system. Still, the structure graph analysis will provide a deeper understanding of this system.

For the strapdown gravimetry system as introduced in Chapter 3, the structure graph is shown in Fig. 4.1. The nodes correspond to the 3-D system states as introduced in Chapter 3. The output nodes are included for the two typical observations in strapdown gravimetry: Coordinate observations \mathbf{z}_r , and velocity observations \mathbf{z}_v (both commonly taken from GNSS measurements). The edges reflect the non-zero entries of \mathbf{F} , \mathbf{H}_r , and \mathbf{H}_v (cf. Eq. 3.62 and Sect. 3.3).

Some of the functional dependencies are marked in Fig. 4.1 as *weak*, meaning that the partial derivative ($\partial \dot{b}/\partial a \neq 0$ or $\partial z/\partial a \neq 0$) is very small for that edge. These are functional dependencies, which are based on relatively small quantities, as the Earth's rotation rate (and thus the Coriolis acceleration), the transport rate, position or velocity errors divided by the Earth's radius, and position or velocity errors of the GNSS antenna coming from attitude errors with a non-zero lever arm (such attitude errors are only of the order of tens of arc seconds in practice when using a navigation-grade IMU). The *quantitative* analysis presented in Sect. 4.2 will justify the negligibility of this *weak* functional relationships. After removing the respective sub-matrices from the matrices \mathbf{F} , \mathbf{H}_r , and \mathbf{H}_v , the simplified linear models are given as

$$\mathbf{F}^{\text{simp}} = \begin{pmatrix} \mathbf{0} & \mathbf{I} & \mathbf{0} & \mathbf{0} & \mathbf{0} & \mathbf{0} \\ \mathbf{0} & \mathbf{0} & -[\mathbf{f}^n \times] & -\mathbf{C}_b^n & \mathbf{0} & \mathbf{I} \\ \mathbf{0} & \mathbf{0} & \mathbf{0} & \mathbf{0} & -\mathbf{C}_b^n & \mathbf{0} \\ \mathbf{0} & \mathbf{0} & \mathbf{0} & \mathbf{0} & \mathbf{0} & \mathbf{0} \\ \mathbf{0} & \mathbf{0} & \mathbf{0} & \mathbf{0} & \mathbf{0} & \mathbf{0} \\ \mathbf{0} & \mathbf{0} & \mathbf{0} & \mathbf{0} & \mathbf{0} & \mathbf{0} \end{pmatrix} \quad (4.1)$$

$$\mathbf{H}_r^{\text{simp}} = \begin{pmatrix} \mathbf{I} & \mathbf{0} & \mathbf{0} & \mathbf{0} & \mathbf{0} & \mathbf{0} \end{pmatrix} \quad (4.2)$$

$$\mathbf{H}_v^{\text{simp}} = \begin{pmatrix} \mathbf{0} & \mathbf{I} & \mathbf{0} & \mathbf{0} & \mathbf{0} & \mathbf{0} \end{pmatrix} \quad (4.3)$$

The structure graph of the simplified model is shown in Fig. 4.2. Note, that the accelerometer biases are neglected in Fig. 4.2. They will be discussed separately in the next section.

Between $\delta \mathbf{b}_\omega^b$ and $\delta \boldsymbol{\psi}^n$, the full permutation of nine edges is shown, because each of the body-fixed sensor biases may be mapped to any direction in the n -frame by means of the current attitude (\mathbf{C}_b^n). (The same holds for the nine edges between $\delta \mathbf{b}_a^b$ and \mathbf{v}^n shown in Fig. 4.3).

Looking at a structure graph, a system is observable, if and only if the following two conditions hold (*Commault et al.*, 2005):

1. A (directed) path exists from each of the system state nodes to at least one output node.
2. The graph is free of any *contractions*. A contraction is defined as a set of nodes \mathcal{N} , for which the combined set of targets of \mathcal{N} , denoted as $T(\mathcal{N})$, has less elements than \mathcal{N} , i.e. $|T(\mathcal{N})| < |\mathcal{N}|$.

An example is provided here to clarify this notation: In Fig. 4.2, consider the following target sets:

$$T(\{\delta dg^N\}) = \{\delta v^N\} \quad (4.4)$$

$$T(\{\delta \psi^E\}) = \{\delta v^N\} \quad (4.5)$$

$$T(\{\delta dg^N, \delta \psi^E\}) = \{\delta v^N\} \quad (4.6)$$

Note, that the set $\{\delta dg^N, \delta \psi^E\}$ is indeed a contraction, because $|T(\{\delta dg^N, \delta \psi^E\})| = 1 < 2 = |\{\delta dg^N, \delta \psi^E\}|$.

For a non-accelerated motion, the measured specific force equals the negative gravity. With the above simplifications, and

$$-\mathbf{f}^n \approx \mathbf{g}^n \approx \begin{pmatrix} 0 \\ 0 \\ g \end{pmatrix}, \quad (4.7)$$

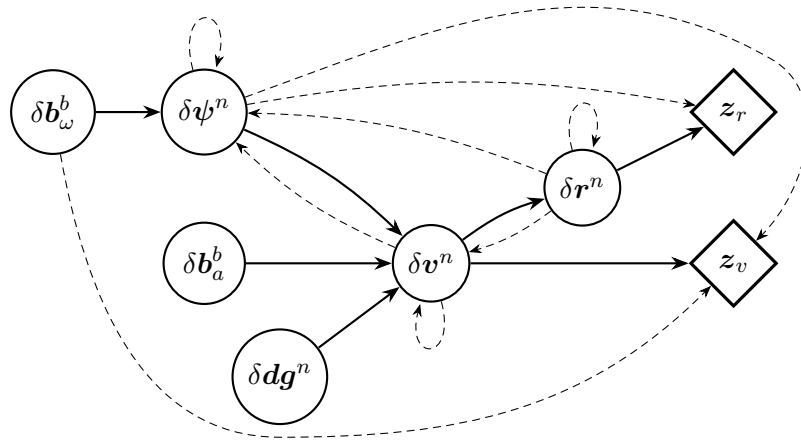


Figure 4.1: Structure graph of the full strapdown gravimetry system. For easier viewing, the 3-D states are plotted as single nodes. Measurements (also called *system outputs*) are diamond-shaped. Weak functional dependencies are shown as dashed lines, see text.

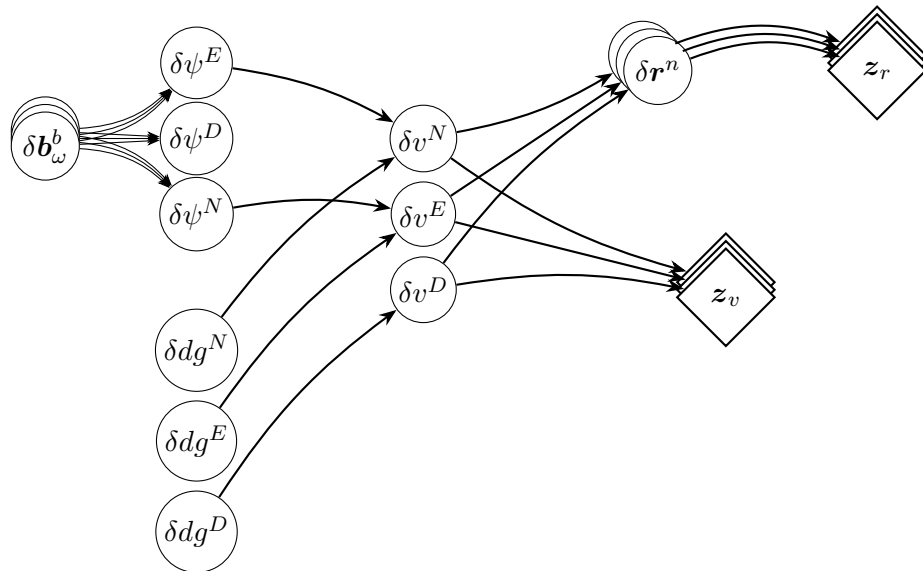


Figure 4.2: Structure graph for the simplified model \mathbf{F}^{simp} , $\mathbf{H}_r^{\text{simp}}$, and $\mathbf{H}_v^{\text{simp}}$, neglecting accelerometer biases and assuming a linear (non-accelerated) motion. Output nodes (measurements) are diamond-shaped. Some 3-D states are plotted as stacks of scalar states for easier viewing.

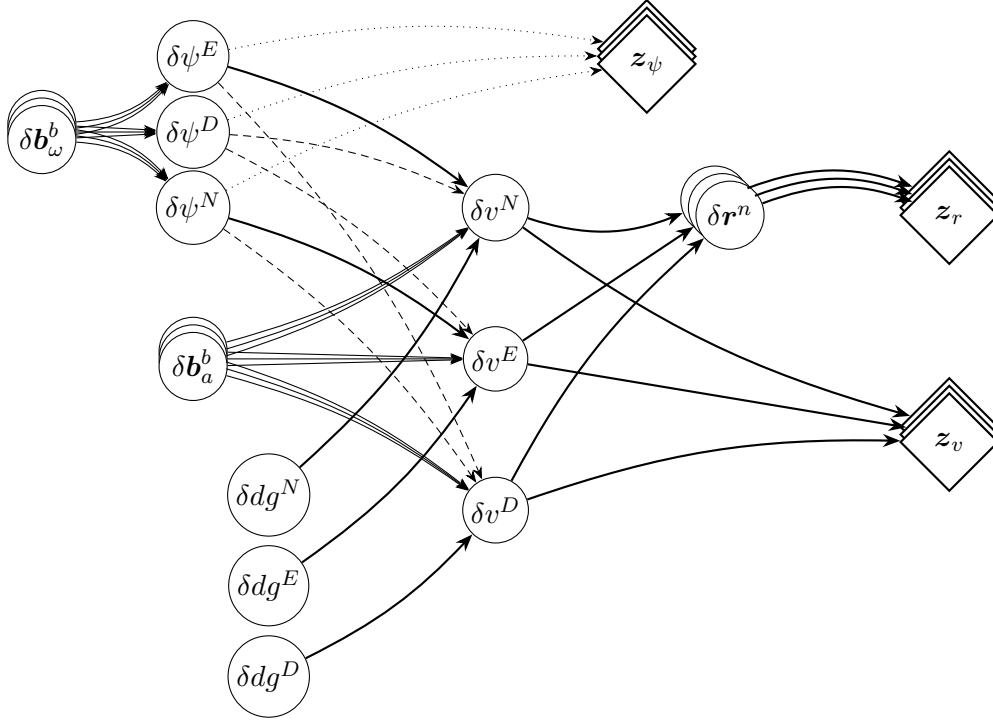


Figure 4.3: Structure graph for the simplified model, \mathbf{F}^{simp} , $\mathbf{H}_r^{\text{simp}}$, and $\mathbf{H}_v^{\text{simp}}$, including accelerometer biases. Output nodes (measurements) are diamond-shaped. The dashed lines are only valid for *accelerated* vehicle motion. Additional attitude observations z_ψ (dotted arrows) may resolve some of the contractions.

the partial derivative $\partial \dot{\mathbf{v}}^n / \partial \psi^n$ reduces to

$$-[\mathbf{f}^n \times] = \begin{pmatrix} 0 & -g & 0 \\ g & 0 & 0 \\ 0 & 0 & 0 \end{pmatrix}, \quad (4.8)$$

leading to $\partial \dot{v}^D / \partial \psi^n = \mathbf{0}$ (third row in the above matrix). The structure graph shown in Fig. 4.2 assumes non-accelerated motion. This implies for the simplified model, that attitude errors around the vertical axis (i.e. heading errors) are not observable during non-accelerated motion, because the first condition for observability is not fulfilled for $\delta \psi^D$. This is a well-known property of IMU/GNSS integrated systems, see for example *Lee et al. (2012)*; *Hong et al. (2005)*. As a direct consequence, the gyroscope biases $\delta \mathbf{b}_\omega^b$ are only observable in the local tangent plane (North/East components), independent of the current \mathbf{C}_b^n .

For the application of gravimetry, we are particularly interested in the observability of the gravity states, which will be discussed in the following. Some remarks on this topic can be found in *Deurloo (2011)*.

Gravity versus attitude

The separation of attitude errors and the horizontal components of gravity is difficult, because the gravity signal is much stronger in the vertical component. In other words, the quality of the measured deflections of the vertical is limited by the accuracy of the attitude estimate (*Jekeli, 1994*). The same misalignment yields a much smaller error for the measured vertical gravity component. Fig. 4.4 shows this effect for measurements in the horizontal directions ($\beta = 90^\circ$), in the vertical direction ($\beta = 0^\circ$), and for intermediate tilt angles. Reading example: A misalignment of 10 arc seconds yields errors of ≈ 0.001 mGal for a (perfectly)

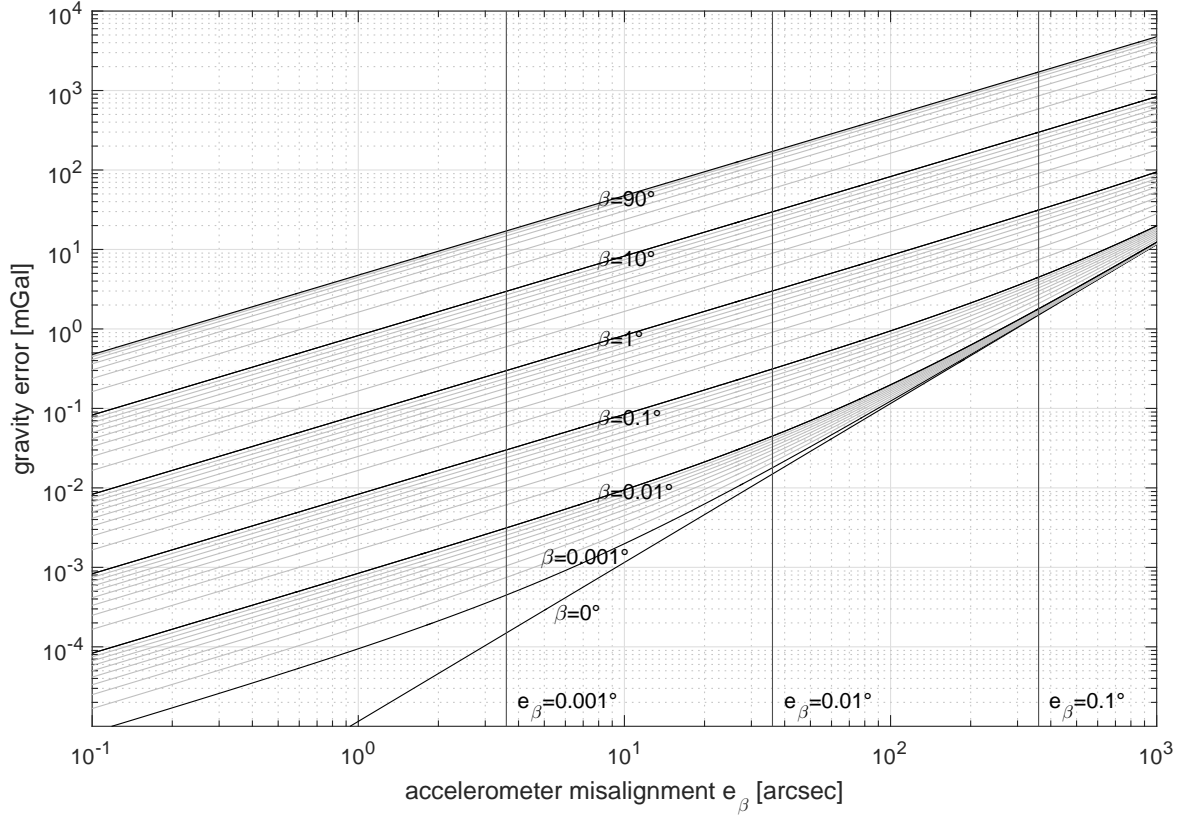


Figure 4.4: Gravity measurement errors for different nominal tilt angles of a gravimeter ($\beta = 0^\circ$, if the gravimeter is aligned with the local vertical), and different misalignments e_β of the gravimeter (the difference between true and nominal tilt angle).

vertically aligned gravimeter, and ≈ 45 mGal for a horizontally aligned gravimeter. Thus the sensitivity to attitude errors differs by a factor of 45,000!

Looking again at the structure graph of Fig. 4.2, the following contractions can be found in the simplified system model during non-accelerated motion:

$$T(\{\delta dg^N, \delta\psi^E\}) = \{\delta v^N\}, \quad \text{and} \quad (4.9)$$

$$T(\{\delta dg^E, \delta\psi^N\}) = \{\delta v^E\}. \quad (4.10)$$

These contractions reveal the important fact, that the horizontal gravity components are inseparable from roll and pitch errors during a non-accelerated flight.

When introducing attitude observations, this contraction is resolved, which can be easily seen in Fig. 4.3. However, it is difficult in practice to obtain attitude observations at a sufficient accuracy level (as will be shown in Sect. 4.2). Therefore, for the remainder of this section, attitude observations are assumed to be unavailable.

However, when introducing horizontal accelerations \ddot{r}^N and \ddot{r}^E (for example coming from course changes of an aircraft), it can be seen with Eq. 1.12, that

$$\frac{\partial \dot{\boldsymbol{\psi}}^n}{\partial \boldsymbol{\psi}^n} = -[\mathbf{f}^n \times] = \begin{pmatrix} 0 & -g & -\ddot{r}^E \\ g & 0 & \ddot{r}^N \\ \ddot{r}^E & -\ddot{r}^N & 0 \end{pmatrix}, \quad (4.11)$$

thereby resolving the above contractions. However, the requirement of linear independence of the functional relationship is not fulfilled for these particular edges, i.e. the strapdown gravimetry system is not a structured system. This can be seen by

$$\text{rank}(-[\mathbf{f}^n \times]) = 2. \quad (4.12)$$

(However, all other non-zero 3×3 sub-matrices in \mathbf{F}^{simp} , $\mathbf{H}_r^{\text{simp}}$, and $\mathbf{H}_v^{\text{simp}}$ have full rank.) Also, the overall system is *not* observable due to the contraction

$$|T(\{\delta dg^N, \delta dg^E, \delta dg^D, \delta \psi^N, \delta \psi^E, \delta \psi^D\})| = 3. \quad (4.13)$$

Still neglecting accelerometer biases, this implies however observability for the *vertical* gravity component during a non-accelerated flight: The states δdg^D , δv^D , δr^D , and the measurements z_r^D and z_v^D are not connected to any of the other states in this case, yielding a completely independent sub-system for the vertical components. There is obviously no contraction in this sub-system, and all states are clearly connected to output states: along the paths $\delta dg^D \rightarrow \delta v^D \rightarrow \delta r^D \rightarrow z_r^D$, and $\delta dg^D \rightarrow \delta v^D \rightarrow z_v^D$.

On the other hand, the vertical gravity is *not* observable (i.e. fully separable from attitude errors) in the case of horizontal accelerations (i.e. when including the dashed edges in Fig. 4.3).

Gravity versus accelerometer biases

Now looking at the accelerometer biases $\delta \mathbf{b}_a^b$ (Fig. 4.3), it can be seen, that even when neglecting attitude errors,

$$|T(\{\delta dg^N, \delta dg^E, \delta dg^D, \delta b_a^X, \delta b_a^Y, \delta b_a^Z\})| = 3, \quad (4.14)$$

showing another important property of the strapdown gravimetry system: that gravity and accelerometer biases are inseparable. Note, that this property also holds during accelerated flight manoeuvres, and independent of the (constant) IMU orientation \mathbf{C}_b^n .

When accounting also for the attitude errors, the discrepancy between the number of states $|\mathcal{N}| = 9$ and the number of states in the target set $|T(\mathcal{N})| = 3$ is even stronger.

Velocity observations

For the simplified system model (Figs. 4.2 and 4.3), note that velocity observations \mathbf{z}_v do not at all affect the observability of the system: the path from \mathbf{v}^n via \mathbf{r}^n to \mathbf{z}_r is clearly connected and free of contractions, also if the velocity observations are omitted.

It will be shown in Sect. 4.2, that velocity observations have also a lower relevance for strapdown gravimetry from a *quantitative* perspective.

4.1.2 Algebraic analysis

The structure graphs introduced in the previous section allowed an intuitive understanding of the strapdown gravimetry system, pointing out particular inseparabilities between system states. This section presents a more thorough analysis, based on the well-established algebraic definition of observability, using the observability matrix. Different scenarios, including time-variable vehicle accelerations, and a time-variable attitude, can be analysed in view of the observability of the system.

For a number of N epochs, the *observability matrix* Ξ is given with the definitions of Chap. 3 as

$$\Xi = \begin{pmatrix} \mathbf{H}_k \\ \mathbf{H}_{k+1} \Phi_k \\ \mathbf{H}_{k+2} \Phi_{k+1} \Phi_k \\ \vdots \\ \mathbf{H}_{k+N-1} \Phi_{k+N-2} \Phi_{k+N-3} \dots \Phi_k \end{pmatrix} \quad (4.15)$$

As introduced in Chap. 3, each matrix \mathbf{H}_k maps the n -dimensional system state to the measurement(s) \mathbf{z}_k of a given epoch: $\mathbf{z}_k = \mathbf{H}_k \delta \mathbf{x}_k$, where \mathbf{z}_k can be a combination of multiple

observations, of different types. Further, the type and number of observations may change from epoch to epoch. A necessary condition for the system's observability is, that the number of observations d is equal or greater than the number of system states n , i.e.

$$d = \sum_{i=k}^{k+N-1} \dim(\mathbf{z}_i) \geq n. \quad (4.16)$$

Thus, Ξ is a $d \times n$ matrix, with $d \geq n$. Example: A series of $N = 6$ 3-D measurements (as GNSS coordinates) is sufficient to fulfil this condition for the 18-state strapdown gravimetry system.

The rank deficiency r is then defined for the square symmetric matrix $\Xi^* = \Xi^T \Xi$ as

$$r = n - \text{rank}(\Xi^*). \quad (4.17)$$

Note, that the rank is only defined for square matrices. Assuming $d = n$, also $\text{rank}(\Xi)$ could be used, because $\text{rank}(\Xi) = \text{rank}(\Xi^*)$ in this case.

A system is called observable, if and only if $r = 0$, i.e. the $n \times n$ matrix Ξ^* has a full rank of n . If $r > 0$, only a $n - r$ dimensional subspace of the state space is observable.

In particular, if a system is not observable, a principal component analysis of Ξ^* can be performed based on an Eigen decomposition of Ξ^* in order to further investigate the system properties. An Eigen value of zero indicates an unobservable direction in the state space, which is given by the corresponding Eigen vector.

A more thorough, analytical observability analysis of an integrated IMU/GNSS navigation system is provided in *Rothman et al.* (2014). A method is shown for the analytical determination of the unobservable subspace of a system. In this thesis, the analysis is limited to the computation of rank deficiencies of the observability matrix for different system configurations and scenarios. The next section shows, that such an analysis can provide a valuable insight into the system characteristics.

4.1.3 Scenarios and examples

The rank deficiency r , as introduced in the previous section, is computed for different system state configurations (with particular system states being enabled or disabled). A system state is disabled by removing the respective rows and columns from \mathbf{F} , and from \mathbf{H}_r and \mathbf{H}_v .

Further, four different vehicle motion scenarios are evaluated for each of the system configurations:

- S1: Non-accelerated motion, and no attitude changes,
- S2: non-accelerated motion, with roll and pitch angle changes,
- S3: accelerated motion, no attitude changes, and
- S4: accelerated motion, with roll and pitch angle changes.

The motion is always horizontal (i.e. $v^D = 0$). For S1 and S2, the track is a straight line pointing North. For S1 and S3, the body-fixed coordinate frame is aligned with the navigation frame without losing generality, i.e. $\mathbf{C}_b^n = \mathbf{I} = \text{const}$. A series of $N = 6$ observations is being used.

The rank deficiency is evaluated for both the full system model of Eqs. 3.62ff, and the simplified system model of Eqs. 4.1ff. The results are summarized in Tab. 4.1. It is expected, that the rank deficiencies for the simplified model (first value in each cell of the table) are more realistic in a quantitative sense, because the very small quantities (the weak edges in

	$\delta\psi^n$ N/E/D	active states			rank deficiency r for the simplified / full model			
		$\delta\mathbf{b}_a^b$ x/y/z	$\delta\mathbf{b}_\omega^b$ x/y/z	$\delta d\mathbf{g}^n$ N/E/D	S1	S2	S3	S4
0	● ● ○	○ ○ ○	○ ○ ○	○ ○ ○	0 / 0	0 / 0	0 / 0	0 / 0
1	● ● ●	○ ○ ○	○ ○ ○	○ ○ ○	1 / 0	1 / 0	0 / 0	0 / 0
2	● ● ●	● ● ○	○ ○ ○	○ ○ ○	3 / 1	1 / 0	1 / 0	0 / 0
3	● ● ●	○ ○ ●	○ ○ ○	○ ○ ○	1 / 0	1 / 0	0 / 0	0 / 0
4	● ● ●	● ● ●	○ ○ ○	○ ○ ○	3 / 1	1 / 0	1 / 0	0 / 0
5	● ● ●	○ ○ ○	● ● ●	○ ○ ○	2 / 2	1 / 0	1 / 1	0 / 0
6	● ● ●	● ● ○	● ● ●	○ ○ ○	4 / 4	1 / 0	2 / 2	0 / 0
7	● ● ●	○ ○ ●	● ● ●	○ ○ ○	2 / 2	1 / 0	1 / 1	0 / 0
8	● ● ●	● ● ●	● ● ●	○ ○ ○	4 / 4	1 / 0	2 / 2	0 / 0
9	● ● ●	○ ○ ○	○ ○ ○	● ● ○	3 / 1	3 / 1	1 / 0	1 / 0
10	● ● ●	● ● ○	○ ○ ○	● ● ○	5 / 3	3 / 1	3 / 2	1 / 0
11	● ● ●	○ ○ ●	○ ○ ○	● ● ○	3 / 1	3 / 1	1 / 0	1 / 0
12	● ● ●	● ● ●	○ ○ ○	● ● ○	5 / 3	3 / 1	3 / 2	1 / 0
13	● ● ●	○ ○ ○	● ● ●	● ● ○	4 / 4	3 / 2	2 / 2	1 / 1
14	● ● ●	● ● ○	● ● ●	● ● ○	6 / 6	3 / 2	4 / 4	1 / 1
15	● ● ●	○ ○ ●	● ● ●	● ● ○	4 / 4	3 / 2	2 / 2	1 / 1
16	● ● ●	● ● ●	● ● ●	● ● ○	6 / 6	3 / 2	4 / 4	1 / 1
17	● ● ●	○ ○ ○	○ ○ ○	○ ○ ●	1 / 0	1 / 0	0 / 0	0 / 0
18	● ● ●	● ● ○	○ ○ ○	○ ○ ●	3 / 1	1 / 0	1 / 0	0 / 0
19	● ● ●	○ ○ ●	○ ○ ○	○ ○ ●	2 / 1	1 / 0	1 / 1	0 / 0
20	● ● ●	● ● ●	○ ○ ○	○ ○ ●	4 / 2	1 / 0	2 / 1	0 / 0
21	● ● ●	○ ○ ○	● ● ●	○ ○ ●	2 / 2	1 / 0	1 / 1	0 / 0
22	● ● ●	● ● ○	● ● ●	○ ○ ●	4 / 4	1 / 0	2 / 2	0 / 0
23	● ● ●	○ ○ ●	● ● ●	○ ○ ●	3 / 3	1 / 0	2 / 2	0 / 0
24	● ● ●	● ● ●	● ● ●	○ ○ ●	5 / 5	1 / 0	3 / 3	0 / 0
25	● ● ●	○ ○ ○	○ ○ ○	● ● ●	3 / 1	3 / 1	1 / 0	1 / 0
26	● ● ●	● ● ○	○ ○ ○	● ● ●	5 / 3	3 / 1	3 / 2	1 / 0
27	● ● ●	○ ○ ●	○ ○ ○	● ● ●	4 / 2	3 / 1	2 / 1	1 / 0
28	● ● ●	● ● ●	○ ○ ○	● ● ●	6 / 4	3 / 1	4 / 3	1 / 0
29	● ● ●	○ ○ ○	● ● ●	● ● ●	4 / 4	3 / 2	2 / 2	1 / 1
30	● ● ●	● ● ○	● ● ●	● ● ●	6 / 6	3 / 2	4 / 4	1 / 1
31	● ● ●	○ ○ ●	● ● ●	● ● ●	5 / 5	3 / 2	3 / 3	1 / 1
32	● ● ●	● ● ●	● ● ●	● ● ●	7 / 7	3 / 2	5 / 5	1 / 1

Table 4.1: Observability matrix rank deficiencies $r = n - \text{rank}(\Xi^*)$, for different system state configurations (black dot = active state, white dot = inactive state), and vehicle motion scenarios (S1 to S4). The rank deficiency r is evaluated for both the simplified system (Eqs. 4.1ff), and the full system (Eqs. 3.62ff). Only coordinate and velocity observations are introduced to the system. The system states for position and velocity, $\delta\mathbf{r}^n$ and $\delta\mathbf{v}^n$, are always active (not shown in the table).

Fig. 4.3) show barely any effect on the state estimation in practice (as will be confirmed in Sect. 4.2). In other words, the rank deficiencies of the full system can be regarded as too optimistic (too low) in practice. For each of the configurations, the full system model yields an equal or lower rank deficiency compared to the simplified model.

While it may be difficult to understand the reasons causing the rank deficiencies when looking at a particular rank deficiency, the *comparison* of different table entries can provide a good understanding of the system, confirming the properties that were found using the structure graphs in the previous section.

A turn was chosen for S3 and S4, because it is more common during real gravity flights, compared to constant accelerations. Note, that the scenario S_3 still comprises a *constant* attitude during this right turn, facing North). Such a manoeuvre is in practice not possible when using a fixed-wing aircraft. It is still useful here as an illustrative example.

For a right turn along a circular track, there is a constant acceleration to the right with respect to the direction of travel $\arctan(v^E/v^N)$, with the consequence, that $\mathbf{f}^n \neq \text{const}$ among the N epochs. This resolves the linear dependency of the edges between attitude and velocity: Comparing row 1, S1 versus S3, apparently the heading error $\delta\psi^D$ becomes observable for accelerated motion, cf. *Hong et al.* (2005). This also yields the separability of attitude and the horizontal gravity components (row 9, S1 vs. S3).

During a typical aerogravity flight, small changes of the roll- and pitch angles can not be avoided on a *nominally* straight measurement line, and clearly such changes happen during turns, and during the take-off and landing phases. The change of \mathbf{C}_b^n among the N epochs can resolve linear dependencies in the system, reducing the rank deficiencies for those system configurations including $\delta\mathbf{b}_a^b$ and $\delta\mathbf{b}_\omega^b$, e.g. rows 4, 5, or 8, comparing S1 against S2, or S3 against S4.

Such reductions of the rank deficiencies have led to statements in the literature, that manoeuvres, as e.g. turns, can be useful for an *in-flight calibration* of the IMU, i.e. the in-flight determination of the sensor biases (*Deurloo*, 2011; *Skaloud et al.*, 2015).

More findings can be drawn from the results of Tab. 4.1, in particular supporting the findings of Sect. 4.1.1:

- Compare rows 1 and 17, S1: r is equal for both rows, indicating that the vertical gravity component is observable during non-accelerated motion (as was shown using the sub-system of vertical components in Sect. 4.1.1).
- Compare rows 1 and 9, S1: When adding the two horizontal gravity components, r increases by 2, reflecting that these states are inseparable from attitude (all gravity states are connected to output nodes in Fig. 4.3, thus this deficiency *must* come from a contraction, i.e. an inseparability of system states).
- Compare rows 17 and 19, S1 or S3: The vertical gravity component, and an accelerometer bias in the same direction are inseparable (r increases by 1). This does not hold, if $\mathbf{C}_b^n \neq \text{const}$: no increase for S2 and S4. The same can be seen for the horizontal components (compare rows 9 and 10), and for the full 3-D gravity vector (rows 25 and 28).
- Row 32: Note, that the full 18-state strapdown gravimetry system is unobservable for *all* vehicle motion scenarios.
- Row 8 represents the integrated, 15-state IMU/GNSS *navigation* system, for which the observability has been analysed by several authors (*Rothman et al.*, 2014; *Lee et al.*, 2012; *Hong et al.*, 2005).

4.2 Estimability

Note: Parts of the work presented in this section have been published by the author before the publication of this thesis (Becker et al., 2015a).

The question, *to what extent* the system (or particular system states) is observable, is addressed by the concept of *estimability* (Baram and Kailath, 1987). The estimability analysis done in this section will address two major questions:

- *How much* is the gravity estimation affected by vehicle manoeuvres (i.e., accelerations)?
- *How much* is the gravity estimation affected by the observation accuracy (for coordinate, velocity, and attitude observations)?

4.2.1 Definition

For a series of N upcoming observations $\mathbf{z}_i = \mathbf{H}_i \mathbf{x}_i$ (with $i = k \dots (k + N - 1)$), the estimability ν is a measure of how much these observations can reduce the a-priori system state covariances \mathbf{P}_k^- at epoch k .

Note, that estimability does *not* account for the system noise $\mathbf{w}^s \sim \mathcal{N}(\mathbf{0}, \mathbf{Q})$. The a-priori and a-posteriori system state covariance matrices, \mathbf{P}^- and \mathbf{P}^+ , are used in this sense in the scope of this section.

The *information matrix* of such a series of observations is given as (Moon et al., 2008)

$$\mathbf{L}_{k,k+N-1} = \sum_{i=0}^{N-1} \Phi_{k+i,k}^T \mathbf{H}_{k+i}^T \mathbf{R}_{k+i}^{-1} \mathbf{H}_{k+i} \Phi_{k+i,k}, \quad (4.18)$$

where $\Phi_{k+i,k} = \Phi_{k+i-1} \Phi_{k+i-2} \dots \Phi_k$ is the system state transition matrix from epoch k to epoch $k + i$. As for the algebraic definition of observability, the matrix \mathbf{H} may combine multiple observations for each epoch, and the number and the types of observations may change among the N epochs.

The estimability ν may then be calculated with respect to \mathbf{P}_k^- and a direction in the state space, \mathbf{u} , as

$$\nu(\mathbf{L}_{k,k+N-1}, \mathbf{P}_k^-, \mathbf{u}) = \frac{\mathbf{u}^T (\mathbf{P}_k^- - \mathbf{P}_{k+N-1}^+) \mathbf{u}}{\mathbf{u}^T \mathbf{P}_k^- \mathbf{u}}, \quad \text{with} \quad (4.19)$$

$$\mathbf{P}_{k+N-1}^+ = [(\mathbf{P}_k^-)^{-1} + \mathbf{L}_{k,k+N-1}]^{-1}. \quad (4.20)$$

This relation of a-priori covariances \mathbf{P}_k^- and a-posteriori covariances \mathbf{P}_{k+N-1}^+ yields an estimability ν in the range between

- $\nu = 0$: The observations do not reduce the system state uncertainty in the state space direction \mathbf{u} , i.e. the system is not observable in the direction \mathbf{u} ; and
- $\nu = 1$: The a-posteriori covariances become zero (this is impossible in practice, if the observations have a non-zero uncertainty). $\nu \approx 1$ indicates a high estimability, i.e. the variances reduce significantly.

Negative values for ν are not possible, since observations will never increase a system's uncertainty estimates.

For the analysis, \mathbf{u} is taken from the standard basis \mathbf{e}_j of the state space. Thus, estimability values for distinct system states are computed, in particular for the vertical and horizontal gravity components. Eq. 4.19 can then be rewritten for the j -th system state as

$$\nu_j = \frac{(\sigma_{j,k}^-)^2 - (\sigma_{j,k+N-1}^+)^2}{(\sigma_{j,k}^-)^2} = 1 - \frac{(\sigma_{j,k+N-1}^+)^2}{(\sigma_{j,k}^-)^2}, \quad (4.21)$$

where $\sigma_{j,i}^-$ and $\sigma_{j,i}^+$ denote the a-priori and a-posteriori standard deviations for the j -th system state at epoch i . Since the comparison of standard deviations is usually more intuitive than a comparison of variances, a modified estimability measure is introduced here based on Eq. 4.21:

$$\nu_j^* = \frac{\sigma_{j,k}^- - \sigma_{j,k+N-1}^+}{\sigma_{j,k}^-} = 1 - \frac{\sigma_{j,k+N-1}^+}{\sigma_{j,k}^-} = 1 - \sqrt{1 - \nu_j}, \quad (4.22)$$

or in general: $\nu^* = 1 - \sqrt{1 - \nu}$.

Alternative computation

In *Moon et al. (2008)*, an equivalent formulation of ν can be found, based on a singular value decomposition (SVD) of the information matrix:

$$\text{SVD} : \mathbf{USV}^T = \sqrt{\mathbf{P}_k^-} \mathbf{L}_{k,k+N-1} \sqrt{\mathbf{P}_k^-}, \quad (4.23)$$

where \mathbf{S} is a diagonal matrix with elements s_i . Then,

$$\mathbf{D} = \text{diag}\left(\frac{s_i}{1 + s_i}\right), \quad \mathbf{z} = \frac{\sqrt{\mathbf{P}_k^-} \mathbf{u}}{\|\sqrt{\mathbf{P}_k^-} \mathbf{u}\|_2}, \quad (4.24)$$

$$\nu(\mathbf{L}_{k,k+N-1}, \mathbf{P}_k^-, \mathbf{u}) = \mathbf{z}^T \mathbf{U} \mathbf{D} \mathbf{U}^T \mathbf{z}. \quad (4.25)$$

This formulation will be used for the following evaluation of test scenarios, due to its higher numerical stability.

4.2.2 Simulated flight trajectories

For a first analysis, basic flight trajectories are simulated:

1. A non-accelerated, northbound, horizontal flight with $|\mathbf{v}^n| = 100$ m/s. In addition to the coordinate observation accuracy, the impacts of velocity and attitude observations (as e.g. available from GNSS) are analysed for this case.
2. A horizontal circle, yielding cross-track accelerations (here: to the right in the direction of travel), again at 100 m/s.

For the analysis, the full system model \mathbf{F} , \mathbf{H}_r , \mathbf{H}_v , and \mathbf{H}_ψ is being used (cf. Eqs. 3.62 and Sect. 3.3). The modified estimability ν^* is computed for $N = 100$ epochs, at a rate of 1 Hz. An interval of 100 s is typical for the (temporal) along-track gravity resolution of a strapdown gravimetry system (*Glennie and Schwarz, 1999; Bruton et al., 2001; Ayres-Sampaio et al., 2015*). At 100 m/s, it is consistent with a spatial half-wavelength resolution of 5 km.

A crucial parameter for the analysis is the initial system covariance matrix \mathbf{P}_k^- . Obviously, when assuming lower initial standard deviations, the estimability ν (or ν^*) will reduce, and vice versa. Thus, the absolute estimability value is always given with respect to \mathbf{P}_k^- . It is defined here with zero covariances between the states, and with the following initial standard deviations: $\sigma_r = 1$ cm, $\sigma_v = 1$ mm/s, $\sigma_\psi^N = \sigma_\psi^E = 5''$, $\sigma_\psi^D = 20''$, $\sigma_{b_\omega} = 1 \cdot 10^{-3}''/\text{s}$, and $\sigma_{dg} = \sigma_{b_{acc}} = 5$ mGal.

Example: The estimability of $\nu^* = 0.8$ for the vertical gravity component reflects a observation-driven reduction of the a-priori accuracy of 5 mGal, down to 1 mGal, as can be seen from Eq. 4.22.

Non-accelerated horizontal flight

For the non-accelerated flight, the inseparability of accelerometer biases and gravity becomes evident again (for a horizontal flight, the respective vertical components span the 12th and the 18th dimension of the state space, respectively). The estimability is evaluated for the following directions in state space:

$$\mathbf{u}_1 = -\mathbf{e}_{12} + \mathbf{e}_{18} \quad (4.26)$$

$$\mathbf{u}_2 = \mathbf{e}_{12} + \mathbf{e}_{18} \quad (4.27)$$

The estimability values $\nu_{\mathbf{u}_1}^*$ and $\nu_{\mathbf{u}_2}^*$ are evaluated for different combinations of coordinate and velocity observation accuracies. $\nu_{\mathbf{u}_1}^*$ is shown in Fig 4.5. Points on the same iso-line reflect observation configurations, that equally enable the vertical gravity determination in a quantitative sense.

For the same set of observation combinations, the estimability in the state space direction \mathbf{u}_2 is very close to zero: $\nu_{\mathbf{u}_2}^* < 0.001$ (no figure shown). This clearly reflects the inseparability of the vertical accelerometer bias, and the vertical gravity component: the difference between accelerometer bias and gravity is estimable (\mathbf{u}_1), while their sum can not be estimated (\mathbf{u}_2). (Note, that the signs arise from the arbitrary definition of the states: When modelling accelerometer *corrections* instead of biases, the sum \mathbf{u}_2 becomes estimable, while the difference \mathbf{u}_1 is not.) For separable states however, obviously their sum *and* their difference have to have a non-zero estimability. Therefore, $\nu_{\mathbf{u}_2}^*$ can be regarded as a *measure of separability* of accelerometer biases and gravity.

When removing the accelerometer biases \mathbf{b}_a^b from the system state, the computed estimability values for the vertical gravity component indeed show a very similar picture, Fig. 4.6. For typical carrier-phase differential GNSS (PD-GNSS), or precise point positioning (PPP) solutions, coordinate observations are typically available at an accuracy level of 2 cm to 10 cm, depending on the base line length, and the constellation and number of visible satellites. With velocity observations at the accuracy level of 1 m/s (or even without velocity observations), an estimability of 0.8 to 0.95 can be found in the diagram, reflecting estimated standard deviations in the range from $\sigma_{dg}^D = 0.2 \cdot 5 = 1$ mGal to $\sigma_{dg}^D = 0.05 \cdot 5 = 0.25$ mGal.

Note, that the actual accuracies can be (much) lower in practice, as the states are modelled here for the purpose of the estimability analysis as random constants (i.e., zero system noise). Also, actual observation errors, as GNSS coordinates, can be highly correlated over shorter periods, while uncorrelated Gaussian noise is assumed here. Third, no IMU sensor errors (neither systematic, nor stochastic) are taken into consideration here.

Still, more system characteristics are revealed in Fig. 4.6. For example, having coordinate observations at an accuracy of 5 cm, the vertical gravity estimability remains almost unaffected when adding velocity observations unless they are available at an accuracy of few mm/s, which is difficult to achieve in practice. Velocities taken from two-frequency carrier-phase GNSS are typically available at an accuracy of several cm/s, which (again according to Fig. 4.6) is only beneficial for the gravity determination, if GNSS coordinate observations are only available at the metre-level at the same time.

The horizontal gravity components (i.e. the deflections of the vertical, DoV) are not separable from attitude errors during a non-accelerated flight, as was already shown by the observability analysis of Sect. 4.1 (indeed, $\nu^* \approx 0$ for this case, no figure shown). Additional attitude observations, as e.g. coming from a GNSS vector system comprising multiple antennas, may support the separation of attitude and horizontal gravity. Fig. 4.7 confirms this assumption. However, very accurate roll and pitch observations are required to yield a relevant improvement of the DoV accuracy. Such observations are very difficult to achieve in practice. Typical GNSS vector systems with baselines of up to 5 m can not be expected to provide azimuth and elevation angles better than 0.1° (or: 360 arc seconds) in a kinematic

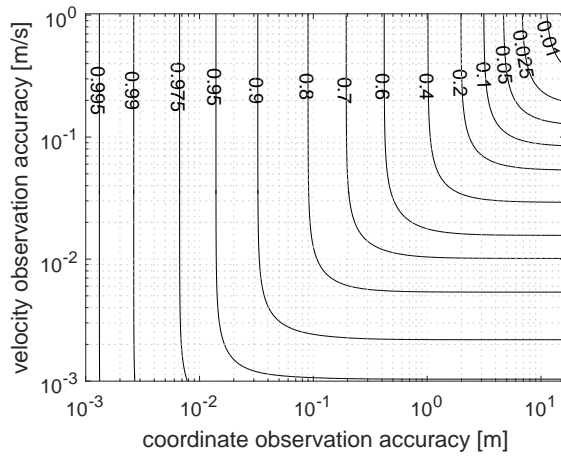


Figure 4.5: Estimability iso-lines $\nu^* = \text{const}$ for different combinations of coordinate and velocity observation accuracies, in the state space direction \mathbf{u}_1 .

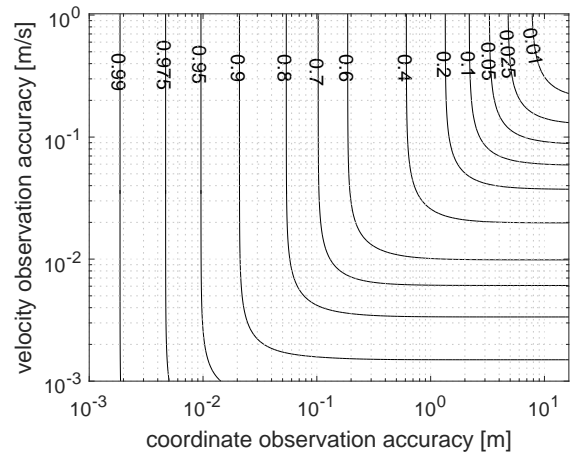


Figure 4.6: Vertical gravity estimability ν^* for different combinations of coordinate and velocity observation accuracies (neglecting accelerometer biases).

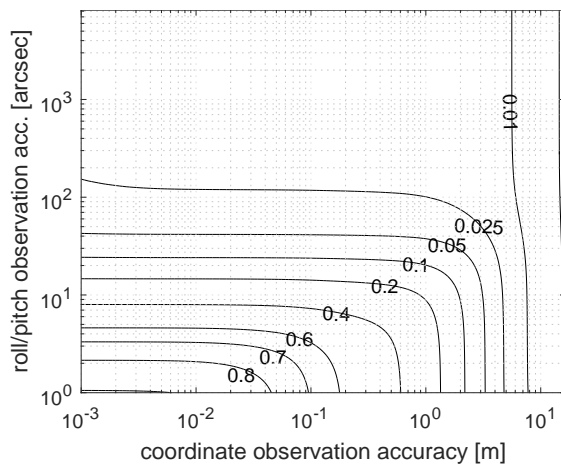


Figure 4.7: DoV estimability ν^* for different combinations of coordinate, and roll and pitch observation accuracies (neglecting accelerometer biases).

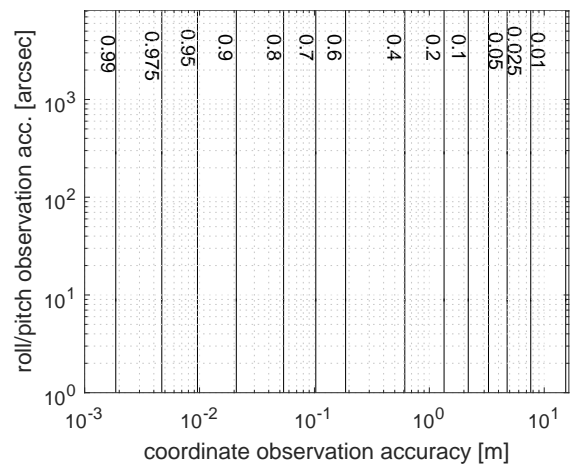


Figure 4.8: Vertical gravity estimability ν^* for different combinations of coordinate, and roll and pitch observation accuracies (neglecting accelerometer biases).

setup (Vander Kuylen *et al.*, 2006; Cohen *et al.*, 1994), thereby not yielding any relevant effect for the DoV determination (Fig. 4.7). With initial roll and pitch angle accuracies of 5 arc seconds, it can be seen in Fig. 4.8, that such an attitude accuracy is sufficient for the vertical gravity determination. The roll and pitch observations do not yield any significant improvements in this case.

Note, that Fig. 4.7 shows estimability values for combinations of coordinate observations, and combined roll *and* pitch observations. The effects are not evaluated separately, because it is clear due to symmetry reasons, that for a horizontal flight, the pitch observations support the DoV determination in *along-track* direction, while the roll observations support it in the *cross-track* direction.

Accelerated manoeuvres

For accelerated flight manoeuvres, Sect. 4.1 already showed that the deflections of the vertical may become observable, also in the absence of attitude observations. To analyse this effect quantitatively, a horizontal planar turn is simulated (invoking cross-track accelerations), at a constant roll angle of 15° and again with constant velocity $v = 100$ m/s. The heading angle is chosen to follow the vehicle's course over ground, i.e. the body-fixed X -axis is aligned with the direction of travel. Such a manoeuvre is typical for aircraft motion. Manoeuvres, which are less relevant in practice, as *vertical* turns (*loopings*), are not taken into consideration here.

First, the estimability along the state space directions \mathbf{u}_1 and \mathbf{u}_2 is evaluated. For typical GNSS coordinate observation accuracies of 2 cm to 10 cm, the horizontal accelerations yield only a slight reduction of $\nu_{\mathbf{u}_1}^*$ (see Fig. 4.9). For \mathbf{u}_2 however, the change of the attitude, $\mathbf{C}_b^n \neq \text{const}$, enables non-zero estimability values in the direction \mathbf{u}_2 (Fig. 4.10), indicating separability of the vertical gravity component and the accelerometer biases (to a low degree, however). This is consistent with the observability analysis of Sect. 4.1, in particular with the findings inferred from Tab. 4.1.

Fig. 4.11 clearly shows, that the DoV can be estimated during manoeuvres comprising sufficiently strong accelerations. Reading example: With coordinate observations at the 1 cm accuracy level, and a cross-track acceleration of 6.5 m/s², the DoV estimability is $\nu^* = 0.6$. With respect to the initial standard deviation of 5 mGal for the horizontal gravity components, this means a reduction to 2 mGal. This is equivalent to a reduction of the angular DoV standard deviations from 1.05 to 0.42 arc seconds. As an example, a cross-track acceleration of $a = 6.5$ m/s² at $v = 100$ m/s is equivalent to a turn radius of

$$R_{\text{turn}} = \frac{v^2}{a} \approx 1.5 \text{ km} . \quad (4.28)$$

Fig. 4.12 shows, that cross-track accelerations yield a slight reduction of the vertical gravity estimability compared to non-accelerated motion.

4.2.3 Real data example

A flight from an airborne gravimetry campaign in Malaysia in 2015 is used as a real-data example. The ground track is shown in Fig 4.13. This flight comprises a 15 minutes phase of idling manoeuvres (this was requested by flight control due to air traffic). The nominal distance between the two main measurement lines is 10 km. The nominal flight altitude is 1829 m (6000 ft). Estimability values are computed for time windows of $N = 100$ epochs, again using intervals of 1 s. For the actual velocity of ≈ 90 m/s, this is consistent with a spatial resolution of ≈ 4.5 km (half wavelength). For the analysis, the actual \mathbf{F} matrices are computed based on the actual estimates of the navigation state (position, velocity, attitude). Two-frequency precise point positioning (PPP) coordinates are introduced as observations,

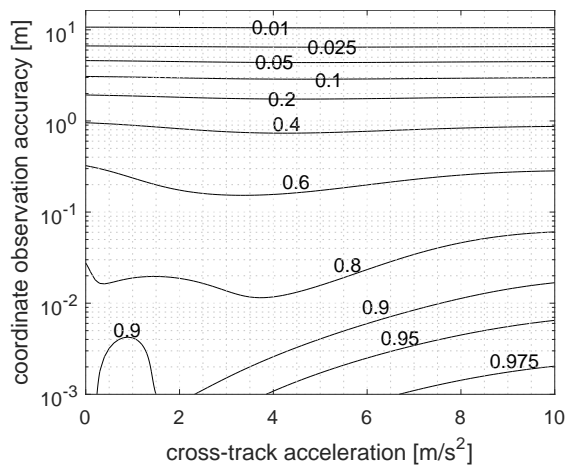


Figure 4.9: Estimability ν^* for different combinations of cross-track accelerations and coordinate observation accuracies, in the state space direction \mathbf{u}_1 .

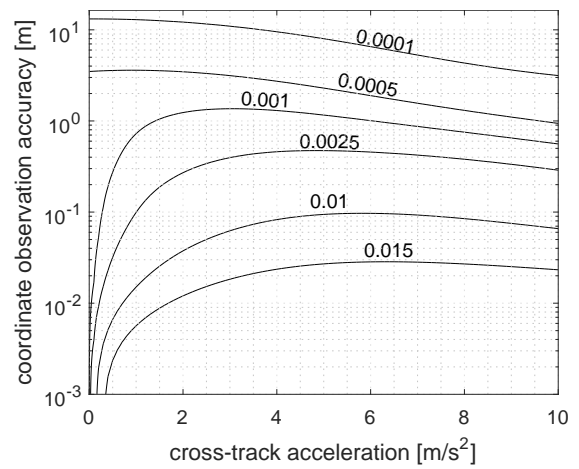


Figure 4.10: Estimability ν^* for different combinations of cross-track accelerations and coordinate observation accuracies, in the state space direction \mathbf{u}_2 .

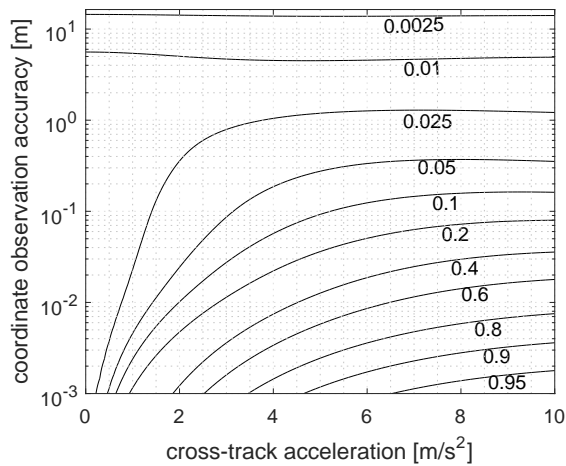


Figure 4.11: DoV estimability ν^* for different combinations of cross-track accelerations and coordinate observation accuracies (neglecting accelerometer biases).

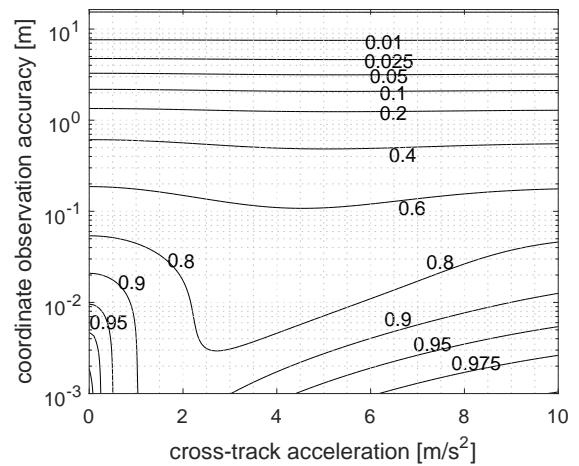


Figure 4.12: Vertical gravity estimability ν^* for different combinations of cross-track accelerations and coordinate observation accuracies (neglecting accelerometer biases).

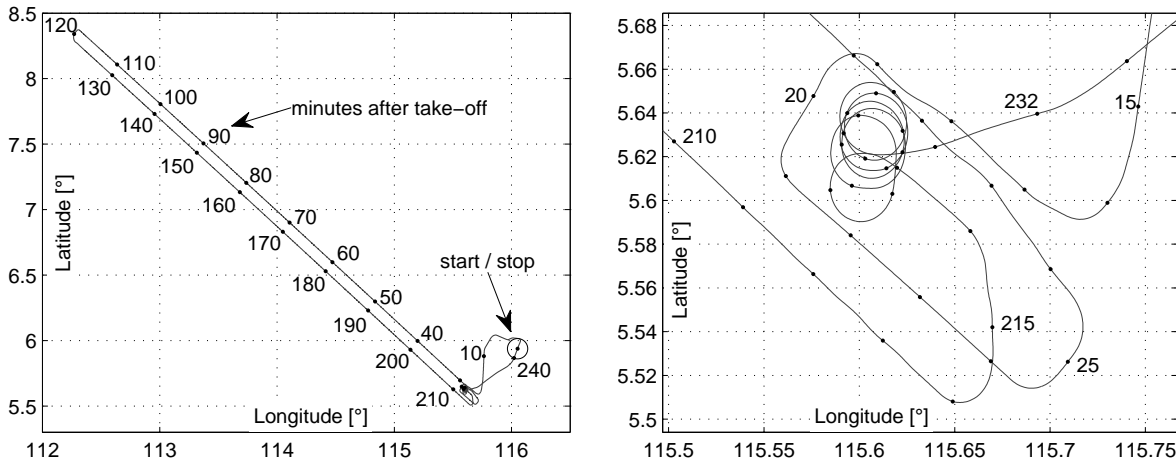


Figure 4.13: *Left:* Ground track of an aerogravity flight out of Kota Kinabalu, Malaysia. The dots indicate 10 minute intervals. *Right:* Detail plot of the south-east part of the track: 15 minutes of idling flight manoeuvres before landing. The radius of the circular idle motion is $R_{\text{turn}} \approx 1.6$ km. The dots indicate one minute intervals.

with actual standard deviations as estimated by the software Waypoint GrafNav (*Novatel Inc.*, 2014). The a-priori covariances \mathbf{P}_k^- are chosen identical for each of the 100-epoch time windows, using the same values as introduced in Sect. 4.2.2.

The flight characteristics: horizontal velocity, horizontal acceleration, and the GNSS coordinate observation accuracy, are shown in Fig. 4.14 (top). Estimability is again evaluated for the state space direction \mathbf{u}_2 to indicate the degree of separability between the vertical gravity component and the accelerometer biases. Fig. 4.14 shows the results of the evaluations. On the main measurement lines, $\nu_{\mathbf{u}_2}^*$ is very close to zero, indicating the inseparability of vertical gravity, and the accelerometer bias in the same direction. As expected, a separation of these states is only possible during phases of attitude changes (c.f. Sect. 4.1 / Tab. 4.1).

Fig. 4.15 shows the estimability for the three attitude system states. As expected, the values increase during flight manoeuvres. $\nu_{\psi, N}^*$ correlates with ν_{η}^* , and $\nu_{\psi, E}^*$ correlates with ν_{ξ}^* , indicating the inseparability of attitude errors and the DoV: On the main measurement lines, ν_{ξ}^* and ν_{η}^* are very close to zero. Note, that this reflects the inability of *accurately* estimating the DoV. However, if the relative attitude *stability* is sufficiently high, the DoV may still be determined with reasonable *precision* in practice, enabling relative DoV measurements along a flight line (*Jekeli*, 1994). This will also be shown in Chap. 8 on real data.

4.3 Implications for SAG

The analyses of sections 4.1 and 4.2 revealed several important properties of the strapdown gravimetry system:

1. In-run changes of the accelerometer biases can not be separated from changes of the sensed gravity. Note, that this also holds during manoeuvres comprising accelerations and/or attitude changes: in any case, a similar change of each of the signals changes *all* available observations equivalently. Separability could be verified in the previous section only under the assumption, that the true system states remain constant for a short period of time (here: 100 seconds).

In practice, however a *spectral separation* may be possible: Short-wavelength gravity changes can be determined, if the accelerometer bias change is assumed to have only long-wavelength components in the spectral domain. Such an assumption can be reasonable in practice. On the other hand, long-term accelerometer bias changes are still

problematic, as they prevent the accurate gravity determination in the respective frequency range.

2. On a straight flight line, the attitude changes are in practice too small to enable the separation of accelerometer biases and gravity.
3. The determination of the DoV requires accurate attitude estimates. Therefore, in addition to the accelerometer biases, the gyroscope stability is a limiting factor in practice (*Jekeli*, 1994). It is noted here again, that an uncompensated accelerometer bias change of 4.75 mGal has the same effect on the DoV determination, as an uncompensated attitude error of only 1 arc second.
4. Heading angles are only estimable during manoeuvres comprising vehicle accelerations.

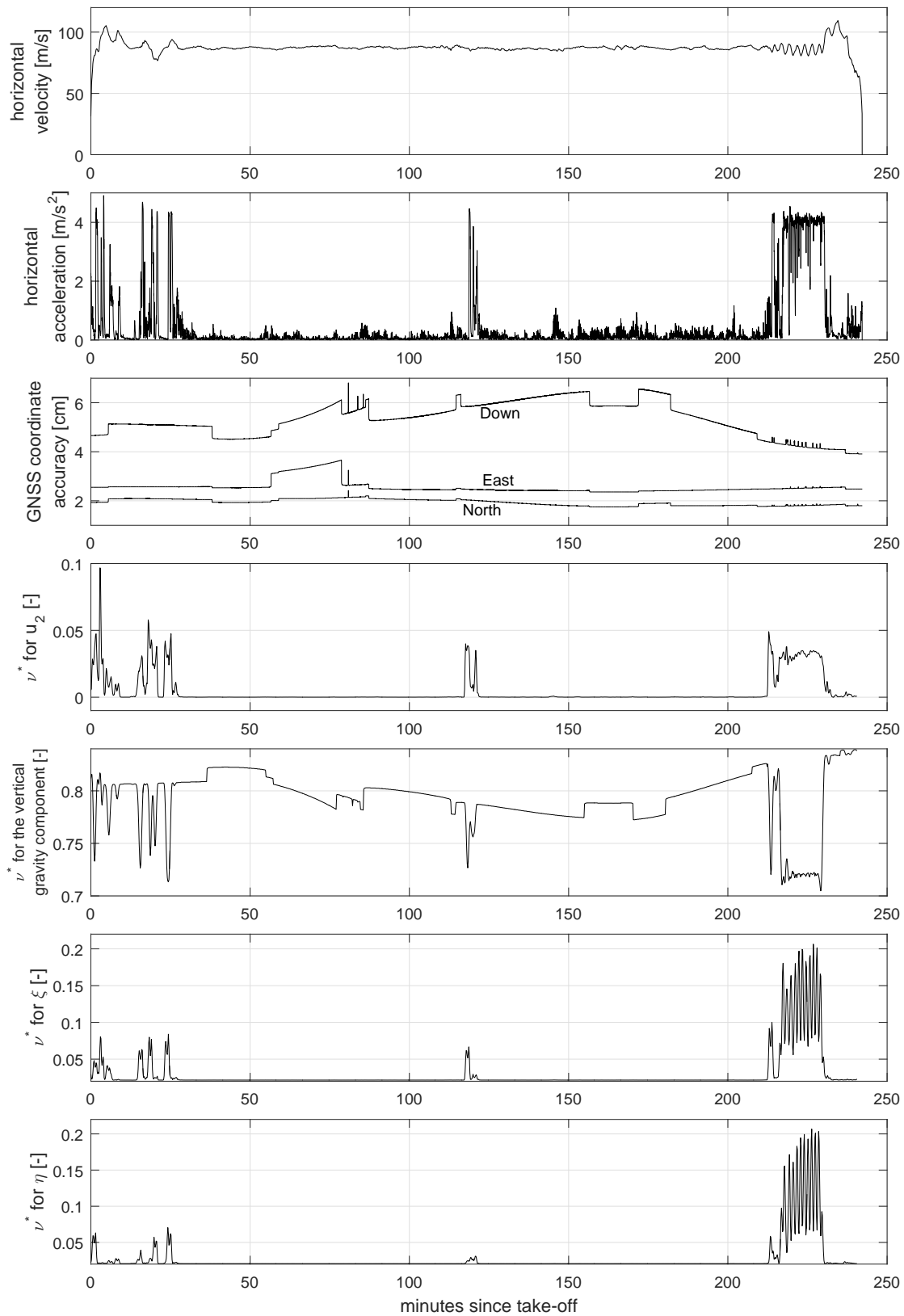


Figure 4.14: Flight characteristics and estimability values ν^* (Eq. 4.22) for the example aerogravity flight shown in Fig. 4.13. $\nu_{u_2}^*$ (plot 4) reflects the separability of the vertical accelerometer bias and the vertical gravity component. The estimability for gravity (plots 5 to 7) was evaluated *neglecting* accelerometer biases.

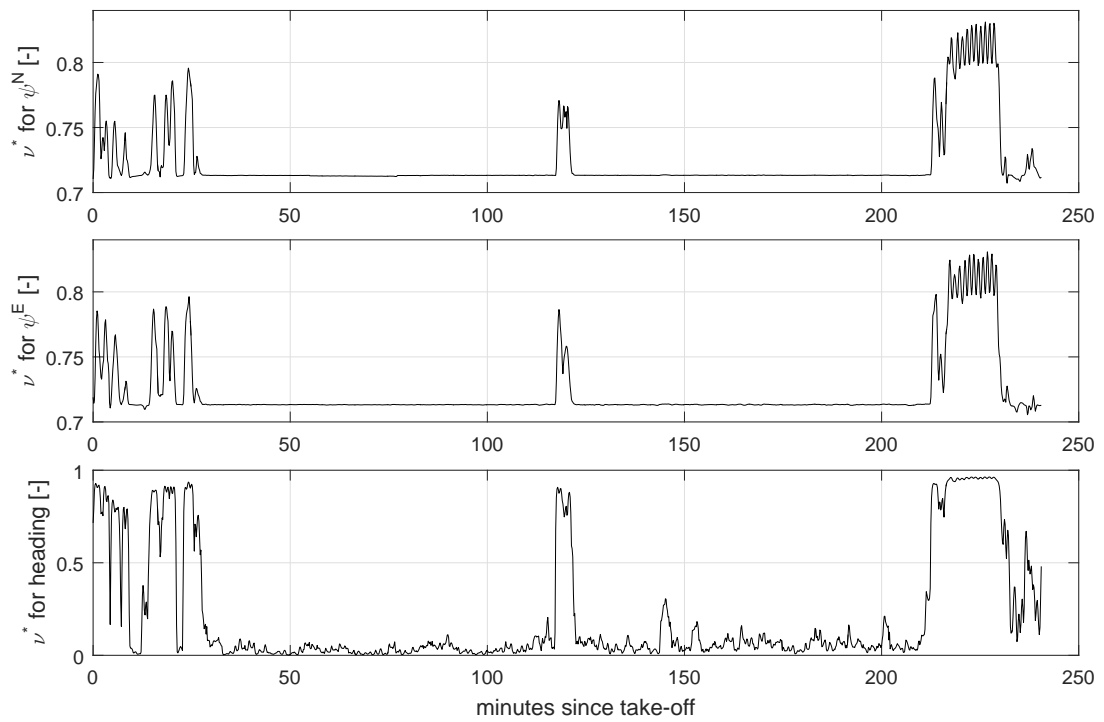


Figure 4.15: Attitude estimability values ν^* (Eq. 4.22) for the example aerogravity flight shown in Fig. 4.13. Note, that the heading is almost inestimable on the main measurement lines.

Chapter 5

Error propagation analysis

Note: Parts of the analysis presented in this chapter have already been published by the author (*Becker and Becker, 2015*).

This chapter addresses the question, to what degree different types of IMU errors propagate into the gravity estimates of the strapdown gravity system introduced in Chap. 3. Such knowledge is important to assess the quality, and the relevance of the IMU calibration methods shown in Chap. 6.

Additionally, an error-free simulation is used in order to confirm the correctness of the integrated IMU/GNSS strapdown gravimetry algorithm, used for the real-data evaluations in Chap. 8.

The error types are separated into two groups:

1. systematic (non-stochastic) errors: constant sensor biases, scale factors, cross-couplings, misalignments, lever arm errors, timestamp errors, and discretisation errors; and
2. stochastic errors: sensor noise of the inertial sensors, and the GNSS coordinate observations.

For each of the investigated error types, a threshold value is derived from simulations, indicating the magnitude of the particular error type, causing an error of the gravity estimates of 1 mGal (vertical component), or 1 arc second (DoV). This allows an easy comparability among the different error types. The results of this chapter can be regarded as a guide for setting up a strapdown gravimetry system: The results indicate, which error types of the system are relevant for the gravity determination in practice, and which are not.

The question how much an error propagates into the gravity estimates, is highly dependent on the characteristics of the vehicle motion. For example, it was already shown in Chapter 4, that the gravity estimate quality is different during manoeuvres compared to linear (non-accelerated) motion. In order to gain *realistic* simulation results, the error propagation analysis presented in this chapter is based on simulations of *imitated* aerogravity flights. The real trajectory is approximated using analytical functions. This enables a simulation of a realistic flight trajectory, with a perfect (error-free) reference trajectory.

5.1 Methodology

A set of twelve gravity flights flown out of Kota Kinabalu (North Borneo, Malaysia) in 2014 is used as the basis for the simulations (Fig. 5.1). Tab. 5.1 summarises the main characteristics of this campaign. Details for each of the twelve flights are provided in the Appendix, Sect. A.2. This set of flights is regarded as a typical representative for a production-oriented aerogravity campaign, including different levels of turbulence, auto-pilot course and

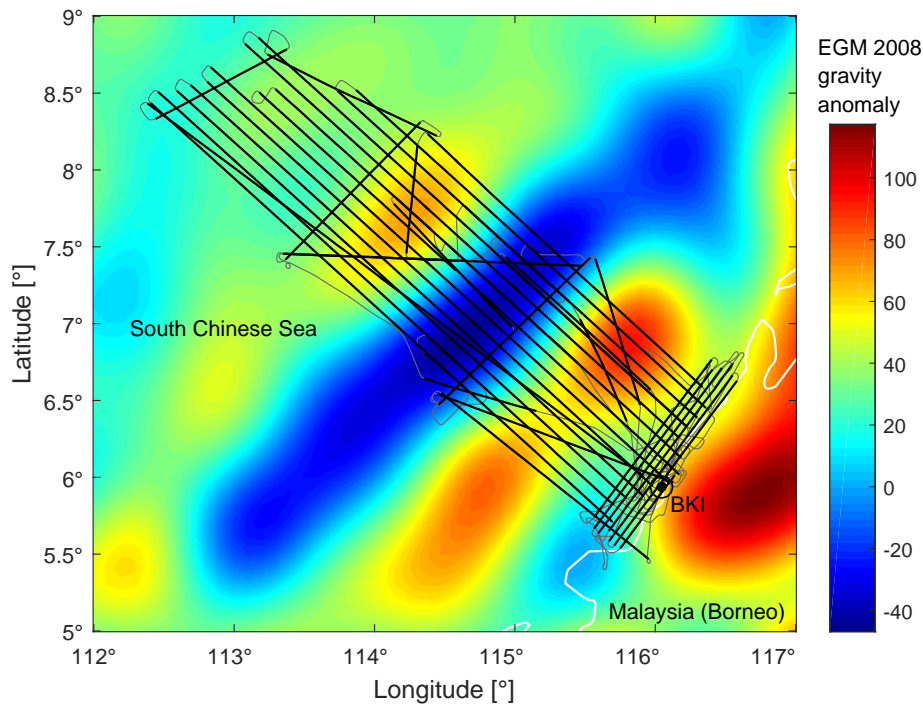


Figure 5.1: Simulated flight tracks, and EGM2008 gravity anomalies, based on the 2014 Malaysia aerogravity campaign, operated out of Kota Kinabalu (airport code *BKI*). The measurement lines are plotted as thick black lines, the coast line is plotted in white.

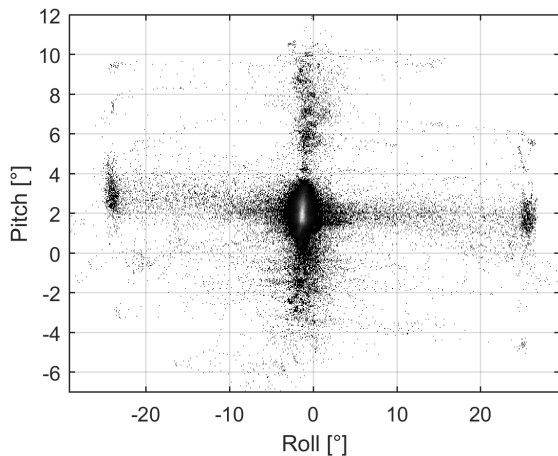


Figure 5.2: Attitude characteristics of the simulated flights (from take-off to touch-down). The brighter points in the centre indicate a larger frequency of occurrence of the respective attitudes.

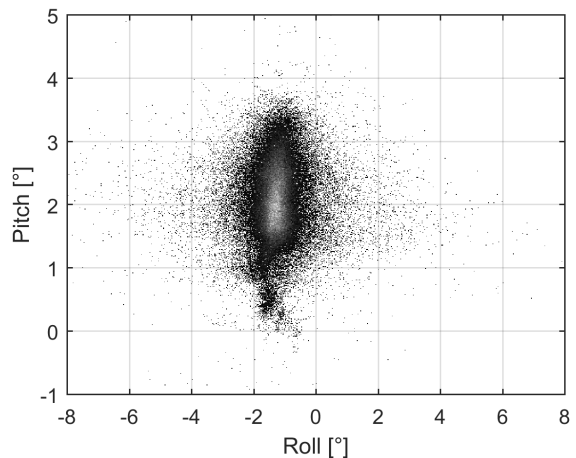


Figure 5.3: Attitude characteristics on the measurement lines. Mean (standard deviation) for the roll and pitch angles are -1.3° (0.75°) and 2.1° (0.60°), respectively. The brighter points in the centre indicate a larger frequency of occurrence of the respective attitudes.

altitude corrections, and the typical transition manoeuvres between flight lines, including turns and altitude changes.

aircraft used for the original data set	KingAir BeechCraft 350, two engines
total distance	12.986 km
total distance on lines	9.666 km
total duration	41.4 h
total duration on lines	30.7 h
minimum line duration	600 s
average velocity on lines	87.6 m/s ($\sigma = 3.7$ m/s)
nominal line altitude	coastal: 3000 ft, offshore: 6000 ft
nominal line spacing	coastal: 5 km, offshore: 10 km
volatility of roll angle per line	σ ranging from 0.24° to 1.86° , average: 0.66°
volatility of pitch angle per line	σ ranging from 0.15° to 1.04° , average: 0.31°
volatility of heading per line	σ ranging from 0.29° to 2.39° , average: 1.03°
initial and final alignment phases	20 minutes each (simulated)
sampling rate	simulated IMU: 600 Hz, simulated GNSS: 1 Hz, (ground-truth positions were evaluated at 2400 Hz)

Table 5.1: Main characteristics of the simulated airborne campaign. Attitude and heading volatilities are shown here as a measure of the flight stability on the measurement lines, see also Fig. 5.3.

A *ground-truth* simulation is carried out, i.e. the sensor observations are first simulated as error-free. EGM2008 gravity disturbances, computed up to degree and order 360, are used for the simulation, see Fig 5.1 (*Pavlis et al.*, 2008).

The simulation is based on the 3-D velocity information \mathbf{v}^n , and the 3-D attitude information $\boldsymbol{\psi}^n$ from the original campaign data set, and three-dimensional EGM2008 gravity disturbances, each at a data rate of 1 Hz. A hermite spline interpolation is then carried out using the given 1 Hz data as knots, resulting in nine independent cubic splines for: velocity ($\mathbf{v}_{\text{sim}}^n(t)$), attitude ($\boldsymbol{\psi}_{\text{sim}}^n(t)$), and gravity disturbance ($\mathbf{d}\mathbf{g}_{\text{sim}}^n(t)$). These splines are steady as well as their first derivatives. The splines are defined over time, allowing the analytical computation of the time derivatives:

$$\mathbf{a}_{\text{sim}}^n(t) = \dot{\mathbf{v}}_{\text{sim}}^n(t) \quad (5.1)$$

$$\boldsymbol{\omega}_{nb,\text{sim}}^n(t) = \frac{d}{dt}(\boldsymbol{\psi}_{\text{sim}}^n(t)) \quad (5.2)$$

Compared to regular cubic splines, a hermite spline $H(t)$ has the important property, that

$$H(t_1) \leq H(t_2) \Rightarrow H(t_1) \leq H(t) \leq H(t_2), \quad \text{for } t \in [t_1 \dots t_2], \quad \text{and} \quad (5.3)$$

$$H(t_1) \geq H(t_2) \Rightarrow H(t_1) \geq H(t) \geq H(t_2), \quad \text{for } t \in [t_1 \dots t_2]. \quad (5.4)$$

As a consequence,

$$H(t_1) = H(t_2) \Rightarrow \dot{H}(t) = 0, \quad \text{for } t \in [t_1 \dots t_2]. \quad (5.5)$$

This allows a more realistic simulation compared to regular splines, which can significantly "run away" between two spline knots. On the other hand, regular cubic splines have steady second derivatives, which does not hold for hermite splines in general.

The continuous hermite spline functions $\mathbf{v}_{\text{sim}}^n(t)$, $\boldsymbol{\psi}_{\text{sim}}^n(t)$, and $\mathbf{d}\mathbf{g}_{\text{sim}}^n(t)$ then enable the computation of the full set of IMU and GNSS observations, in principle by inversely applying

Symbol	Parameter description	Default setting
$\sigma_{0,r}$	Initial position uncertainty	2 cm
$\sigma_{0,v}$	Initial velocity uncertainty	10 cm/s
$\sigma_{0,\psi}$	Initial roll/pitch uncertainty	1°
	Initial heading uncertainty	5°
σ_{0,b_a}	Initial accelerometer bias uncertainty	30 mGal
σ_{0,b_ω}	Initial gyroscope bias uncertainty	0.001 °/h
q_r	Position system noise	0
q_v	Velocity system noise	0.1 mm/ $\sqrt{s^3}$
q_ψ	Attitude system noise	1" / \sqrt{s}
q_{b_a}	Accelerometer bias system noise	0.01 mGal/ \sqrt{s}
q_{b_ω}	Gyroscope system noise	0
$\sigma_{0,dg}$	Initial gravity disturbance uncertainty	0.03 mGal
β_{dg}^{3rd}	3rd order Gauss-Markov correlation parameter	1/20 km ⁻¹
σ_{dg}	Gravity disturbance standard deviation	100 mGal
σ_{z_r}	GNSS coordinate observation accuracy	2 cm

Table 5.2: Default EKF settings used for the error propagation simulations.

Eqs. 3.75ff:

$$\mathbf{C}_{b,\text{sim}}^n = \mathbf{C}_{b,\text{sim}}^n(\boldsymbol{\psi}_{\text{sim}}^n) \quad (5.6)$$

$$\mathbf{g}_{\text{sim}}^n = \boldsymbol{\gamma}(\varphi_{\text{sim}}, h_{\text{sim}}) + d\mathbf{g}_{\text{sim}}^n \quad (5.7)$$

$$\mathbf{f}_{\text{sim}}^n = \mathbf{a}_{\text{sim}}^n - \mathbf{g}_{\text{sim}}^n + 2\boldsymbol{\omega}_{ie,\text{sim}}^n \times \mathbf{v}_{\text{sim}}^n + \boldsymbol{\omega}_{en,\text{sim}}^n \times \mathbf{v}_{\text{sim}}^n \quad (5.8)$$

$$\mathbf{f}_{\text{sim}}^b = (\mathbf{C}_{b,\text{sim}}^n)^T \mathbf{f}_{\text{sim}}^n \quad (5.9)$$

$$\boldsymbol{\omega}_{ib,\text{sim}}^n = \boldsymbol{\omega}_{ie,\text{sim}}^n + \boldsymbol{\omega}_{en,\text{sim}}^n + \boldsymbol{\omega}_{nb,\text{sim}}^n \quad (5.10)$$

$$\boldsymbol{\omega}_{ib,\text{sim}}^b = (\mathbf{C}_{b,\text{sim}}^n)^T \boldsymbol{\omega}_{ib,\text{sim}}^n \quad (5.11)$$

The error propagation analysis is then based on the quantification, how accurate the simulated gravity disturbances (based on the EGM2008 values) can be recovered from the simulated observation data, if different types of errors are artificially introduced to the system.

The continuous functions are discretised using a pre-defined sampling rate. An IMU sensor data rate of 600 Hz is used for all experiments (unless stated differently), and GNSS observations are computed at 1 Hz data rate. The position $(\varphi_{\text{sim}}, \lambda_{\text{sim}}, h_{\text{sim}})$ has to be computed iteratively for discrete time intervals, because the radii of curvature R_N and R_E , which are required for the computation, recursively depend on latitude φ and ellipsoidal height h (cf. Eqs. 3.83 – 3.85). In order to avoid relevant errors coming from this iterative approximation, the ground-truth positions were computed at a higher sampling rate (2400 Hz). The ground truth GNSS coordinate and velocity observations are computed based on $\varphi_{\text{sim}}, \lambda_{\text{sim}}, h_{\text{sim}}, \mathbf{v}_{\text{sim}}^n$, and $\mathbf{C}_{b,\text{sim}}^n$ for a given lever arm \mathbf{l}^b , based on Eqs. 3.64 and 3.68.

The EKF and Kalman smoother as introduced in Chapter 3 are applied to the simulated IMU and GNSS observations. Unless stated differently in the following sections, the set of default settings shown in Tab. 5.2 is used for the EKF processing. Note, that the gyroscope bias is modelled here as a random constant by default.

The quality of the gravity estimates for the simulated flights is based on the measurement lines only (thick lines in Fig. 5.1). For the combined set of all measurement lines, both the RMS and the standard deviation (σ) will be computed for the gravity estimation errors, i.e. the estimated gravity with respect to the ground-truth reference $d\mathbf{g}_{\text{sim}}^n(t)$.

It is just noted here, that the propagated errors tend to be higher during manoeuvres, as take-off, landing, and turns, which is of lower relevance in practice. At least for the simulation, these larger errors arise from stronger discretisation effects.

The full set of combinations of roll and pitch angles for the data set is shown in Fig. 5.2. Apparently, the roll angle was limited to $\approx 25^\circ$ during the turns. On the straight measurement lines, the auto-pilot performed small correction manoeuvres to keep the requested course, in particular during phases of turbulence. Note, that the roll angle on the lines reaches values of $\pm 8^\circ$. While the non-zero average of the pitch angle (here: 2.1° , nose up) is typical for a relatively low aircraft speed, the roll angle bias of -1.3° is probably due to an eccentric centre of mass, or due to non-symmetric power of the two engines (such an issue was indeed reported by the pilots).

5.2 Systematic errors

This section analyses the error propagation of systematic IMU errors, as well as other relevant error sources in a IMU/GNSS strapdown gravimetry system, as small time-stamping offsets, discretisation errors, lever arm errors, or initial alignment errors.

The lever arm is given in body-fixed (front-right-down) coordinates as $\mathbf{l}^b = \begin{pmatrix} 0 & 0 & -1.5 \text{ m} \end{pmatrix}^T$, thus the GNSS antenna is positioned 1.5 m above the IMUs centre of observations, which is a typical value using small aircraft or land vehicles.

It is just noted here, that *all* of the subsequent simulations were also carried out using an alternative lever arm, including a horizontal eccentricity: $\mathbf{l}_2^b = \begin{pmatrix} 2 \text{ m} & 0.5 \text{ m} & -1.5 \text{ m} \end{pmatrix}^T$. However, no significant effect could be observed when using \mathbf{l}_2^b instead of \mathbf{l}^b (the deviation was less than 5% for each of the subsequent simulation experiments). This indicates, that the choice of the lever arm is of lower relevance in practice.

5.2.1 Discretisation error

An IMU always provides measurements \mathbf{f}^b and $\boldsymbol{\omega}_{ib}^b$ for discrete epochs. For the processing of such data, usually the average between two measurements is being used for the respective time interval. The numerical integration then yields velocity and angle increments, which are implicitly based on the assumption, that the measured specific forces and turn rates change *linearly* over time.

However in practice, in particular during dynamic vehicle motion, this assumption is wrong: If both the specific force *and* the turn rate change non-linearly over time, the numerical integration generates systematic errors. This is illustrated here by a simple example: Assume two manoeuvres, taking place between two IMU epochs: the first is a short acceleration to towards the sensor's X-axis, the second is a slight turn around the Y-axis. The IMU measurements were the same, if these two manoeuvres were carried out in reverse order, however the two navigation outcomes are clearly different. Such errors, coming from simultaneous non-linear changes of acceleration and turn rate, are called *coning* and *sculling* motion (Groves, 2013; Wendel, 2011). Appropriate corrections may reduce the error when down-sampling the available IMU data to a lower data rate, typical for time-critical applications with limited computation resources. There is however no possibility of applying such corrections, if the highest available IMU data rate is already used.

It is analysed here, how much the discretisation of the simulated IMU measurements can affect the gravity determination. The IMU and GNSS measurements are error-free. The results are shown in Fig 5.4. The combined RMS of the gravity errors of all measurement lines of the simulated campaign are shown. According to these results,

- IMU data rates of ≥ 20 Hz enable the vertical gravity determination better than 1 mGal, and
- IMU data rates of ≥ 100 Hz enable the determination of the deflections of the vertical at the level of 1 arc second (equivalent to a horizontal gravity accuracy of ≈ 4.75 mGal).

Apparently, the DoV determination is more sensitive to discretisation errors, which can be explained by the sensitivity to attitude errors coming from coning and sculling effects.

For all subsequent simulations shown in this chapter, an IMU data rate of 600 Hz is chosen. Vertical gravity errors less than 0.1 mGal, and DoV errors less than 0.1 arc seconds will be regarded as insignificant (as such error may primarily come from the discretisation error).

The error-free simulation has shown, that the integrated IMU/GNSS strapdown gravimetry algorithm introduced in Chap. 3 is working correctly to this quality level. In other words, this result verifies, that the assumptions and simplifications of the algorithm design introduced in Chap. 3, are justified for the gravity determination better than 0.1 mGal, and better than 0.1", respectively.

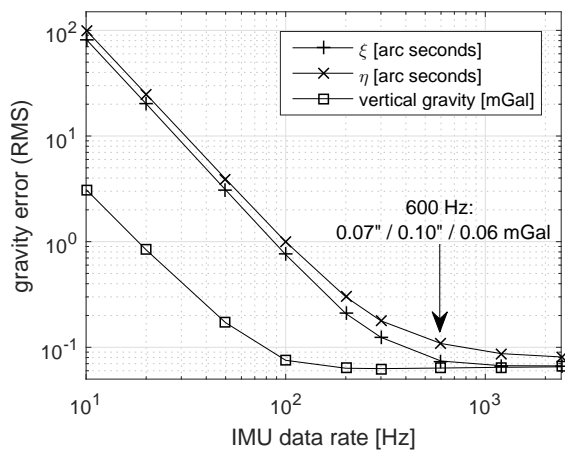


Figure 5.4: Propagation of IMU discretisation errors, for IMU data rates between 10 Hz and 2400 Hz. The data rate of 600 Hz is chosen for all subsequent simulations.

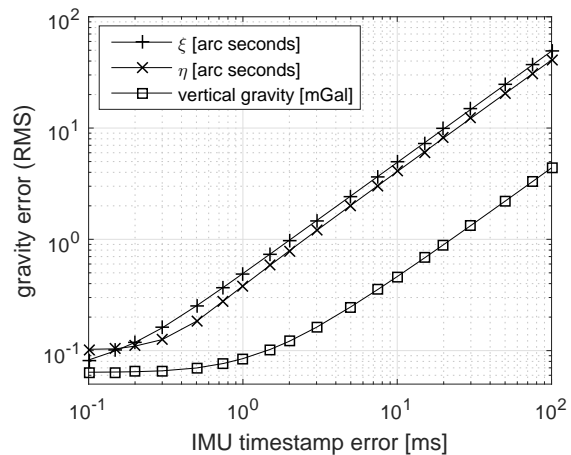


Figure 5.5: Propagation of a constant IMU timestamp error.

5.2.2 IMU timestamp error

Typically, IMU measurements are timestamped using an internal GNSS receiver, or using an external receiver which is forwarding precise pulses, and time and date information to the IMU. Very small timestamping errors may still occur, for both the GNSS coordinates and the IMU measurements. In particular, it is sometimes a-priori unknown, if the IMU timestamps are referenced to the beginning, the middle, or the end of an IMU time interval (between two successive epochs), which alone can correspond to an error of several milliseconds. Fig 5.5 confirms, that such errors can have an impact on the gravity determination. (Only effects of *positive* timestamp errors are shown; negative timestamp errors yield an equivalent effect.)

A timestamp error of ≈ 20 ms results in a vertical gravity error of 1 mGal (RMS). A timestamp error of ≈ 2 ms results in a DOV error of ≈ 1 arcsecond (RMS). This emphasises the requirement of time-stamps at the accuracy level of 1 ms or better for the determination of the DoV. Such an accuracy can be difficult to accomplish in practice, in particular during outages of the GNSS receiver providing the timestamp information.

5.2.3 Lever arm error

In practice, a precise determination of the lever arm can be difficult, in particular if the line of sight between IMU and GNSS antenna is blocked e.g. by the vehicle chassis. The lever arm may then be determined using advanced methods, as precise photogrammetry, or measurements using a geodetic total station. Fig. 5.6 shows the error propagation of errors of the constant lever arm in body-fixed coordinates (front-right-down).

A note on the representation: The diagrams shown in Fig. 5.6 not only contain the combined RMS values of the gravity errors, but additionally their *standard deviation* σ after removing a constant bias from each of the individual measurement lines (shown as dotted lines). This representation will be used for other diagrams shown in this chapter.

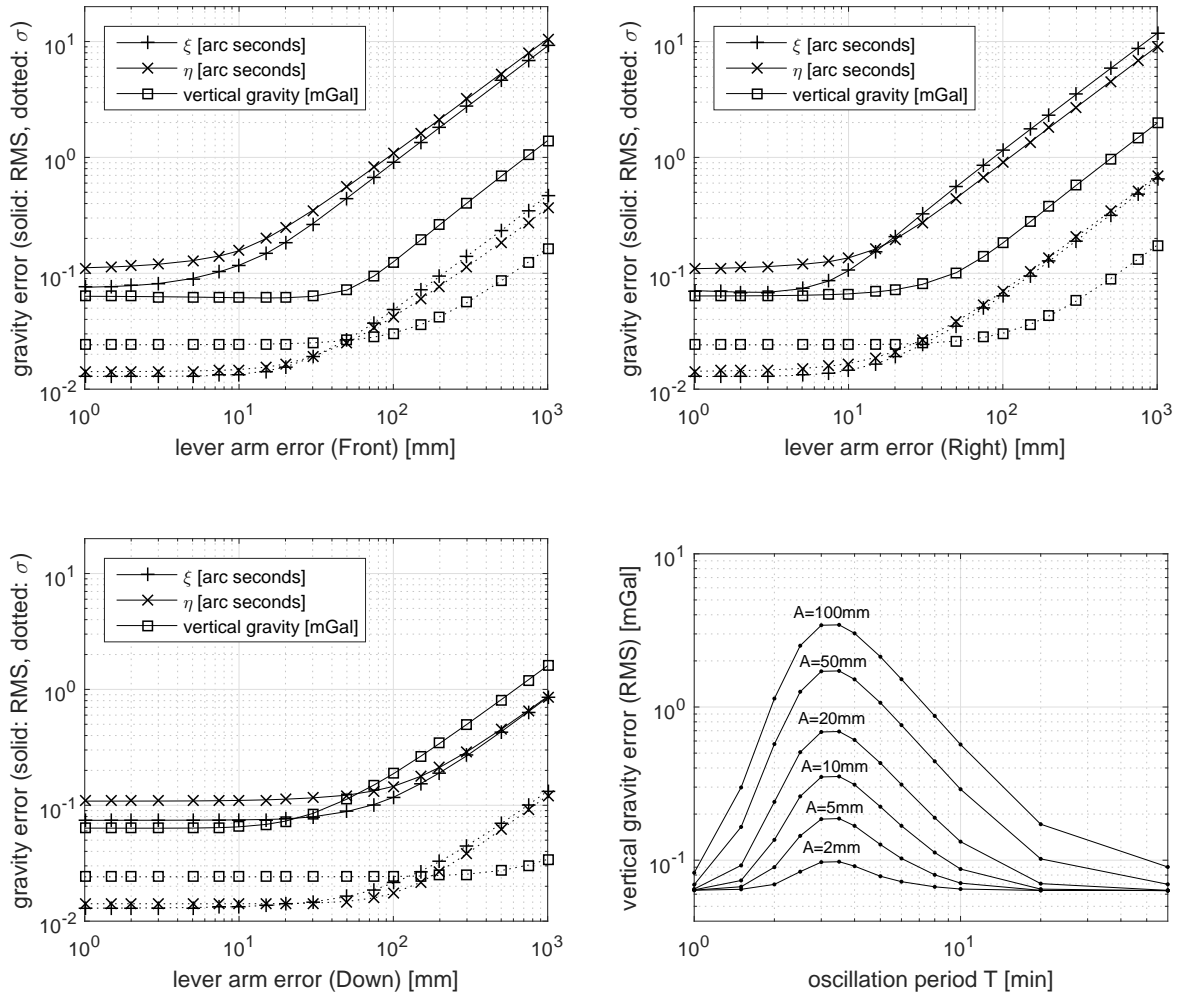


Figure 5.6: Propagation of lever arm errors. *Top:* constant lever arm error in body-fixed directions: front (along-track) and right (cross-track); *Bottom left:* in vertical direction. *Bottom right:* Propagation of an uncompensated oscillation of the vertical lever arm component: $\Delta l^{\text{Down}}(t) = A \sin(2\pi t/T)$, for different oscillation amplitudes A and oscillation periods T .

The assumption of a *constant* lever arm l^b may not be justified in practice: During a flight, it may (slightly) change due to the following reasons:

- When using an aircraft with pressurised cabin, air pressure differences (inside versus outside the cabin) can lead to elastic deformations of the cabin.
- Strong turbulence, or manoeuvres comprising strong accelerations can yield elastic deformations of the cabin.

For the simulation of a lever arm instability $\Delta\mathbf{I}(t)$, a simple sinus oscillation is used. The analysis is limited here to lever arm changes along the body-fixed vertical (Down-)axis, because lateral displacements are expected to be smaller in practice. Fig. 5.6 shows vertical gravity errors for different combinations of amplitude A and period T of the oscillation.

The lever arm oscillation creates an oscillation of the gravity error with the same frequency. The amplitude of the gravity error oscillation can be approximated as the RMS value times $\sqrt{2}$. Reading example: A lever arm oscillation along the vertical component with amplitude 20 mm and period $T = 1/f = 3$ min yields a gravity error of 0.7 mGal (RMS), arising from a gravity error oscillation with an amplitude of ≈ 1 mGal (with the same period).

The amplitude of the gravity error increases with longer periods until its maximum at approximately $T = 3$ min. The smaller effect of higher frequency oscillations can be explained by the Gauss-Markov process that is used to model gravity in the EKF: The parameters are tuned for typical dynamics of along-track gravity changes. For higher frequencies, the EKF acts like a low-pass filter.

For periods *longer* than three minutes, the gravity error decreases, because the average position change of the GNSS antenna per time is becoming smaller, and thus the acceleration of the GNSS antenna relative to the body-fixed frame. It can be summarised, that for lever arm oscillations happening in the same frequency band as gravity changes, both signals can not be separated. Similar results are obtained for an instability of the vertical accelerometer bias, and also for gradual error drifts of the GNSS height observations (Sections 5.3.1 and 5.3.2).

Note, that the positions of the maxima arise from the specific choice of the simulated aircraft speed, and the modelled gravity field characteristics. Still, the results qualitatively show, that there *is* a relevant error propagation in this case, that may have to be addressed in practice.

5.2.4 Sensor misalignments

An IMU consists of six inertial sensors: three accelerometers and three gyroscopes. Each of the six sensors' sensitive axes may be imperfectly oriented with respect to their nominal direction (*misalignment*).

In the following, results of simulated IMU sensor misalignments are shown. For each experiment, the sensitive axis of one of the sensors is altered, while the other five sensors remain unchanged (error-free). For each of the sensors, misalignments may appear in two directions, yielding a total of 12 possible types of misalignments for an IMU. The following six angular misalignments are defined for both the accelerometer and the gyroscope triad:

1. ϵ_{XY} : bending the X-axis towards the Y-axis
2. ϵ_{XZ} : bending the X-axis towards the Z-axis
3. ϵ_{YX} : bending the Y-axis towards the X-axis
4. ϵ_{YZ} : bending the Y-axis towards the Z-axis
5. ϵ_{ZX} : bending the Z-axis towards the X-axis
6. ϵ_{ZY} : bending the Z-axis towards the Y-axis

A note on the nomenclature: If a sensor triad is analysed *without* any external reference direction of the sensitive axes, only the relative, *mutual* misalignments can be modelled. Such mutual misalignments are called *cross-couplings*, because two sensors mutually share a portion of their measured signals (the measurements are then *coupled*). A cross-coupling is non-zero, if the sensitive sensor axes are not mutually perpendicular. In this thesis, the term *misalignment*

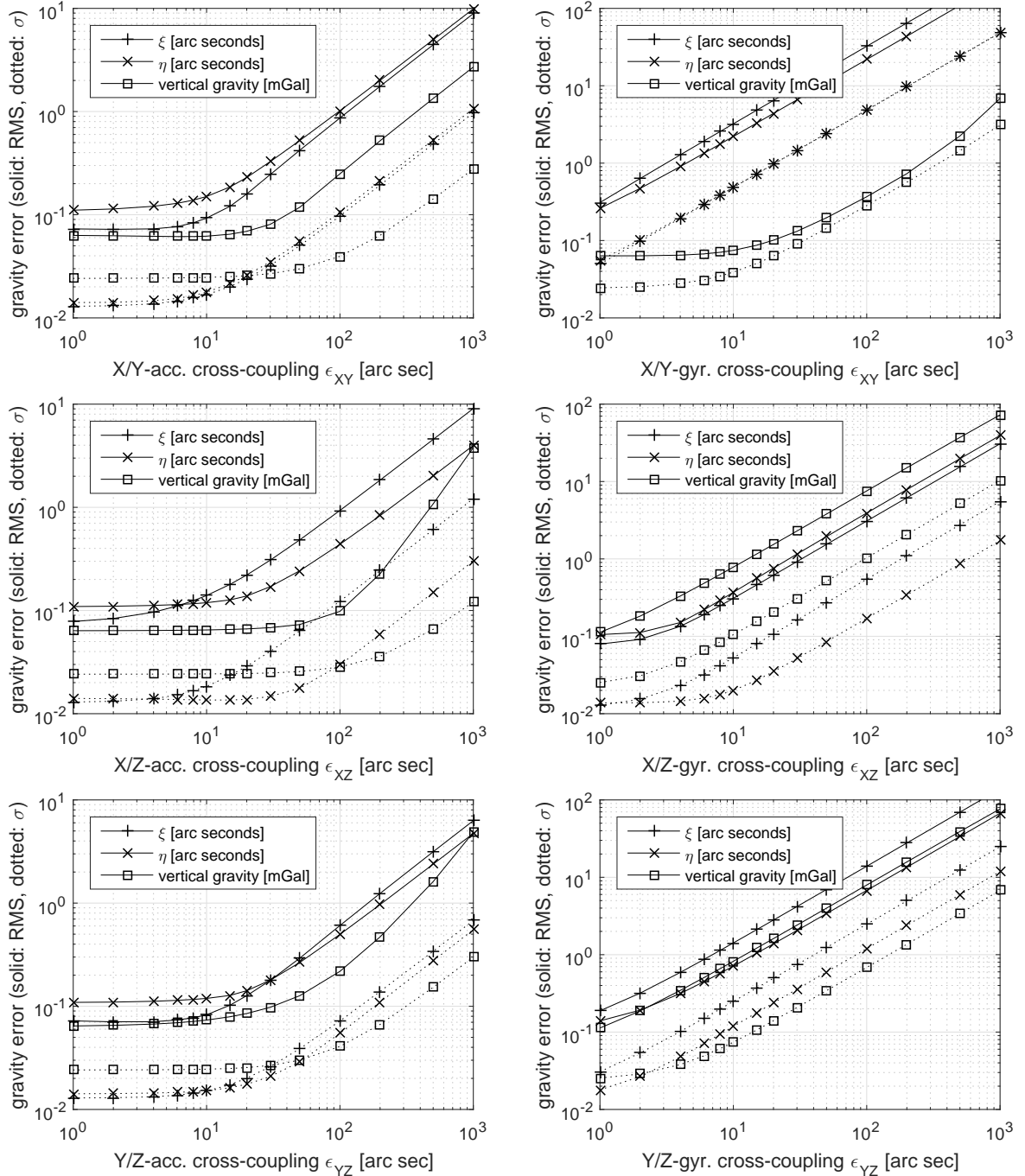


Figure 5.7: Error propagation of mutual angular axis misalignments (cross-couplings) of the six IMU sensors. *Left:* For the accelerometer triad. *Right:* For the gyroscope triad.

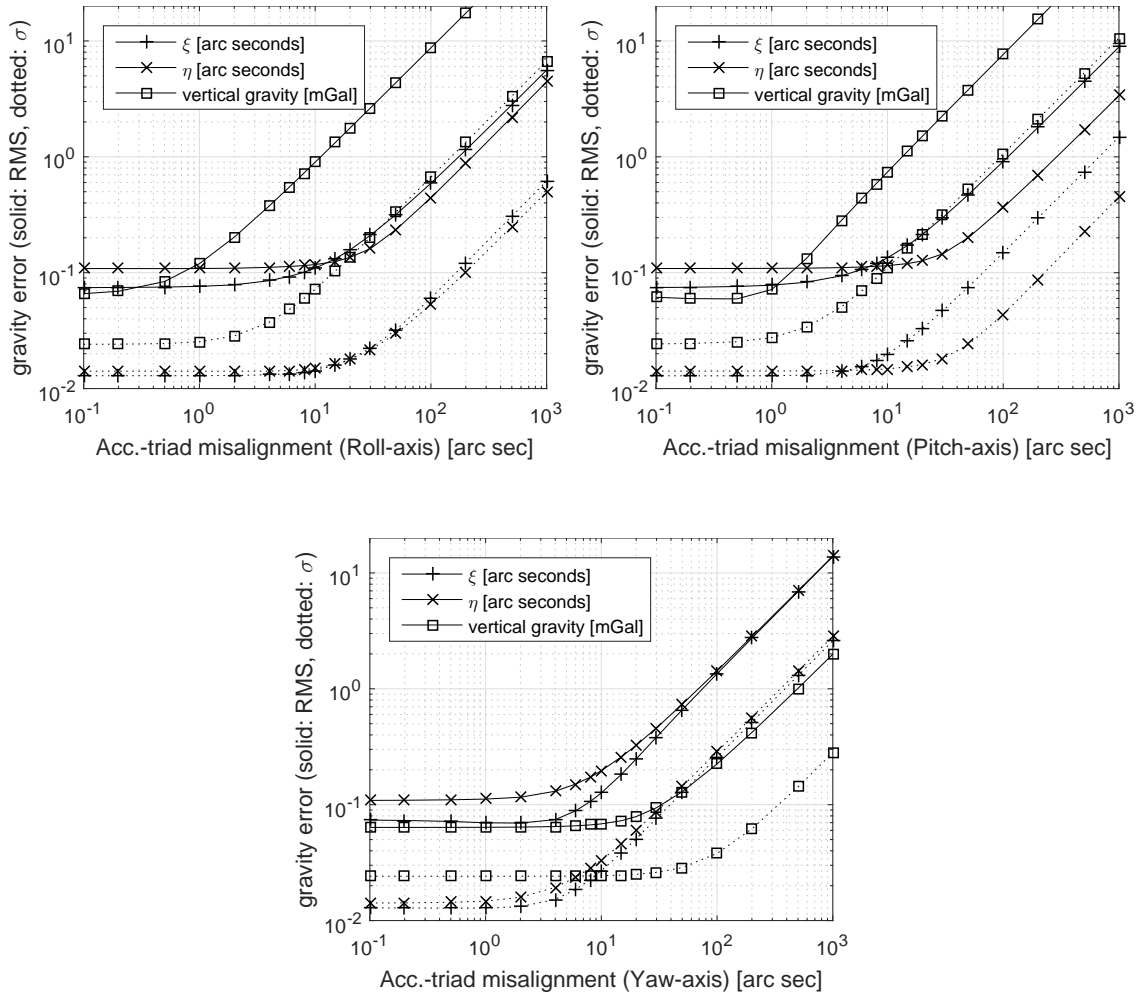


Figure 5.8: Error propagation of accelerometer triad misalignments.

is used, if an external reference direction is given, while the term *cross-coupling* is used for mutually non-orthogonal sensor axis within a triad of (nominally orthogonal) sensors. For a triad of sensors, six independent misalignments can be defined (see above), but only three independent cross-couplings.

Symmetric misalignments ϵ_{ij} and ϵ_{ji} , with $i, j \in \{X, Y, Z\}$ yield very similar gravity estimation errors, with a relative differences of less than $1 \cdot 10^{-3}$. In other words, it was shown to be irrelevant, which axis of a set of two axes is bent, and which remains in its true orientation. Therefore, only results for three cross-couplings per sensor triad are presented. Fig. 5.7 shows the statistics of the gravity determination error arising from such cross-couplings. Accelerometer cross-couplings of the order of 100 arc seconds yield gravity estimation errors of 1 arc second for the DoV, while the same cross-couplings are irrelevant for the vertical gravity component. The DoV estimation shows a higher sensitivity to gyroscope cross-couplings (10 arc seconds yield 1 arc second of error). For cross-couplings of the Z -gyroscope (ϵ_{XZ} and ϵ_{YZ}), also the vertical gravity estimates are significantly affected: Cross-couplings of 10 arc seconds yield a vertical gravity estimation error of 1 mGal. Cross-couplings of such magnitude can be observed in practice for a navigation-grade IMU, as will be shown in Chap. 6.

Depending on the physical design of the IMU, the accelerometer and gyroscope triads may be individually attached to the IMU housing. This raises the question, how strong misalignments of the full triad of sensors propagates into the gravity estimates, while the sensors of the triad remain mutually orthogonal. Again, triad misalignments of the accelerometer triad with respect to the fixed gyroscope triad, or vice versa, yield equivalent results. (In

fact, the only difference is the GNSS antenna lever arm error with respect to the one or the other triad, which is irrelevant for misalignments of the order of tens of arc seconds).

Fig. 5.8 shows the gravity determination error statistics for misalignments of the accelerometer triad, with angular misalignments about the roll-, pitch- and yaw-axis (corresponding to the nominal X/Y/Z IMU sensor axes). Triad misalignments about the roll- and the pitch-axes are the most relevant ones for the vertical gravity determination: triad misalignments of 10 arc seconds propagate into the vertical gravity estimates at the level of 1 mGal.

5.2.5 Initial alignment error

The *alignment* is the initial determination of attitude and heading of an IMU-based navigation or surveying system. A static alignment, having the IMU at rest over a sufficiently long period, commonly consists of two parts (*Groves*, 2013; *Jekeli*, 2001):

1. The *levelling* is based on the approximation, that there is no gravity in the horizontal directions of the local navigation frame. In other words, a transformation matrix C_b^n is being derived, such that with the assumption of $\ddot{\mathbf{r}} = 0$,

$$C_b^n \mathbf{f}^b = \mathbf{f}^n = \begin{pmatrix} 0 \\ 0 \\ \tilde{g} \end{pmatrix} \quad (5.12)$$

with a measured gravity value of \tilde{g} (potentially containing accelerometer biases). The large signal to noise ratio, with $g \approx 9.8 \text{ ms}^{-2}$ versus the accelerometer noise, allows a quick convergence of the levelling process. For example, an observation of the horizontal gravity components at $\approx 5 \text{ mGal}$ accuracy allows the determination of the initial roll and pitch angles at an accuracy of one arc second (cf. Fig. 4.4).

2. The gyroscope-compassing phase (or *gyro-compassing*) is the determination of the initial heading angle, based on the assumption, that independently of the actual latitude φ , no Earth rotation can be observed around the East-axis, while *non-zero* Earth rotation components can only be sensed around the North and Down axes, cf. Eq. 3.34. This process converges much slower in practice, because the signal to noise ratio is much smaller, with $\omega_e \approx 7.292 \cdot 10^{-5} \text{ s}^{-1}$ versus the gyroscope noise. In fact, consumer-grade and tactical-grade devices based on MEMS-gyroscopes or fibre-optic gyroscopes typically do not allow a gyro-compassing at all, having gyroscope *biases* (much) larger than ω_e .

If the vehicle is at rest, as for the static alignment, the system suffers from several inseparabilities of system states, as shown in Tab. 4.1 for the non-accelerated motion without attitude changes (scenario S1). As a consequence, sensor biases can not be fully determined during the alignment, thereby prohibiting the exact determination of the initial attitude and heading (*Groves*, 2013). As soon as the vehicle starts moving (accelerated manoeuvres), the sensor biases may be determined, thereby improving the attitude and heading estimates. Still, the alignment is important for an approximate determination of the initial angles: An initialisation with large attitude and heading errors may cause strong linearisation errors in the EKF, potentially leading to a divergence of the filter.

The simulations however show, that initial attitude and heading errors of up to 90° did *not* yield any significant error for the gravity determination (no figure shown). Apparently, the filter was still able to converge. Only for initial attitude or heading errors of 135° and 180° , a divergence of the filter could be observed (resulting in very large gravity errors, of the order of 1 ms^{-2}). It is however difficult to derive a general statement from this observation, as the

processing of real data, including other sensor errors, may be more sensitive to initial attitude errors. If no static alignment data is available, or if the gyro-compassing is not possible due to the sensor quality or an initial position close to the Earth's poles, a kinematic alignment may be possible from GNSS coordinate and velocity observations, typically starting with the approximation that heading and course over ground are identical.

5.2.6 Accelerometer errors

Simulation results of constant accelerometer biases are shown in Fig. 5.9 (left). For this simulation, the initial accelerometer bias uncertainty σ_{0,b_a} was set to the respective simulated biases. Apparently, accelerometer biases of less than 1000 mGal are irrelevant for the gravity determination. This can be explained by the initial alignment: The gravity disturbance is initialised with a ground-truth value, with an accuracy of 0.03 mGal. This allows the determination of the accelerometer bias at high accuracy. A significant error propagation can only be observed for very large biases (the levelling procedure fails, and bad accelerometer bias estimates reside in the state estimates). Accelerometer biases of this magnitude are in practice not observed for navigation-grade inertial sensors.

While constant accelerometer biases can be estimated accurately by the strapdown algorithm, constant accelerometer *scale factors* are not modelled as system states. Instead, the scale factors can be shown to propagate mainly into the bias estimates. This masking of scale factors as biases is unproblematic for a constant IMU orientation. Attitude changes however necessarily lead to errors of the estimated gravity and attitude. For the simulation of accelerometer scale factors, the initial accelerometer bias uncertainty σ_{0,b_a} was set to the approximate effect of the scale factor on the vertical gravity component, e.g. for a simulated scale factor of 100 ppm, $\sigma_{0,b_a} = 100$ mGal. Fig. 5.9 (right) shows the simulation results.

It can be summarised, that the vertical gravity component is not relevantly affected for scale factors <1000 ppm. The horizontal components are more sensitive to scale factors, however the error propagation is still not relevant for typical scale factors of <100 ppm for navigation-grade inertial sensors (*Honeywell International*, 2016b).

Accelerometer *drifts* are commonly regarded as more relevant in the literature (cf. Sect. 2.2). *Linear* drifts can however be successfully removed from the gravity estimates, if a ground truth gravity observation is known before *and* after the flight. In the context of the strapdown gravimetry algorithm (EKF and Kalman smoother), this can be achieved by a gravity disturbance observation, cf. Sect. 3.3. The simulation of linear accelerometer drifts supports this expectation: No significant gravity errors can be observed (gravity errors are below 1 mGal for linear drifts of hundreds of mGal per hour; no figure shown).

Conversely, if a ground-truth gravity can *not* be introduced at the end of the flight, the Z-accelerometer drifts significantly propagate into the vertical gravity estimates (see Fig. 5.10, left). The horizontal gravity components remain almost unaffected by linear accelerometer drifts of <100 mGal/h, which can be explained by the higher estimability of the horizontal accelerometer biases during manoeuvres comprising horizontal accelerations.

5.2.7 Gyroscope errors

The simulation results of introducing constant gyroscope biases are shown in Fig. 5.11. For the simulation, the initial gyroscope noise uncertainty σ_{0,b_ω} was set to the actual, simulated magnitude. As already discussed in *Jekeli* (1994), the horizontal gravity components are very sensitive to roll and pitch errors, which are arising from uncompensated X- and Y-gyroscope biases in this case. Apparently, constant gyroscope biases can not be estimated reliably by the filter, even though these errors are *explicitly* modelled in the EKF system state. Obviously, *changes* of the gyroscope biases can not be detected by the filter as well (no figure shown).

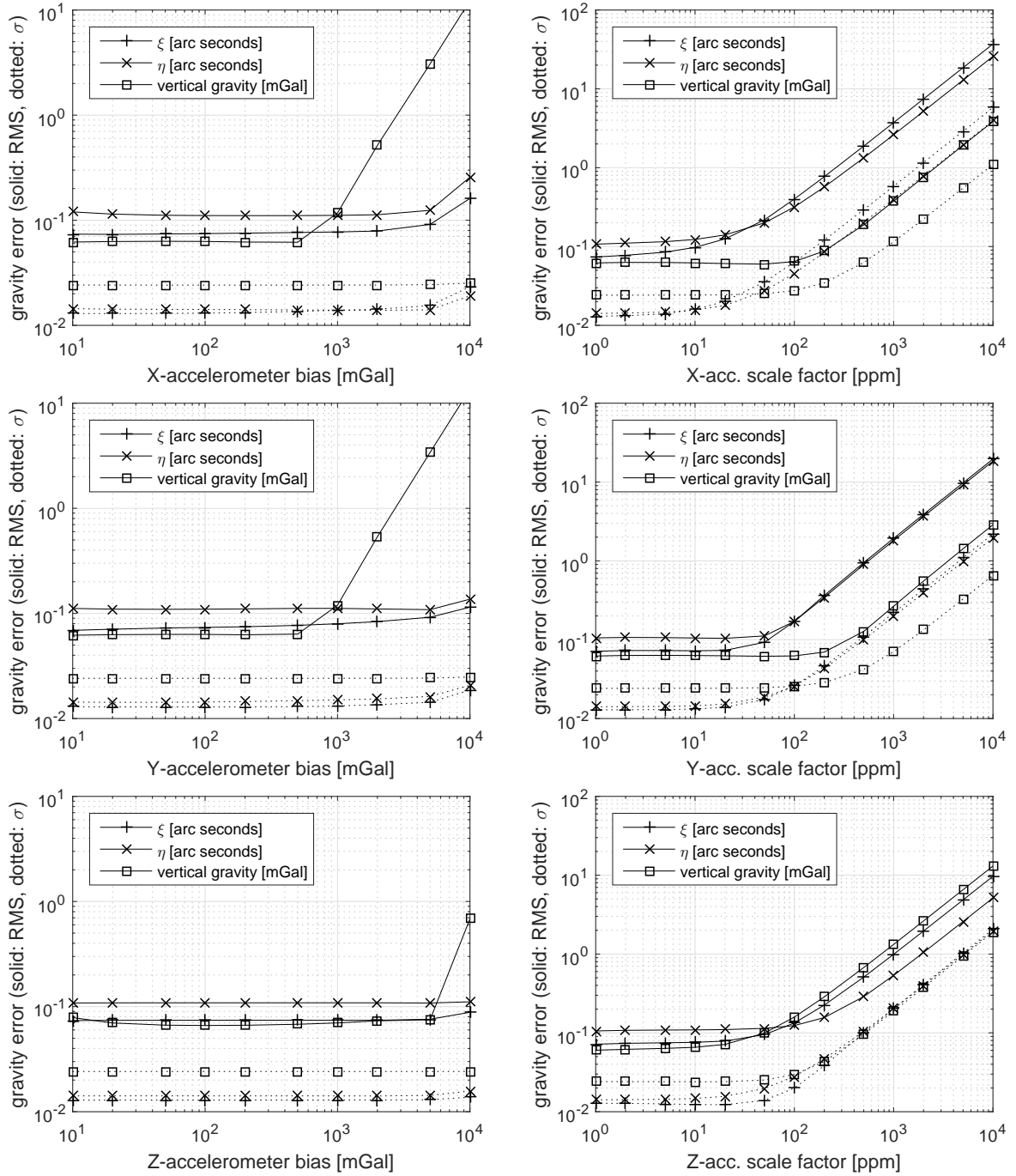


Figure 5.9: Error propagation of systematic accelerometer errors. *Left:* Constant accelerometer biases. *Right:* Constant accelerometer scale factors.

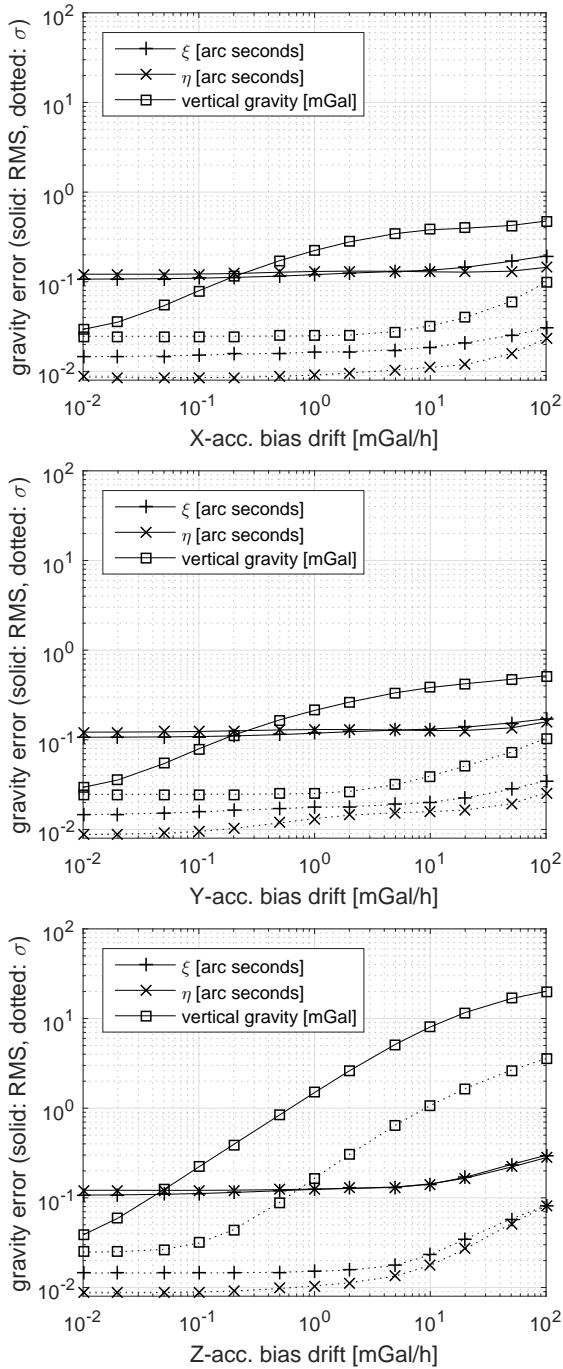


Figure 5.10: Error propagation of linear accelerometer drifts, assuming that no ground-truth gravity information is available for the destination airport.

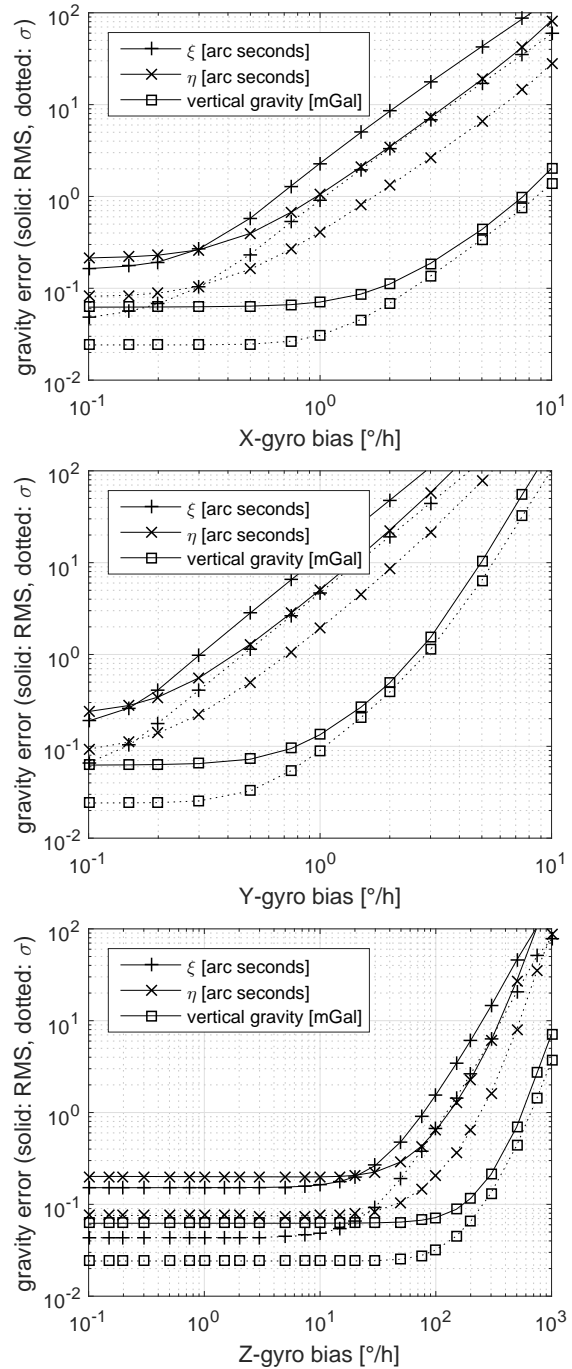


Figure 5.11: Error propagation of constant gyroscope biases.

The vertical gravity component is not significantly affected by gyroscope biases of less than 1° per hour. Such a gyroscope stability (or better) is commonly available for tactical- and navigation-grade strapdown IMUs.

5.3 Stochastic sensor errors

5.3.1 IMU sensor noise

First, Gaussian accelerometer and gyroscope noise $\mathcal{N}(0, \sigma)$ is simulated at the full rate of $f = 600$ Hz. The gravity estimation errors are shown in Figs. 5.12 and 5.13. The velocity and attitude system noise parameters q_v and q_ψ , which reflect such inertial sensor noise, were set to the respective quantities.

In order to simulate *gradual* accelerometer drifts, e.g. coming from thermal effects in practice, the simulation is repeated with Gaussian noise at much smaller frequencies f . The noise is transformed to the base IMU frequency of 600 Hz by interpolation. In order to obtain a more realistic, gradual shape, a spline interpolation is used. As an example, Gaussian noise with $\sigma = 10$ mGal and $1/f = 10$ min is depicted in Fig. 5.14 (left). The error propagation of different combinations of frequency f , and standard deviation σ are shown in Fig. 5.14 (right).

Noise of higher frequencies, in particular for $f = 600$ Hz, is significantly reduced by the Kalman filter, which is acting as a low-pass filter. The important conclusion from these simulations is, that random accelerometer bias variations, appearing in the same spectral interval as gravity changes, are almost inseparable from gravity. In particular, Gaussian noise at wavelengths of several minutes almost entirely propagates into the gravity estimates. It is pointed out, that this strong propagation is observed here for *error-free* GNSS coordinate observations, introduced to the filter as Gaussian distributed measurements with $\sigma = 2$ cm, which is a rather optimistic assumption in practice.

The calibration methods investigated in the scope of this thesis aim at the reduction of such gradual, long-term accelerometer drifts. It will be shown, that the majority of such drifts may be successfully corrected in practice using *thermal* calibration methods.

5.3.2 GNSS coordinate observation noise

For the previous sections, error-free GNSS coordinate observations were introduced to the filter, with a modelled uncertainty of $\sigma_{z_r} = 2$ cm. In this section, actual Gaussian noise will be simulated for the GNSS coordinate observations. The filter parameter σ_{z_r} is set to the according value, cf. Tab. 5.2.

First, Gaussian noise is simulated at the full GNSS coordinate observation rate of 1 Hz, for each of the individual components (North, East, Down). The results are shown in Fig. 5.15. In practice, noise of the order of several centimetres can be observed for phase-differential two-frequency GNSS, among other factors mainly depending on the base line length.

As a second experiment, more gradual drifts in the vertical GNSS coordinate observations are simulated. Long-wavelength Gaussian noise is generated for lower frequencies f , interpolated to the base data rate of 1 Hz using a spline-interpolation (cf. Sect. 5.3.1). The results are shown in Fig. 5.15 (lower right). Such gradual, long-wavelength drifts can be observed in practice arising from gradual variations of the tropospheric and ionospheric error terms, and also from changes of the GNSS satellite constellation. The estimated accuracy of PD-GNSS in a kinematic, airborne set-up can typically be expected to be better than 20 cm for base-line lengths of up to several hundreds of kilometres. The accuracy of PPP solutions can be expected to be on a similar level (*Kouba and Héroux, 2001*).

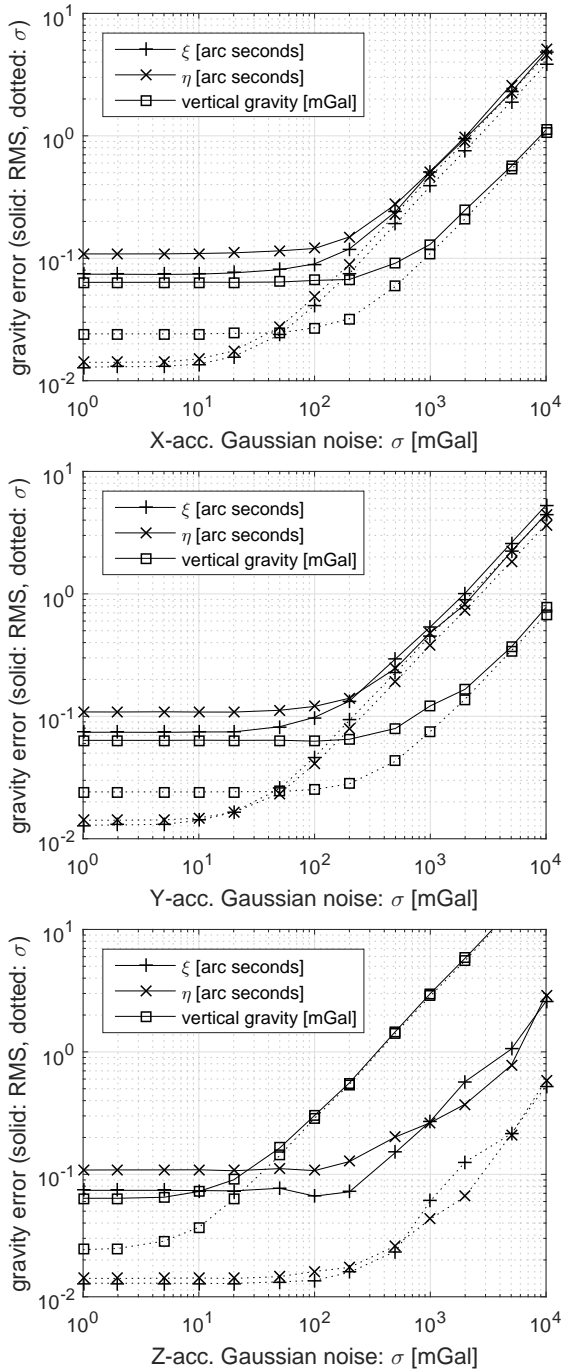


Figure 5.12: Error propagation of Gaussian accelerometer sensor noise, at the full IMU data rate of $f = 600$ Hz, plotted for different Gaussian noise standard deviations σ .

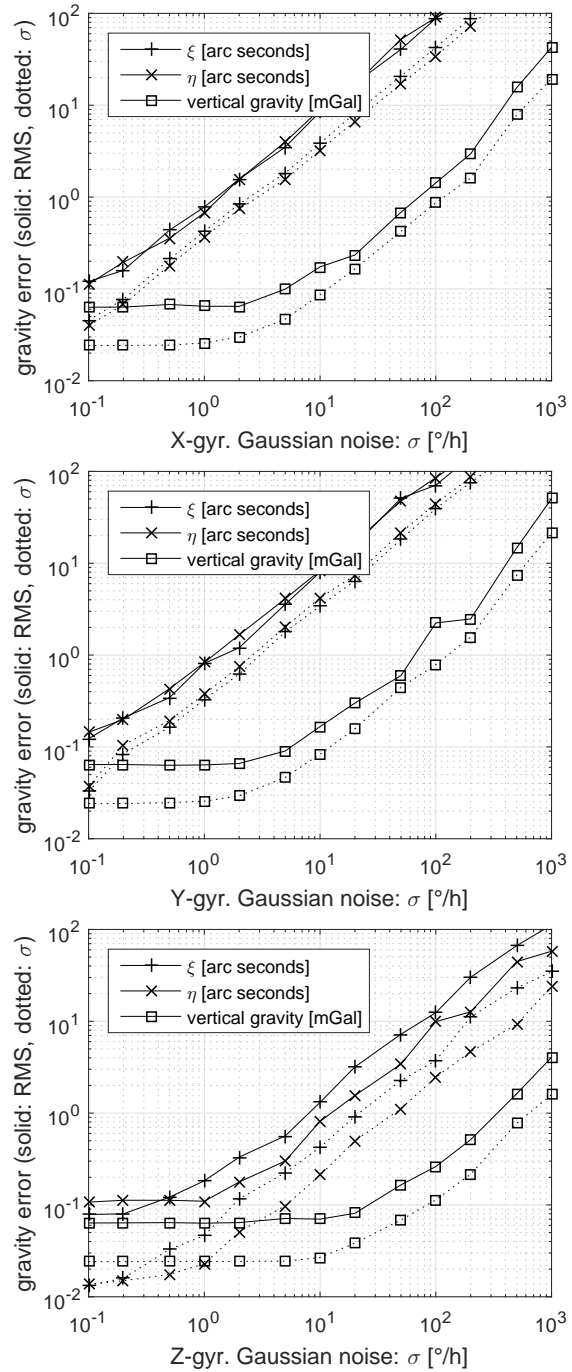


Figure 5.13: Error propagation of Gaussian gyroscope sensor noise, at the full IMU data rate of $f = 600$ Hz, plotted for different Gaussian noise standard deviations σ .

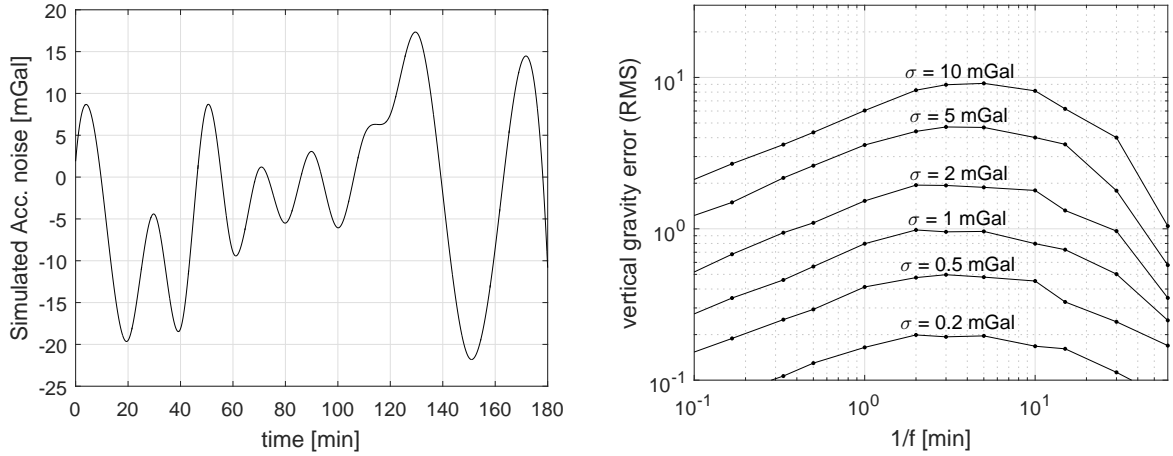


Figure 5.14: *Left:* Example of simulated, spline-interpolated Gaussian accelerometer noise with $1/f = 10$ min and $\sigma = 10$ mGal. *Right:* Error propagation of Gaussian Z-accelerometer noise, for different combinations of frequency f , and standard deviation σ .

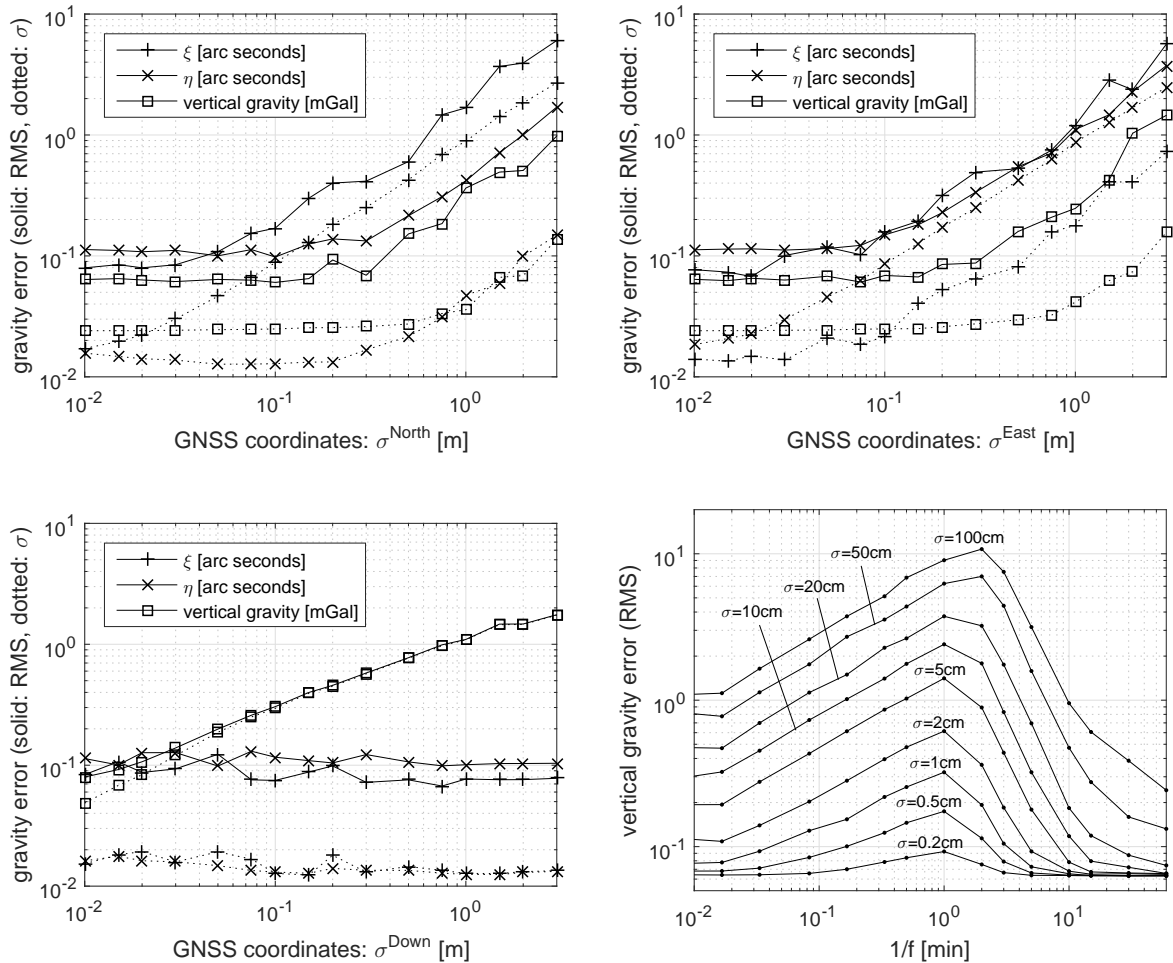


Figure 5.15: Propagation of Gaussian noise in the GNSS coordinate observations. *Top:* 1 Hz noise in the horizontal components, *bottom left:* 1 Hz noise in the vertical component. *Bottom right:* Propagation of *gradual* GNSS height errors, shown for different combinations of frequency f , and standard deviation σ (see text).

5.4 Summary

The simulation results presented in this chapter are summarised in Tab. 5.3. For each of the error types, the error magnitude is shown, which propagates into the gravity estimates

- at the accuracy level of 1 mGal (RMS) for the vertical gravity component, and
- at the accuracy level of 1 arc second (RMS) for the deflections of the vertical.

For the deflections of the vertical, only a single, combined value is shown for ξ and η for each error type, because it is expected, that primarily the (arbitrary) heading and course over ground of the aircraft yield differences among the two DoV components. (Indeed, the effects on ξ and η are almost equal for each of the simulated errors.)

Error magnitudes are highlighted, if they can be expected to have a practical relevance for strapdown gravimetry, when using a navigation-grade IMU in combination with PPP or PD-GNSS coordinate observations. This selection is done here based on the practical experiences with the navigation-grade iMAR RQH-1003 IMU. This particular sensor will be analysed in more detail in the scope of this thesis (cf. Chaps. 6 and 8).

The results from this chapter can be regarded as a guide, indicating which orders of magnitude for the different error types may require a special handling in practice, as a dedicated error modelling in the filter, or accurate calibrations. Conversely, the non-highlighted error types can be expected to be less relevant in practice.

Error type	Component	Unit	dg^{Down}	DoV
IMU data rate (higher is better)		[Hz]	20	100
IMU timestamp error		[msec]	20	2
Lever arm error	along-track	[mm]	700	100
Lever arm error	cross-track	[mm]	500	100
Lever arm error	vertical	[mm]	500	> 1000
Lever arm instability ($1/f = 3$ min)	vertical	[mm]	30	–
Lever arm instability ($1/f = 5$ min)	vertical	[mm]	50	–
Lever arm instability ($1/f = 8$ min)	vertical	[mm]	100	–
Accelerometer cross-coupling	$\epsilon_{XY}/\epsilon_{YX}$	[arc sec]	400	100
Accelerometer cross-coupling	$\epsilon_{XZ}/\epsilon_{ZX}$	[arc sec]	500	150
Accelerometer cross-coupling	$\epsilon_{YZ}/\epsilon_{ZY}$	[arc sec]	350	200
Gyroscope cross-coupling	$\epsilon_{XY}/\epsilon_{YX}$	[arc sec]	250	4
Gyroscope cross-coupling	$\epsilon_{XZ}/\epsilon_{ZX}$	[arc sec]	10	30
Gyroscope cross-coupling	$\epsilon_{YZ}/\epsilon_{ZY}$	[arc sec]	10	10
Mutual sensor triad misalignment	roll-axis	[arc sec]	10	200
Mutual sensor triad misalignment	pitch-axis	[arc sec]	10	100
Mutual sensor triad misalignment	yaw-axis	[arc sec]	500	80
Attitude or heading initialisation error			<i>not relevant</i>	
Constant accelerometer bias	X	[mGal]	3000	$>1 \cdot 10^4$
Constant accelerometer bias	Y	[mGal]	3000	$>1 \cdot 10^4$
Constant accelerometer bias	Z	[mGal]	$>1 \cdot 10^4$	$>1 \cdot 10^4$
Accelerometer scale factor	X	[ppm]	$1 \cdot 10^4$	300
Accelerometer scale factor	Y	[ppm]	3000	500
Accelerometer scale factor	Z	[ppm]	800	1500
Gyroscope bias	X	[$^\circ/h$]	7	0.8
Gyroscope bias	Y	[$^\circ/h$]	3	0.4
Gyroscope bias	Z	[$^\circ/h$]	500	100
Accelerometer Gaussian noise (600 Hz)	X	[mGal]	$1 \cdot 10^4$	2000
Accelerometer Gaussian noise (600 Hz)	Y	[mGal]	$>1 \cdot 10^4$	2000
Accelerometer Gaussian noise (600 Hz)	Z	[mGal]	350	5000
Gyroscope Gaussian noise (600 Hz)	X	[$^\circ/h$]	80	2
Gyroscope Gaussian noise (600 Hz)	Y	[$^\circ/h$]	80	2
Gyroscope Gaussian noise (600 Hz)	Z	[$^\circ/h$]	400	9
Accelerometer Gaussian noise ($1/f = 3$ min)	Z	[mGal]	1	–
Accelerometer Gaussian noise ($1/f = 30$ min)	Z	[mGal]	2	–
Accelerometer Gaussian noise ($1/f = 60$ min)	Z	[mGal]	10	–
GNSS coordinate Gaussian noise (1 Hz)	North	[m]	3	0.8
GNSS coordinate Gaussian noise (1 Hz)	East	[m]	2	1
GNSS coordinate Gaussian noise (1 Hz)	Down	[m]	1	> 3
GNSS coordinate Gaussian noise ($1/f = 1$ min)	Down	[m]	0.04	–
GNSS coordinate Gaussian noise ($1/f = 4$ min)	Down	[m]	0.2	–
GNSS coordinate Gaussian noise ($1/f = 10$ min)	Down	[m]	1	–

Table 5.3: Summary of the error propagation simulation experiments. Magnitudes for different error types are shown, propagating into the gravity estimates at the level of approximately 1 mGal (vertical gravity component), and 1 arc second (DoV). Those errors are **highlighted**, which are expected to be relevant in practice when using a modern navigation-grade strapdown IMU in combination with precise GNSS (PPP or phase-differential GNSS). The sensor axes X/Y/Z are aligned with the along-track/cross-track/vertical directions.

Chapter 6

Calibration methods for strapdown gravimetry

It was shown in Chap. 5, that certain types of IMU errors significantly propagate into the gravity estimates. In particular, misalignments of the accelerometers, as well as in-run changes of the accelerometer biases have been shown to have a relevant effect on the gravity determination.

This chapter addresses the question, how systematic IMU errors can be calibrated using off-line laboratory calibration methods. A systematic error is regarded here as an error, which can be reproduced in a laboratory set-up, in contrast to non-reproducible, stochastic errors. Corrections are then derived from the observed systematic sensor errors.

An uncertainty of such calibrations arises from the fact, that the dynamics of a typical measurement flight can usually not be simulated in a laboratory set-up when using basic calibration equipment, as a calibration turn table. An effect, which is reproducible in the laboratory, may turn out to be different during real vehicle motion. Thus, such laboratory calibration methods are "trial-and-error" methods, i.e. the benefits of the derived corrections have to be evaluated using real aerogravity data. A good reproducibility in the lab set-up can be seen as an indicator, but not as a proof, that the gravity determination can benefit from applying the respective corrections.



Figure 6.1: iMAR RQH-1003 strapdown IMU

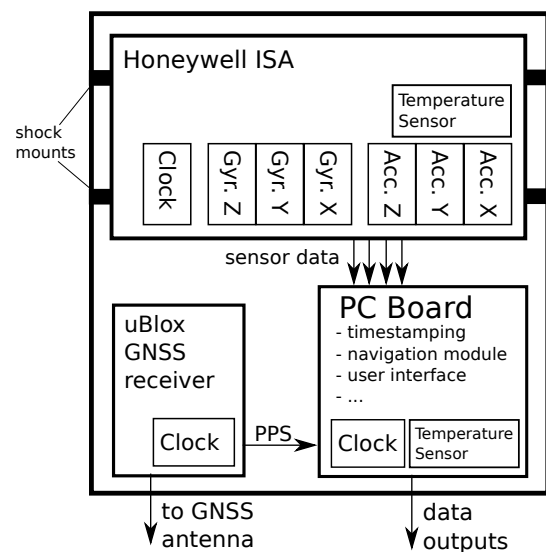


Figure 6.2: System design of the iMAR RQH-1003 strapdown IMU (only relevant components and modules are shown).

	Accelerometers	Gyroscopes
Model	Honeywell Q-Flex [®] QA-2000	Honeywell GG1320A
Technology	etched-quartz-flexure seismic system	Ring-laser
Sensor range	± 20 g	$\pm 400^\circ/s$
Resolution	$< 1 \mu\text{g}$ (depending on data rate)	1.13 arc seconds
Linearity error	< 100 ppm	< 5 ppm
Sensor bias	$< 25 \mu\text{g}$	$< 0.003^\circ/h$
Random walk	$< 8 \mu\text{g}/\sqrt{\text{Hz}}$	$< 0.002^\circ/\sqrt{h}$

Table 6.1: Manufacturer specifications of the inertial sensors of the iMAR RQH-1003 strapdown IMU (Honeywell International, 2016a,b)

internal / output data rate	1800 Hz / ≤ 300 Hz
data latency	< 3 ms (cf. Sect. 5.2.2)
outer dimensions	$\approx 310^* \times 213 \times 180$ mm (*no cables attached)
weight	≈ 12.5 kg
operating temperatures	-40°C to 60°C

Table 6.2: Manufacturer specifications (relevant excerpt) of the iMAR RQH-1003 strapdown IMU.

The methods presented in this chapter are carried out for an iMAR RQH-1003 strapdown IMU (Fig. 6.1). This particular IMU was flown during several aerogravity campaigns in the years 2013 to 2016. The evaluation of the proposed calibration methods will be presented in Chap. 8, applying the different corrections to the available aerogravity data sets.

Because of the limited access to a professional calibration turn table, 3 out of the 4 proposed calibration approaches could only be carried out once. Thus, a second uncertainty comes from the fact, that some of the calibrations were carried out years after the acquisition of the aerogravity data, on which the calibrations are to be evaluated in Chap. 8. The IMU error characteristics may have changed in the meantime. In practice, it is advisable to repeat the proposed calibrations on a regular basis.

6.1 iMAR RQH-1003 functional system design

The most important functional components of the iMAR RQH-1003 strapdown IMU are depicted in Fig. 6.2. The six inertial sensors are bundled in a physical sensor box, called *inertial sensor assembly* (ISA). The ISA also contains (at least) one temperature sensor, and a clock. Details about the internal design of the ISA, in particular the position of the inertial sensors and the temperature sensor(s), are classified and unknown to the author. The ISA is physically attached to the main IMU chassis using *shock mounts*, which allow a dampening of mechanical shocks and also higher frequency vibrations.

It is important to note, that misalignments of the ISA module with respect to the nominal IMU axes do not yield a mutual misalignment of the sensors' axes with respect to each other. For the IMU/GNSS integrated system, such an ISA-misalignment *only* affects the body-fixed lever arm l^b . According to the manufacturer, for typical flight dynamics including turbulence, the ISA-misalignments can reach magnitudes of $\pm 0.1^\circ$. For example, for a lever arm component of 2 m, such a misalignment is consistent with a lever arm error of 3.5 mm, which is not relevant in practice (cf. Sect. 5.2.3).

Independent of the ISA misalignments, individual inertial sensor misalignments may be observed. Later in this chapter it will be shown, that both the ISA misalignments, and the

mutual sensor misalignments (cross-couplings) show a thermal dependency, of which the latter will be calibrated.

An internal single-frequency GPS receiver is used to supplement the inertial sensor data with GPS timestamps. The internal transmission of timestamps is a combination of a pulse-per-second (PPS) signal, and an NMEA data stream containing date and time information. A miniature PC board is used to gather all information, and provide time-stamped inertial raw data, and optionally also a real-time navigation solution to the user. An internal memory allows the storage of any user-selectable data (including the timestamped raw inertial sensor data). For the application of airborne gravimetry, an *offline*-processing is commonly feasible, i.e. the recording of the inertial sensor raw data (turn rates and accelerations) is in general sufficient.

The PC board also allows the output of the ISA temperature data, as well as data from the PC board's temperature sensor. In particular the output of ISA temperature data is crucial for the thermal calibrations shown in this chapter. Since the ISA temperature sensor is sitting closer to the inertial sensors, it is the preferred temperature sensor for any thermal calibration of the IMU. However, only data from a *single* temperature sensor is given out by the ISA (there might be more temperature sensors; details are unknown to the author). The position of this temperature sensor, as well as the positions of the six inertial sensors are unknown. As a consequence, an inhomogeneous temperature inside of the ISA may introduce an uncertainty for any thermal modelling. For thermal calibrations, only small temperature gradients, or sufficient waiting times have to be guaranteed in order to reduce this error source. Tests showed, that the latency of temperature changes sensed at the temperature sensor, and at the inertial sensors, can be of the order of tens of minutes.

6.2 Honeywell QA-2000 sensor characteristics

The Honeywell QA-2000 accelerometer sensor readings (*Honeywell International, 2016b*) show a fissured shape: At the maximum output data rate of 300 Hz, jumps of up to 1 m/s^2 with respect to the average reading can be observed for a static raw-data recording, see Fig. 6.3. No information on this behaviour could be provided by the manufacturer Honeywell, nor by the IMU manufacturer iMAR. It can be expected, that it arises from the quantisation electronics, transforming the electric current, which is required to keep the proof-mass in the zero-position, into a discrete, digital signal.

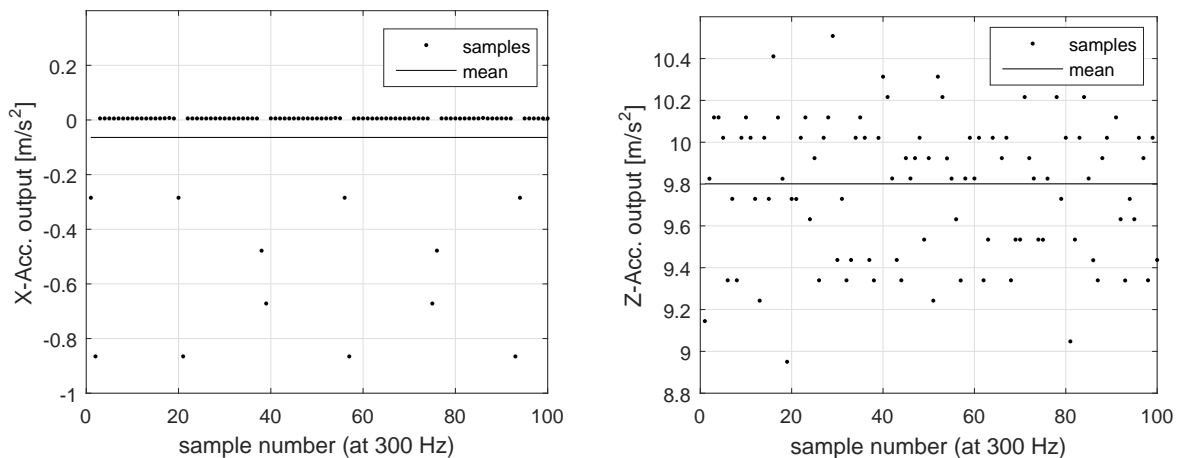


Figure 6.3: 100 samples of a static QA-2000 recording at 300 Hz. *Left:* for the horizontally aligned X-Accelerometer; *Right:* for the vertically aligned Z-accelerometer.

Such jumps of 100.000 mGal are apparently very large compared to the goal of strapdown gravimetry at the 1 mGal level. When averaging the QA-2000 outputs over longer time-windows, the standard deviation of the sliding mean of static data reduces quickly.

In general, when averaging accelerometer outputs over very long periods (tens of minutes or hours), the respective long-term sensor instabilities, for example coming from thermal effects or other purely stochastic effects, can be expected to eventually dominate the standard deviation of the data window, while quantisation effects become negligible for such long averaging periods (*El-Sheimy et al.*, 2008).

The Allan variance (*Allan*, 1966) is a tool for quantifying such effects. While originally being intended for the analysis of long data sets of atomic clock frequencies, the concept can be equivalently applied to other sensors, and in particular to inertial sensors (*El-Sheimy et al.*, 2008).

In the typical double-logarithmic plots showing the Allan standard deviations, the characteristics of the sensor errors can be interpreted based on the slope of the curves in that diagram (*El-Sheimy et al.*, 2008). The relevant categories are repeated here:

- a slope of -1 indicates quantisation noise;
- a slope of -0.5 indicates a random walk (angular random walk for gyroscopes, or velocity random walk for accelerometers);
- a slope of 0 indicates a bias instability;
- a slope of 0.5 indicates a rate random walk;
- a slope of 1.0 indicates a drift rate ramp.

Fig. 6.4 shows the Allan standard deviation (being the square root of the Allan variance) for static 60-hour recordings of the iMAR RQH-1003 unit (Sect. 6.1). The three recordings were done using different IMU orientations, see Fig. 6.5. It can be seen, that the *horizontally* aligned accelerometers show larger standard deviations compared to the *vertically* aligned accelerometer. Note, that this is consistent among the three different IMU orientations, i.e. the three accelerometers are apparently of similar quality. However, the individual sensor precisions depend on the relative sensor orientation with respect to the stimulus signal (here: gravity).

For a time window size of 15 minutes ($\tau = 900$ s), the horizontally aligned accelerometers show a minimum standard deviation of >0.3 mGal. For the *same* accelerometers being in *vertical* orientation, standard deviations as low as $70 \mu\text{Gal}$ can be observed for $\tau \approx 2500$ s. For shorter window lengths, the quantisation errors are the predominant error source. Random walks, bias instabilities, rate random walks, and drift rate ramps are difficult to separate in the plots. For large time window sizes τ , slopes of up to 1.0 can be observed.

For larger time window sizes (tens of minutes or more), the dissimilarity of the curves among the different IMU orientations potentially comes from small bends of the sensors' sensitive axes, arising e.g. from an attitude instability of the shock mounts. Such bends mainly affect the readings of the horizontally aligned accelerometers (cf. Fig. 4.4).

The important conclusion from this analysis is the fact, that the vertically aligned QA-2000 accelerometer consistently shows a higher precision compared to the horizontally aligned accelerometers. For typical averaging periods used for the calibrations in this chapter (90 s to 180 s), the Allan standard deviations differ by a factor of approximately 2.5–3. For example, for $\tau = 100$ s, the standard deviations are 0.65 mGal and 2 mGal, respectively.

In the default orientation of the iMAR RQH-1003 unit, as it was used for the data acquisition for the aerogravity data sets shown in Chap. 6, the Z-axis is (approximately) in vertical orientation (third row in Fig. 6.4).

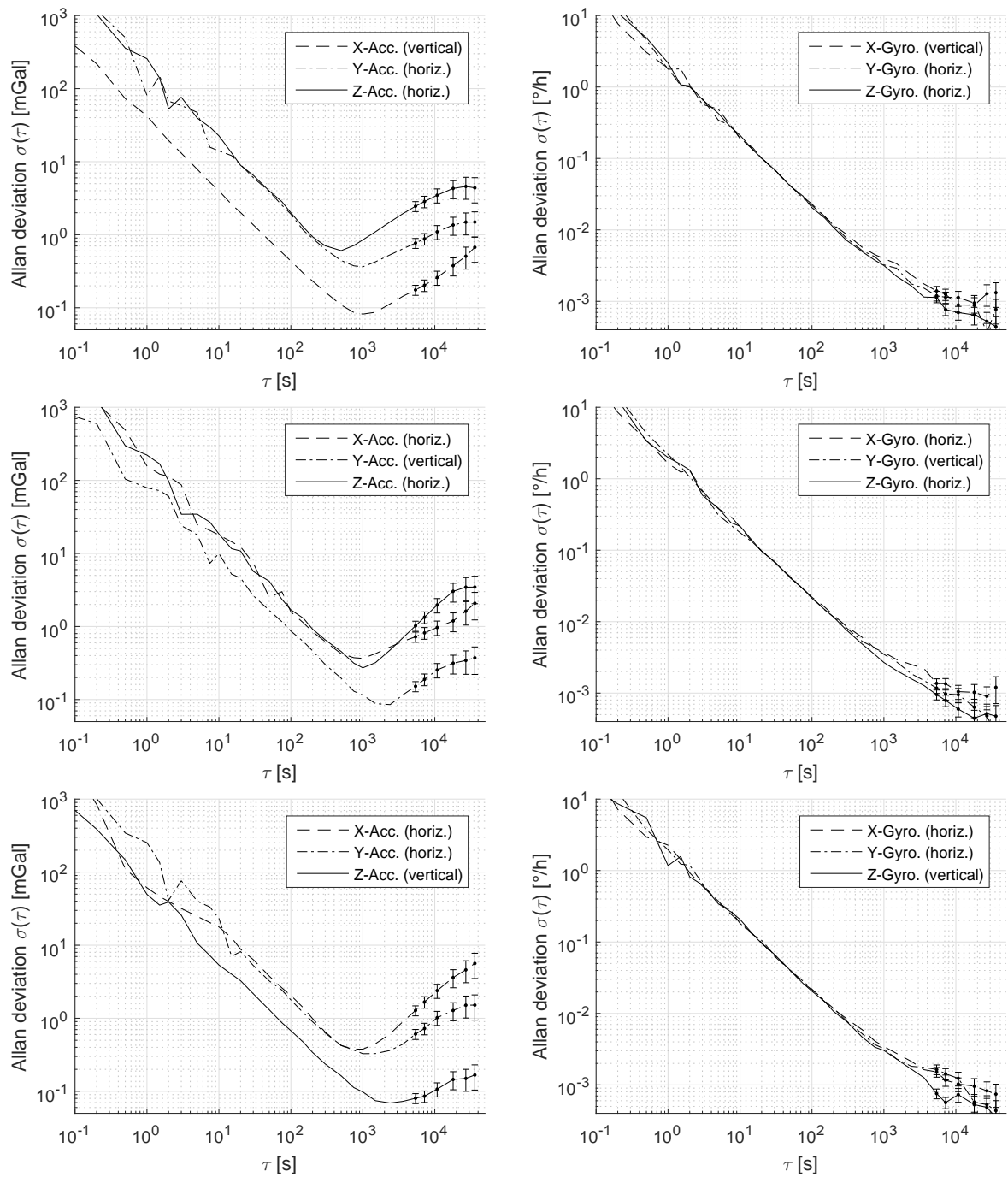


Figure 6.4: Allan standard deviations $\sigma(\tau)$ for different time window sizes τ . *Left:* The QA-2000 accelerometers. *Right:* The GG1320A ring laser gyroscopes. The Allan standard deviation has itself an uncertainty, shown here as $1\text{-}\sigma$ bars for the relevant, longer window sizes. The Allan standard deviation of the six inertial sensors are shown for three different IMU orientations: With the X-, Y-, and Z-axis (approximately) aligned to the local vertical (rows 1, 2, and 3, respectively). In the default set-up of the IMU, the Z-axis is pointing downwards (third row), see Fig. 6.5.



Figure 6.5: Set-up of the 60-hour recordings for the determination of the Allan standard deviations. *Left:* X-axis pointing downwards; *Middle:* Y-axis pointing downwards; *Right:* Z-axis pointing downwards (default orientation).

Fig. 6.4 (right) shows the Allan standard deviations of the three GG1320A ring laser gyroscopes. For the gyroscopes, no significant dependency of the precision on the sensor orientation can be recognised. Again, the predominant error source is the quantisation. For long time windows of several hours, the slope reduces to approximately -0.5, indicating an angular random walk.

6.3 Manufacturer calibrations

The inertial sensor manufacturer (Honeywell) and also the IMU manufacturer (iMAR) apply calibrations to the sensor data:

1. It is expected, that a calibration is carried at the sensor manufacturer Honeywell for each of the gyroscopes. However, no details about such a calibration is known to the author.

According to the QA-2000 specification sheet (*Honeywell International*, 2016b), a thermal laboratory calibration is regularly carried out for the QA-2000 accelerometers. Details about this calibration are probably classified, and unknown to the author.

2. iMAR uses a standard IMU calibration method to determine biases and scale factors for each of the six inertial sensors, and also the sensor misalignments with respect to the nominal IMU axes (which are parallel to the surfaces of the chassis). This calibration is regularly done at an ambient temperature of 20°C. No (additional) thermal calibration is carried out.

Note, that these two calibrations are applied sequentially, i.e. the second calibration (carried out by iMAR) only accounts for residual effects after the corrections of the first calibration are applied. The device allows the inertial data output of either

1. $\tilde{\mathbf{f}}^{b,\text{raw}}$ and $\tilde{\boldsymbol{\omega}}_{ib}^{b,\text{raw}}$: as provided by the ISA (calibrated by Honeywell), or
2. $\tilde{\mathbf{f}}^{b,\text{IMU}}$ and $\tilde{\boldsymbol{\omega}}_{ib}^{b,\text{IMU}}$: with *both* manufacturer corrections applied.

For the results presented in this chapter for the iMAR RQH-1003 unit, only the residual effects after applying *both* manufacturer corrections are calibrated, i.e. only $\tilde{\mathbf{f}}^{b,\text{IMU}}$ and $\tilde{\boldsymbol{\omega}}_{ib}^{b,\text{IMU}}$ are used.

6.4 Thermal calibration of the vertical accelerometer

It can be seen from long recordings of static IMU data, that there is a correlation between the ISA temperature, and the readings of the vertical (Z-)accelerometer. For a 38-hour

recording, this correlation can be easily recognised in Fig. 6.6. Note again, that this thermal effect is only the *residual* thermal effect: It is expected, that the majority of any thermal effects is already corrected internally, based on the manufacturer’s thermal calibration (cf. Sect. 6.3). Still, the correlation shown in Fig. 6.6 indicates the potential of an *additional* calibration of this residual thermal effect.

After switching on the IMU, the internal ISA temperature increases due to the heat generated by the internal electronic components. Note, that it can take several hours, until the ISA temperature stabilises (Fig. 6.6).

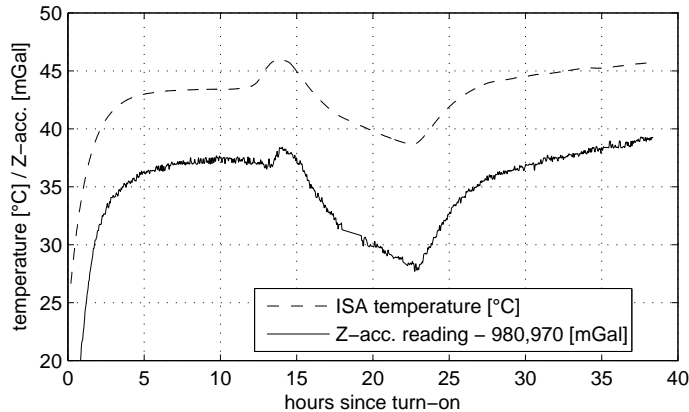


Figure 6.6: A recording of ISA temperature, and Z-accelerometer readings over 38 hours. The ambient room temperature was altered to show the correlation between the two measurements. The acclimatisation of the sensor can be seen in the beginning of the recording. The ISA temperature can be observed to stabilise at 10 °C to 20 °C above the ambient temperature. A third-order two-pass Butterworth filter with cut-off frequency $1/30 \text{ min}^{-1}$ was applied for illustration purposes.

6.4.1 Warm-up calibration

For most of the campaign data evaluated in Chap. 8, the IMU could not entirely warm up before the aerogravity flights. This was due to practical limitations, as a lack of power supply during the nights, or the general safety requirement of not letting any devices run unsupervised inside the aircraft. Therefore, a thermal calibration of this warm-up phase appears reasonable, because for most of the flights shown in Chap. 8, the temperature changes primarily arise from this warming up of the IMU.

A rather simplistic set-up is chosen for the calibration of the warm-up phase of the sensor: The IMU is put on a solid concrete floor. It is switched on, and the recording of data is initiated immediately after the start-up. At this point, the internal components of the IMU, including the core inertial sensors, have a stable temperature equivalent to the ambient room temperature of $\approx 19 - 21^\circ\text{C}$. Sensor data is then collected for a period of approximately eight hours. During that period, the device is warming up gradually, caused by the heat of the internal components, as the PC board, and also the inertial sensors (‘ramp’ method). After eight hours, the device is switched off, allowing the sensors to cool down again for at least 16 hours. This procedure was repeated for ten times, during Feb. 12th and Feb. 27th, 2014.

Note, that this simplistic method does not require any facilities for the calibration. In particular, it can be carried out in the field, during a measurement campaign.

The gradual increase of temperature can be seen in Fig. 6.8. The Z-accelerometer readings are shown in Fig. 6.7 (low-pass filtered for clarity). Within the first 10 min to 15 min after start-up, the sensor reading shows a steep drop (barely visible in Fig. 6.7, on the left). This effect can reproducibly be observed immediately after start-up. It is *not* correlated with the ISA temperature reading, and therefore taken out of consideration for the calibration.

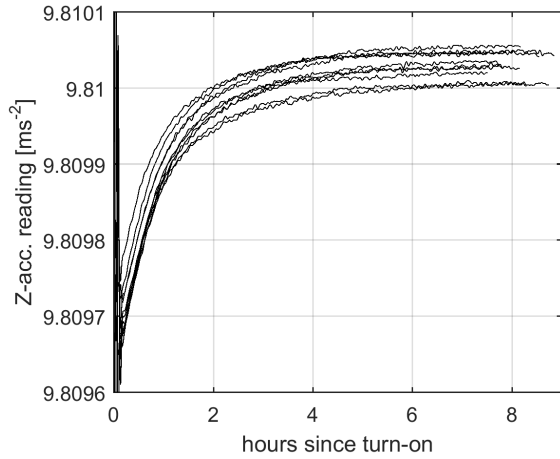


Figure 6.7: Z-accelerometer sensor readings for the ten data sets, low-pass filtered using a third-order 2-pass Butterworth filter, with $1/10 \text{ min}^{-1}$ cut-off frequency.

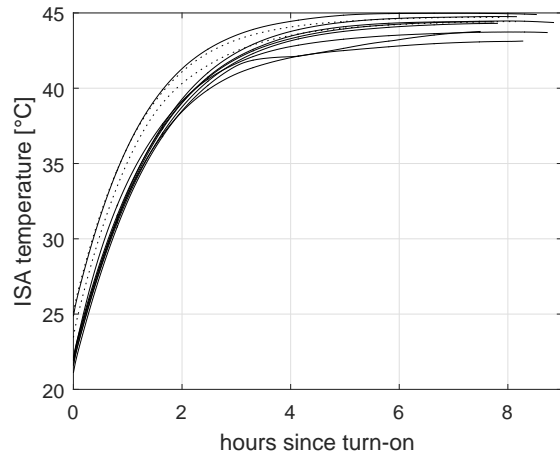


Figure 6.8: Internal temperatures as given out by the ISA.

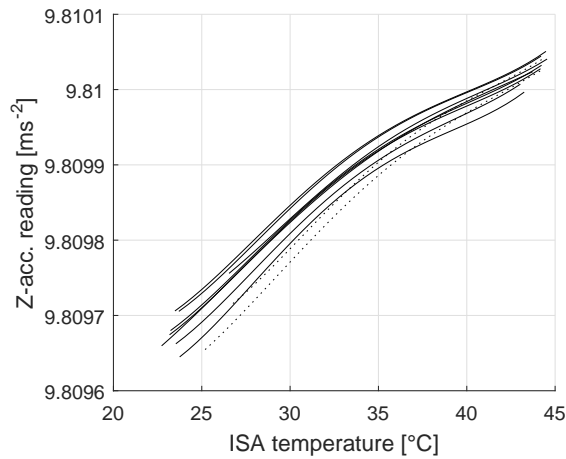


Figure 6.9: Temperature dependency curves of Z-accelerometer readings (fourth-order regression polynomials are shown). Day-to-day bias changes can be observed, with a spread of $\sigma \approx 2 \text{ mGal}$.

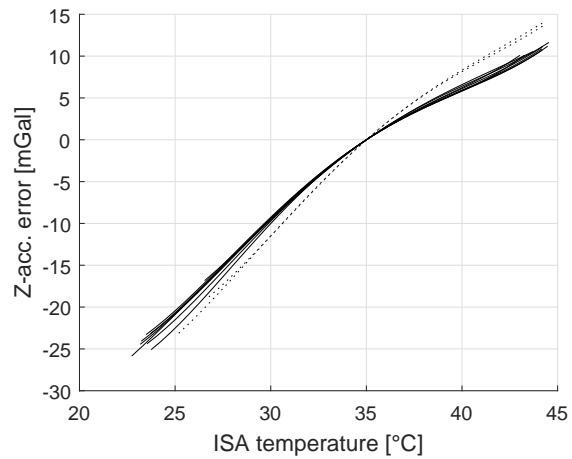


Figure 6.10: Temperature dependency after removing the turn-on-turn-on biases, by shifting the curves to their value at 35°C . The two outlier data sets are shown as dotted curves.

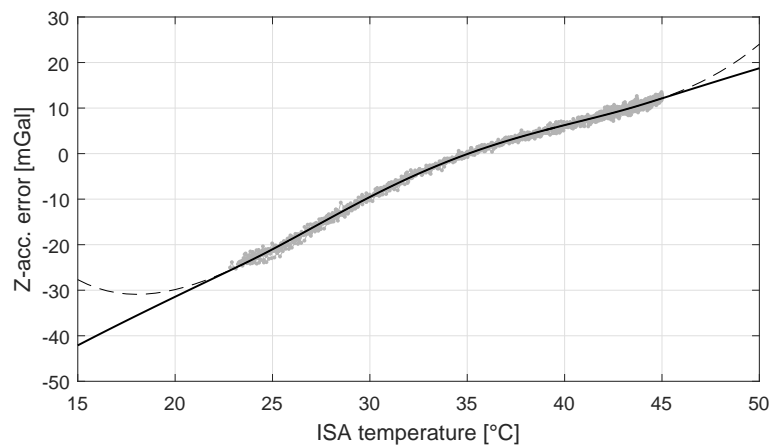


Figure 6.11: Final Z-accelerometer thermal error model: A regression polynomial of degree four (dashed line) and a smoothing spline (solid line). The low-pass filtered Z-accelerometer readings are shown as grey dots.

Fig. 6.9 shows the dependency between ISA temperature reading, and the Z-accelerometer reading. The figure shows fourth-order regression polynomials. The slopes are in the range between 1.2 mGal/h and 2.3 mGal/h. The curves of the ten runs have vertical offsets with a standard deviation of ≈ 2 mGal, apparently being random day-to-day bias changes. These vertical offsets are removed, by shifting the curves such that they mutually intersect at the point 35°C / 0 mGal (Fig. 6.10). It can be seen, that two of the ten curves have a slightly different shape (dotted curves in Fig. 6.10), compared to the other eight curves. The reason for this is unknown. A possible explanation could be the relatively large temperature gradient at these two days (see dotted curves in Fig. 6.8), perhaps coming from larger gradients of the ambient room temperature. For the following derivation of a thermal correction, these two curves are regarded as outliers. The remaining eight (shifted) curves show a good agreement: The bias differences between 25°C and 42°C have a variation of $\sigma = 0.7$ mGal.

A final approximation function is derived based on the joint original data from the eight remaining data sets (grey dots in Fig. 6.11). Two different functions are derived:

1. a regression polynomial of degree four as used for the individual daily curves in Figs. 6.9 and 6.10 (shown as dashed line in Fig. 6.11),
2. a smoothing spline (shown as solid line in Fig. 6.11).

One disadvantage of this calibration method is the limited temperature range covered, with ISA temperatures between 23°C and 45°C. An extrapolation to lower and higher temperatures is in general not advisable. Still, an attempt is done here, in order to enable the correction of aerogravity data sets being up to 5°C outside of the given range. The smoothing spline yields a more reasonable extrapolation compared to the fourth-order polynomial (Fig 6.11). The smoothing spline is therefore selected. It is applied as correction (with negative sign) to the Z-accelerometer readings.

Using such a simple set-up, it is not possible to separate different contributions of the overall error, as sensor biases, scale factors, and also sensor misalignments coming from thermal deformations. In fact, all these effects are masked here by a single temperature-dependent scalar quantity. However, the calibration is still useful for the application of strapdown gravimetry, since the sensor is almost in horizontal position during the main measurement lines (cf. Fig. 5.3). For airborne gravimetry, the aircraft accelerations on the measurement lines are typically small compared to the magnitude of the Earth's gravity.

The following section shows a similar calibration, this time using a temperature oven. For this calibration, however, the IMU is given time to acclimatise first ('soak' method). The thermal effects then arise only from the internal temperature following the ambient temperature changes.

Later in this chapter, more sophisticated calibration methods will be introduced. Some of the discussed methods are based on parametric models, trying to accurately *separate* biases, scale factors and sensor cross-couplings, and thereby refining the simplistic model shown in this section.

6.4.2 Temperature oven calibration

For a more controlled set-up, the iMAR RQH-1003 IMU is installed in a temperature oven. The sensor is then exposed to 22 different nominal oven temperatures, ranging from -20 °C to 48°C, see Fig. 6.13. The larger temperature interval will enable a thermal correction for operations in very cold or hot environments (see for example the Antarctica data set shown in Chap. 8, with ISA temperatures starting at -5 °C). Due to the limited availability of the temperature oven, the experiment was limited to a single run.

Before the experiment, the IMU was running for approximately 3 hours at an oven temperature of -20 °C, to let the sensors acclimatise. Note however, that until one hour after



Figure 6.12: iMAR RQH-1003 in a temperature oven.

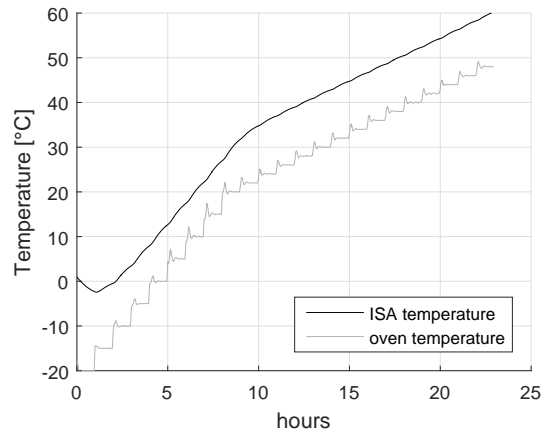


Figure 6.13: Oven temperatures and ISA temperatures.

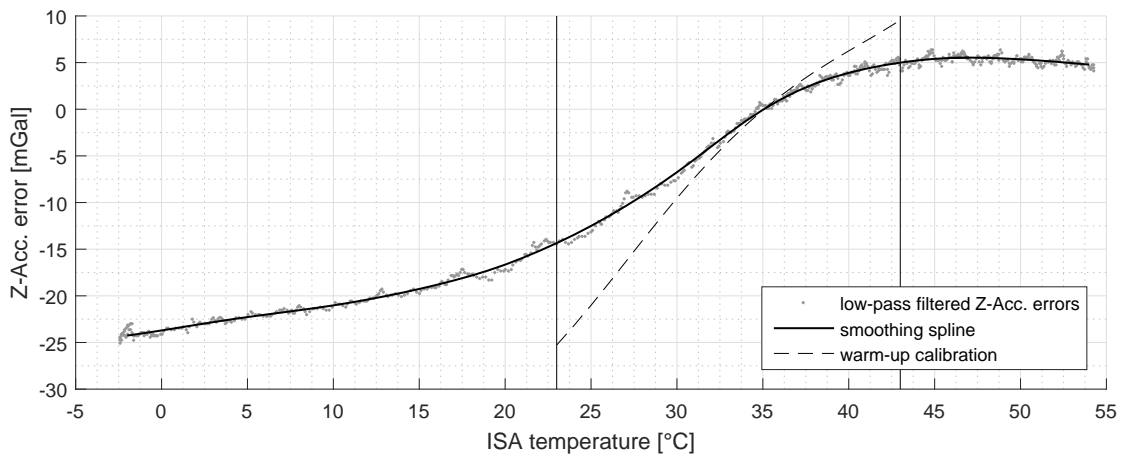


Figure 6.14: Temperature oven calibration of the vertical Z-accelerometer.

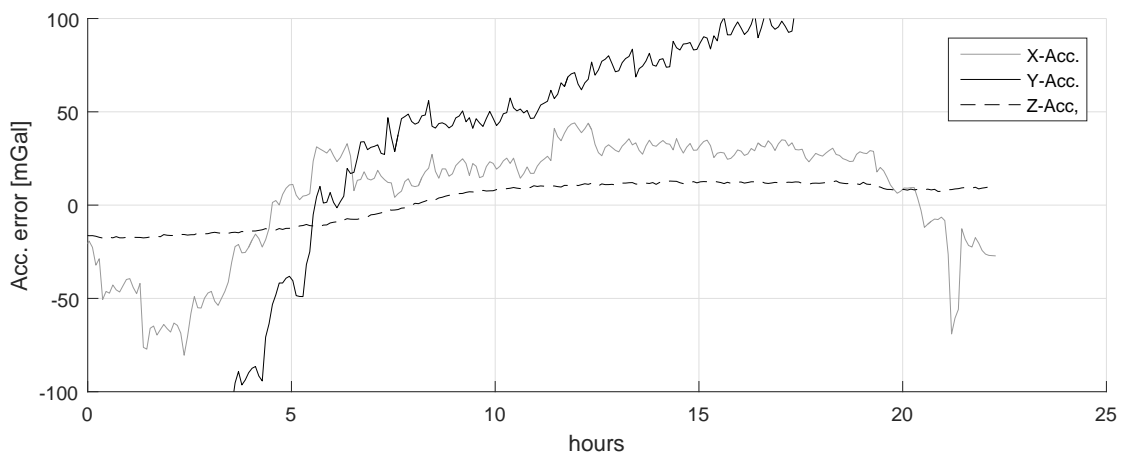


Figure 6.15: Comparison of the three accelerometer readings. The horizontally aligned X- and Y-accelerometers show a large instability, cf. Sect. 6.2.

the start of the experiment, the internal ISA temperature was *still* reducing, indicating that the sensor was not yet fully acclimatised. This part of the data recording was not used for the calibration.

In contrast to the warm-up calibration presented in the previous section, the observed sensor drifts only come from the oven temperature variations. The ISA temperature is *gradually* following the oven temperature changes, as can be seen in Fig. 6.13.

For oven temperatures up to 22 °C, the ISA temperature gradient is ≈ 6 °C/h. For the higher temperatures, a finer spacing of the oven temperature setting was chosen, leading to an ISA temperature gradient of ≈ 2 °C/h. Note, that these gradients differ significantly from those of the warm-up calibration (Fig. 6.8), for which the gradients decrease from 10 °C/h in the beginning (lower temperatures), down to zero (stabilised ISA temperature) in the end.

As in the previous section, a smoothing spline is fitted to the Z-accelerometer readings. Fig. 6.14 shows the results of the calibration. (The Z-accelerometer readings are shown after applying a third-order 2-pass Butterworth low-pass filter with $1/600$ s⁻¹ threshold frequency for clarity.)

The result of the warm-up calibration (cf. Fig. 6.11) is also included in Fig. 6.14 in the interval between 23 °C to 43 °C, to allow a direct comparison of the two results. The significant differences are expected to come from the different temperature gradients in combination with a thermal latency.

The horizontally aligned X- and Y-accelerometers show a large instability compared to the vertical Z-accelerometer (Fig. 6.15). This instability is expected to come from small bends of the accelerometers' sensitive axes, cf. Sect. 6.2. It is not expected, that a reasonable thermal correction can be derived from this data. Again, the calibration is therefore limited to the vertically aligned Z-accelerometer.

6.5 Parametric error models

Parametric error models are based on a predefined set of parameters. The most common parameters are bias and scale factor, and additionally cross-couplings for triads of sensors, and sensor misalignments, if an external reference orientation is given.

It is commonly expected, that this set of standard parameters is suited to model the majority of inertial sensor errors. For the iMAR RQH-1003 strapdown IMU, this expectation is true: The majority of sensor errors is accounted for by such parametric models, used for the manufacturer calibrations. However, when aiming at a 1 mGal precision for the accelerometers, extended models are required.

6.5.1 Bias, scale factor, cross-coupling (BSC)

The calibrations presented in this section are mainly based on the work of *Shin and El-Sheimy* (2002), who published a particular calibration method for bias, scale factor, and cross-couplings (*BSC-calibration*) of a sensor triad, only using a known scalar value of a stimulus signal (e.g. gravity for accelerometer calibrations, and the Earth rotation rate for gyroscope calibrations). The sensor triad is turned to different, *arbitrary* orientations, and the 1-D measurements of *scalar* gravity $|\mathbf{f}|$, or *scalar* turn rate $\tilde{\omega}_{ib}$, are compared to the external reference value. An important assumption for this calibration method is, that the estimated parameters (bias, scale factor, cross-coupling) are constant for the set of different IMU orientations. This section provides a brief overview of the method. A more detailed mathematical derivation, including the Jacobian matrix of the observation equation, can be found in *Shin and El-Sheimy* (2002). The calibration is repeated for different nominal oven temperatures, following the approach presented in *Yang et al.* (2013). Thereby, a set of nine

thermal correction functions is deduced for the QA-2000 accelerometer triad (three biases, three scale factors, and three cross-couplings).

Note: This approach is in theory suited for the calibration of accelerometer *and* gyroscope triads. The latter however can only be calibrated using the Earth rotation rate as stimulus signal (unless a 3-axis turn table is available). Such a weak stimulus signal does not allow a reasonable determination of gyroscope cross-couplings, or scale factors. For example, for the application of navigation, the scale factors would have to be extrapolated from 0.004° per second (Earth rotation rate) to turn rates of the order of tens of degrees per second (or more).

The approach is however well suited for an accelerometer triad, for navigation applications with low or medium dynamics, because the actual specific forces during the vehicle motion are of the same order as the stimulus signal during the calibration (the Earth's gravity). In the following, the BSC calibration will be introduced for accelerometer triads only, as the author did not have access to a *three*-axis turn table with combined temperature oven.

Basic equations

Only based on the known scalar gravity g_{ref} , the following nine parameters are determined by a least-squares estimation:

1. three biases: b^X, b^Y, b^Z ,
2. three scale factors: s^X, s^Y, s^Z , and
3. three cross-couplings: $\epsilon_{YX}, \epsilon_{ZX}, \epsilon_{ZY}$ (as defined in Sect. 5.2.4).

It is assumed, that the IMU axes (X/Y/Z) form a right-handed Cartesian coordinate frame. The approach is based on observations of the *scalar* gravity value only. As a consequence, a minimum of nine poses is required to fully determine the set of the nine parameters shown above. In order to stabilize the estimation process (and also to enable a statistical evaluation), an over-determination is commonly suggested. For example, the following set of 26 poses are proposed by *Shin and El-Sheimy* (2002):

1. "face down": with the IMU at rest on each of the six surfaces (6 poses),
2. "edge down": with the IMU at rest on each of the 12 edges (12 poses), and
3. "corner down": with the IMU at rest on each of the 8 corner points (8 poses).

Since the approach does not involve any restriction or knowledge on the actual, *absolute* orientation of the sensor triad with respect to the gravity vector, only mutual cross-couplings of the sensors can be calibrated ($\epsilon_{YX}, \epsilon_{ZX}, \epsilon_{ZY}$). Conversely, the calibration of misalignments with respect to an externally defined reference orientation is not possible with this approach. The cross-couplings of a sensor triad are fully determined by the given set of three independent parameters. Therefore, only three out of the six possible misalignments introduced in Sect. 5.2.4 are chosen, by selecting one out of each pair of symmetric misalignments ($\epsilon_{ij}, \epsilon_{ji}$).

The measured specific forces \tilde{f} for the X-, Y-, and Z-accelerometers of a sensor triad are then given as

$$\tilde{f}^X = b^X + (1 + s^X)f^X \quad (6.1)$$

$$\tilde{f}^Y = b^Y + (1 + s^Y)(f^Y \cos(\epsilon_{YX}) - f^X \sin(\epsilon_{YX})) \quad (6.2)$$

$$\tilde{f}^Z = b^Z + (1 + s^Z)(f^Z \cos(\epsilon_{ZX}) \cos(\epsilon_{ZY}) - f^X \sin(\epsilon_{ZX}) - f^Y \sin(\epsilon_{ZY}) \cos(\epsilon_{ZX})) \quad (6.3)$$

where f^a is the true specific force along the given axis a . For small misalignments of the order of tens of arc seconds, these equations can be approximated by

$$\tilde{f}^X \approx b^X + (1 + s^X)f^X \quad (6.4)$$

$$\tilde{f}^Y \approx b^Y + (1 + s^Y)(f^Y - f^X \epsilon_{YX}) \quad (6.5)$$

$$\tilde{f}^Z \approx b^Z + (1 + s^Z)(f^Z - f^X \epsilon_{ZX} - f^Y \epsilon_{ZY}). \quad (6.6)$$

(The error of the approximation $\sin(\epsilon) \cdot g \approx \epsilon \cdot g$ is smaller than $0.02 \mu\text{Gal}$, if $\epsilon < 100$ arc seconds.) These equations can be rearranged to

$$f^X \approx \bar{f}^X \quad (6.7)$$

$$f^Y \approx \bar{f}^Y + \bar{f}^X \epsilon_{YX} \quad (6.8)$$

$$f^Z \approx \bar{f}^Z + \bar{f}^X \epsilon_{ZX} + (\bar{f}^Y + \bar{f}^X \epsilon_{YX}) \epsilon_{ZY}, \quad \text{with} \quad (6.9)$$

$$\bar{f}^a := \frac{\tilde{f}^a - b^a}{1 + s^a}, \quad \text{for } a \in \{X, Y, Z\}. \quad (6.10)$$

Note: Since the calibration is done with the sensor triad at rest (without accelerations, $\ddot{\mathbf{r}} = 0$), the specific forces are equal to the respective components of the negative gravity vector, i.e. $f^a =: -g^a$ and $\tilde{f}^a =: -\tilde{g}^a$ for a given axis a .

The main condition equations for the mixed model (also called *Gauss-Helmert model*) are given by the equality of the scalar gravity as measured by the accelerometer, and the reference value. For the error-free observations of the specific force f^a , this condition is given as

$$g^2 - g_{\text{ref}}^2 = (f^X)^2 + (f^Y)^2 + (f^Z)^2 - g_{\text{ref}}^2 = 0. \quad (6.11)$$

Now accounting for sensor errors, each of the condition equations yields a contradiction w :

$$\tilde{g}^2 - g_{\text{ref}}^2 = (\tilde{f}^X)^2 + (\tilde{f}^Y)^2 + (\tilde{f}^Z)^2 - g_{\text{ref}}^2 = w. \quad (6.12)$$

The set of all of these condition equations (one condition per IMU orientation) can be written in short form as $\mathbf{F}(\tilde{\mathbf{L}}, \mathbf{X}) = \mathbf{w}$, where $\tilde{\mathbf{L}}$ denotes the vector of observations, and \mathbf{X} denotes the 9-D vector of parameters (biases, scale factors, cross-couplings).

The Gauss-Helmert adjustment provides the vectors of adjusted observations, $\hat{\mathbf{L}}$, and adjusted parameters, $\hat{\mathbf{X}}$. The adjustment is based on the minimisation of $\mathbf{v}^T \mathbf{v}$, where \mathbf{v} denotes the vector of residuals of the observations, with $\hat{\mathbf{L}} = \tilde{\mathbf{L}} + \mathbf{v}$. For the adjusted quantities, $\mathbf{F}(\hat{\mathbf{L}}, \hat{\mathbf{X}}) = \mathbf{0}$ in general, i.e. the adjusted observations $\hat{\mathbf{L}}$ in combination with the adjusted parameters $\hat{\mathbf{X}}$ do not yield any contradiction in general. Note, that this is a non-linear system. For the required Jacobian matrices for the least-squares adjustment, the reader is referred to *Shin and El-Sheimy* (2002). Starting with the approximation \mathbf{X}_0 , with

$$b_0^X = b_0^Y = b_0^Z = s_0^X = s_0^Y = s_0^Z = \epsilon_{YX,0} = \epsilon_{ZX,0} = \epsilon_{ZY,0} = 0, \quad (6.13)$$

the adjustment is executed in an iterative manner, as suggested by the non-linearity of the functional relationship. The iteration loop was stopped as soon as the maximum absolute parameter change was less than 10^{-15} (which is approximately the resolution of a matrix inversion, when using a 64 bit floating point representation). For the actual calibration measurements, this was the case after a maximum of 6 iteration steps.

Based on the set of adjusted error model parameters, $\hat{\mathbf{X}}$, the *original* observations $\tilde{\mathbf{L}}$ still yield non-zero contradictions in general, i.e. $\mathbf{F}(\tilde{\mathbf{L}}, \hat{\mathbf{X}}) = \mathbf{w} \neq \mathbf{0}$. These contradictions \mathbf{w} can be regarded as the residuals of the adjustment. Assuming, that the adjustment was done using a sufficient number of iterations, w can therefore be seen as a measure, of how good the estimated error model fits the original measurements, and thus, how good it fits the actual sensor error characteristics. Contradictions, which are large compared to the expected effects of the sensor noise may lead to the conclusion, that the error model could not adequately model the actual sensor error characteristics.

Implementation of a BSC accelerometer calibration

The calibration was carried out on Aug. 19th and 20th, 2015. The iMAR RQH-1003 IMU was mounted on a professional 2-axis turn table with combined temperature oven (Fig. 6.16). The turn table precision for re-approaching a pose is specified to be better than one arc second. The actual pose is measured by angular sensors sitting in the two joints of the table, with a precision of better than 0.1 arc seconds. A temperature sensor measures the air temperature in the oven.



Figure 6.16: 2-axis turn table with combined temperature oven. The RQH-1003 system is fixed to a rotating plate inside of the temperature oven.

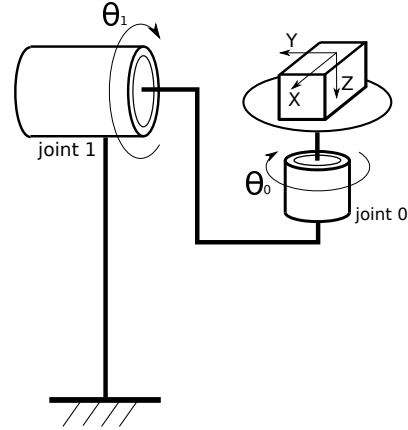


Figure 6.17: Schematic turn table configuration. The orientation of the IMU axes (X/Y/Z) is shown for $\theta_0 = \theta_1 = 0^\circ$.

An accelerometer triad calibration was implemented as follows:

- The BSC-calibration was repeated for four different nominal oven temperatures: 10°C, 20°C, 30°C, and 40°C (in this order). When changing to a new temperature, 2.5 hours without measurements were inserted to allow the inertial sensors to thermally stabilise. Note, that the ISA temperature was approximately 10 K to 15 K above the oven air temperatures.
- For each of the nominal oven temperatures, the calibration was repeated for three times in order to analyse the repeatability.
- For each temperature and repetition, the full set of 26 poses were approached by the turn table. For each pose, the IMU was kept at rest for 90 seconds. This period was chosen as a trade-off between the precision of the averaged sensor readings (Sect. 6.2), and the limited overall experiment duration.

This configuration yields a total of 312 measurements, and an overall duration of the experiment of approximately 19 hours.

Reference gravity from terrestrial gravimetry

The scalar reference gravity value g_{ref} was determined using a LaCoste & Romberg G-type gravimeter (Fig. 6.18). A point on the laboratory floor (point id: 10) was tied to two nearby official gravity points established by the Saarland surveying office. These points are denoted here as P1 and P2, each of them situated within a range of ≈ 3 km from the calibration laboratory. The points were measured in the sequence P1–10–P2–10–P1–10–P2. Accounting for Earth tides and uncertainties for the points P1 and P2, and adjusting a linear sensor drift of the gravimeter, yields

$$g_{\text{ref},10} = 980938.781 \pm 0.012 \text{ mGal}. \quad (6.14)$$



Figure 6.18: A LaCoste and Romberg G-gravimeter (G-258) standing on the calibration laboratory floor (point 10).

The gravity gradient was determined on site by repeated measurements of two points with a vertical offset of 3.756 m, using the same gravimeter. The measurement sequence was low–high–low–high–low. Again, accounting for Earth tides, and adjusting a linear sensor drift of the gravimeter, yields a vertical gravity gradient of

$$\left. \frac{\partial g}{\partial H} \right|_{\text{ref},10} = 279.8 \pm 2.3 \mu\text{Gal}/\text{m}. \quad (6.15)$$

A constant height of the IMU’s centre of observations above the laboratory floor of 1.45 ± 0.05 m yields the final reference gravity value of

$$g_{\text{ref,IMU}} = 980938.389 \pm 0.016 \text{ mGal}. \quad (6.16)$$

Calibration results and discussion

Fig. 6.19 shows the results of the Gauss-Helmert adjustment, for each of the nine parameters (biases, scale factors, and misalignments), and for each of the 12 runs (four nominal oven temperatures, with three repetitions each). Regression polynomials of degree three are used for the interpolation. Again, as for the warm-up calibration (Sect. 6.4), an extrapolation to lower or higher temperature appears only reasonable for small temperature differences of several Kelvin.

Fig. 6.19 also shows accelerometer triad misalignments for a subset for six out of the 26 poses. The absolute level of these misalignments was arbitrarily defined (close to zero for the first temperature setting). Since the three accelerometers are firmly mounted to the ISA sensor package, these triad misalignment changes indicate a thermal dependency of the shock mounts (cf. Fig. 6.2). It is noted here again, that misalignments of tens of arc seconds of the ISA with respect to the nominal IMU axes have *no* practical relevance for strapdown gravimetry (cf. Sect. 5.2.4).

Note, that the accelerometer cross-couplings are significantly smaller than the ISA misalignments (Fig. 6.19, bottom left vs. bottom right). According to the manufacturer, the six inertial sensors (*not* triads of sensors) are individually mounted to the ISA. Therefore, the *relative* misalignments between accelerometers and gyroscopes are expected to be of a similar magnitude as the accelerometer cross-couplings (several arc seconds). Such relative misalignments between accelerometers and gyroscopes can however not be determined by this calibration method.

For each parameter, a standard deviation is computed based on the misfits of the three repetitions (Tab. 6.3). There are no significant differences among the parameters of the same type, as can be seen in Tab. 6.3. Also, these estimated precisions show a good agreement with

param.	unit	oven/ISA temperature				average	$\hat{\sigma}$
		10°C/23°C	20°C/32°C	30°C/42°C	40°C/51°C		
b^X	[mGal]	0.34	0.24	0.68	0.78	0.51	0.70
b^Y	[mGal]	0.26	1.02	1.21	0.55	0.76	0.70
b^Z	[mGal]	0.54	0.69	0.24	0.99	0.62	0.63
s^X	[ppm]	0.77	0.47	0.30	1.77	0.82	1.07
s^Y	[ppm]	0.98	0.99	0.43	0.84	0.81	1.07
s^Z	[ppm]	0.97	2.01	0.40	0.01	0.85	0.94
ϵ_{YX}	[arc sec]	0.10	0.41	0.25	0.34	0.27	0.34
ϵ_{ZX}	[arc sec]	0.22	0.32	0.22	0.18	0.23	0.30
ϵ_{ZY}	[arc sec]	0.37	0.21	0.07	0.28	0.23	0.30

Table 6.3: Repeatability statistics of the BSC-calibration. For each parameter and temperature, the standard deviation among the three repetitions is shown. The empirical spread is in good accordance with the a-posteriori parameter standard deviations $\hat{\sigma}$, as estimated by the Gauss-Helmert adjustment.

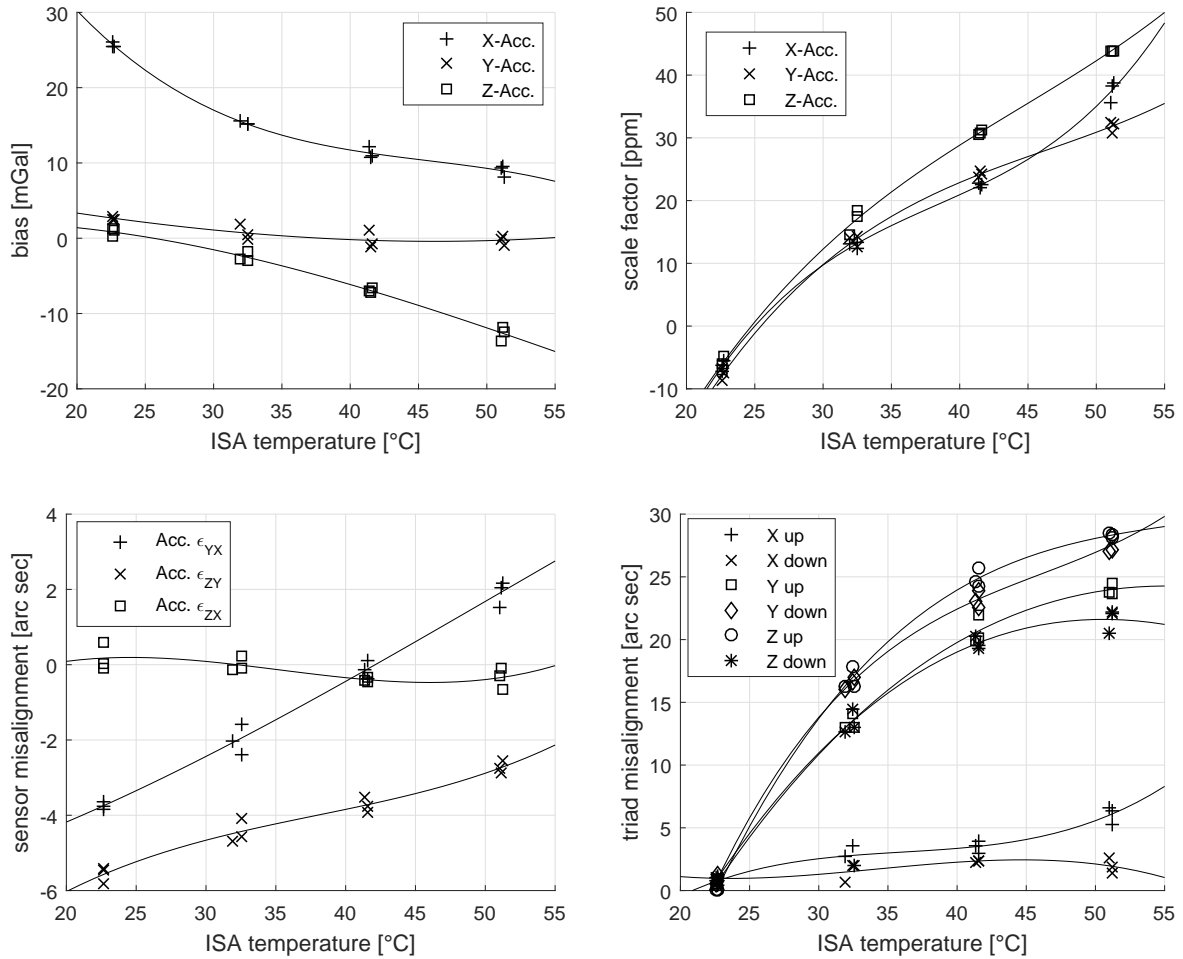


Figure 6.19: Results from the thermal calibration of accelerometer biases, scale factors and internal triad cross-couplings. Bottom right: For a selection of the six "face-down" poses, the relative change of the accelerometer triad misalignment over temperature is shown. A third-order regression polynomial is shown for each of the parameters.

Set	ISA temperature	BSC residuals [mGal ²]			BSSC residuals [mGal ²]		
		RMS	min.	max.	RMS	min.	max.
1	22.7°C	76.8	-222.8	148.1	37.7	-60.7	58.8
2	22.6°C	82.1	-206.6	167.6	38.0	-82.1	83.6
3	22.6°C	79.5	-180.1	180.6	36.8	-69.6	74.2
4	31.9°C	70.7	-186.1	156.5	29.5	-53.3	58.7
5	32.5°C	85.4	-205.1	173.2	31.8	-58.5	68.9
6	32.5°C	81.8	-203.4	189.3	44.9	-82.3	96.3
7	41.3°C	77.3	-210.8	159.6	33.6	-53.6	60.8
8	41.5°C	76.3	-212.6	153.7	33.7	-72.7	61.8
9	41.6°C	81.4	-233.6	149.1	36.0	-72.5	72.4
10	51.0°C	69.8	-190.7	132.6	31.8	-56.3	59.6
11	51.2°C	82.6	-190.3	166.7	40.5	-55.3	69.8
12	51.2°C	80.9	-202.9	199.0	35.9	-55.6	91.8
total		78.7	-233.6	199.0	35.9	-72.7	91.8

Table 6.4: Adjustment residuals w , after applying the final parameter estimates to the observations. Statistics are shown for each of the 12 data sets. Note, that the residuals are expressed in units of [mGal²] due to the squared gravity quantities compared in the condition equations.

the a-posteriori parameter standard deviations as estimated by the Gauss-Helmert adjustment (see rightmost column in Tab. 6.3).

The a-posteriori standard deviations of approximately 0.7 mGal (biases), 1 ppm (scale factors), and 0.3 arcseconds (cross-couplings), overall suggest a good calibration result. However, after applying the final parameter estimates $\hat{\mathbf{X}}$ to the original observations $\tilde{\mathbf{L}}$, the residual contradictions $\mathbf{w} = \mathbf{F}(\tilde{\mathbf{L}}, \hat{\mathbf{X}})$, with $\sqrt{w} \approx 8.9$ mGal (RMS) are significantly higher than the expected *precision* of the scalar gravity measurements of <3 mGal (cf. Sect. 6.2). Tab. 6.4 (column "BSC") shows the statistics of the contradictions w . The relatively large values can in general have the following reasons:

1. the a-priori observation precision of 1 mGal to 3 mGal is too optimistic, or
2. the bias / scale factor / cross-coupling error model for the accelerometer triad, as used for this calibration, is not suited to model the actual sensor error characteristics at a higher accuracy.

The latter is expected to be the primary reason. Thus, motivated by these relatively large contradictions, a more extended error model is investigated in the next section.

6.5.2 Bias, two scale factors, cross-coupling (BSSC)

As an extension of the above set of parameters, additional scale factors are introduced to the error model. The extended error model is similar to the one given in Eqs. 6.1ff, but using an extended definition for the scale factors:

$$s^a := \begin{cases} s^{a,\text{pos}} & \text{if } \tilde{f}^a \geq 0 \\ s^{a,\text{neg}} & \text{else} \end{cases}, \quad (6.17)$$

for a sensor axis $a \in \{X, Y, Z\}$. Thus, for each of the three accelerometers, two independent scale factors are used, one for positive, and the other for negative sensor readings. Together

param.	unit	oven/ISA temperature				average	$\hat{\sigma}$
		10°C/23°C	20°C/32°C	30°C/42°C	40°C/51°C		
b^X	[mGal]	1.98	1.14	1.72	0.78	1.41	2.97
b^Y	[mGal]	0.23	1.23	1.73	2.63	1.46	2.97
b^Z	[mGal]	1.48	3.50	0.16	1.87	1.75	4.18
$s^{X,\text{pos}}$	[ppm]	3.22	1.41	1.23	1.48	1.83	4.19
$s^{Y,\text{pos}}$	[ppm]	0.41	2.33	2.72	4.21	2.42	4.19
$s^{Z,\text{pos}}$	[ppm]	2.52	5.47	0.74	3.06	2.95	5.58
$s^{X,\text{neg}}$	[ppm]	1.78	2.06	1.69	2.06	1.90	4.19
$s^{Y,\text{neg}}$	[ppm]	1.54	2.57	2.71	2.73	2.39	4.19
$s^{Z,\text{neg}}$	[ppm]	2.47	3.54	0.07	3.07	2.29	5.58
ϵ_{YX}	[arc sec]	0.10	0.41	0.25	0.34	0.27	0.34
ϵ_{ZX}	[arc sec]	0.22	0.32	0.22	0.18	0.23	0.30
ϵ_{ZY}	[arc sec]	0.37	0.21	0.07	0.28	0.23	0.30

Table 6.5: Repeatability statistics of the BSSC-calibration. For each parameter and nominal oven temperature, the standard deviation among the three repetitions is shown. The a-posteriori parameter standard deviations $\hat{\sigma}$, as estimated by the Gauss-Helmert adjustment, appear slightly too pessimistic compared to the agreement among the repetitions.

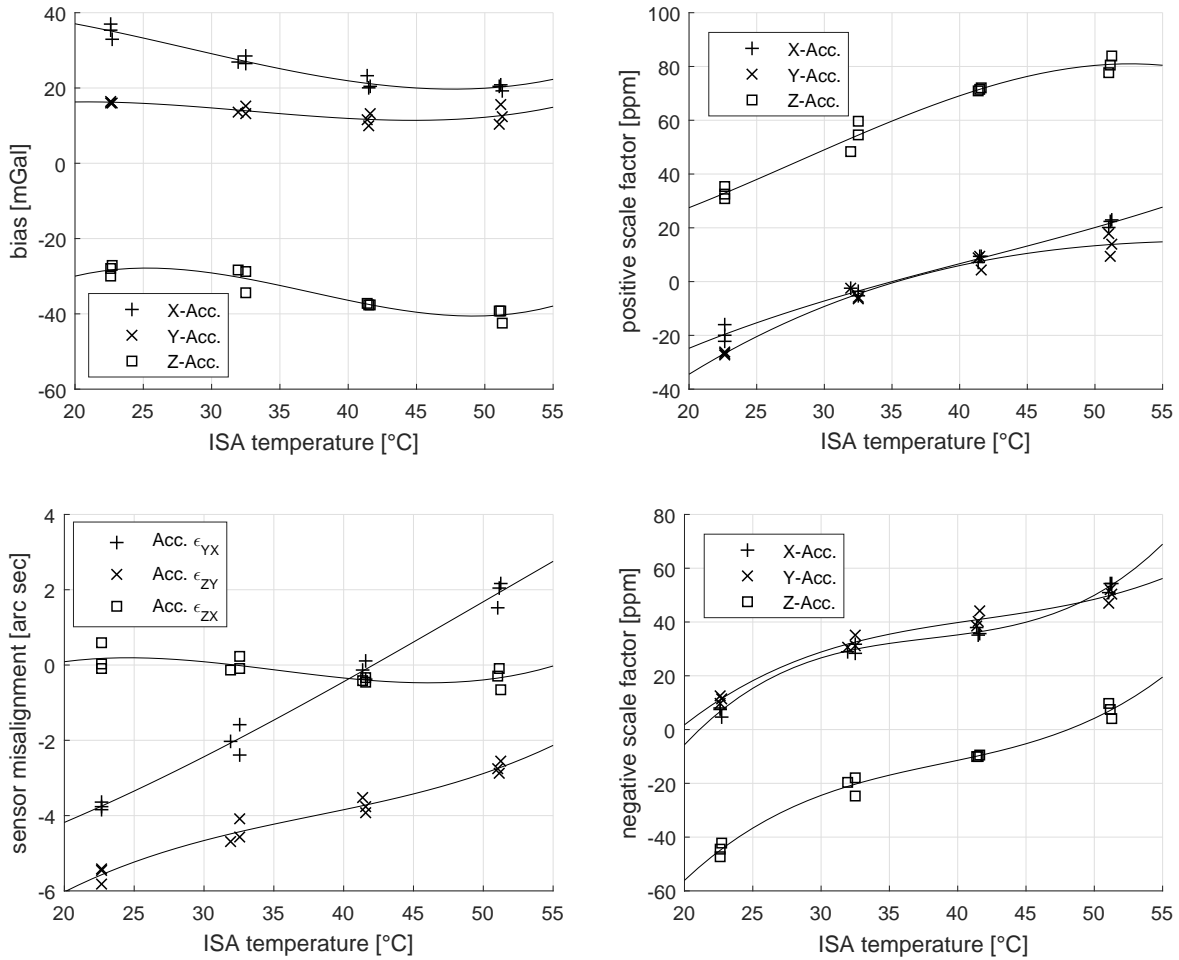


Figure 6.20: Results from the thermal calibration of accelerometer biases, positive and negative scale factors, and triad cross-couplings (BSSC). A third-order regression polynomial is shown for each of the parameters.

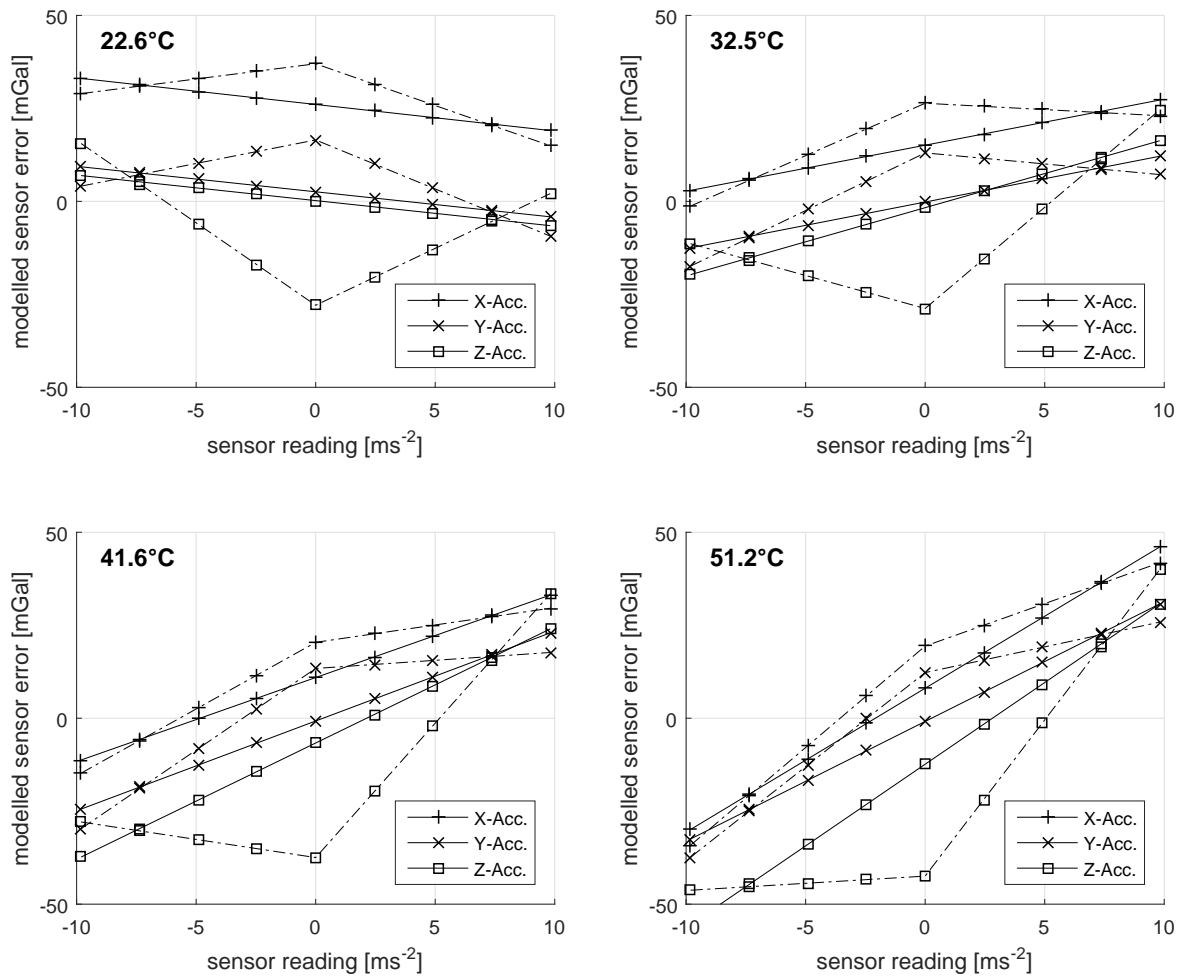


Figure 6.21: Comparison of the estimated accelerometer error models of the BSC calibration (solid lines) versus the BSSC calibration (dashed lines). Cross-couplings are not taken into account in this representation. Only a single comparison is shown for each of the nominal temperature levels (sets 3, 6, 9, and 12), as there is only little change among the repetitions. Significant differences can be recognised between the two models.

with the sensor biases and cross-couplings as introduced in the previous section, this forms a vector of twelve (instead of nine) parameters:

$$\mathbf{X}' = (b^X, b^Y, b^Z, s^{X,\text{pos}}, s^{Y,\text{pos}}, s^{Z,\text{pos}}, s^{X,\text{neg}}, s^{Y,\text{neg}}, s^{Z,\text{neg}}, \epsilon_{YX}, \epsilon_{ZX}, \epsilon_{ZY})^T. \quad (6.18)$$

This extended model will be referred to as *BSSC* model, indicating the double scale factors for each of the sensors. Besides this extended scale factor definition, the calibration is carried out with the same data set introduced in the previous section.

The results of the BSSC calibration are shown in Fig. 6.20. The statistics are shown in Tab. 6.5. Apparently, the lower over-determination leads to higher a-posteriori standard deviations of the biases and scale factors. By comparison with Fig. 6.19, it can be seen, that the cross-coupling estimates are not affected by the extended error model. The same holds for the triad misalignments (no figure shown is for the BSSC calibration).

As an important result of the BSSC calibration, it can be seen that the positive and negative scale factors differ significantly (Fig. 6.20). Apparently, the true sensor errors can not be adequately represented by a single scale factor. A direct comparison of the error models as estimated by the BSC and the BSSC calibrations is shown in Fig. 6.21. The BSSC sensor error models are "V"- or "Λ"-shaped, and differ significantly from the linear error models (straight lines in the plots) estimated in the scope of the BSC-calibration.

Statistics of the adjustment residuals $\mathbf{w} = \mathbf{F}(\tilde{\mathbf{L}}, \hat{\mathbf{X}}')$, i.e. after applying the final BSSC parameter estimates $\hat{\mathbf{X}}'$ to the original observations $\tilde{\mathbf{L}}$, are shown in Tab. 6.4. The residuals are significantly smaller compared to the BSC calibration, indicating a better fit of the error model with the actual sensor error characteristics. Still, the RMS of the contradictions of 35.9 mGal^2 , consistent with a scalar gravity residual of $\approx 6.0 \text{ mGal}$, is relatively large compared to the expected measurement precision.

6.5.3 Discussion

It was shown in the previous sections, that a BSSC error model is better suited for the error modelling of the accelerometers compared to a BSC error model. However, the large misfits of the corrected observations versus the reference gravity value of 6.0 mGal ($1\text{-}\sigma$) for the BSSC calibration shows, that the error model may still not be the optimal choice. The higher repeatability of the parameters of 3 mGal and 4 ppm supports the expectation, that this misfit is *not* a purely stochastic effect. Thus, a different, probably finer error model may improve the fit, which can be accomplished by the introduction of additional parameters, as for example

- coefficients of second-, third- or higher-degree polynomials, approximating the individual sensor errors (instead of bias and scale factors),
- coefficients for smoothing splines approximating the error functions (linear functions were used for the BSC and BSSC models), or
- parameters taking into account the different orientations of the IMU. In other words, the core assumption, that the parameters only depend on the sensor temperature, may have to be relaxed.

Fig. 6.22 illustrates the different error models. Instead of adding more parameters to the model, the illustration shows, that a sensor error look-up table might be a reasonable alternative. In fact, the thermal correction of the vertical accelerometer shown in Sect. 6.4 is already a simple example of a one-dimensional look-up table. This approach will be pursued in more detail in the following section.

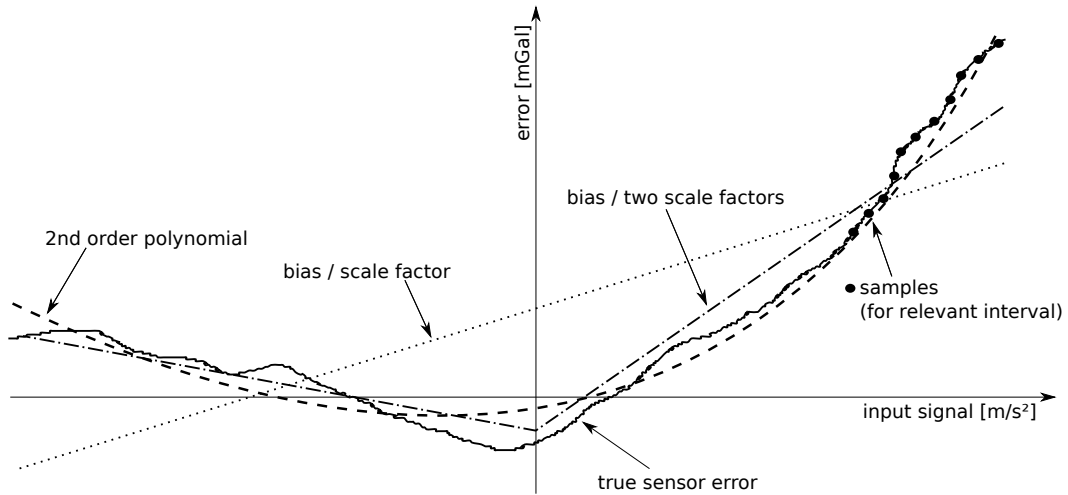


Figure 6.22: An illustration of different error models for a single accelerometer (thus, cross-couplings are neglected here). The reproducible, true sensor error is assumed to be highly non-linear (solid line). The different parametric approaches show residual errors. The sample-based approach is based on a look-up table of calibrated error values. This look-up table may be limited to a relevant interval (as shown here).

6.6 Extended sample-based error models

A sample-based error model is defined here as a look-up table of sensor errors, defined in a certain state space. For the application of strapdown gravimetry, reasonable dimensions for such a state space could be

- sensor temperature,
- sensor attitude, e.g. given as roll- or pitch-angles,
- sensor reading.

Reasonable state-space definitions for calibrating the iMAR RQH-1003 system should always include the sensor temperature as a dimension: Significant and reproducible thermal effects could already be shown in the previous sections. Thus, reasonable state space definitions could be

- temperature only (1-D): as used for the simple thermal calibration shown in Sect. 6.4;
- [temperature \times sensor reading] (2-D): assuming, that apart from temperature, the sensor errors only depend on the actual specific force. Note, that different combinations of roll-angle, pitch-angle and aircraft acceleration result in the same measured specific force.
- [temperature \times roll-angle \times pitch-angle] (3-D): assuming that, apart from temperature, the sensor errors can be defined as a function of the sensor's attitude (assuming the sensor being at rest, only measuring gravity). In particular, it can be expected that sensor misalignments are dependent on the sensor attitude, as different mechanical forces act on the shock mounts and the internal components. This state space assumes identical sensor errors for different aircraft accelerations. It is therefore expected to allow a reasonable error modelling only for low-dynamic motion, e.g. on the measurement lines when doing strapdown airborne gravimetry.
- [temperature \times roll-angle \times pitch-angle \times sensor reading] (4-D): This state space allows a more complete error model: By including the sensor reading, it can account

for different aircraft accelerations in combination with different sensor attitudes. Being the most general state space definition, it appears worthwhile to use this approach for a calibration. However, it is in practice impossible to perform such a calibration in a laboratory: It would require a set-up, that is actually able to perform an acceleration of the IMU for different orientations of the IMU. An acceleration of 1 ms^{-2} for a period of two minutes (to allow the average sensor reading to converge) already involves a position change of the sensor of 7200 m.

- [temperature \times roll-angle \times sensor reading] (3-D): Reasonable, if a sensor shows no significant dependency on the pitch-angle. Again, the sensor readings are limited to the interval $[-g; g]$, because the IMU can not be moved over long distances during the calibration.
- [temperature \times pitch-angle \times sensor reading] (3-D): Reasonable, if a sensor shows no significant dependency on the roll-angle.

In this section, a [temperature \times roll-angle \times pitch-angle] (*TRP*) 3-D state space will be used for the calibration of the QA-2000 accelerometer triad. In contrast to the calibrations shown in the previous section, this calibration is not only a thermal calibration, but it also accounts for different sensor orientation. In particular, a similar calibration, but in the 2-D state space [roll-angle \times pitch-angle], appears reasonable also for thermally stabilised IMUs.

Based on the discussion of the results, it will be argued later in this section, why a [temperature \times sensor reading] state space is not suitable for the given QA-2000 accelerometer triad. A similar conclusion will be drawn for the [temperature \times roll-angle \times sensor reading] and [temperature \times pitch-angle \times sensor reading] state space definitions.

6.6.1 A sample-based TRP calibration for strapdown airborne gravimetry

Note: Since the author had only limited access to a professional 2-axis turn table with combined temperature oven, the calibration had to be designed under the constraint of a limited overall calibration duration of approximately 64 hours.

Selection of roll- and pitch-angle combinations

It was shown in Figs. 5.2 and 5.3, that the typical combinations of roll and pitch angles, that can be observed during the flights, and in particular on the measurement lines, are limited to certain intervals. Similar diagrams are shown for the other aerogravity campaigns evaluated in the scope of this thesis in the Appendix (Fig. A.1), showing similar intervals.

In order to reduce the overall duration of the calibration, the following design criteria were defined:

- Pitch angles of more than 15° (or less than -15°) are unlikely to happen during a fixed-wing aerogravity flight. Such angles are taken out of consideration.
- Similarly, roll angles of more than 45° (or less than -45°) are unlikely to happen during a fixed-wing aerogravity flight.
- Large roll- and pitch angles can mainly be observed during the take-off and landing phases, and during the turns. For such combinations of roll and pitch angle, a *coarse* sample grid appears to be sufficient. A finer grid shall be used for those combinations of roll- and pitch angles, which can typically be observed on the measurement lines (plots of real data are shown in Sect. A.1).

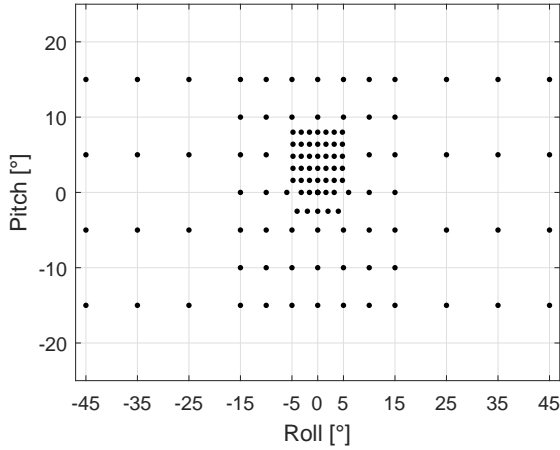


Figure 6.23: Selected combinations of roll- and pitch-angles for the sample-based TRP calibration.

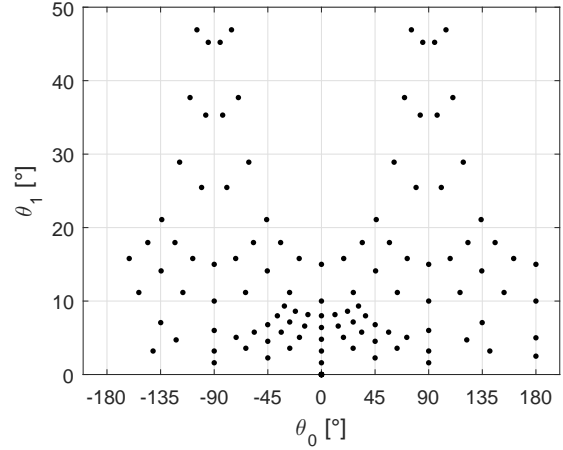


Figure 6.24: Equivalent combinations of turn table joint angles, cf. Fig. 6.17

(It is just noted here, that the roll- and pitch-angle intervals can be expected to be narrower for land vehicles, in particular the roll-angle.)

These considerations have led to a set of 113 combinations of roll and pitch angle, depicted in Fig. 6.23. The design of the 2-DOF turn table (Fig. 6.17) requires a transformation of these poses into equivalent turn table joint angles, θ_0 and θ_1 .

A local table-fixed coordinate frame t is introduced here as follows: When the table joints are both at 0° (as depicted in Fig. 6.17), the t -frame coincides with the IMU sensor frame b . (Changing the joint angles will change the b -frame, while the t -frame remains constant.) The transformation between the two frames is given as the concatenation of two rotations:

$$\mathbf{C}_b^t = \text{Rot}_Y(-\theta_1) \cdot \text{Rot}_Z(-\theta_0) \quad (6.19)$$

The resulting joint angle combinations, which are equivalent to the roll and pitch combinations of Fig. 6.23, are shown in Fig. 6.24.

For each of the 113 poses, the sensor readings are averaged for a duration of 110 s, being a compromise between the precision of sensor reading averages (Sect. 6.2), and the limited overall calibration duration. Accounting for additional approximate moving times of the turn table of 5 s per pose, the calibration duration for a set of 113 poses takes 3:36 h.

During these almost four hours, relevant random sensor drifts or jumps might distort the calibration. To enable the detection and elimination of such potential drifts or jumps, additional zero-poses (with $\theta_0 = \theta_1 = 0^\circ$) were inserted once every 20 poses (≈ 40 minutes) and in the end, yielding a total of 120 poses.

Deflections of the vertical

As a result of the angle transformation, the IMU is not only turned to the requested roll- and pitch-angles, but it is necessarily also turned to different *heading* (or: azimuth) angles. Although the heading angle variations are not covered by the calibration state space, they are still important for the calibration: Assume the IMU is mounted on the turn table, with both table joints in zero-position. Still, even error-free horizontal (X and Y) accelerometers would measure non-zero components of the Earth's gravity for the following reasons:

- the calibration laboratory floor is not perfectly aligned with the local tangent plane of the geopotential surface,
- the table geometry may have imperfections,

- the mounting of the IMU may involve small angular errors, and
- the ISA sensor package may have a constant offset with respect to the nominal axes of the IMU, which are defined by the surfaces of the housing.

While the n -frame was defined based on the *normal* plumb line direction, another auxiliary frame n' is introduced here: the $z^{n'}$ axis is pointing downward along the *true* local plumb line of the gravity field. The $x^{n'}$ -axis is the projection of the x^t axis onto the local tangent plane of the actual plumb line. Equivalently, the $y^{n'}$ -axis is the projection of the y^t axis onto the local tangent plane. Note, that the n' -frame is not aligned with the local North- and East-directions. Instead, the $x^{n'}$ and $y^{n'}$ axes are basically aligned with the (arbitrary) directions of the turn table, x^t and y^t .

Thus, the t -frame and the n' -frame only differ by small deflections ξ' and η' , which are superpositions of the different inseparable effects listed above. The coordinate transformation between both frames can be accomplished with a small angle approximation using

$$\mathbf{C}_t^{n'} = \text{Rot}_X(\eta') \cdot \text{Rot}_Y(\xi') \approx \begin{pmatrix} 1 & 0 & -\xi' \\ 0 & 1 & \eta' \\ \xi' & -\eta' & 1 \end{pmatrix}. \quad (6.20)$$

The reference gravity is then given with Eq. 6.16 as

$$\mathbf{g}_{\text{ref}}^{n'} = \begin{pmatrix} 0 \\ 0 \\ g_{\text{ref,IMU}} \end{pmatrix}, \text{ and} \quad (6.21)$$

$$\mathbf{g}_{\text{ref}}^t = (\mathbf{C}_t^{n'})^T \mathbf{g}_{\text{ref}}^{n'}. \quad (6.22)$$

Finally, for each of the different poses, the accelerometer readings $\tilde{\mathbf{f}}^b$ will be compared against the reference gravity, which needs to be transformed into the b -frame:

$$\delta \tilde{\mathbf{f}}^b = \tilde{\mathbf{f}}^b + (\mathbf{C}_b^t)^T (\mathbf{C}_t^{n'})^T \mathbf{g}_{\text{ref}}^{n'} \quad (6.23)$$

The result of the calibration is then a set of three look-up tables (one per accelerometer), containing the residuals $\delta \tilde{f}^a$ for different combinations of temperature, roll and pitch angles (with $a \in \{X, Y, Z\}$).

For the determination of the deflections ξ' and η' , three additional poses are added to the calibration program, basically rotating the IMU at $\theta_1 = 0^\circ$ around its vertical axis by steps of $\Delta\theta_0 = 90^\circ$. The last *four* poses of the program then are

1. $\theta_0 = \theta_1 = 0^\circ$
2. $\theta_0 = 90^\circ, \theta_1 = 0^\circ$
3. $\theta_0 = 180^\circ, \theta_1 = 0^\circ$
4. $\theta_0 = 270^\circ, \theta_1 = 0^\circ,$

each of them averaged over a slightly longer period of 180 s.

A least-squares adjustment is then carried out based on the observations of the horizontal accelerometers, \tilde{g}_i^X and \tilde{g}_i^Y , in order to estimate ξ' and η' . For this adjustment, random sensor offsets o^X and o^Y , which are assumed to be constant among the four observations, have to be accounted for. This yields a four-element vector of parameters:

$$\mathbf{x} = \left(\xi' \quad \eta' \quad o^X \quad o^Y \right)^T. \quad (6.24)$$

Using the common notation, the observation equation is then given with the design matrix \mathbf{A} and the vector of residuals \mathbf{v} as

$$\mathbf{L} = \mathbf{A}\mathbf{x} - \mathbf{v} = \begin{pmatrix} 1 & 0 & 1 & 0 \\ 0 & -1 & 0 & 1 \\ 0 & 1 & 1 & 0 \\ 1 & 0 & 0 & 1 \\ -1 & 0 & 1 & 0 \\ 0 & 1 & 0 & 1 \\ 0 & -1 & 1 & 0 \\ -1 & 0 & 0 & 1 \end{pmatrix} \begin{pmatrix} \xi^t \\ \eta^t \\ o^X \\ o^Y \end{pmatrix} - \mathbf{v} = \begin{pmatrix} \tilde{g}_1^X \\ \tilde{g}_1^Y \\ \tilde{g}_2^X \\ \tilde{g}_2^Y \\ \tilde{g}_3^X \\ \tilde{g}_3^Y \\ \tilde{g}_4^X \\ \tilde{g}_4^Y \end{pmatrix} \quad (6.25)$$

Temperature setting

The set of 123 poses as introduced above is repeated for a set of oven temperatures. It could be seen in Sect. 6.5.1, that a temperature spacing of 10 K may be too coarse for a reasonable interpolation. Given the limited overall calibration time, the following oven temperature settings were selected:

- A spacing of 5 K is used for lower temperatures, which are in practice mainly required for the warming-up phases of the IMU: -15°C , -10°C , -5°C , 0°C , 5°C , 10°C , 15°C , and 20°C ;
- A finer spacing of 3 K is used for the predominant ambient temperatures that can be observed during actual gravity surveys: (20°C) , 23°C , 26°C , 29°C , 32°C , 35°C , 38°C , and 41°C .

Note, that the internal ISA temperature is typically 10 K to 15 K higher compared to the ambient air temperature.

The three-dimensional look-up table will allow arbitrary combinations of temperature, roll-, and pitch-angle. Thus, the requirement of an identical temperature for all poses of a set (as for the parametric calibrations) can be relaxed. For each of the sensor readings (averaged over 110 s), also the average ISA temperature will be used. Still, strong temperatures gradients are to be avoided, to reduce thermal latency effects (as discussed in Sect. 6.4).

For the initial oven temperature setting (-15°C), three hours were given to let the ISA temperature stabilize. Then, for each of the 5 K steps, a temperature stabilisation period of 25 minutes was added, and 15 minutes for each of the 3 K steps. This yields an overall calibration duration of approximately 64 hours.

Note: The actual calibration took 76 hours, because the maximum angular speed for the table joint motors were by mistake set to low numbers, resulting in an additional time requirement of almost 12 hours.

Implementation

The calibration was carried out between March 11th and March 14th, 2016. The nominal oven temperature settings and the actual ISA temperature measurements are shown in Fig. 6.25. After the thermal stabilisation period (25 or 15 minutes), the measured oven temperatures differed by less than 0.2 K from the nominal temperature. These differences are not relevant for the calibration, which is anyway based on the ISA temperature measurement. It can be seen, that it takes several hours for the ISA temperature to stabilise. Thus, for the sets of 123 poses each, the ISA temperature is slightly increasing among the poses (decreasing for the first set, cf. Fig. 6.25). For the last four poses of each set, the temperature was nearly

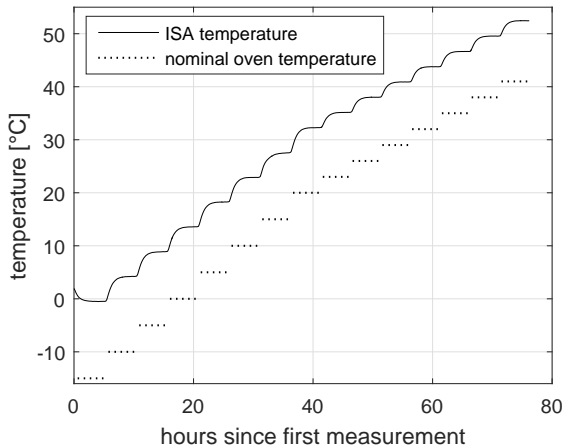


Figure 6.25: Nominal oven temperatures, and measured ISA sensor temperatures.

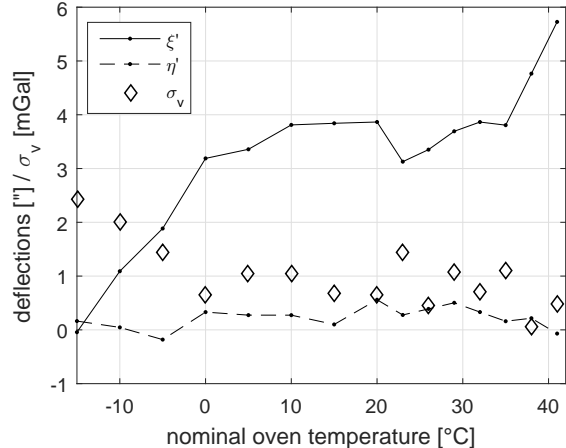


Figure 6.26: Deflections between the n' and the t coordinate frames, as determined from the last four poses of each set. The empirical standard deviations of the residuals σ_v are shown in units of mGal.

constant ($\sigma < 0.1^\circ\text{C}$), allowing the assumption of constant sensor offsets o^X and o^Y for the determination of the deflections ξ' and η' .

The estimated deflections are shown in Fig. 6.26. In order to keep the deflections low, the zero-levels of the joint angle sensors were re-calibrated based on the accelerometer outputs, shortly before the first measurements. Indeed, the initial deflections are close to zero. While ξ' shows a temperature dependency, η' remains rather stable. The residuals v are slightly higher for the lower temperatures. The empirical standard deviations of the residuals, σ_v , are also shown in Fig. 6.26, being in accordance with the expected noise level of the accelerometer measurements (cf. Sect. 6.2).

With Fig. 4.4, it can be seen, that these deflections are indeed relevant for the calibration. For example, a deflection of $\xi' = 5$ arc seconds shows up in the horizontal accelerometer measurements at a magnitude of ≈ 20 mGal.

Look-up table generation

The resulting look-up tables (one per accelerometer) contain 1695 entries each (113 measurements of $\delta \tilde{f}^b$ for each of the 15 nominal temperatures). A special interpolation method for scattered three-dimensional sample data, based on a Delaunay triangulation, is used to interpolate these entries to any state space coordinate (temperature, roll, pitch).

The entries of the look-up table still contain significant noise (cf. Sect. 6.2). In order to enable a two-dimensional low-pass filtering, the scattered table data is transformed into a regular 3-D grid, with a finer sample spacing (1 K, and 0.25° for roll and pitch). Based on the Allan standard deviations shown in Sect. 6.2, a two-dimensional Gaussian low-pass filter is applied for each temperature level.

The low-pass filtered regular 3-D grids are shown in Figs. 6.27, 6.28, and 6.29, for a selection of ISA temperatures.

Results and Discussion

The figures indicate strong effects for different attitudes, up to ± 100 mGal for larger roll and pitch angles. The shown errors are the superposition of all error types: biases, scale factors, any non-linear sensor errors, cross-couplings, and triad-misalignments. For almost

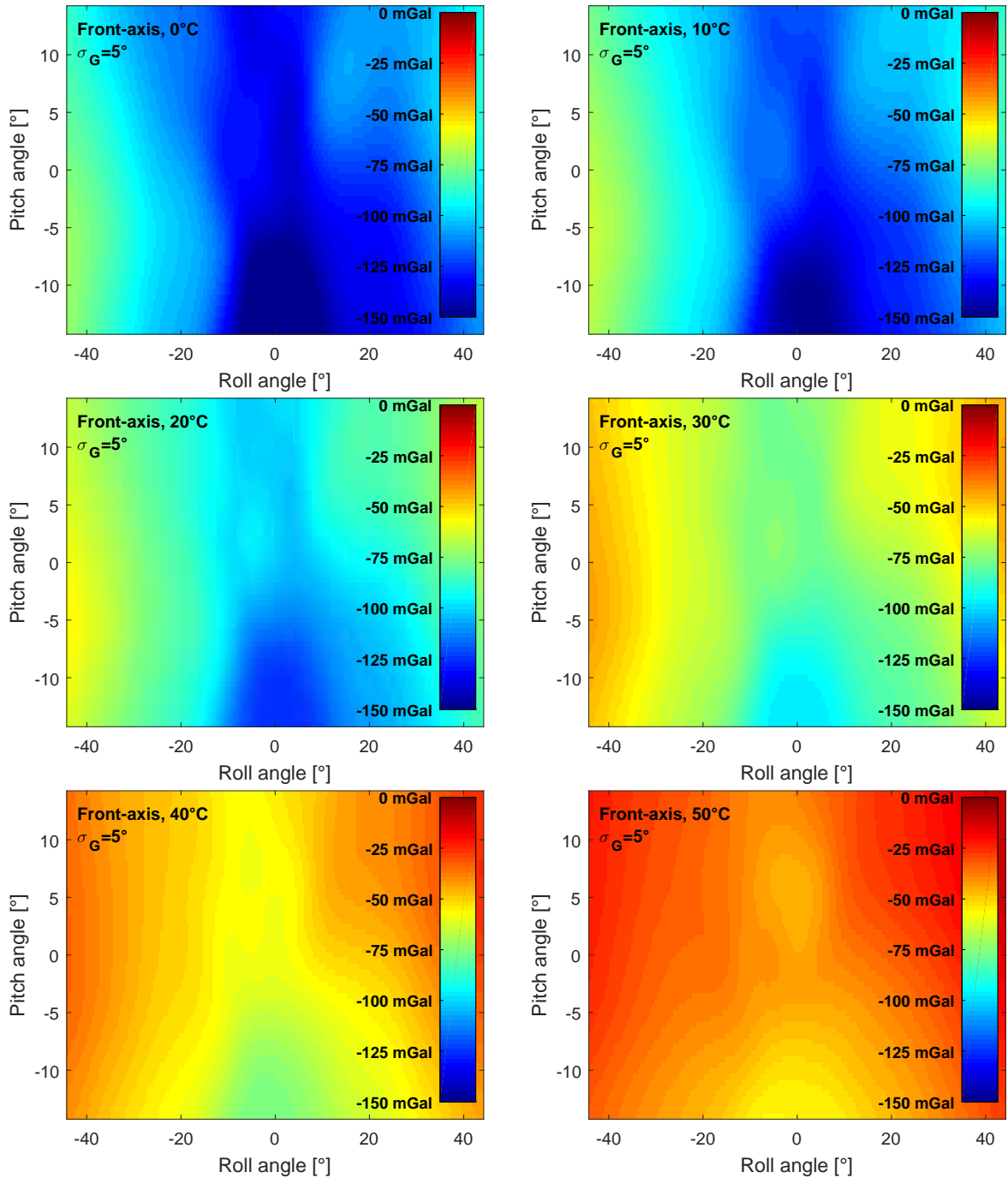


Figure 6.27: Look-up table of sensor errors for the X-accelerometer (pointing to the front for the standard mounting in a vehicle). A two-dimensional Gaussian low pass filter with $\sigma_G = 5^\circ$ was applied.

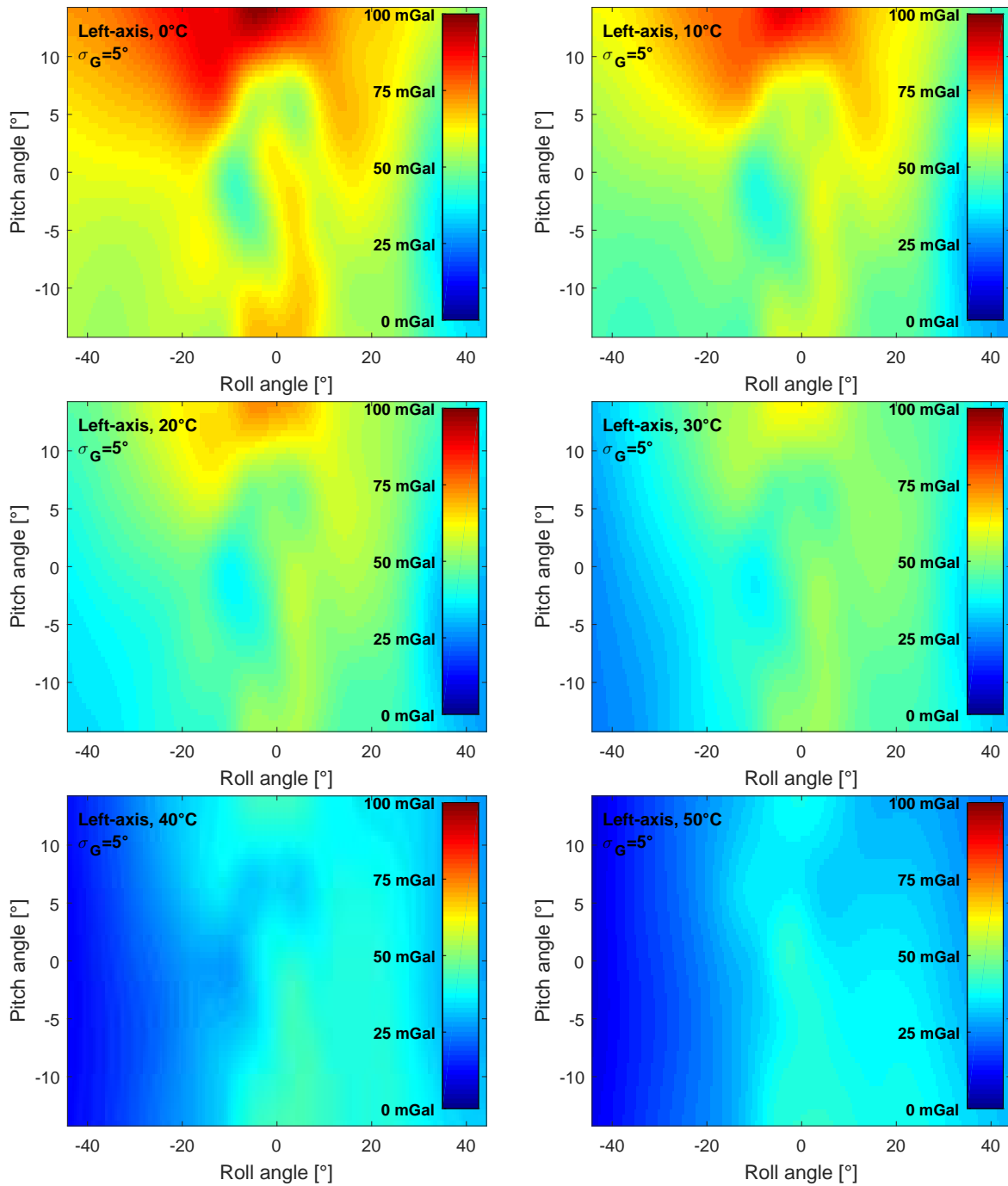


Figure 6.28: Look-up table of sensor errors for the Y-accelerometer (pointing to the left for the standard mounting in a vehicle). A two-dimensional Gaussian low pass filter with $\sigma_G = 5^\circ$ was applied.

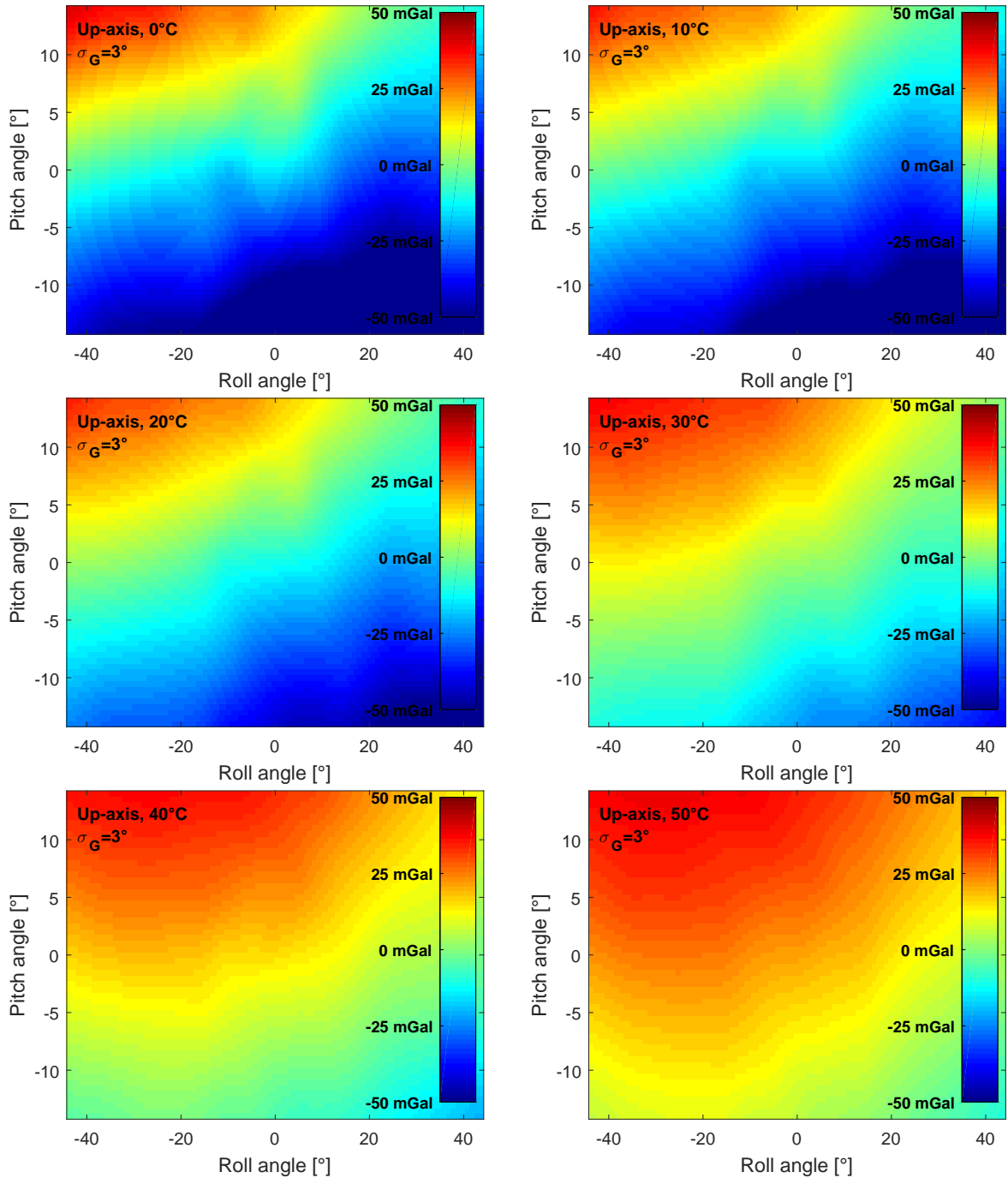


Figure 6.29: Look-up table of sensor errors for the Z-accelerometer (pointing upwards for the standard mounting in a vehicle). A two-dimensional Gaussian low pass filter with $\sigma_G = 3^\circ$ was applied.

levelled orientations of the IMU (zero roll and pitch), gradients of up to 3 mGal per degree of attitude change can be observed for the vertical accelerometer.

This emphasises the practical relevance of the modelling an attitude dependency: For example in airborne gravimetry, long-term changes of the wind strength and direction (relative to the aircraft) can yield attitude changes during non-accelerated motion of one or more degrees, to maintain the aircraft's speed and course. Contrary, short-term attitude changes, as correction manoeuvres of an auto pilot, are expected to be less relevant for the gravity determination, because of the low-pass filtering nature of the strapdown gravimetry EKF algorithm.

For each of the three accelerometers, it can be seen that the *absolute* error level changes among different temperatures, verifying strong thermal effects for the accelerometers. In addition to the temperature effect, the error *structure* for different combinations of roll- and pitch angles changes only slightly among the different temperatures. While such a structural similarity could not be expected a-priori, it can be seen here as an indicator of a good reproducibility of the calibration.

The results also show, that using a [temperature \times sensor reading] state space can not be expected to adequately model the errors:

- The Front-accelerometer shows a reproducible dependency on the roll-angle. (Such a dependency can not be modelled using a [temperature \times sensor reading] state space.)
- The Left-accelerometer shows a reproducible dependency on the pitch-angle.
- If the Up-accelerometer was only dependent on the specific force in up-direction, the plots in Fig. 6.29 would show a concentric symmetry around the plot centre, which is clearly not the case.

For the same reasons, the state space definitions [temperature \times roll-angle \times sensor reading], and [temperature \times pitch-angle \times sensor reading] are taken out of consideration. The analysis of sample-based calibrations is limited here to the calibrations shown in Sect. 6.4, and the TRP-calibration shown in this section.

It is again noted here, that this choice of the sample space, [temperature \times roll-angle \times pitch-angle], can not adequately model aircraft accelerations. The chosen calibration was rather a simulation of a *non-accelerated* flight segment, for different IMU orientations. It is a-priori unclear, if the sensor characteristics are similar among different vehicle accelerations for a constant sensor orientations, or if structure and/or intensity of the errors change significantly. Again, there is no practical way of implementing a laboratory calibration accounting for both sensor orientation (with respect to the local gravity vector), *and* vehicle acceleration, i.e. scalar specific force, $|\mathbf{f}|$, is limited by the scalar gravity, g .

It is noted again, that the calibration presented hereby was designed as an *augmentation* of the standard manufacturer calibrations. This way, the temperature independent portions of sensor biases, scale factors, and cross-couplings are *already* corrected, before processing the measurements for the TRP-calibration. Thus, the TRP calibration presented hereby is designed for the correction of the *residual* errors (after applying the manufacturer corrections).

6.7 Comparisons of the calibration results

The different accelerometer corrections derived in this chapter are summarised and compared.

For the first comparison, the IMU is assumed to be levelled (zero roll and pitch), and the Z-accelerometer only senses gravity (9.81 m/s²). The resulting corrections are shown for different temperatures in Fig. 6.30. Note again, that the absolute offsets between the corrections are

not relevant for the gravity determination, because a *constant* accelerometer bias can be estimated with sufficient accuracy in practice. Apparently, the warm-up calibration yields significantly different corrections, while all other corrections are rather similar (neglecting the constant offsets).

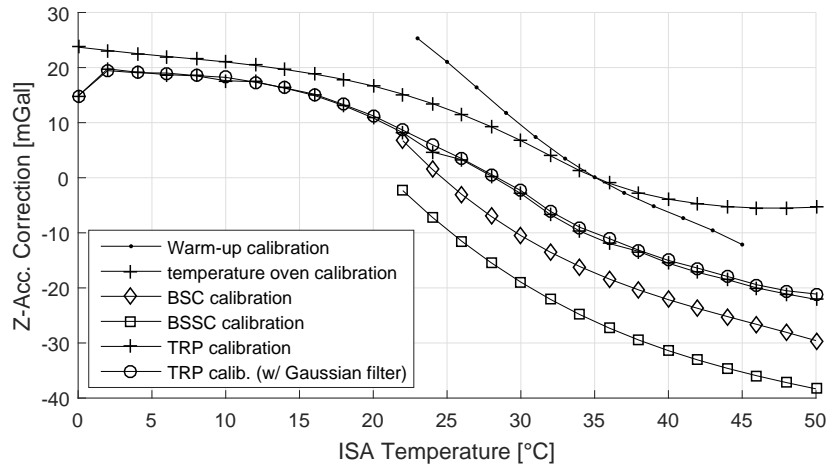


Figure 6.30: Comparison of different Z-accelerometer corrections.

The roll- and pitch-dependent calibrations (BSC, BSSC, and sample based TRP) are compared in more detail. Note, that for the BSC and BSSC calibrations, the attitude (roll and pitch angles) are not modelled *explicitly*, but the cross-couplings and scale factors *implicitly* model the sensor attitude, as the sensor readings vary for different sensor attitudes. Again, the accelerometers only sense gravity.

For this second comparison, the correction is evaluated for different combinations of roll and pitch angles, at a constant ISA temperature of 30 °C. The results can be found in Fig. 6.31. Apparently, the BSC and BSSC calibration methods can not adequately model the roll- and pitch-dependent effects. The TRP correction differs significantly from the others in terms of range and structure, thereby indicating the higher potential of sample-based calibration methods.

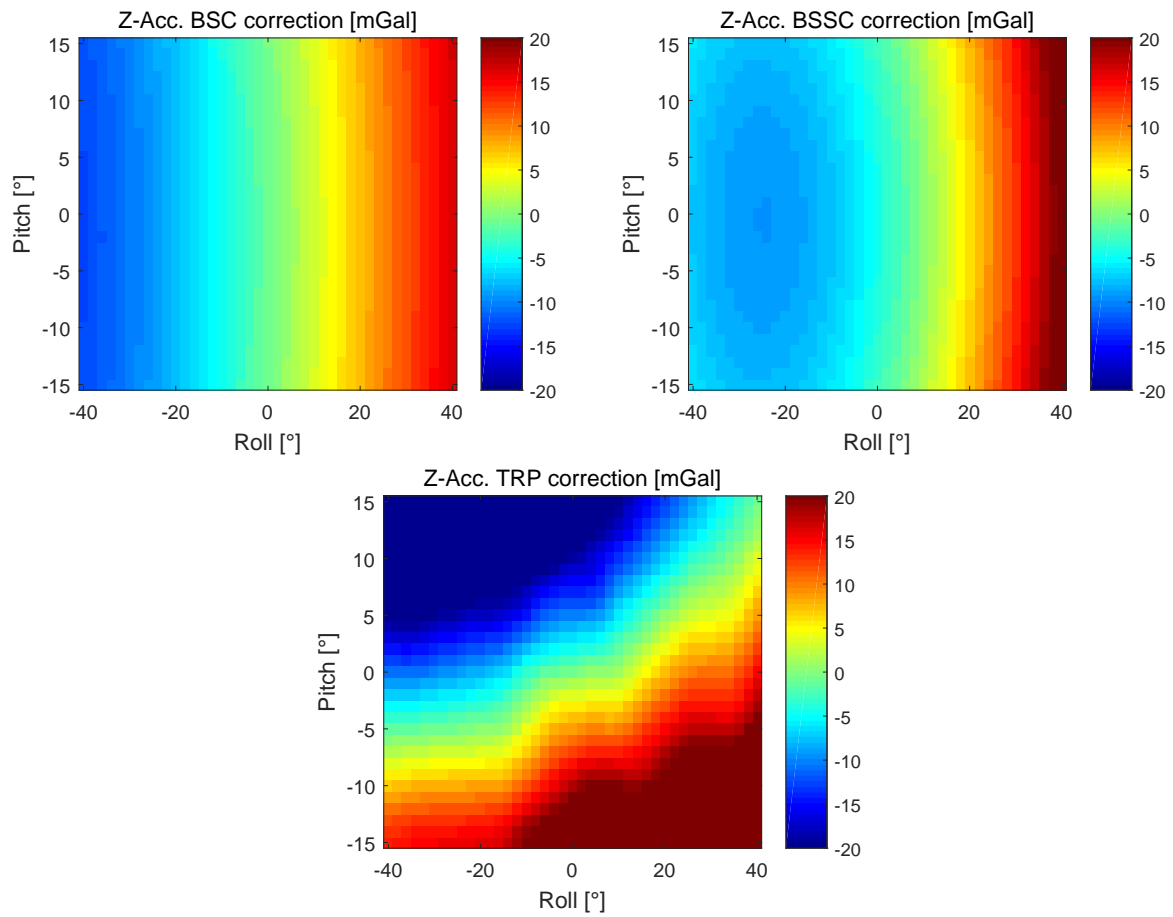


Figure 6.31: Comparison of Z-accelerometer correction, for the BSC, BSSC, and TRP calibration methods, for a constant ISA temperature of 30 °C.

Chapter 7

Quality assessment

As a preparation for Chap. 8, different existing evaluation methods of airborne gravimetry will be briefly introduced and discussed.

The chapter is split into two parts: the internal quality assessment for the determination of the precision of the gravity data, and the comparison against external reference data for the accuracy determination.

7.1 Internal quality assessment

7.1.1 Cross-over residuals

The cross-over point residual analysis is one of the most common quality assessment procedures in airborne gravimetry. It is based on the assumption, that gravity is constant over time for any given earth-fixed point. The vector difference of the individual gravity estimates at an intersection of two flight tracks A and B (a cross-over point) are the basis for this quality measure:

$$\boldsymbol{\chi}'_{A,B} = \hat{\boldsymbol{g}}_A - \hat{\boldsymbol{g}}_B = -\boldsymbol{\chi}'_{B,A}. \quad (7.1)$$

Typically, the North- and East-components of these vector residuals are transformed from units of mGal into arc seconds (Eq. 1.5). The scalar equivalent of Eq. 7.1 is given as

$$\chi'_{A,B} = \hat{g}_A - \hat{g}_B = -\chi'_{B,A}. \quad (7.2)$$

The gravity at a given point is in fact time-varying:

1. Tides depend mainly on the positions of the Moon and the sun with respect to a local coordinate frame. This effect reaches a level of $\pm 150 \mu\text{Gal}$ (*Torge, 1989*), and is therefore usually neglected for airborne gravity at accuracy levels of $> 1 \text{ mGal}$.
2. Seasonal effects, mainly coming from hydrological effects, as different ground-water levels and ocean loading effects, constitute an overall effect of less than $\pm 30 \mu\text{Gal}$ (*Torge, 1989*), and are therefore also neglected. The same holds for deformations of the Earth's crust (Earth tides).
3. The nutation, precession, and drift of the Earth's axis of revolution yields small changes in the centrifugal acceleration (which is by definition included in the gravity). Such effects are even smaller (less than $\pm 10 \mu\text{Gal}$), and are also neglected (*Torge, 1989*).
4. The Earth's atmospheric masses also contribute to the measured gravity. The air pressure, reflecting the local density of the Earth's atmosphere, is also a time-varying quantity. The gravitational effect of such density variations is also smaller than $\pm 10 \mu\text{Gal}$ (*Torge, 1989*).

These time-varying effects are therefore negligible, and the assumption of constant gravity at a given point is valid for the expected accuracy level of airborne gravimetry of 1 mGal or more.

Full bandwidth comparison

An important property of the cross-over point residual analysis is, that the *full spectrum* of the estimated gravity signal is taken into account. In particular, an along-track low-pass filtering of the estimated gravity will yield an *increase* of the cross-over residuals, if more signal than noise is filtered out, and if the two along-track signals are uncorrelated (or only weakly correlated). This effect is for example evident in the results presented in *Glennie and Schwarz* (1999). The requirement of uncorrelated signals is true for orthogonal measurement line intersections, and the correlation can still be assumed to be sufficiently small for the typical intersection angles of $60^\circ - 120^\circ$. This invariance against the parameters of the along-track low-pass filtering of the gravity data allows the use of a *single* value as a meaningful metric.

Note: An along-track low-pass filtering is *generally* applied to airborne gravity data. This is either done explicitly, or implicitly by applying a Kalman Filter (which in fact acts as a low-pass filter). The nature of the used sensors does not allow the gravity determination without applying a low-pass filter. This emphasises, that the invariance against the low-pass filter parameters is a desirable property for a quality metric.

Vertical offset and gravity gradient

Three-dimensional flight trajectories never intersect exactly at the same point: In practice, relevant differences in altitude can be observed. Even for identical *nominal* flight altitudes, vertical offsets of up to $\Delta h = 100$ m can be observed, coming from air-pressure based altitude definitions used for the aircraft navigation system, as it is common for aviation.

Obviously, the free-air gravity gradient of $\partial g/\partial h \approx 309 \mu\text{Gal}/\text{m}$ then yields different gravity values for the two individual flights. However, when comparing gravity *disturbances*, being gravity residuals with respect to the normal gravity field (as introduced in Chap. 3), the majority of this effect will be accounted for by the normal gravity gradient $\partial\gamma/\partial h$. The cross-over residual for the *true* gravity disturbances \mathbf{dg}_A and \mathbf{dg}_B is still non-zero, if the true gravity gradient differs from the normal gravity gradient:

$$\begin{aligned}
\chi_{A,B} &= \mathbf{dg}_A - \mathbf{dg}_B \\
&= \mathbf{g}_A - \gamma_A - \mathbf{g}_B + \gamma_B \\
&\approx \mathbf{g}_A - \gamma_A - \mathbf{g}_A + \left. \frac{\partial \mathbf{g}}{\partial h} \right|_{A,B} \Delta h_{A,B} + \gamma_B \\
&= \mathbf{g}_A - \gamma_A - \mathbf{g}_A + \left. \frac{\partial(\gamma + \mathbf{dg})}{\partial h} \right|_{A,B} \Delta h_{A,B} + \gamma_B \\
&= -\gamma_A + \gamma_B + \left(\left. \frac{\partial \gamma}{\partial h} \right|_{A,B} + \left. \frac{\partial \mathbf{dg}}{\partial h} \right|_{A,B} \right) \Delta h_{A,B} \\
&\approx -\gamma_A + \gamma_A - \left. \frac{\partial \gamma}{\partial h} \right|_{A,B} \Delta h_{A,B} + \left(\left. \frac{\partial \gamma}{\partial h} \right|_{A,B} + \left. \frac{\partial \mathbf{dg}}{\partial h} \right|_{A,B} \right) \Delta h_{A,B} \\
&= \left. \frac{\partial \mathbf{dg}}{\partial h} \right|_{A,B} \Delta h_{A,B},
\end{aligned} \tag{7.3}$$

where $\left. \right|_{A,B}$ denotes mean quantities along the local normal plumb line, between the points A and B .

In practice, the vertical free air gravity gradient disturbance $\partial dg^{\text{Down}}/\partial h$ can reach $\pm 100 \mu\text{Gal}/\text{m}$ and more on the topography, while the horizontal gradients $\partial dg^{\text{North}}/\partial h$ and $\partial dg^{\text{East}}/\partial h$ are significantly smaller (Torge, 1989).

For the aerogravity data sets evaluated in Chap. 8, the impact of the topography on the three diagonal components of the gravity gradient tensor at flight altitude were computed using the software GRAVSOF TC (Tscherning et al., 1992). The Chile campaign data set is used here to provide a exemplary magnitudes: The topography-induced horizontal gravity gradients are in the range of $\pm 30 \mu\text{Gal}/\text{m}$. The respective vertical gradient disturbance ranges from $-80 \mu\text{Gal}/\text{m}$ to $130 \mu\text{Gal}/\text{m}$. (These examples are shown here just to provide an order of magnitude.)

The vertical cross-over offset Δh can reach hundreds of metres or more in practice. Thus, the gravity gradient disturbance indeed yields relevant errors for the cross-over analysis. This problem may be coped by two different strategies:

1. By limiting the vertical offsets Δh to a certain limit Δh_{max} , as e.g. 100 m. Cross-over points with larger vertical offsets will not be used for the quality assessment. In practice, this can significantly reduce the number of available cross-over points, thereby increasing the statistical uncertainty of the method.
2. By estimating the vertical gravity gradient based on a geoid model. Note, that this may introduce uncertainties, depending on the quality of the available geoid model.

In the scope of this thesis, the first strategy will be pursued, due to the lack of sufficiently accurate geoid models for the investigated regions.

Cross-over adjustment

It is a rather common procedure in airborne gravimetry to apply a so-called *cross-over adjustment* (or sometimes *cross-over levelling*, *network adjustment*, or just *adjustment*) to a set of measurement lines. Based on the cross-over points of the whole set, a constant, three-dimensional shift $\boldsymbol{\kappa}$ is computed for each measurement line, such that

- either the sum of squares of the cross-over residuals along a measurement line is minimised (second moments), or
- the mean residual of all cross-over-points along a measurement line becomes zero (first moments).

The results are similar in practice, unless strong outliers are in the data. (Note, that the shifts $\boldsymbol{\kappa}$ are scalar (1-D) when doing scalar gravimetry.)

The *adjusted* cross-over residuals $\bar{\boldsymbol{\chi}}$ are given for an intersection of the i -th cross over point on line A and the j -th cross-over point on line B as

$$\bar{\boldsymbol{\chi}}_{A,B} = (\mathbf{dg}_{A_i} + \boldsymbol{\kappa}_A) - (\mathbf{dg}_{B_j} + \boldsymbol{\kappa}_B). \quad (7.4)$$

The statistics for an adjusted line, or for an adjusted campaign data set, is then commonly computed as the root-mean-square (RMS) of the adjusted cross-over residuals: $\text{RMS}(\bar{\boldsymbol{\chi}}_i)$.

The computation of the line-shifts $\boldsymbol{\kappa}$ can be performed using a least-squares adjustment of the cross-over residuals. The adjusted cross-over residuals $\bar{\boldsymbol{\chi}}$ may then be regarded as a per-line-precision of the gravity data. Comparing $\bar{\boldsymbol{\chi}}$ against $\boldsymbol{\chi}$ (where necessarily $\bar{\boldsymbol{\chi}} \leq \boldsymbol{\chi}$) may provide insight in the characteristics of the gravity estimation errors. Such a comparison can be done separately for each component of the gravity vector estimates, therefore a scalar definition is sufficient here:

$$\tau = \frac{\bar{\boldsymbol{\chi}}}{\boldsymbol{\chi}}, \quad \text{where } 0 \leq \tau \leq 1. \quad (7.5)$$

A small $\tau \approx 0$ indicates a constant offset of the gravity estimates along the entire line, while the gravity determination along the line is very *precise*. Thus, small values of τ can be expected for gravity data with considerable long-term drifts.

In contrast, $\tau \approx 1$ indicates that the majority of errors is coming from short-term effects along the line, while the average line offset is relatively small. Thus, a large τ (close to one) indicates a good long-term stability of the gravity data.

Note in particular, that $\tau = 1$ indicates, that the mean of all cross-overs was already zero before applying the adjustment. It does however not guarantee $\kappa = 0$ for that gravity component of a particular line, because the full network of measurement lines may be shifted to an arbitrary level (thereby indicating that κ_L is not useful as a quality measure).

A closer look at the cross-over adjustment technique is in order here. Assuming a Gaussian distribution of the cross-over residuals, the adjustment may yield a too optimistic quality measure, if the number of cross-over points adjacent to a particular measurement line is small.

As an example, consider a measurement line with only a single cross-over point: The residual after shifting the gravity estimates of that line is *necessarily zero*, being apparently a useless measure for the precision of the gravity data of that line.

As a second example, assume a measurement line with a zero-mean Gaussian error e_{dg} in the scalar gravity estimates: $e_{dg} = \mathcal{N}(\mu = 0, \sigma_0)$. Since the error is zero-mean, the adjustment *should not* affect the quality estimate for that line. The next paragraphs however show, that the empirical determination of $\hat{\sigma}$ with respect to an unconstrained *empirical* average $\hat{\mu}$ (with $\hat{\mu} \neq 0$ in general), *systematically* leads to a too optimistic standard deviation estimate ($\hat{\sigma} < \sigma_0$). This difference between empirical and true standard deviation is in particular shown to be significant when using small sample sets (i.e. small numbers of cross-over points on a measurement line). Fig. 7.1 illustrates this example, assuming only two cross-over points. Note, that a zero-mean error was chosen here for illustration purposes. In fact, any other mean of the true Gaussian error distribution ($\mu \neq 0$) leads to an *equivalent* effect.

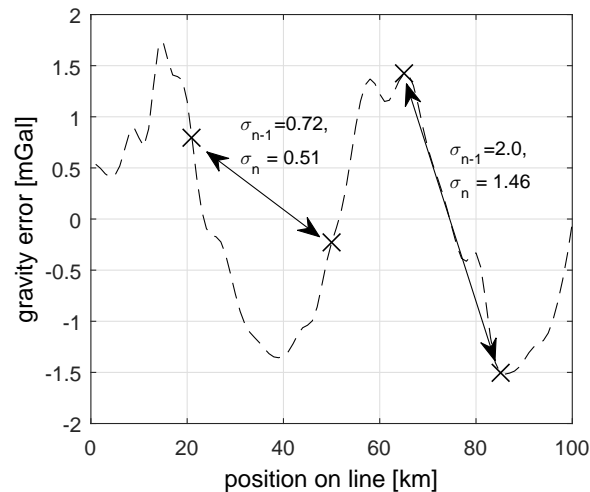


Figure 7.1: Illustration of the empirical estimation of a gravity error standard deviation, based on only two cross-over points. The standard deviation of the true gravity error (dashed line) is $\sigma_0 = 1$ mGal. Two examples are shown: *Left pair*: A too optimistic estimate. The (wrong) line shift $\kappa = -\hat{\mu} \approx -0.3$ will be derived from the two cross-over points (while the *true* mean of the error is $\mu = 0$ mGal). *Right pair*: A too pessimistic estimate. (The empirical standard deviation measures $\hat{\sigma}_{n-1}$ and $\hat{\sigma}_n$ are explained in the text.)

A correction factor will be derived in the following paragraphs, allowing a correction of the empirical standard deviation $\hat{\sigma}$, thereby enabling adjusted cross-over statistics which are independent of the number of cross-over points.

It should be noted, that the (arbitrary) positions of the cross-over points may also lead to too *pessimistic* results for some particular cases ($\hat{\sigma} > \sigma_0$), see Fig. 7.1. However, the too optimistic estimates are dominant in a statistical sense, as will be shown by simulations.

Assume a vector of samples \mathbf{x} , drawn from a one-dimensional normal distribution

$$\mathbf{x} \sim \mathcal{N}(0, \sigma_0), \quad (7.6)$$

where the number of samples is $N = |\mathbf{x}| \geq 2$. There are two common definitions for the computation of the empirical standard deviation $\hat{\sigma}$ of a normal distribution from a vector of samples:

$$\hat{\mu} = \frac{1}{N} \sum_{i=1}^N x_i, \quad (7.7)$$

$$\hat{\sigma}_n^2 = \frac{1}{n} \sum_{i=1}^N (x_i - \hat{\mu})^2, \quad \text{and} \quad (7.8)$$

$$\hat{\sigma}_{n-1}^2 = \frac{1}{n-1} \sum_{i=1}^N (x_i - \hat{\mu})^2. \quad (7.9)$$

Note, that the empirical mean $\hat{\mu}$ differs in general from the mean of the true distribution (here: 0). A simulation of the repeated drawing of N samples from the normal distribution $\mathcal{N}(0, 1)$ clearly shows, that both definitions systematically yield too small standard deviations compared to the true standard deviation σ_0 , with

$$\hat{\sigma}_n < \hat{\sigma}_{n-1} < \sigma_0. \quad (7.10)$$

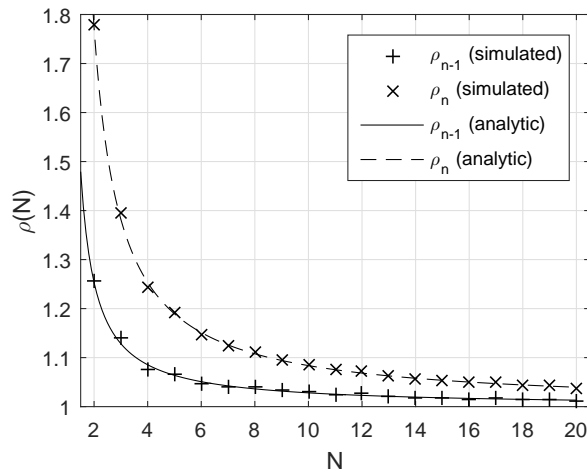


Figure 7.2: Correction factors ρ for the empirical determination of the standard deviation of a normal distribution, based on small sets of N drawn samples.

The fractions

$$\rho_n = \sigma_0 / \hat{\sigma}_n \quad \text{and} \quad \rho_{n-1} = \sigma_0 / \hat{\sigma}_{n-1} \quad (7.11)$$

are introduced here as correction factors, to get a more realistic estimate $\hat{\sigma}_0$ of the true standard deviation σ_0 :

$$\hat{\sigma}_0 = \hat{\sigma}_n \cdot \rho_n = \hat{\sigma}_{n-1} \cdot \rho_{n-1}. \quad (7.12)$$

The simulation results are shown in Fig. 7.2. 10,000 repetitions were carried out for each N in order to get accurate simulation results. It is just noted here, that these correction factors

N	$\rho_{n-1}(N)$	$\rho_n(N)$
2	1.25	1.77
3	1.13	1.38
4	1.09	1.25
5	1.06	1.19
6	1.05	1.15
8	1.04	1.11
10	1.03	1.08
15	1.02	1.05
20	1.01	1.04
50	1.01	1.02
100	1.00	1.01

Table 7.1: Correction factors ρ for a selection of sample set sizes N .

may also be expressed as analytic functions of N (also shown in Fig. 7.2):

$$\rho_{n-1}(N) = \sqrt{\frac{N-1}{2} \frac{\Gamma(\frac{N-1}{2})}{\Gamma(\frac{N}{2})}}, \quad (7.13)$$

$$\rho_n(N) = \sqrt{\frac{N}{2} \frac{\Gamma(\frac{N-1}{2})}{\Gamma(\frac{N}{2})}}, \quad (7.14)$$

where Γ denotes the Gamma-function. Tab. 7.1 shows correction factors $\rho(N)$ computed with Eqs. 7.13 and 7.14.

These correction factors $\rho(N)$ will be applied to the adjusted cross-over residuals for each line, where N is the number of cross-over points adjacent to that line. Statistics may then be computed based on these corrected residuals, e.g. to get combined cross-over statistics for a larger set of lines (typically RMS values are computed, as shown above).

Aggregated cross-over statistics

It is important to note, that neither $\hat{\sigma}_0$, nor $\hat{\sigma}_n$, nor $\hat{\sigma}_{n-1}$ provide reliable quality estimates for the gravity estimates of a particular line with a small number of adjacent cross-over points, N . Only when looking at larger sets of cross-over residuals (potentially on different lines), aggregated statistics, as standard deviation or RMS of the full set of *corrected* cross-over residuals $\bar{\chi}^\rho$ can be expected to provide meaningful quality estimates when performing a network adjustment.

If a network adjustment is *not* applied, the aggregated statistics are based on the original cross-over residuals χ . In this case, also lines with only a single adjacent cross-over point may be included in the aggregated statistics. No correction factors (ρ) are required in this case.

In both cases, the cross-over analysis is based on the comparison of two stochastic quantities (because the gravity estimates of both intersecting lines are both stochastic). It is a common first-order assumption, that these two stochastic quantities have an equal uncertainty, if sensors of similar grades have been used for the two lines (or, in particular, if the *same* sensor has been used). The difference of two normal distributions with the same standard deviation σ has a standard deviation of $\sqrt{2}\sigma$. Thus, a normalisation factor of $1/\sqrt{2}$ may be applied to the cross-over residuals. If this factor is applied to an RMS value of a set of residuals, the estimated error of the individual lines is denoted as *RMS-error* (RMSE):

$$\text{RMSE} = \frac{\text{RMS}}{\sqrt{2}}. \quad (7.15)$$

The RMSE measure is commonly used in the literature (*Becker et al.*, 2015b; *Bruton*, 2002; *Glennie et al.*, 2000; *Glennie and Schwarz*, 1999).

7.1.2 Repeated lines or line segments

The concept of repeated lines is very similar to that of cross-over point residuals. Two measurement lines or line segments have the same (nominal) ground track. For a difference of flight altitudes Δh , the findings of the previous section hold equivalently. For repeated line segments at different heights, the gravity signal of the higher segment shows in general a smoother gravity signal, because of the attenuation of the true gravity signal with increasing height (*Torge*, 1989).

In addition to altitude differences, *horizontal* offsets between the two lines may affect the comparison. In practice it is advisable to limit the maximum horizontal distance for this analysis. As mentioned above, the horizontal gravity gradient can be as high as $\pm 40 \mu\text{Gal/m}$ at flight altitude (for high-mountain topography).

Obviously, the two gravity signals are highly correlated (for identical flight trajectories, the correlation is maximal, i.e. 100%). This implies, that a lower cut-off frequency for the along-track low-pass filtering yields in general a *better* agreement between the two signals. This property can again be recognised in the results shown in *Glennie and Schwarz* (1999). In the extreme case, only the average of the two data sets is being compared. If in addition an adjustment is performed, the residual is necessarily zero.

The important conclusion is, that repeated line residuals are only a valid metric for comparisons among different campaigns, sensors, or algorithms, if exactly the same filtering was applied to the different data sets. Thus, a single-value comparison as for the cross-over residual analysis is not sufficient in this case; The characteristics of the low-pass filtering always have to be taken into account.

In practice, repeated lines have a lower relevance compared to cross-over lines for production-oriented campaigns. A repeated line only allows the quality assessment for a single line, while a set of several cross-over lines can allow quality estimates for a whole network of lines, and thereby also enable the discovery of outliers. A regular repetition of all of the measurement lines is too costly in practice for production-oriented airborne gravimetry.

The aerogravity data sets of Chap. 8 contain several shorter repeated line segments. The repetition of these segments was mainly motivated by an unsatisfying initial measurement, which needed to be redone (e.g. if strong turbulence disturbed the measurements).

Again, a factor of $1/\sqrt{2}$ may be applied to the RMS of the two lines to get an individual accuracy estimate (RMSE), if the assumption of equal individual gravity accuracies for both lines is justified.

7.1.3 Error of closure

For an aerogravity flight, usually a tied gravity value determined by terrestrial gravimetry is known for the aircraft parking positions of both the origin and the destination airports. In many cases, both airports (and the parking positions) are identical, hence the term *error of closure*.

During the initial alignment phase, standing on the initial parking position \mathbf{r}_O , the filter is initialised using a terrestrial gravity value:

$$d\hat{\mathbf{g}}_{\mathbf{r}_O} = d\mathbf{g}_{\mathbf{r}_O} = \mathbf{g}_{\mathbf{r}_O} - \gamma_{\mathbf{r}_O}. \quad (7.16)$$

After the flight, the estimated gravity value $d\hat{\mathbf{g}}_{\mathbf{r}_F}$ at the final parking position \mathbf{r}_F is compared against the known ground-truth gravity value $d\mathbf{g}_{\mathbf{r}_F}$, yielding the error of closure \mathbf{e} :

$$\mathbf{e}_{OF} = d\hat{\mathbf{g}}_{\mathbf{r}_F} - d\mathbf{g}_{\mathbf{r}_F}. \quad (7.17)$$

If only *scalar* ground truth gravity values are known, the above equation can only be evaluated for the scalar gravity estimates (or the vertical component).

The gravity error of closure is a useful measure for determining the average long-term drift of the estimated gravity values. For the analysis, the ground-truth reference is commonly assumed to be error-free, typically having an accuracy of $100 \mu\text{Gal}$ or better for the vertical channel (scalar gravity).

As for the cross-over points, the redundant knowledge of the gravity value at the final parking position (ground-truth versus IMU estimate) may not only be used for deriving a quality measure. It can also be exploited for improving the gravity estimates, by assuming a linear drift of the gravity estimates. Such a linear drift interpolation is a common method in terrestrial gravimetry. Although the drift may be highly non-linear, the linear interpolation is usually the best justified guess. It will be shown in Chap. 8, that this linear drift interpolation significantly helps to increase the overall accuracy of the gravity estimates. As shown in Chap. 3, the known ground-truth gravity values can be introduced as measurements to the EKF.

7.2 Comparisons against external reference data

For a production-oriented aerogravity campaign, dense terrestrial reference gravity data is usually not available, as the campaigns naturally take place in areas with sparse gravity data coverage. Still, several methods are introduced here, utilising global Earth gravity models or topography data, which are available today at an almost global coverage.

7.2.1 Inter-system comparison

For the data sets shown in Chap. 8, the navigation-grade iMAR RQH-1003 IMU was flown side-by-side with the two-axis stabilised-platform LaCoste & Romberg S-type spring gravimeter. Comparisons will be shown for some of the flights. From cross-over analyses it is known, that the individual sensor results are of similar quality, thus data sets can not be used as a mutual reference. Still, the degree of agreement between both sensors can be used as a quality measure, assuming that both sensors' gravity estimate errors are uncorrelated (which is in general a justified assumption). If the assumption of equivalent sensor accuracies is justified, the gravity differences may again be divided by $\sqrt{2}$ in order to obtain an estimate for the individual sensor accuracy.

7.2.2 Global Earth gravity models

Since the implementation of satellite-based gravimetry, gravity models with almost global coverage are available to the public. The used satellites are low-Earth-orbit (LEO) satellites, with altitudes of several hundreds of kilometres. Tab. 7.2 summarises the characteristics of the three satellite gravimetry missions that were implemented so far: CHAMP, GRACE, and GOCE. For details on these satellite gravity missions, the reader is referred to *Torge and Müller (2012)*. Due to the attenuation of the gravity field at high altitudes, these satellite missions are limited to a relatively low spatial resolution.

Several combined global gravity models (GGM) are published in the literature, augmenting satellite gravity data with local gravity data, as terrestrial, airborne, or shipborne data. Such models contain coefficients up to degree and order 2190 ($\lambda/2 \approx 9 \text{ km}$). One of the most famous combined models is the Earth Gravity Model (EGM) 2008, see *Pavlis et al. (2008)*. It is however important to note, that the use of the higher order coefficients is only justified in regions with an equivalently dense data basis.

¹based on the availability of gravity models published in the ICGEM data base (*Barthelmes and Förste, 2011*)

	CHAMP	GRACE	GOCE
in-orbit operation	2000-2010	2002-	2009-2013
altitude	≈ 450 km	450 km to 500 km	≈ 280 km
up to degree and order ¹	120	200	280
equivalent resolution $\lambda/2$	140 km	100 km	70 km
accuracy (for degree)		$3 \mu\text{Gal}$ (180)	$3 \mu\text{Gal}$ (224)

Table 7.2: Main characteristics of satellite gravimetry missions (*Torge and Müller, 2012*).

For the comparisons carried out in Chap. 8, the satellite-only GGM05C model is being used (*Ries et al., 2016*), because no or only sparse ground data was available for the investigated regions, i.e. the use of combined GGMs up to high degree and order is not justified here.

The limited resolution of the satellite-based GGM's (Tab. 7.2) infers a use of this data as a long-term / large-scale reference for the airborne gravity data. The satellite-based GGM data is commonly used for comparisons against strapdown airborne gravity data in the following ways:

1. An along-track comparison of low-pass filtered airborne gravity estimates and GGM gravity disturbances evaluated at flight altitude (*Deurloo, 2011; Deurloo et al., 2015; Ayres-Sampaio et al., 2015*). Due to the half-wavelength resolution of >70 km, such a comparison is only reasonable for sufficiently long measurement lines: The low-pass filter requires at least a half wave-length to 'swing in' at the beginning and the end of a line, thereby shortening the flight line by 140 km or more for the comparison.
2. The bias determination (airborne gravity versus GGM) for larger sets of airborne gravity data, based on equidistant grids (details are provided in the next section).

Note: The degree and order specifications shown in Tab. 7.2 have to be regarded as an upper bound. It is a-priori not exactly determined, up to which degree the satellite data contains significant gravity information, where significant means, that the contribution of a certain degree is larger than its actual noise level. Several authors publish models with lower maximum degree, claiming that the higher degrees do not contain significant contributions, cf. the published models listed in the ICGEM data base of global Earth models (*Barthelmes and Förste, 2011*).

Bias determination based on a grid

For a grid-based bias determination of airborne gravity data with respect to a global gravity model, it is important to use an (almost) equidistant regular grid in order to avoid biases towards regions with a denser airborne data coverage (e.g., typically more lines are available close to the airports). For this, a *quasi*-regular grid is used in the scope of this thesis. Such a grid can be generated as follows:

1. All flight line coordinates, e.g. available at 1 Hz taken from GNSS, are transformed into UTM coordinates, with a common prime meridian (average longitude of the data set).
2. An (exact) regular UTM grid, e.g. using a 20 km grid spacing, is extended over the whole region.
3. Those grid points, for which the distance to the closest airborne gravity point is larger than the half grid spacing (e.g. >10 km), are removed from the set.
4. Each remaining regular grid point is replaced by the closest airborne gravity data point.

The term *quasi-regular* is used here to indicate, that the resulting grid is of course not perfectly equidistant (examples are depicted in Chap. 8). The advantage of this method is, that the comparison against the global model can be done without performing a up- or downward continuation, and without the requirement of a spatial interpolation of the airborne gravity data.

Since high-resolution airborne gravity (half-wavelength resolution of 3 km to 5 km) is being compared to satellite-based gravity (resolutions of 100 km and more), the comparison only yields useful results in general, if a larger region is used for the comparison. For smaller regions, effects arising from the low resolution of the reference GGM data can significantly propagate into the comparison. The reference data points are then biased with respect to the true gravity signal, and a reasonable comparison is not possible. In contrast, for a large area of coverage (multiple wavelengths of the reference data set in both latitudinal and longitudinal directions), such effects are expected to level out on average.

For the real-data examples analysed in Chap. 8, the GGM data is only used for the grid-based bias determination. The *overall* accuracy of the gravity estimates of a data set can then be estimated by the combination of the *absolute* bias of a data set (from comparison against GGM), and the *relative* precision of the system (determined e.g. from cross-over residuals).

7.2.3 Topographic gravity effect

While global gravity models can be used as a reference for the longer wavelength components of the estimated airborne gravity data, the topographic effect can be used as a quasi-reference for the short wavelength components. Such a comparison is based on the assumption, that the majority of the short-wavelength contributions to the gravity field comes from the topography. Therefore, such comparisons are only viable for mountainous regions, or regions with rugged terrain; In flat terrain regions, sub-surface density changes may equally, or even stronger contribute to the gravity signal over the whole frequency spectrum, compared to the topographic effect.

For the comparisons shown in Chap. 8, the topographic effect is computed using the software GRAVSOFTE TC (*Tscherning et al.*, 1992). The computation is based on gridded terrain data, taken from the SRTMPlus 15 data set (*Becker et al.*, 2009), assuming a standard topography density of 2.67 g/cm^3 . The SRTMPlus 15 data set includes bathymetry data. The mass of the ocean water is accounted for assuming a density of 1.025 kg/dm^3 .

For each discrete point \mathbf{r} on the flight trajectory, the topographic effect is computed as a sum of gravity contributions of rectangular prisms within a radius of 100 km around \mathbf{r} . For reasons of computational efficiency, the surrounding area is split into two zones: within a radius of 40 km, high resolution terrain information is processed, while in the outer zone (between 40 km and 100 km), a coarse terrain grid appears sufficient for the computation of the individual prism contributions (the contributions to the total gravity reduce with the square of the distance). Also, approximations are introduced for distant prisms (e.g. assuming a point mass) to save computation time. More details on such prism-based computations of the topographic effect can be found in *Forsberg* (1984); *Heck and Seitz* (2007).

7.2.4 Ground control points

Ground control points may serve as a reference for airborne gravity data. For a sufficiently dense set of terrestrial gravity points, a combination of grid-interpolation and upward continuation may be performed to get reference data at flight altitude.

In the scope of this thesis, such a reference could not be computed due to the lack of dense terrestrial gravity data in the relevant regions (see Chap. 8). The approach is mentioned here for the sake of completeness.

7.3 A Turbulence Metric

Turbulence is a limiting factor for production-oriented airborne gravimetry in general. In particular the classical spring-gravimeters tend to have larger sensor errors during dynamic motion of the aircraft, which can be caused by turbulence and also the corresponding manoeuvres of the pilot or auto pilot to maintain a certain altitude, velocity, and course over ground. The predominant causes for turbulence are abrupt changes of the vector of wind speeds, and air pressure.

In order to analyse the impact of turbulence, a measure of turbulence needs to be defined. It is desirable to quantify turbulence apart from subjective categories, as 'weak' or 'strong', in order to unify the findings and deductions among different airborne gravity campaigns and authors.

Two common metrics are being in use for both commercial and military aviation:

1. The Eddy Dissipation Rate (EDR) is an *aircraft-independent* measure for the atmospheric turbulence state. It is based on 'the steady-state rate at which energy is being put into the system in much larger eddies and removed by viscous effects related to small eddies' (*MacCready, 1962*). It is therefore a solely weather-dependent measure.
2. Larger aircraft have a tendency to show less reaction to the same weather situation (having a given EDR) compared to smaller aircraft. The so-called *RMS-g* value is defined as the standard deviation of the vertical aircraft accelerations. It is therefore a measure of the actual reactions of an aircraft to atmospheric turbulence.

Aircraft accelerations coming from steered flight manoeuvres are also included in this value. The term *RMS-g* appears misleading, since actually the standard deviation (not the RMS) is computed. The difference is however small, if the average vertical acceleration is close to zero, as it is typically the case if the aircraft moves at constant (nominal) altitude.

There exist aircraft-dependent models, which allow the computation of *expected* RMS-g values for a given EDR. In aviation, such models are of practical relevance for the risk assessment: For a given EDR value, a large commercial jet may face relatively small RMS-g values compared to a small aircraft, for which the same atmospheric state can cause severe aerodynamic instabilities.

For airborne gravimetry, the actual RMS-g value can easily be computed based on GNSS velocities, or based on the high-rate strapdown IMU navigation solution (if available). For both approaches, the acceleration can be approximated by numerical differentiation of the vertical velocity components. It is known from experience, that relevant turbulence reactions can have periods of less than one second, thus a GNSS velocity data rate of at least 10 Hz is suggested. The standard deviations are computed using a sliding window of a predefined width.

As an example, RMS-g values are computed for an aerogravity flight (flight id 298) carried out in Chile in October 2013 (Fig. 7.3, cf. Sect. 8.1). The following RMS-g values are being compared:

1. using velocity values from two-frequency PPP at 10 Hz data rate, and
2. using velocity estimates from the strapdown navigation solution, at 300 Hz data rate. The strapdown inertial data was acquired with the iMAR RQH-1003 system introduced in Sect. 6.1.

Fig. 7.4 shows the computed RMS-g values. Both curves look similar, indicating that both data bases (PPP only at 10 Hz and IMU/PPP integrated data at 300 Hz) are suitable for the determination of the RMS-g value.

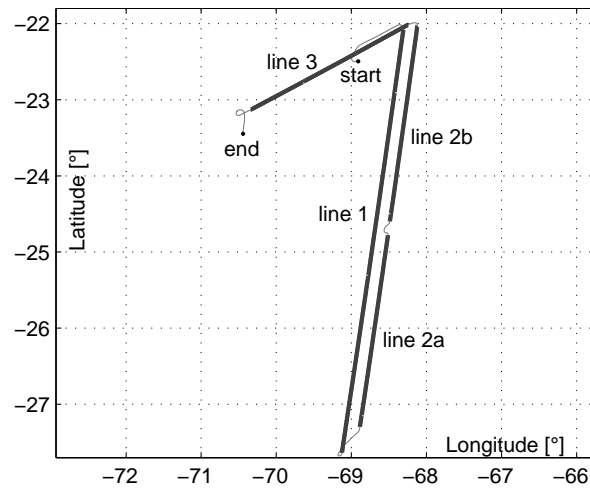


Figure 7.3: Aerogravity flight in northern Chile (DoY 298), used as an example for the computation of RMS-g values. Approximate flight altitudes are 7400 m for line 1, 7750 m for lines 2a and 2b, and 7100 m for line 3.

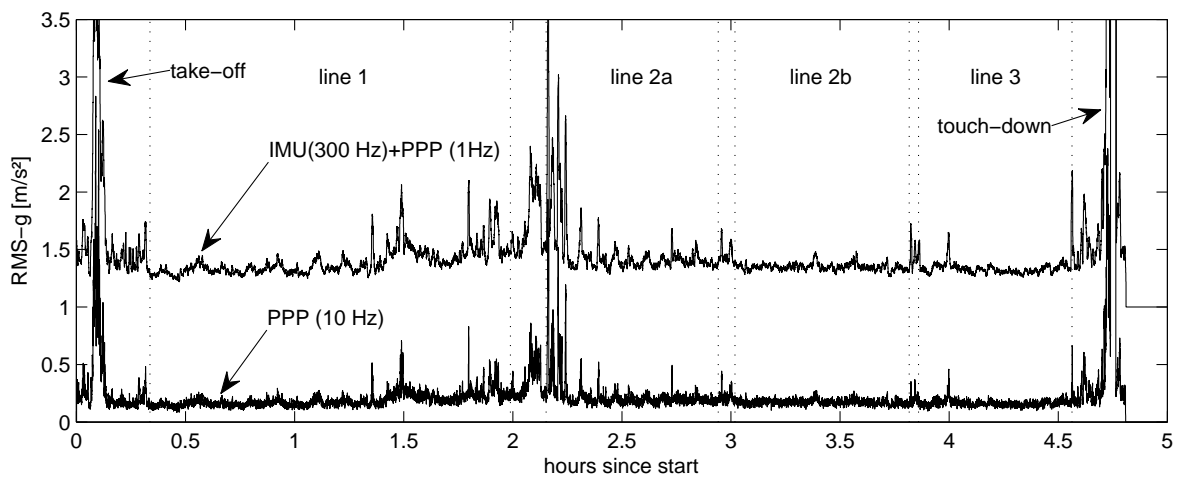


Figure 7.4: Comparison of RMS-g values. The values computed from the integrated IMU/PPP solution are shifted by +1 for clarity. A window size of 5 s was used for the computations. Apart from the take-off, landing, and turn phases, turbulence can be recognised in the beginning of line 2a, and in the end of line 1. The PPP-derived RMS-g values show a slightly higher noise.

For the aerogravity data sets presented in Chap. 8, only high-rate accelerations from the IMU/PPP integration are being used, because only 1 Hz or 2 Hz GNSS data is available for most of the flights.

Chapter 8

Results

Note: Some of the results presented in this chapter have already been published by the author (*Becker et al.*, 2015b, 2016).

For the evaluation of the investigated calibration methods, strapdown IMU and GNSS data sets are available for five different aerogravity campaigns, carried out between October 2013 and January 2016. The main characteristics of these data sets are shown in Tab. 8.1.

Each of the available data sets is evaluated for six different calibration methods (C_1 – C_6), which are listed in Tab 8.2. In addition, the uncalibrated data sets are also evaluated for comparison (C_0).

All campaign data sets were collected with the same navigation-grade strapdown IMU, an iMAR RQH-1003. The same system was used for the calibrations shown in Chap. 6. Fig. 8.1 shows a time line, including all campaigns and calibrations evaluated in this chapter. It can be seen, that some of the calibrations have a considerable temporal distance to the investigated aerogravity campaigns (up to 2.5 years). Due to the limited access to the device and also to professional calibration facilities, the calibrations could not be repeated.

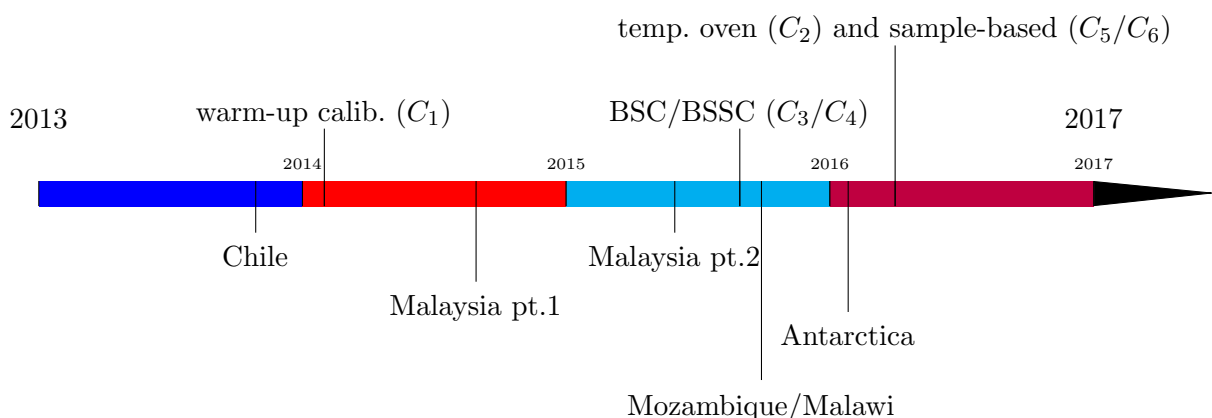


Figure 8.1: Temporal overview of all calibrations (above time bar) and aerogravity campaigns (below time bar), which are evaluated in the scope of this thesis.

	Chile	Malaysia		Mozambique and Malawi	Antarctica
		pt. 1	pt. 2		
data acquisition period	Oct. 2013	Aug. 2014	May/June 2015	Oct. 2015	Dec. 2015 / Jan. 2016
aircraft model	KingAir BeechCraft 350i	KingAir BeechCraft 350		Cessna 208 'Caravan'	DHC-6 'Twin Otter'
auto pilot?	yes	yes	yes	yes	no
number of flights	19	12	34	21	32
number of measurement lines >10 min	81	48	146	131	121
total airborne duration [h:mm]	91:25	41:26	111:15	101:08	142:06
total airborne distance [km]	33,959	12,986	34,715	27,285	32,391
total distance on lines [km]	25,730	9,666	23,586	20,553	27,948
Characteristics ($\mu/\sigma/\text{min.}/\text{max.}$)					
velocity on lines [m/s]	101/7.6/82/155	87.6/3.7/75/112	87.4/2.1/80/120	75.7/4.5/60/88	63.7/5.4/41/79
flight altitude on lines [km]	5.8/1.2/3.8/8.4	1.9/0.3/1.0/4.2	2.0/0.24/1.9/4.9	3.3/0.53/2.4/4.7	2.9/0.46/1.5/4.3
terrain altitude on lines [km]	1.6/1.6/-3.2/6.1	-1.3/1.0/-3.1/0.21	-0.7/0.9/-3.1/0.4	0.7/0.4/0.0/2.5	-
terrain clearance on lines [km]	4.2/1.1/0.92/10.0	3.2/1.1/1.0/6.9	2.8/0.96/1.6/5.7	2.5/0.57/0.6/4.1	-
RMS-g [mm/s ²]	69/79/12/1006	76/68/14/1160	65/49/12/924	95/95/10/1100	121/68/21/642
GGM05C gravity disturbance [mGal]	69/51/-99/221	28/31/-44/89	36/30/-44/121	-20/36/-118/105	-25/28/-103/62
GGM05C geoid height N [m]	31/7.9/14/46	37/5.7/25/47	41/9.9/21/60	-12.4/3.1/-26/-7	-24/6.9/-38/-4
Number of cross-over points					
$\Delta h < 50$ m	15	101	268	43	28
$\Delta h < 100$ m	15	101	282	43	42
$\Delta h < 350$ m	31	101	282	122	67
$\Delta h < 700$ m	47	101	314	172	87
$\Delta h < 1050$ m	57	129	314	201	97
total	102	133	317	229	99
Repeated line segments >5 min					
number of segments ($\Delta h < 700$ m)	3	12	13	7	2
total distance [km]	757	722	713	395	57

Table 8.1: Overview of the available strapdown aerogravity data sets used for the evaluation. For 5 out of the total of 123 flights, the strapdown data could not be processed due to large data gaps or other severe problems with the IMU or GNSS data acquisition. These flights are not included in the statistics. Details on the particular measurement lines are shown in Appendix A.

Code	Description
C_0	no calibration applied.
C_1	warm-up calibration of the Z-accelerometer (Sect. 6.4.1).
C_2	temperature oven calibration of the Z-accelerometer (Sect. 6.4.2).
C_3	thermal BSC calibration (Sect. 6.5.1).
C_4	thermal BSSC calibration (Sect. 6.5.2).
C_5	sample-based TRP calibration (unfiltered; Sect. 6.6.1).
C_6	sample-based TRP calibration (with Gaussian filter applied; Sect. 6.6.1).

Table 8.2: Summary of the different accelerometer calibration methods introduced in the scope of this thesis. The respective corrections will be applied to the real-data sets. The codes C_0 – C_6 will be used throughout this chapter.

For each of the campaigns except for the Antarctica data set, the effect of global gravity model (GGM) reductions is analysed (cf. Sect. 3.5), and a bias between the airborne gravity estimates is computed based on gridded GGM data (Sect. 7.2.2).

High-frequency terrain information is used for all except for the Antarctica data set, taken from the SRTM15plus data set (*Becker et al.*, 2009). For the Antarctica data set, no reliable high-frequency terrain information is available. The terrain-induced gravity effects will be used for the evaluation in two different ways:

1. It will be introduced as a reduction to the specific force observations (Sect. 3.5), *or*
2. it is used as a short-wavelength quasi-reference to assess the high-resolution quality of the data (cf. Sect. 7.2.3).

Different combinations of GGM and terrain reductions yield a total of four different combinations, which are listed in Tab. 8.3.

Code	Type of gravity reduction
R_0	no reductions applied.
R_1	GGM gravity reductions, using the GGM05C gravity model up to degree and order 360 (<i>Ries et al.</i> , 2016), evaluated at flight altitude.
R_2	Full-spectrum isostatic terrain reductions, using the SRTM15plus data set with 15 arc seconds terrain resolution (<i>Becker et al.</i> , 2009). The topography and bathymetry effects are computed using the software GRAVSOF TC (<i>Tscherning et al.</i> , 1992).
R_3	A combination of R_1 , and short wavelength terrain effects. The latter are computed for a residual terrain model (RTM), by subtracting long-wavelength terrain information of 1° full-wavelength spatial resolution from the full terrain model (resolution: 15 arc seconds). This RTM method is used in order to avoid a signal overlap of the two applied reductions, cf. Sect. 3.5.

Table 8.3: Summary of the different gravity reduction types. The codes R_0 – R_3 will be used throughout this chapter.

The default set of parameters used for the extended Kalman filter as introduced in Chap. 3 is shown in Tab. 8.4. Unless stated differently, these settings are being used for the strapdown airborne gravity processing of the data sets presented in this chapter.

For each of the data sets, PPP solutions (*Kouba and Héroux*, 2001) were computed using the commercial software Waypoint GrafNav (*Novatel Inc.*, 2014), at a data rate of 1 Hz. For some of the data sets, GNSS raw data was available at a higher data rate. However, using such higher-rate PPP solutions, as 2 Hz or 5 Hz, did not yield any significant improvements

Symbol	Parameter description	Default setting
$\sigma_{0,r}$	Initial position uncertainty	2 cm
$\sigma_{0,v}$	Initial velocity uncertainty	10 cm/s
$\sigma_{0,\psi}$	Initial roll/pitch uncertainty	1°
	Initial heading uncertainty	5°
σ_{0,b_a}	Initial accelerometer bias uncertainty	30 mGal
σ_{0,b_ω}	Initial gyroscope bias uncertainty	0.001 °/h
q_r	Position system noise	0
q_v	Velocity system noise	0.05 mm/ $\sqrt{s^3}$
q_ψ	Attitude system noise	0.2"/ \sqrt{s}
q_{b_a}	Accelerometer bias system noise	0.01 mGal/ \sqrt{s}
q_{b_ω}	Gyroscope system noise	0
$\sigma_{0,dg}$	Initial gravity disturbance uncertainty	0.03 mGal
β_{dg}^{3rd}	3rd order Gauss-Markov correlation parameter	1/20 km ⁻¹
σ_{dg}	Gravity disturbance standard deviation	100 mGal
$\sigma_{z_{dg}}$	Terrestrial scalar gravity observation accuracy	0.03 mGal

Table 8.4: EKF settings used for the processing of the strapdown gravity data sets presented in this chapter.

of the results. Thus, 1 Hz solutions were chosen for computational efficiency. For the results shown in this chapter, only PPP *coordinates* were introduced as observations to the EKF.

The real-data processing results revealed a reproducible, heading-dependent bias shift of the vertical gravity estimates (maximum: 3 mGal), depending on the latitude φ . This error was compensated using the empirically derived correction $-0.038 \text{ mGal s/m} \cdot v^{\text{North}} \cos^2(\varphi)$. The reason for this effect is unclear, and subject to further research. The effect showed up independently of the used gravity reduction method, and independently of the used accelerometer calibration method. Note, that no such bias was observed for the simulations shown in Chap. 5. Possible explanations are

- a yet unknown, systematic instrument error, propagating into the gravity estimates via the Coriolis acceleration, or
- a systematic computation error in the navigation update, e.g. arising from an approximation, which is not justified for measurements at this accuracy level.

A note on nomenclature: The aerogravity flights are denoted using the day of the year on which they were carried out. Multiple flights on the same day are numbered using small Latin letters, e.g. 140a (first flight on day of the year 140), and 140b (second flight on the same day).

8.1 Chile (2013)

The Chile aerogravity campaign was carried out in October 2013, see Fig. 8.2. The KingAir BeechCraft 350i aircraft was equipped with

- the iMAR RQH-1003 strapdown IMU system, that was introduced in Chap. 6, connected to an external GNSS antenna for the time-stamping,
- the LaCoste & Romberg S-99 sea/air gravimeter (LCR), owned by the University of Bergen, Norway,

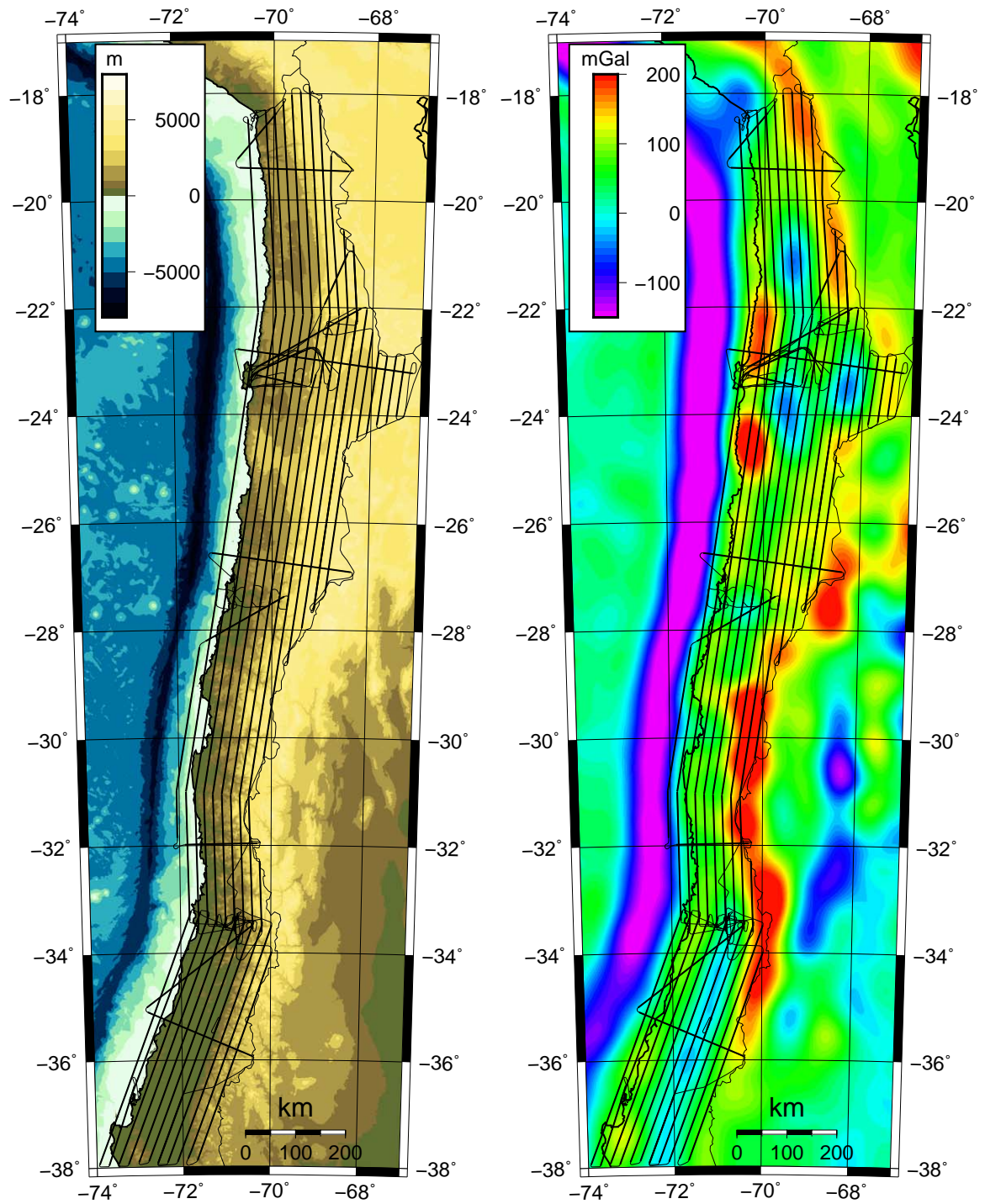


Figure 8.2: Overview of the Chile aerogravity campaign. The measurement lines are highlighted (bold lines), all other parts of the flights are shown as thin lines. Left: Topography / bathymetry. Right: Gravity anomalies of the GGM05C global gravity model (*Ries et al., 2016*), computed up to its maximum degree of 360.

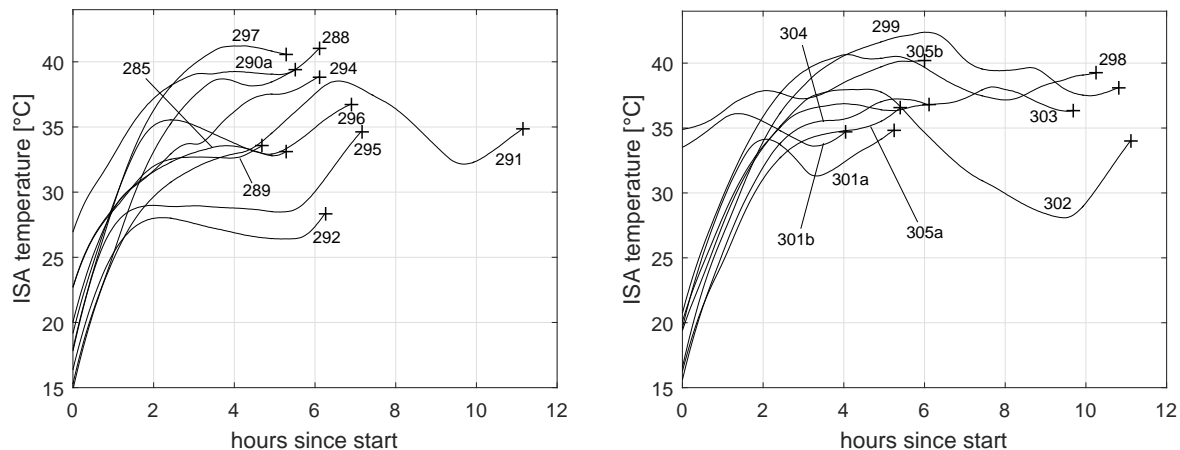


Figure 8.3: Sensor temperatures for the Chile campaign. *Left:* Flights 285 to 297; *Right:* Flights 298 to 305b.

- two Javad Delta-3 GNSS receivers (for redundancy reasons), collecting two-frequency phases and pseudo-ranges from GPS and GLONASS at a rate of 1 Hz. Both receivers share a single Novatel GNSS Antenna, type ANT-A72GA-TW-N, using an active GNSS signal splitter.

The campaign was production-oriented, leading to the practical requirement of an aircraft velocity of ≈ 100 m/s. This velocity is relatively high compared to similar airborne gravimetry campaigns documented in the literature. It has an immediate impact on the maximum resolution: For the typical low-pass filter frequency of 100 s to 150 s, the half wavelength resolution would be 5 km to 7.5 km, which is relatively large compared to the flight altitudes above topography in this campaign. Most flight segments were done above rugged high-mountain terrain, up to 6100 m above sea level.

The Chile 2013 data set consists of 19 flights. Some of these flights contain an intermediate stop for fuelling the aircraft. Those flights, for which no terrestrial gravity tie was available for the intermediate stop, are processed as *single* flights, in order to enable the determination of the error of closure, and in order to enable the removal of a linear drift of the gravity estimates (cf. Sect. 7.1.3). These flights are 291, 298, 299, 302, and 303. In contrast, the flights 301 and 305 both had a fuelling stop on an airport *with* available terrestrial gravity tie. Therefore these flights were split into two flights each (301a, 301b, 305a, 305b). Detailed information on the individual flights and measurement lines is provided in Appendix A.2.

8.1.1 Cross-over analysis

As shown in Tab. 8.1, the Chile data set contains only relatively few cross-over points. Some of the measurement lines do not contain a single cross-over point with a height difference of $\Delta h < 100$ m (cf. App. A.2). Therefore, no cross-over adjustment is applied to the residuals for this data set. Only cross-over points with $\Delta h < 100$ m are used for the aggregated cross-over statistics. The results are shown in Tab. 8.5. The gravity is modelled as a third-order Gauss-Markov process, with $\beta_{dg}^{3rd} = 1/10 \text{ km}^{-1}$ for R_0 and R_1 , and $\beta_{dg}^{3rd} = 1/20 \text{ km}^{-1}$ for R_2 and R_3 , accounting for the smoother signal characteristics. These correlation parameters were determined empirically, based on the estimated gravity data itself, using a single iteration. The correlation parameters are equally used for all 19 flights.

The most relevant conclusion from the cross-over evaluation is, that a precision of 1 mGal appears to be possible using an off-the-shelf navigation-grade IMU, when applying an appropriate calibration to the accelerometers. In more detail, the conclusions are:

	Cross-over residuals: RMS [mGal] (RMSE [mGal])						
	C_0	C_1	C_2	C_3	C_4	C_5	C_6
R_0	4.8 (3.4)	1.6 (1.2)	2.9 (2.1)	2.0 (1.4)	2.0 (1.4)	2.2 (1.5)	2.2 (1.6)
R_1	4.8 (3.4)	1.6 (1.1)	2.9 (2.1)	2.0 (1.4)	1.9 (1.4)	2.2 (1.5)	2.3 (1.6)
R_2	4.7 (3.3)	1.3 (0.9)	2.9 (2.0)	1.8 (1.3)	1.8 (1.2)	1.8 (1.3)	1.9 (1.4)
R_3	4.6 (3.3)	1.4 (1.0)	2.8 (2.0)	1.8 (1.3)	1.8 (1.3)	1.7 (1.2)	1.8 (1.3)

Table 8.5: Cross-over residual statistics for the Chile 2013 campaign, for different combinations of applied gravity reductions (R_0 – R_3 , see Tab. 8.3), and accelerometer calibration methods (C_0 – C_6 , see Tab. 8.2). No cross-over adjustment was applied. The analysis is limited to cross-over points with a height difference of $\Delta h < 100$ m (15 points). $\text{RMSE} = \text{RMS}/\sqrt{2}$, cf. Sect. 7.1.1. The best result is highlighted.

1. The reduction of topographic effects yields considerably lower cross-over residuals. Apparently, the topography-induced high-frequency portion of the gravity signal is difficult to estimate for the given terrain characteristics, flight altitude, and aircraft speed. While such high-resolution signal components can be crucial for small-scale geophysical measurements, they are typically of lower relevance for the local geoid determination on a medium scale (hundreds of kilometres), because the topographic effect is anyway removed from the full-range gravity signal for the downward-continuation.
2. Neither a long-wavelength GGM gravity reduction, nor the long wavelengths of the topographic reduction do significantly affect the results (R_0 results are similar to R_1 ; R_2 results are similar to R_3).
3. The warm-up calibration introduced in Sect. 6.4.1 yields the best results among all evaluated accelerometer calibration methods. This emphasises the importance of temperature gradients: For most of the flights, a long warm-up phase of the IMU happens during the flights (cf. Fig. 8.3), while sensor temperature changes due to changes of the ambient temperature are less significant. Apparently, the warm-up calibration is the most appropriate method to model such in-flight warm-up effects.

8.1.2 Errors of closure

	Cross-over residuals: RMS [mGal] (RMSE [mGal])						
	C_0	C_1	C_2	C_3	C_4	C_5	C_6
R_0	5.8 (4.1)	2.5 (1.8)	2.7 (1.9)	2.4 (1.7)	2.5 (1.7)	3.1 (2.2)	3.0 (2.1)
R_1	5.8 (4.1)	2.5 (1.8)	2.6 (1.9)	2.3 (1.7)	2.4 (1.7)	3.1 (2.2)	3.0 (2.1)
R_2	5.7 (4.0)	2.3 (1.6)	2.7 (1.9)	2.4 (1.7)	2.4 (1.7)	2.5 (1.8)	2.5 (1.8)
R_3	5.6 (4.0)	2.5 (1.8)	2.6 (1.8)	2.2 (1.6)	2.4 (1.7)	2.6 (1.8)	2.5 (1.8)

Table 8.6: Cross-over residual statistics for the Chile 2013 campaign, *not using the terrestrial gravity tie at the destination airport*. No cross-over adjustment was applied. The analysis is limited to cross-over points with a height difference of $\Delta h < 100$ m (15 points). $\text{RMSE} = \text{RMS}/\sqrt{2}$, cf. Sect. 7.1.1.

For all flights except 290a, a terrestrial gravity tie is available at both the origin and the destination airports. For the cross-over residuals shown in Tab. 8.5, the destination airport terrestrial gravity tie was introduced to the EKF as an observation. This enables the Kalman smoother to eliminate a linear drift in the gravity estimates (cf. Sect. 7.1.3). To illustrate the importance of using this observation, the data set was reprocessed, *without* using this information. The cross-over statistics for this case are shown in Tab. 8.6, showing considerable larger residuals compared to the results shown in Tab. 8.5.

The error of closure can be regarded as an indicator for the long-term stability of the estimated gravity disturbance. It is defined here as the difference between the gravity estimate at the destination airport, and the terrestrial gravity tie (*not* introducing it as an observation to the EKF). The errors of closure are only evaluated for the vertical gravity component, as no ground-truth information was available for the deflections of the vertical at the different airports. The observed errors of closure can be found in Tab. 8.7 for different calibration methods. The type of gravity reduction (R_0 – R_3) did not show any significant effect (<5%), therefore results are only shown for R_3 . If no calibration is applied (C_0), the errors of closure reach up to 6.5 mGal/h. Again, the warm-up calibration of the Z-accelerometer (C_1) yields the best results, reducing the drifts from 3.4 mGal/h to 0.3 mGal/h.

flight ID	Errors of closure [mGal] (average drift per hour [mGal/h])						
	C_0	C_1	C_2	C_3	C_4	C_5	C_6
285	11.5 (2.2)	0.9 (0.2)	4.8 (0.9)	3.8 (0.7)	3.5 (0.7)	2.4 (0.5)	2.5 (0.5)
288	14.2 (2.3)	-2.0 (-0.3)	3.6 (0.6)	2.4 (0.4)	1.7 (0.3)	0.4 (0.1)	0.7 (0.1)
289	7.4 (1.6)	-1.6 (-0.3)	1.4 (0.3)	0.9 (0.2)	1.0 (0.2)	-0.6 (-0.1)	-0.4 (-0.1)
290a	-	-	-	-	-	-	-
291	19.0 (1.7)	-3.5 (-0.3)	6.3 (0.6)	0.4 (0.0)	0.9 (0.1)	0.3 (0.0)	0.5 (0.0)
292	12.8 (2.0)	0.2 (0.0)	7.1 (1.1)	0.5 (0.1)	1.0 (0.2)	3.9 (0.6)	3.9 (0.6)
294	21.4 (3.5)	2.0 (0.3)	8.8 (1.4)	7.1 (1.2)	6.5 (1.1)	4.5 (0.7)	4.9 (0.8)
295	25.6 (3.6)	-3.3 (-0.5)	9.8 (1.4)	-0.2 (-0.0)	0.2 (0.0)	5.0 (0.7)	5.1 (0.7)
296	30.5 (4.4)	2.6 (0.4)	14.6 (2.1)	7.0 (1.0)	7.2 (1.0)	8.3 (1.2)	8.4 (1.2)
297	34.6 (6.5)	2.1 (0.4)	16.3 (3.1)	7.0 (1.3)	6.9 (1.3)	8.5 (1.6)	8.9 (1.7)
298	23.5 (2.3)	-1.8 (-0.2)	8.4 (0.8)	3.6 (0.4)	3.4 (0.3)	2.3 (0.2)	2.8 (0.3)
299	23.5 (2.2)	-0.1 (-0.0)	9.2 (0.9)	5.0 (0.5)	4.7 (0.4)	3.9 (0.4)	4.3 (0.4)
301a	27.1 (5.1)	3.0 (0.6)	13.4 (2.5)	7.1 (1.3)	7.1 (1.3)	7.9 (1.5)	8.0 (1.5)
301b	2.1 (0.5)	2.1 (0.5)	2.1 (0.5)	2.4 (0.6)	2.5 (0.6)	1.4 (0.4)	1.3 (0.3)
302	25.2 (2.3)	0.2 (0.0)	12.1 (1.1)	2.6 (0.2)	3.5 (0.3)	4.5 (0.4)	4.4 (0.4)
303	25.6 (2.6)	1.9 (0.2)	12.1 (1.2)	5.8 (0.6)	6.4 (0.7)	4.1 (0.4)	4.0 (0.4)
304	30.6 (5.0)	1.0 (0.2)	14.3 (2.3)	4.2 (0.7)	4.6 (0.8)	7.4 (1.2)	7.3 (1.2)
305a	26.5 (4.9)	-1.6 (-0.3)	10.4 (1.9)	2.7 (0.5)	2.6 (0.5)	5.6 (1.0)	5.6 (1.0)
305b	5.3 (0.9)	1.0 (0.2)	2.9 (0.5)	2.1 (0.4)	1.9 (0.3)	1.1 (0.2)	1.3 (0.2)
RMS	22.3 (3.4)	2.0 (0.3)	9.8 (1.5)	4.3 (0.7)	4.3 (0.7)	4.8 (0.8)	4.9 (0.8)
μ	20.3 (3.0)	0.2 (0.1)	8.7 (1.3)	3.6 (0.6)	3.6 (0.6)	3.9 (0.6)	4.1 (0.6)
σ	9.4 (1.6)	2.0 (0.3)	4.6 (0.8)	2.5 (0.4)	2.4 (0.4)	2.9 (0.5)	2.8 (0.5)
min	2.1 (0.5)	-3.5 (-0.5)	1.4 (0.3)	-0.2 (-0.0)	0.2 (0.0)	-0.6 (-0.1)	-0.4 (-0.1)
max	34.6 (6.5)	3.0 (0.6)	16.3 (3.1)	7.1 (1.3)	7.2 (1.3)	8.5 (1.6)	8.9 (1.7)

Table 8.7: Errors of closure for 18 out of 19 flights of the Chile 2013 campaign. No terrestrial gravity tie was available at the destination airport for flight 290a.

8.1.3 Comparison against LCR

For the whole data set, the LaCoste & Romberg S-99 sea/air gravimeter (LCR) was flown side-by-side with the strapdown system. For an inter-system comparison of the longer wavelengths, both gravity data sets are preprocessed using a third-order, two-pass Butterworth low-pass filter at cut-off frequency 1/500 Hz (consistent with a spatial half-wavelength of

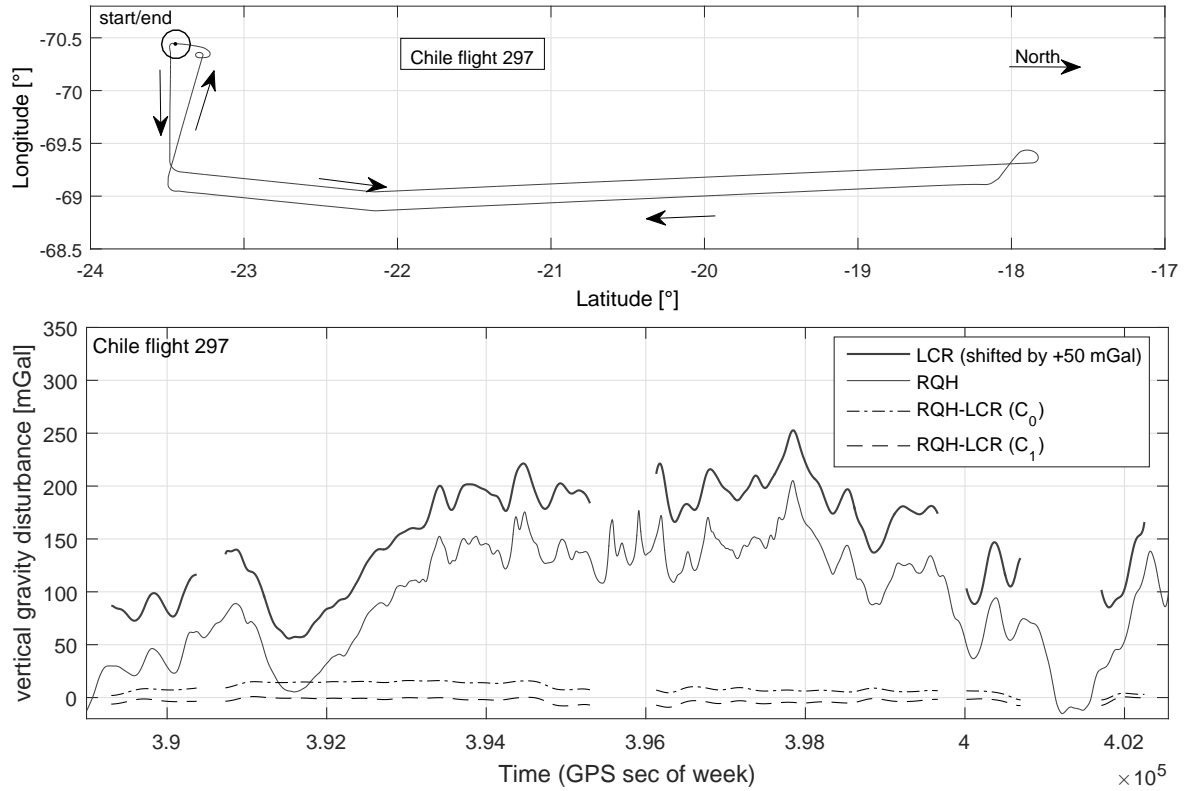


Figure 8.4: Chile flight 297: Comparison between LCR and RQH. The differences are shown here after applying a third-order, two-pass Butterworth filter with 1/500 Hz cut-off.

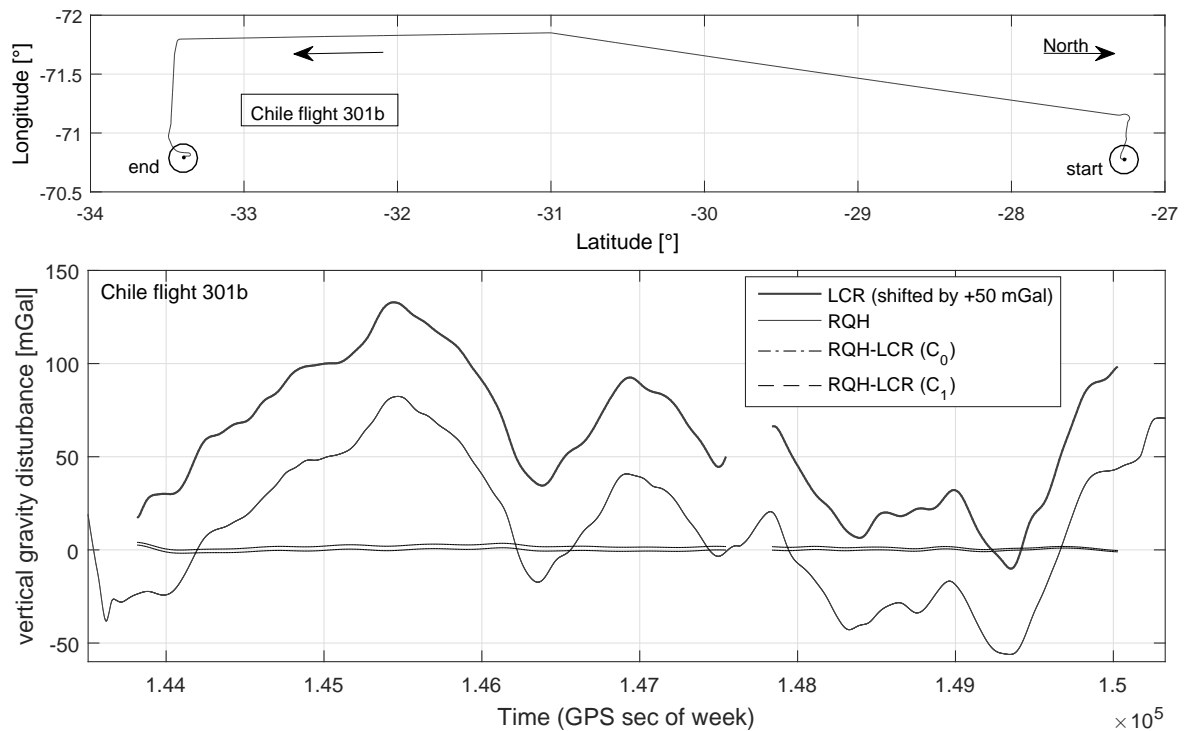


Figure 8.5: Chile flight 301b: Comparison between LCR and RQH. The differences are shown here after applying a third-order, two-pass Butterworth filter with 1/500 Hz cut-off.

≈ 25 km). (Shorter wavelengths will be compared in the next section against the topographic effect.)

The statistics of the inter-system comparison is shown in Tab. 8.8. Again, only results for the gravity reduction method R_3 are shown here for brevity (applying R_0 – R_2 yields again similar results). Each of the IMU calibration methods yield a considerable improvement compared to the uncorrected results (C_0). The best agreement of the two devices can be found for the calibration methods C_1 and C_5 : The overall mean of the two data sets shows an agreement of -0.3 mGal, and -0.1 mGal, respectively. Further, the average standard deviations from 1.9 mGal to 2.1 mGal are within the expected precision of the two sensors.

Note: The statistics shown in Tab. 8.8 are based on the full differences of the two sensors, i.e. a factor of $1/\sqrt{2}$ was *not* applied. When assuming a similar sensor accuracy for both sensors, the estimated *individual* sensor precision may be computed by applying this factor to the shown results.

flight ID	RQH–LCR: mean [mGal] (σ [mGal])						
	C_0	C_1	C_2	C_3	C_4	C_5	C_6
285	2.3 (2.6)	-1.8 (2.4)	-0.2 (2.6)	-0.6 (2.4)	-0.6 (2.4)	-0.1 (2.1)	0.1 (2.1)
288	3.2 (2.0)	-2.2 (2.2)	-0.6 (1.9)	-0.6 (2.0)	-0.6 (2.0)	-3.9 (2.5)	-4.1 (2.5)
289	3.3 (0.7)	0.0 (1.1)	1.2 (0.9)	1.2 (1.0)	1.2 (1.0)	-0.7 (0.8)	-0.9 (0.8)
290a	8.4 (2.4)	-1.4 (0.6)	3.7 (1.2)	-0.9 (1.5)	-0.5 (1.3)	0.6 (0.8)	0.2 (0.8)
291	12.1 (4.5)	-0.0 (3.7)	5.3 (4.6)	2.2 (2.6)	2.3 (2.9)	2.2 (3.6)	2.1 (3.6)
292	7.2 (3.3)	1.6 (0.8)	4.7 (2.0)	2.2 (0.9)	2.5 (1.0)	0.9 (0.9)	0.5 (1.0)
294	4.3 (1.4)	0.8 (1.3)	2.2 (1.4)	1.9 (1.4)	2.1 (1.4)	-1.0 (1.9)	-1.2 (1.9)
295	10.8 (4.6)	2.9 (1.5)	7.4 (3.1)	2.7 (1.7)	3.4 (1.8)	2.0 (2.4)	1.6 (2.4)
296	15.2 (4.2)	1.4 (1.1)	7.8 (2.1)	3.3 (1.6)	3.6 (1.5)	3.6 (1.7)	3.5 (1.6)
297	9.5 (4.5)	-2.8 (2.3)	2.8 (3.1)	-1.1 (2.4)	-0.8 (2.4)	-1.7 (3.2)	-2.2 (3.3)
298	10.1 (4.2)	-1.2 (2.4)	3.6 (2.3)	1.3 (2.0)	1.4 (2.0)	-1.0 (2.6)	-1.4 (2.6)
299	12.4 (5.9)	-0.7 (2.3)	4.9 (3.6)	2.3 (2.7)	2.3 (2.8)	-0.1 (1.9)	-0.2 (1.9)
301a	9.8 (5.3)	1.5 (1.5)	5.5 (2.3)	3.0 (1.6)	3.2 (1.6)	1.3 (1.5)	1.3 (1.5)
301b	1.6 (0.8)	-0.2 (0.7)	0.3 (0.7)	0.6 (0.7)	0.7 (0.7)	-1.4 (0.6)	-1.7 (0.6)
302	15.1 (7.4)	0.4 (1.4)	7.2 (3.0)	2.0 (2.3)	2.4 (2.2)	2.2 (1.6)	2.0 (1.7)
303	9.5 (6.7)	-1.5 (4.7)	3.5 (5.0)	0.3 (4.6)	0.5 (4.6)	-0.4 (4.4)	-0.5 (4.4)
304	10.0 (3.8)	-0.7 (2.1)	4.7 (2.4)	-0.1 (2.4)	0.5 (2.3)	-0.4 (3.9)	-0.4 (3.9)
305a	6.5 (2.6)	-1.0 (1.5)	3.0 (1.9)	-0.4 (1.7)	-0.0 (1.6)	-1.3 (1.7)	-1.5 (1.6)
305b	-0.6 (1.7)	-0.6 (1.7)	-0.7 (1.7)	-0.4 (1.7)	-0.3 (1.6)	-2.2 (1.7)	-2.5 (1.7)
μ	7.9 (3.6)	-0.3 (1.9)	3.5 (2.4)	1.0 (2.0)	1.2 (1.9)	-0.1 (2.1)	-0.3 (2.1)
min	-0.6 (0.7)	-2.8 (0.6)	-0.7 (0.7)	-1.1 (0.7)	-0.8 (0.7)	-3.9 (0.6)	-4.1 (0.6)
max	15.2 (7.4)	2.9 (4.7)	7.8 (5.0)	3.3 (4.6)	3.6 (4.6)	3.6 (4.4)	3.5 (4.4)

Table 8.8: Long-wavelength comparison between strapdown gravimetry (RQH) and stable-platform gravimetry (LCR). Both data sets were low-pass filtered using a third-order 2-pass Butterworth filter with cut-off frequency 1/500 Hz. Means and standard deviations of the scalar gravity differences are shown for the different IMU calibration methods C_0 – C_6 . Best results are highlighted.

The comparison of the two instruments is shown in more detail in Figs. 8.4 and 8.4 for two flights:

- flight 297: this flight has a large temperature range, from 16 °C to 42 °C; and

- flight 301b: this flight has the lowest temperature variation among all flights, ranging from 34 °C to 36 °C (see Fig. 8.3).

For flight 297, the benefit of applying calibration method C_1 is evident. For flight 301b (Fig. 8.5), it is worth noting that even for small temperature variations, the thermal corrections yield a better agreement with the long-wavelength LCR results, cf. Tab. 8.8. This improvement is however not reflected by the error of closure for that flight. A possible explanation is, that the internal sensor temperature was almost identical at the two airports, cf. Fig. 8.3 and Tab. 8.7.

Note, that strapdown gravity estimates are available for the whole flight, including the turns. Conversely, due to technical limitations, the LCR gravimeter is not capable of collection data during these phases. Therefore, the LCR time-lines shown in Figs. 8.4 and 8.5 contain gaps. Also, it can be visually recognised in the figures, that the IMU results contain more high-frequency information compared to the LCR results, emphasising the requirement of applying an identical low-pass filter to both data sets for the comparison.

8.1.4 High-frequency comparison against topographic effect

For a comparison against the gravimetric effect of the topography, flight 288 of the Chile campaign is selected for the following two reasons:

- It is almost entirely flown above high-mountain terrain, and
- on the measurement lines, it has a relatively low clearance above the topography (1100 m).

Therefore, the recovery of the short-wavelength components of the gravity field can be regarded as particularly challenging for this flight. Topography and flight altitude are depicted in Fig. 8.6. No gravity reductions were applied to the strapdown data for this comparison.

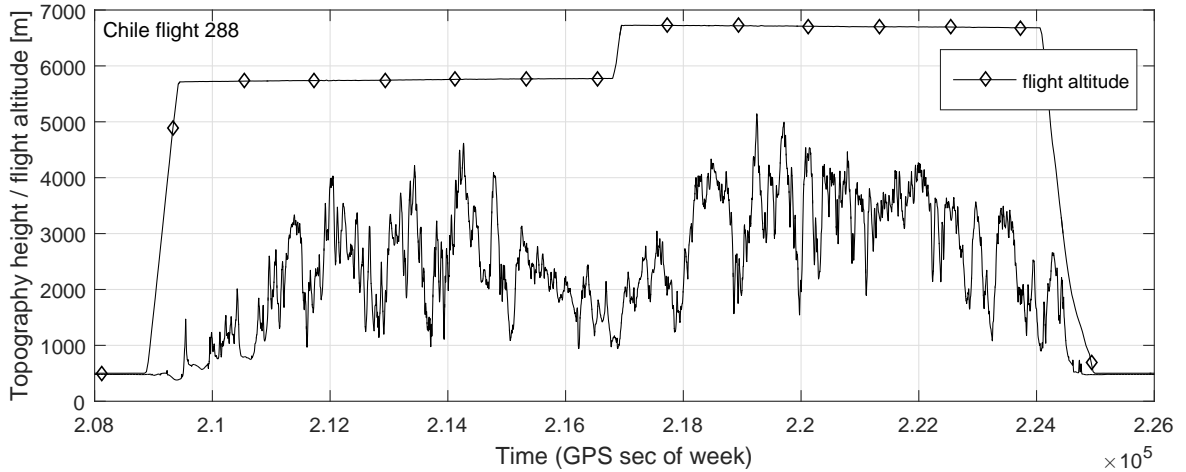


Figure 8.6: Chile flight 288: Along-track flight altitude and topography height.

The along-track gravimetric effect of the topography was computed using the software GRAVSOFT TC, based on the SRTMplus data set at 15 arc seconds resolution (*Becker et al.*, 2009). Both, the topographic gravity effect and the strapdown gravimetry estimates are *high-pass* filtered using a third-order, two-pass Butterworth filter at threshold frequency 1/200 Hz. The high-pass filtered topographic effect is regarded for this comparison as a quasi-reference, as the majority of the high-frequency gravity signal is expected to come from the topographic effect for this flight.

$1/\beta_{dg}^{3rd}$	North-component RMS [mGal]						
	C_0	C_1	C_2	C_3	C_4	C_5	C_6
4 km	2.16	2.16	2.16	2.16	2.16	2.18	2.15
6 km	1.66	1.66	1.66	1.66	1.66	1.70	1.66
8 km	1.47	1.47	1.47	1.47	1.47	1.51	1.47
10 km	1.53	1.53	1.53	1.53	1.53	1.55	1.53
12 km	1.74	1.74	1.74	1.75	1.74	1.76	1.74
14 km	2.00	2.00	2.00	2.00	2.00	2.01	2.00
16 km	2.24	2.24	2.24	2.25	2.24	2.25	2.24

$1/\beta_{dg}^{3rd}$	East-component RMS [mGal]						
	C_0	C_1	C_2	C_3	C_4	C_5	C_6
4 km	4.12	4.12	4.12	4.12	4.12	3.97	4.14
6 km	2.69	2.69	2.69	2.69	2.69	2.68	2.68
8 km	1.95	1.95	1.95	1.96	1.96	1.97	1.94
10 km	1.48	1.48	1.48	1.49	1.49	1.48	1.47
12 km	1.23	1.23	1.23	1.24	1.24	1.21	1.22
14 km	1.18	1.18	1.18	1.18	1.18	1.16	1.17
16 km	1.24	1.24	1.24	1.24	1.24	1.22	1.24

$1/\beta_{dg}^{3rd}$	Down-component RMS [mGal]						
	C_0	C_1	C_2	C_3	C_4	C_5	C_6
4 km	2.98	2.98	2.98	2.98	2.98	2.95	2.92
6 km	2.41	2.41	2.41	2.40	2.41	2.40	2.38
8 km	1.86	1.87	1.87	1.86	1.87	1.89	1.88
10 km	1.64	1.64	1.64	1.64	1.65	1.68	1.67
12 km	1.68	1.68	1.68	1.68	1.68	1.70	1.70
14 km	1.79	1.79	1.79	1.79	1.79	1.81	1.81
16 km	1.92	1.92	1.92	1.92	1.92	1.93	1.93

Table 8.9: Short wavelength comparison between the topographic effect, and the strapdown gravity results, for different settings of the third-order Gauss-Markov correlation parameter β_{dg}^{3rd} . Individual tables are shown for the three components of the 3-D gravity vector. Both data sets are *high-pass* filtered using a third-order, two-pass Butterworth filter with threshold frequency 1/200 Hz (consistent with a spatial resolution of 10 km half wavelength). For each of the three vector components, the optimal choice of $1/\beta_{dg}^{3rd}$ is highlighted.

The IMU results are compared to this quasi-reference for different combinations of calibration methods and correlation parameters β_{dg}^{3rd} for the third-order Gauss-Markov process (cf. Sect. 3.2.6). The results are shown in Tab. 8.9. The following conclusions can be drawn from the comparison results:

1. The accelerometer calibrations do not have any significant effect on the short-wavelength estimation of gravity. Clearly, the temperature changes within a full wavelength of 200 s are almost negligible in practice. Apparently, also gravity estimation errors arising from different roll- and pitch-angles (relevant for C_3, C_4, C_5, C_6) could not be reduced.
2. The high-frequency components (wavelengths smaller than ≈ 20 km) are indeed difficult to determine: For this particularly challenging flight, the RMS of the differences is larger than the expected *overall* (full spectrum) system precision, as indicated by Tab. 8.5.
3. As expected, there is no fixed optimal setting for the correlation parameter β_{dg} of the Gauss-Markov process modelling the along-track gravity signal.
4. The determination of the horizontal and vertical gravity components can be done at an equal precision for the high frequencies. It is again noted here, that this is not the case for longer wavelengths, due to the high sensitivity of the horizontal components to attitude errors (cf. Fig. 4.4).

It is just noted here, that using different Gauss-Markov models (first-, second-, or fourth-order) did not significantly affect the comparison results: The best agreement (highlighted rows in Tab. 8.9) was consistent within 0.15 mGal among the different Gauss-Markov models.

8.1.5 Comparison against GGM05C

An quasi-regular grid of sample points is computed with 20 km sample spacing, yielding a total of 1098 sample points depicted in Fig. 8.7 (cf. Sect. 7.2.2). At the same grid points, the GGM05C model is evaluated (at flight altitude). Tab. 8.10 shows biases between the two data sets, for different combinations of applied gravity reductions and calibration methods.

As for the comparison against LCR, the accelerometer calibrations in general yield a considerably better (sub-mGal) agreement with the GGM05C reference data set compared to the uncorrected results (C_0). It is noted in particular, that the roll- and pitch-angle dependent calibration methods (C_3 – C_6) yield a better agreement compared to the Z-accelerometer calibrations C_1 and C_2 . A possible explanation for this is the systematic difference of the average pitch angles on ground (where the strapdown gravity estimates are tied to the terrestrial base value), and the average pitch angles on the measurement lines, see Fig. 8.8. Any uncorrected, systematic pitch-dependent error of the strapdown gravimetry system will propagate into the data set as a bias, *independently* of temperature effects.

For this type of comparison, the standard deviation of the difference of the two data sets can *not* be regarded as a quality measure (Sect. 7.2.2): Since full-spectrum strapdown results are compared to long-wavelength GGM values, the standard deviation reflects the contribution of the shorter wavelengths in this case. For the combinations shown in Tab. 8.10, the standard deviation is $\sigma = 23.2 \pm 0.1$ mGal.

	mean(RQH-GGM05C) [mGal]						
	C_0	C_1	C_2	C_3	C_4	C_5	C_6
R_0	7.9	-1.5	2.8	-0.1	0.1	-0.9	-1.1
R_1	7.9	-1.5	2.8	-0.1	0.1	-0.9	-1.1
R_2	8.2	-1.0	3.2	0.4	0.6	-0.5	-0.7
R_3	8.1	-1.1	3.1	0.3	0.6	-0.6	-0.7

Table 8.10: Bias estimates between the RQH strapdown airborne gravity results, and the GGM05C global gravity model, for a grid of 1098 sample points (Fig. 8.7).

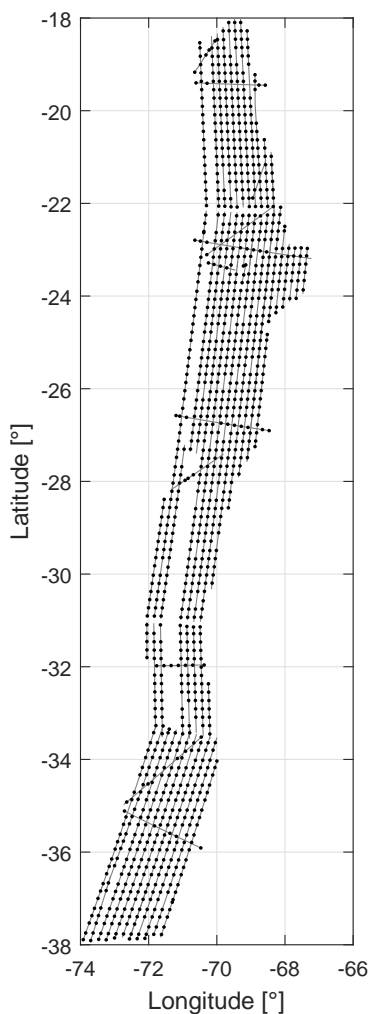


Figure 8.7: Quasi-regular grid with 20 km average grid spacing for the Chile campaign, used for the comparison of the strapdown airborne gravity data against the GGM05C global gravity model (1098 points). The statistics are shown in Tab. 8.16.

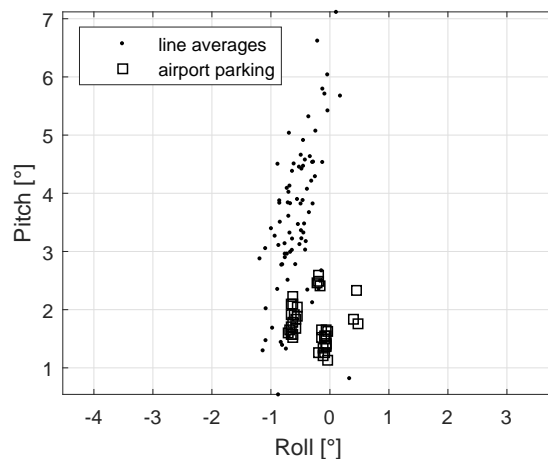


Figure 8.8: Combinations of average roll- and pitch-angles for the Chile campaign. The day-to-day aircraft parking positions were almost identical for each of the used airports, reflected in the figure by the groups of square markers. In particular, the average pitch-angles on the measurement lines are systematically higher compared to those at the airport parking positions.

8.2 Malaysia (2014 and 2015)

The Malaysia campaign is split into two parts, flown in 2014 (12 flights) and 2015 (34 flights). The flights were carried out in the Northern part of Malaysian Borneo. The flight line spacing was 5 km in the coastal regions, and 10 km for the offshore flights (Fig. 8.9).

The temperature plots are shown for all 46 flights in Fig. 8.10. For the 2014 campaign, the IMU was still warming up after take-off for all flights except flights 240, 241, and 243b. For the 2015 campaign, two flights were done for most of the days. The IMU was usually not switched off between two flights at the same day, yielding a higher initial sensor temperature for the respective second flight of a day.

8.2.1 Cross-over analysis: Scalar gravity

Most of the measurement lines were flown at a nominal altitude of 1830 m (6000 ft), yielding a total of more than 400 cross-over points with a height difference of $\Delta h < 50$ m for the 2014 and 2015 campaigns combined (5 cross-over points are adjacent to each measurement line, on average).

The non-adjusted cross-over residuals of the Malaysia 2014 campaign are depicted in Figs. 8.11 (top). For an unknown reason, a systematic offset of approx. -3 mGal can be recognised for flight 240. The non-adjusted cross-over statistics are shown in Tab. 8.11, including all flights (top), and after removing flight 240 from the statistics (bottom). The results indicate an accuracy level of 0.8 mGal (RMSE) when applying the sample-based TRP correction C_6 , and approx. 1 mGal (RMSE) for the other calibration methods (C_1 – C_5), and 1.6 mGal (RMSE), if no calibration is applied to the sensor data (C_0), which is also a remarkable result. Compared to the Chile campaign (see previous section), the non-calibrated results (C_0) are considerably better for the Malaysia 2014 campaign, presumably arising from the smaller interval of observed sensor temperatures (compare Figs. 8.3 and 8.10).

The Malaysia 2015 statistics are shown in Tab. 8.12. Applying the warm-up calibration yields the lowest non-adjusted residuals (1.0 mGal RMSE).

For both data sets, the gravity reductions R_0 – R_3 show only little impact on the cross-over statistics. Apparently, high-frequency terrain-induced gravity signal components (as for the Chile campaign) are *not* the limiting factor for these campaigns. This is consistent with the a-priori expectation, as the terrain (or the bathymetry) has a rather smooth shape compared to the Chilean Andes.

Cross-over adjustment

Having 5 cross-over points adjacent to each measurement line (on average) allows the determination of meaningful *adjusted* cross-over statistics (cf. the paragraph on cross-over adjustment in Sect. 7.1.1). The results are shown in Tabs. 8.13 and 8.14. The correction factor ρ_n was applied to the cross-over residuals, depending on the number of cross-over points adjacent to each line (cf. Sect. 7.1.1). For the Malaysia 2015 campaign, the adjusted cross-over residuals are as low as 0.5 mGal (RMSE), which is a remarkable precision for strapdown gravimetry, and for airborne gravimetry in general.

When using a cross-over adjustment, the effect of the accelerometer calibration methods reduces significantly for both of the campaigns: The improvement compared to the uncorrected results is only of the order of 20%, compared to approx. 55% if *no* cross-over adjustment is applied. This emphasises the importance of calibration methods in particular for *geodetic* applications, for which the cross-over adjustment can not be suggested in general, as it may generate unwanted systematic errors in the gravity data.

For the Malaysia 2014 data set, the concept of applying the correction factor ρ_n before computing the RMS of all residuals is analysed (see Sect. 7.1.1). The number of cross-over

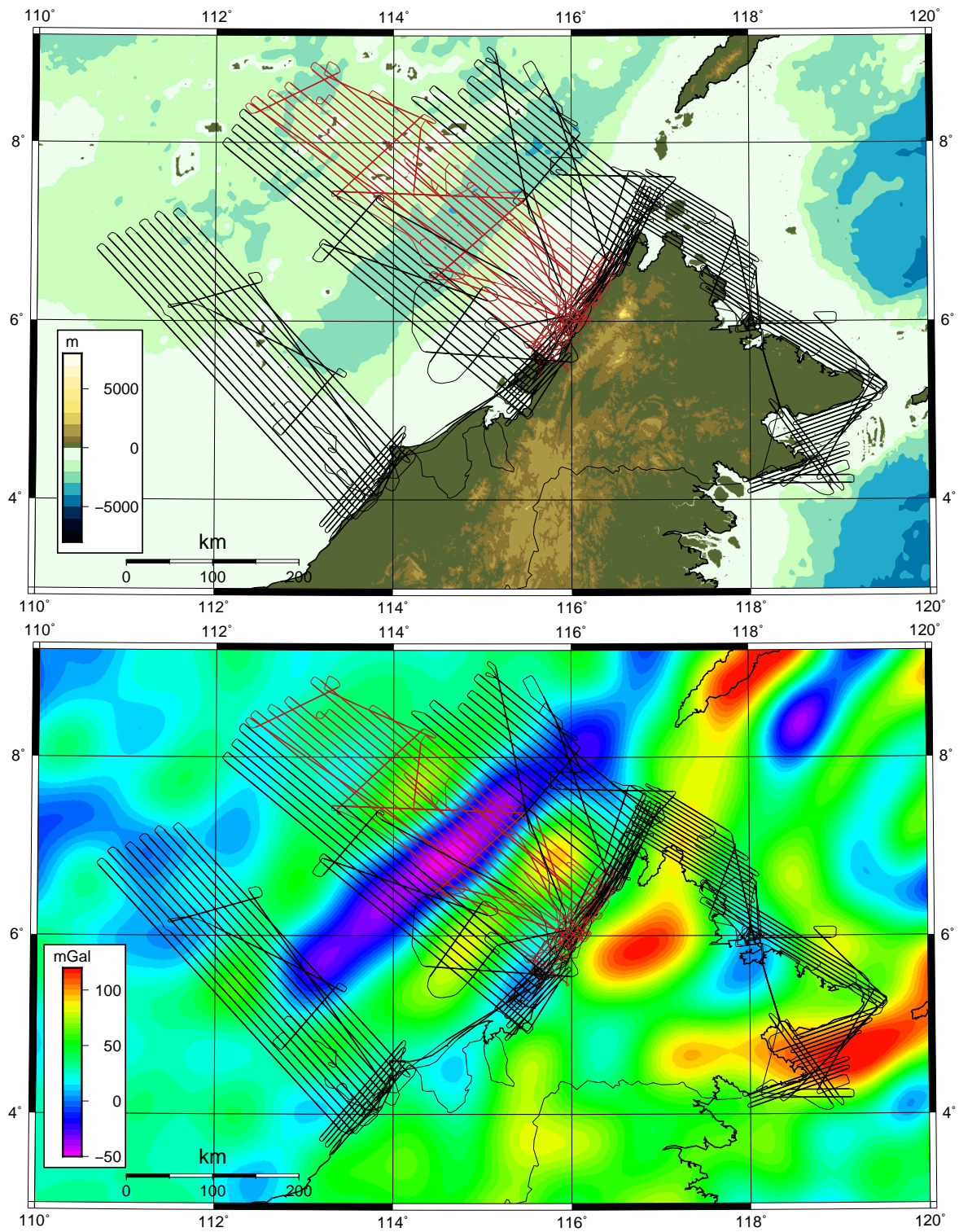


Figure 8.9: Combined overview of the 2014 and 2015 Malaysia aerogravity campaigns. The 2014 flight tracks is shown in dark-red color. The measurement lines are highlighted (bold lines), all other parts of the flights are shown as thin lines. Top: Topography / bathymetry. Bottom: Gravity anomalies of the GGM05C global gravity model (*Ries et al., 2016*), computed to degree and order 360.

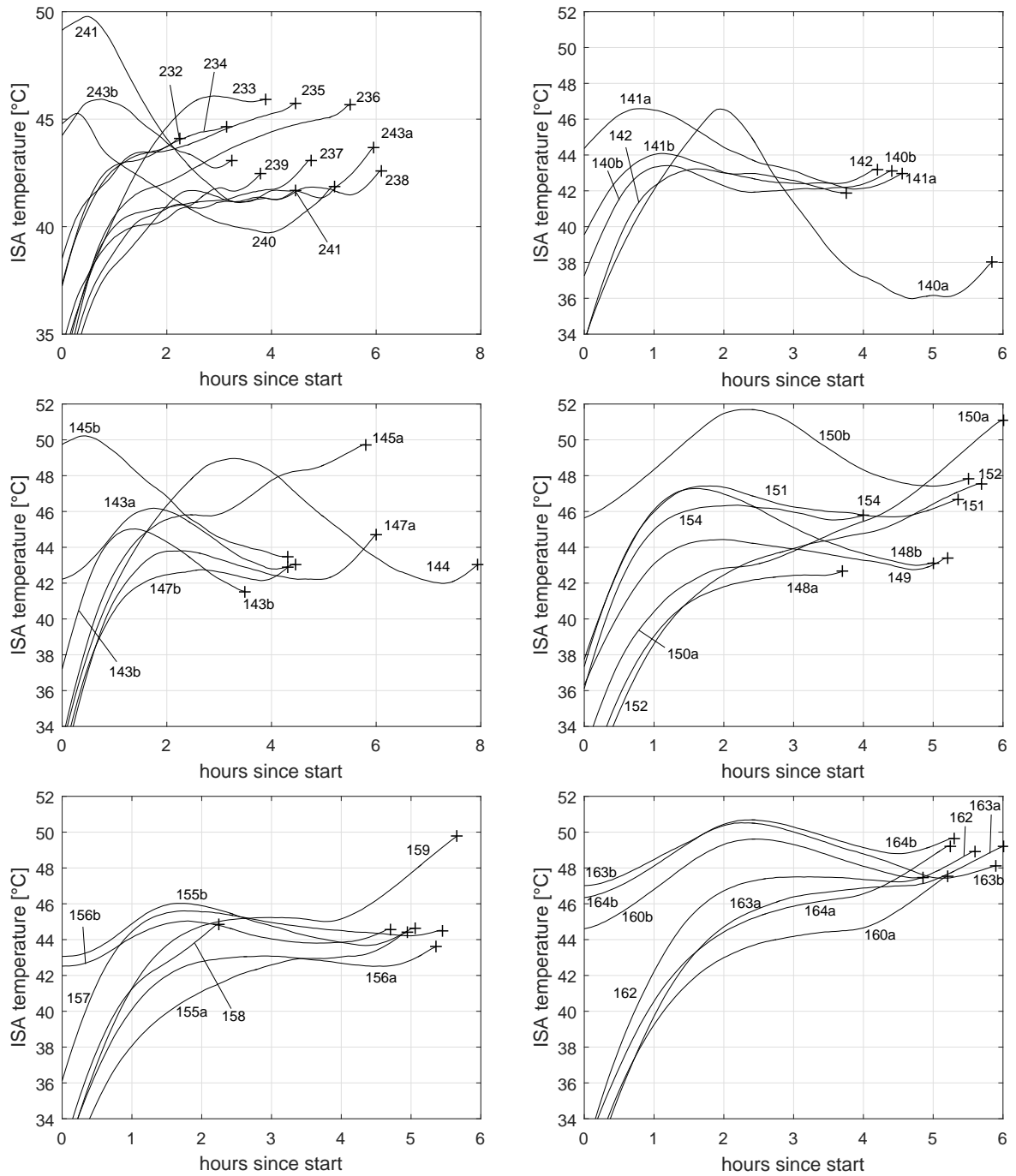


Figure 8.10: Sensor temperatures for the Malaysia campaigns. *Top left:* Malaysia 2014; *All other plots:* Malaysia 2015.

points is artificially reduced by removing randomly selected points from the full set. The RMS of the adjusted cross-over residuals is then computed for the reduced set of cross-over points. The experiment is repeated for more than 1500 times. The results are shown in Fig. 8.12, including linear regression polynomials, confirming the concept of these correction factors: The statistics of the uncorrected residuals clearly show a dependency on the number of cross-over points (the average RMS reduces by 25 %). Thus, lower numbers of cross-over points yield too optimistic estimates. Conversely, the *corrected* residuals show barely any dependency on the number of cross-over points (the average RMS reduces by only 4 %).

For the full set of 99 cross-over points, the RMS of the uncorrected residuals of 0.82 mGal can be expected to be too optimistic by 15 % (0.14 mGal).

8.2.2 Cross-over analysis: Deflections of the Vertical

The determination of the deflection of the vertical (DoV) heavily depends on the attitude stability of the system, as was shown by the observability and estimability analyses in Chap. 4, and also by the error propagation simulations of Chap. 5. Therefore, the accelerometer calibrations are expected to have only a small effect on the DoV determination. This is indeed reflected by the results shown in Tab. 8.15.

For a navigation-grade strapdown IMU, the *absolute* attitude errors can be expected to be of the order of 5–15 arc seconds, directly propagating into the DoV estimates (again, 5–15 arc seconds). DoV estimates at this accuracy level usually do not have any practical use. Conversely, when applying a cross-over adjustment, the residual cross-over differences indicate the *relative stability* of the DoV estimates along the flight lines.

The adjusted cross-over residuals for the deflections of the vertical are shown in Tab. 8.15, again corrected using the factor ρ_n . The Malaysia 2015 DoV estimates show significantly lower residuals. The reason for this is unknown, possible explanations are:

- The same aircraft was used for the two campaigns. However, between the two surveys, one of the engines underwent a major servicing due to some technical issue leading to a lower power for that engine (i.e. an asymmetric power balance between the two aircraft engines). Perhaps this malfunction had negatively influenced the aircraft motion characteristics for the 2014 campaign.
- A manufacturer firmware update was applied to the iMAR RQH-1003 IMU between the two campaigns.

The shown DoV precision of approx. 0.8 to 1.2 arc seconds (RMSE) may be usable in practice, e.g. for geophysical inversion, or as constraints for the local geoid determination, at the borders of the region of available gravity data.

8.2.3 Comparison against GGM05C

The comparison against GGM05C is based on a quasi-regular grid of comparison points, with a grid-spacing of ≈ 20 km, cf. Sect. 7.2.2. The grid is depicted in Fig. 8.13. The coastal flight lines in the Eastern part of Borneo (see Fig. 8.13) are not used for the comparison, because the covered area is narrower than a single wavelength of the GGM05C data.

The statistics of the comparison are shown in Tab. 8.16. The biases can be shown to be well below 1 mGal for the sample-based calibration approaches. The uncorrected results (C_0) show a significantly higher bias compared to the calibrated data sets. The applied gravity reductions show barely any effect for this comparison.

	Cross-over residuals: RMS [mGal] (RMSE [mGal]), full data set.						
	C_0	C_1	C_2	C_3	C_4	C_5	C_6
R_0	3.8 (2.7)	1.8 (1.3)	2.7 (1.9)	2.2 (1.6)	2.2 (1.5)	2.0 (1.4)	2.0 (1.4)
R_1	3.7 (2.7)	1.8 (1.3)	2.7 (1.9)	2.2 (1.6)	2.2 (1.5)	2.0 (1.4)	2.0 (1.4)
R_2	3.8 (2.7)	1.8 (1.3)	2.7 (1.9)	2.3 (1.6)	2.2 (1.6)	2.1 (1.5)	2.1 (1.5)
R_3	3.9 (2.7)	1.9 (1.3)	2.8 (2.0)	2.3 (1.7)	2.3 (1.6)	2.1 (1.5)	2.2 (1.5)
RMS	3.8 (2.7)	1.8 (1.3)	2.7 (1.9)	2.3 (1.6)	2.2 (1.6)	2.0 (1.4)	2.1 (1.5)

	Cross-over residuals: RMS [mGal] (RMSE [mGal]), outlier removed.						
	C_0	C_1	C_2	C_3	C_4	C_5	C_6
R_0	2.2 (1.6)	1.5 (1.0)	1.6 (1.1)	1.5 (1.0)	1.5 (1.0)	1.4 (1.0)	1.2 (0.9)
R_1	2.2 (1.6)	1.5 (1.0)	1.6 (1.1)	1.5 (1.0)	1.5 (1.0)	1.4 (1.0)	1.2 (0.9)
R_2	2.2 (1.5)	1.5 (1.0)	1.6 (1.1)	1.4 (1.0)	1.5 (1.0)	1.4 (1.0)	1.2 (0.8)
R_3	2.2 (1.6)	1.5 (1.0)	1.6 (1.1)	1.5 (1.0)	1.5 (1.0)	1.3 (0.9)	1.2 (0.8)

Table 8.11: Malaysia 2014: *Non-adjusted* cross-over residual statistics, for different combinations of applied gravity reductions (R_0 – R_3), and accelerometer calibration methods (C_0 – C_6 , see Tab. 8.2). *Top:* Including all flights. *Bottom:* After removing flight 240, which is regarded as an outlier (see Fig. 8.11). The analysis is limited to cross-over points with a height difference of $\Delta h < 100$ m (*Top:* 101 points; *Bottom:* 73 points). RMSE = RMS/ $\sqrt{2}$, cf. Sect. 7.1.1. The best results are highlighted.

	Cross-over residuals: RMS [mGal] (RMSE [mGal])						
	C_0	C_1	C_2	C_3	C_4	C_5	C_6
R_0	2.9 (2.1)	1.5 (1.0)	2.3 (1.6)	1.7 (1.2)	1.7 (1.2)	1.9 (1.3)	1.9 (1.3)
R_1	3.0 (2.1)	1.5 (1.0)	2.3 (1.6)	1.7 (1.2)	1.7 (1.2)	1.9 (1.3)	1.9 (1.3)
R_2	2.9 (2.1)	1.5 (1.0)	2.2 (1.6)	1.7 (1.2)	1.7 (1.2)	1.8 (1.3)	1.8 (1.3)
R_3	3.0 (2.1)	1.5 (1.0)	2.3 (1.6)	1.7 (1.2)	1.7 (1.2)	1.9 (1.3)	1.9 (1.3)

Table 8.12: Malaysia 2015: *Non-adjusted* cross-over residual statistics, for different combinations of applied gravity reductions (R_0 – R_3), and accelerometer calibration methods (C_0 – C_6 , see Tab. 8.2). Flight 149 has severe GNSS data errors and is not included in the statistics. The analysis is limited to cross-over points with a height difference of $\Delta h < 100$ m (282 points). The best result is highlighted.

	Adjusted cross-over residuals: RMS [mGal] (RMSE [mGal])						
	C_0	C_1	C_2	C_3	C_4	C_5	C_6
R_0	1.14 (0.81)	0.96 (0.68)	0.96 (0.68)	0.96 (0.68)	0.96 (0.68)	0.99 (0.70)	0.94 (0.66)
R_1	1.14 (0.81)	0.96 (0.68)	0.96 (0.68)	0.96 (0.68)	0.96 (0.68)	0.99 (0.70)	0.93 (0.66)
R_2	1.17 (0.83)	0.98 (0.70)	0.99 (0.70)	0.98 (0.69)	0.98 (0.70)	1.02 (0.72)	0.97 (0.69)
R_3	1.19 (0.84)	1.03 (0.73)	1.05 (0.74)	1.03 (0.73)	1.03 (0.73)	1.08 (0.76)	1.03 (0.73)

Table 8.13: Malaysia 2014: *Adjusted* cross-over residual statistics. A constant bias was estimated and removed from each of the lines. All 12 flights are included in the statistics, $\Delta h < 100$ m (99 points). The correction factor ρ_n was applied (Sect. 7.1.1). RMSE = RMS/ $\sqrt{2}$, cf. Sect. 7.1.1. The best result is highlighted.

	Adjusted cross-over residuals: RMS [mGal] (RMSE [mGal])						
	C_0	C_1	C_2	C_3	C_4	C_5	C_6
R_0	0.91 (0.64)	0.72 (0.51)	0.76 (0.54)	0.72 (0.51)	0.72 (0.51)	0.76 (0.54)	0.75 (0.53)
R_1	0.91 (0.64)	0.72 (0.51)	0.76 (0.54)	0.72 (0.51)	0.72 (0.51)	0.76 (0.54)	0.75 (0.53)
R_2	0.87 (0.62)	0.69 (0.48)	0.72 (0.51)	0.69 (0.48)	0.68 (0.48)	0.72 (0.51)	0.71 (0.50)
R_3	0.89 (0.63)	0.70 (0.49)	0.74 (0.53)	0.70 (0.50)	0.70 (0.50)	0.74 (0.52)	0.73 (0.51)

Table 8.14: Malaysia 2015: *Adjusted* cross-over residual statistics. A constant bias was estimated and removed from each of the lines, $\Delta h < 100$ m (271 points). The correction factor ρ_n was applied (Sect. 7.1.1). $\text{RMSE} = \text{RMS}/\sqrt{2}$, cf. Sect. 7.1.1. The best result is highlighted.

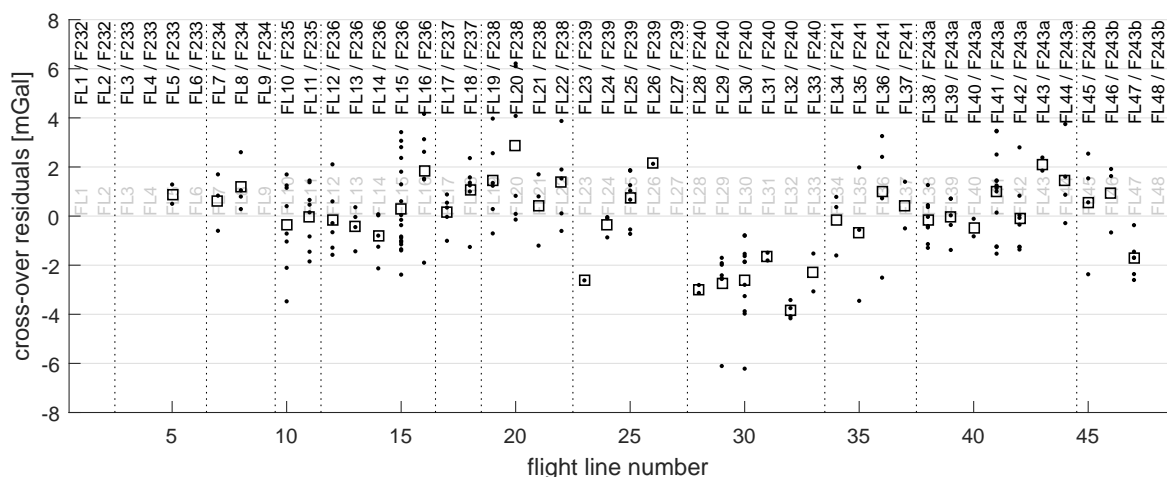


Figure 8.11: Malaysia 2014: Overview of non-adjusted cross-over residuals, by flight (F) and flight line (FL). Each dot indicates a cross-over residual. The squares indicate the average of all cross-over residuals adjacent to a particular measurement line. Flight 240 shows a systematic offset of ≈ -3 mGal among all of its measurement lines. It is therefore regarded as an outlier. The statistics can be found in Tab. 8.5.

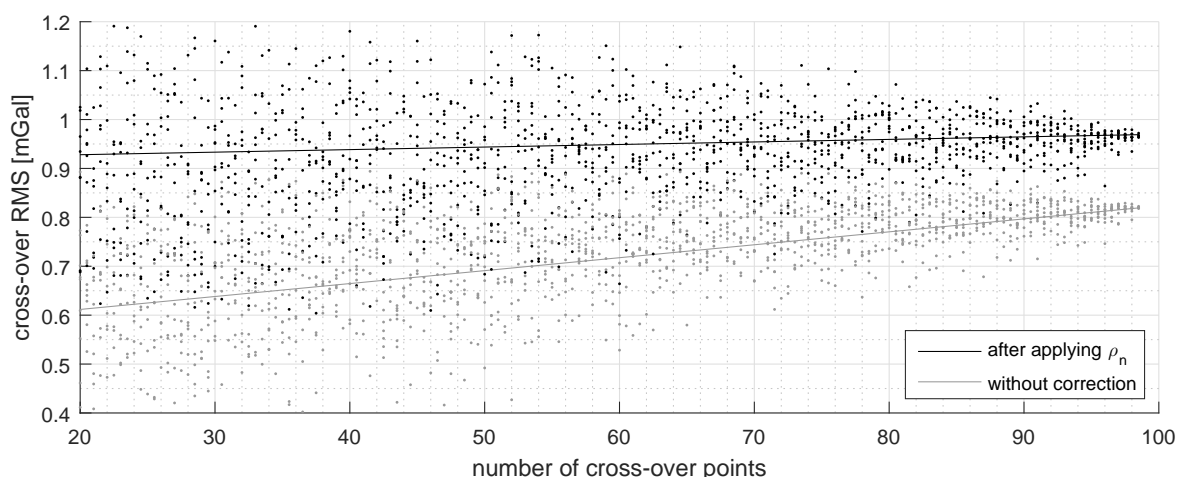


Figure 8.12: Adjusted cross-over residuals (RMS) for the Malaysia 2014 data set, after randomly removing subsets of cross-points from the total set of 99 cross points. In addition, linear regression polynomials are shown. The figure illustrates the effectiveness of applying the correction factor ρ_n (cf. Sect. 7.1.1).

		Malaysia 2014 DoV cross-over residuals: RMS ["] (RMSE ["])						
		C_0	C_1	C_2	C_3	C_4	C_5	C_6
ξ		1.60 (1.13)	1.60 (1.13)	1.60 (1.13)	1.60 (1.13)	1.60 (1.13)	1.64 (1.16)	1.65 (1.16)
η		1.66 (1.17)	1.66 (1.17)	1.66 (1.17)	1.65 (1.17)	1.65 (1.16)	1.67 (1.18)	1.65 (1.17)

		Malaysia 2015 DoV cross-over residuals: RMS ["] (RMSE ["])						
		C_0	C_1	C_2	C_3	C_4	C_5	C_6
ξ		1.07 (0.76)	1.07 (0.76)	1.07 (0.76)	1.07 (0.76)	1.06 (0.75)	1.09 (0.77)	1.08 (0.77)
η		1.10 (0.78)	1.10 (0.78)	1.10 (0.78)	1.10 (0.78)	1.11 (0.78)	1.08 (0.77)	1.06 (0.75)

Table 8.15: DoV cross-over residual statistics. A constant bias was estimated and removed from each of the lines. The analysis is limited to cross-over points with a height difference of $\Delta h < 100$ m (2014: 99 points, 2015: 271 points).

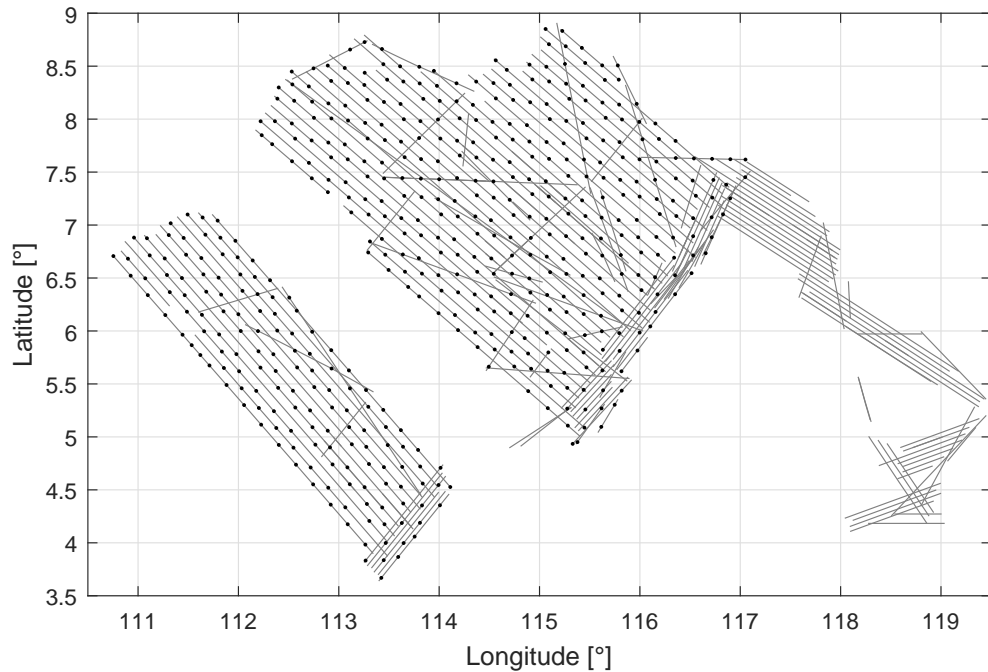


Figure 8.13: Quasi-regular grid with 20 km average grid spacing for the Malaysia campaigns, used for the comparison of the strapdown airborne gravity data against the GGM05C global gravity model (cf. Tab. 8.16).

		Malaysia: mean(RQH-GGM05C) [mGal]						
		C_0	C_1	C_2	C_3	C_4	C_5	C_6
R_0		2.93	1.15	2.02	1.81	1.79	0.32	0.03
R_1		3.00	1.22	2.10	1.88	1.87	0.39	0.10
R_2		2.89	1.12	1.99	1.78	1.77	0.29	0.02
R_3		2.91	1.14	2.01	1.81	1.79	0.32	0.04

Table 8.16: Mean difference of the strapdown gravity data minus GGM05C, evaluated at flight altitude for the quasi-regular grid depicted in Fig. 8.13 (488 points).

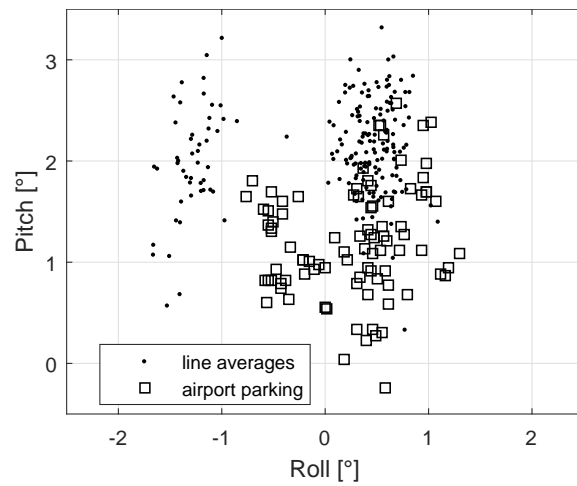


Figure 8.14: Combinations of average roll- and pitch-angles for the Malaysia campaigns. The 2014 campaign measurement lines have a systematically lower roll angle (around -1.3°). The same aircraft and hardware set-up was used for the 2015 campaign, however one of the aircraft engines underwent a major maintenance, presumably explaining the shift of the average roll-angle to approximately 0.5° . See also App. A.1.

8.3 Northern Mozambique and Malawi (2015)

An overview of the Northern Mozambique and Malawi campaign is shown in Fig. 8.15. The air-conditioning system of the Cessna 208 aircraft apparently yielded a very stable cabin temperature, which is evident from the sensor temperature curves shown in Fig. 8.16. Initially, all of the curves indicate a considerable warm-up of the sensor. At the final parking position on the destination airport, the sensor temperature increases, because the air conditioning system was turned off.

8.3.1 Cross-over analysis

The non-adjusted cross-over statistics are shown in Tab. 8.17, again for different combinations of gravity reduction (R_0 – R_3) and accelerometer calibrations (C_0 – C_6). The same correlation parameters were used as for the Chile campaign: $\beta_{dg}^{3rd} = 1/10 \text{ km}^{-1}$ for R_0 and R_1 (no terrain reduction), and $\beta_{dg}^{3rd} = 1/20 \text{ km}^{-1}$ for R_2 and R_3 (with terrain reduction). These settings were determined empirically, on the data.

Flights 285, 287, and 299 are *not* included in the cross-over statistics, because they could not be processed from start to end due to IMU data acquisition problems: Short power outages resulted in gaps in the data recordings. These flights could still be processed, but the linear drift removal based on the terrestrial gravity ties (cf. Sect. 7.1.3) was impossible for these flights. It is just noted here, that *including* these flights in the statistics leads to higher cross-over residuals of approximately 1.9 mGal (RMS) instead of 1.3 mGal. Again, this emphasises the importance of a gap-free data recording from the original airport to the destination airport.

Again, the accelerometer calibrations lead to considerable improvements, with cross-over residuals decreasing from 3 mGal to approximately 1 mGal (RMSE). The terrain reductions (R_2 and R_3) yield equal or slightly better results among the different calibration methods. Best results are again provided by the sample-based TRP calibration methods, C_5 and C_6 (Sect. 6.6.1).

Due to the lack of sufficient cross-over points at equal altitude, no meaningful adjusted cross-over statistics are available for this data set. Consequently, no cross-over statistics are presented for the deflections of the vertical.

	Cross-over residuals: RMS [mGal] (RMSE [mGal])						
	C_0	C_1	C_2	C_3	C_4	C_5	C_6
R_0	4.10 (2.90)	1.69 (1.20)	1.58 (1.12)	1.61 (1.14)	1.52 (1.07)	1.28 (0.91)	1.29 (0.91)
R_1	4.11 (2.91)	1.69 (1.19)	1.58 (1.12)	1.60 (1.13)	1.51 (1.07)	1.28 (0.90)	1.29 (0.91)
R_2	4.20 (2.97)	1.47 (1.04)	1.62 (1.14)	1.42 (1.00)	1.34 (0.95)	1.44 (1.02)	1.44 (1.02)
R_3	4.22 (2.98)	1.41 (1.00)	1.66 (1.17)	1.37 (0.97)	1.30 (0.92)	1.44 (1.01)	1.43 (1.01)

Table 8.17: Mozambique/Malawi: Cross-over residual statistics, excluding flights 285, 287, and 299 (see text). No cross-over adjustment was applied. The analysis is limited to cross-over points with a height difference of $\Delta h < 100 \text{ m}$ (33 points). The best result is highlighted.

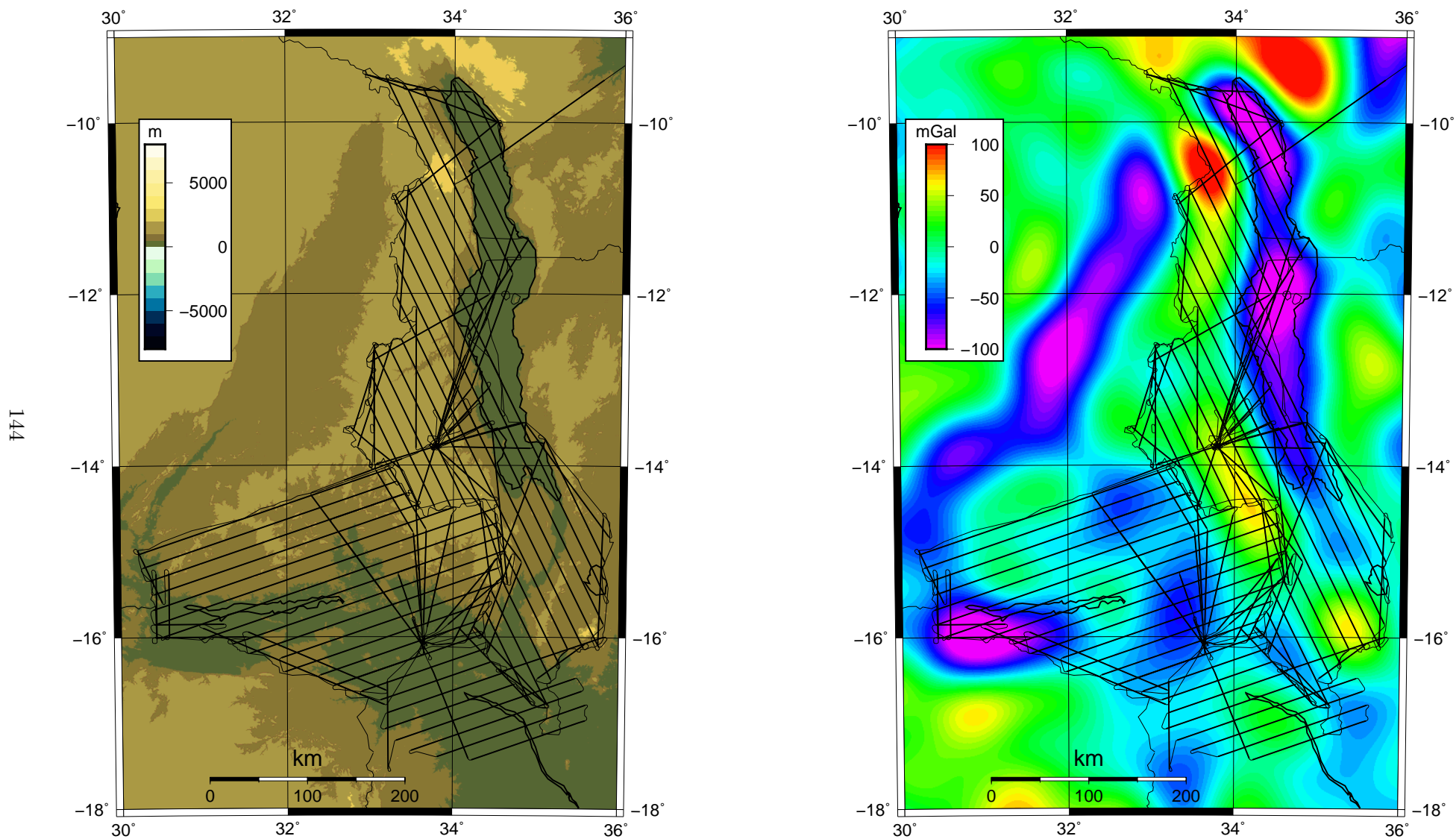


Figure 8.15: Overview of the Northern Mozambique and Malawi aerogravity campaigns. The measurement lines are highlighted (bold lines). *Left:* Topography. *Right:* Gravity anomalies of the GGM05C global gravity model (*Ries et al., 2016*), computed to degree and order 360.

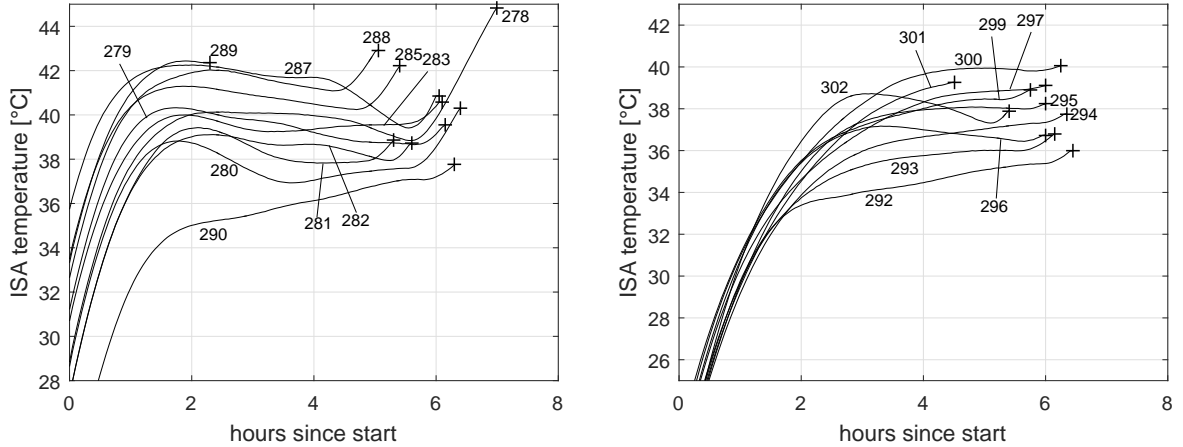


Figure 8.16: Temperature over time. *Left*: Mozambique flights, *Right*: Malawi flights.

8.3.2 Comparison against GGM05C

The comparison statistics against the GGM05C global gravity model (*Ries et al.*, 2016) are shown in Tabs. 8.18 and 8.19. For the Mozambique flights, the comparison again indicates best results for the sample-based TRP calibration methods, again showing an agreement better than 1 mGal (as for the Chile and Malaysia campaigns).

The comparison for the Malawi flights however indicates a significant bias between the two data sets of several mGal. The reason for this is unknown. Possible explanations are:

- The terrestrial gravity tie at the Lilongwe base airport in Malawi has an error of several mGal. However, the cross-over points connecting the two data sets (Northern Mozambique and Malawi) do not show such a systematic offset. The internal agreement is at the level of 1 mGal to 1.5 mGal.
- The different combinations of roll- and pitch angles at the airport parking positions may allow systematic roll- and pitch-dependent errors to propagate into the estimates. The average roll- and pitch angles of the measurement lines and the airport alignment phases are shown in Fig. 8.18. The airport averages differ by 1.5° for the roll angle, and 0.5° for the pitch angle. While this is indeed a significant offset, it appears too small to yield a systematic offset of the order of 5 mGal (cf. Sect. 6.6.1). Again, the good internal agreement between the two data sets contradicts this hypothesis.
- It can be seen in Fig. 8.15 (right), that some structures in the GGM05C gravity data systematically correlate with the shape of the covered region of airborne data, mainly the North-Eastern region, along Lake Malawi (34.5° latitude). This strong negative gravity disturbance apparently yields systematic effects for the comparison, as can be seen by the cluster of 13 outliers with a difference RQH–GGM05C of less than -65 mGal, depicted in Fig. 8.17. The histograms of the point differences of both data sets are shown in Figs. 8.19 and 8.20.
- The strapdown airborne gravity estimates contain large errors, which could not be discovered using the cross-over analysis. However, the outliers shown in Fig. 8.20 are spread among two flights (292 and 293), making this hypothesis less probable.

No final conclusion can be drawn here regarding this systematic bias of the Malawi data set with respect to the gridded GGM05C data. The cluster of outliers in the Northeast however strongly supports the assumption, that the GGM05C grid points do not provide an accurate reference mean gravity value for this region.

This example also shows, that adjusting airborne gravity data based on data from global gravity models may introduce systematic errors, potentially *worsening* the airborne gravity data.

	Mozambique: mean(RQH–GGM05C) [mGal]						
	C_0	C_1	C_2	C_3	C_4	C_5	C_6
R_0	6.47	1.37	3.05	2.62	2.47	-0.40	-0.69
R_1	6.41	1.30	2.99	2.56	2.41	-0.46	-0.76
R_2	6.58	1.48	3.16	2.73	2.58	-0.29	-0.58
R_3	6.52	1.41	3.09	2.66	2.52	-0.35	-0.65

Table 8.18: Mozambique 2015: Mean difference of the strapdown gravity data minus GGM05C, evaluated at flight altitude for the quasi-regular grid depicted in Fig. 8.17 (257 points, black dots). Flights 285 and 287 are excluded from the analysis.

	Malawi: mean(RQH–GGM05C) [mGal]						
	C_0	C_1	C_2	C_3	C_4	C_5	C_6
R_0	3.02	-7.18	-2.53	-5.27	-5.14	-6.48	-6.65
R_1	2.95	-7.26	-2.61	-5.35	-5.22	-6.56	-6.73
R_2	3.07	-7.13	-2.48	-5.22	-5.09	-6.43	-6.61
R_3	2.97	-7.24	-2.59	-5.33	-5.20	-6.54	-6.71

Table 8.19: Malawi 2015: Mean difference of the strapdown gravity data minus GGM05C, evaluated at flight altitude for the quasi-regular grid depicted in Fig. 8.17 (278 points, grey dots). Flight 299 is excluded from the analysis.

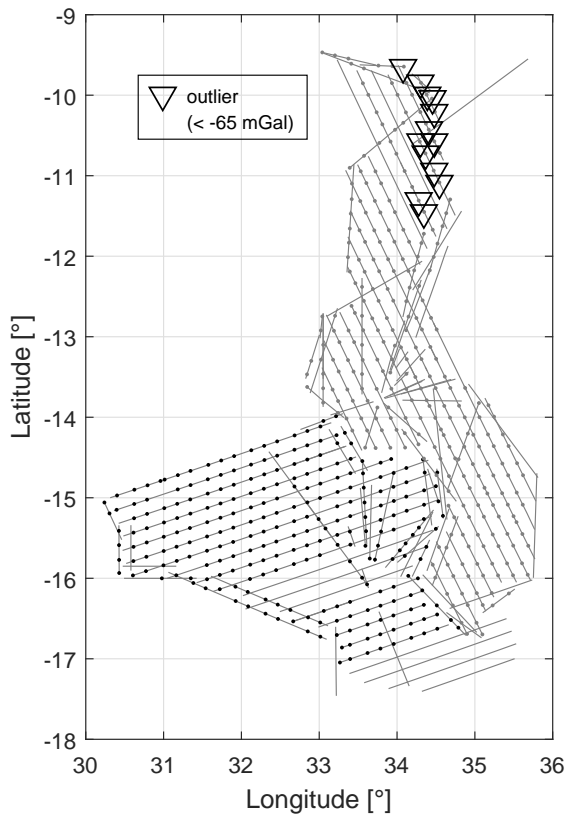


Figure 8.17: Quasi-regular grid with 20 km average grid spacing for the Mozambique (lower left) and Malawi (right) campaign, used for the comparison of the strapdown airborne gravity data against the GGM05C global gravity model (cf. Tab. 8.16). Again, flights 285, 287, and 299 are excluded from the comparison. Outliers of the comparison against GGM05C are highlighted.

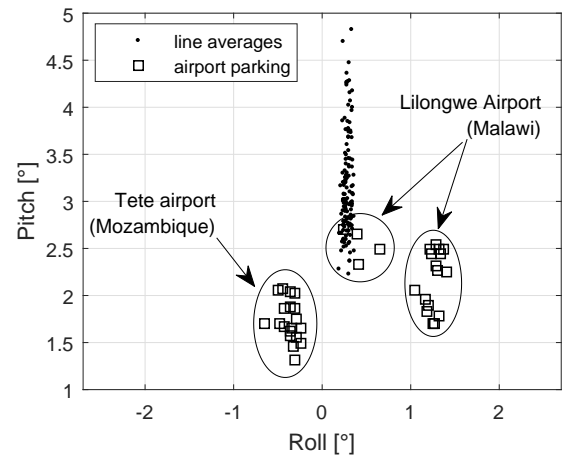


Figure 8.18: Mozambique/Malawi: Average roll- and pitch angles on the measurement lines, and at the airport parking positions.

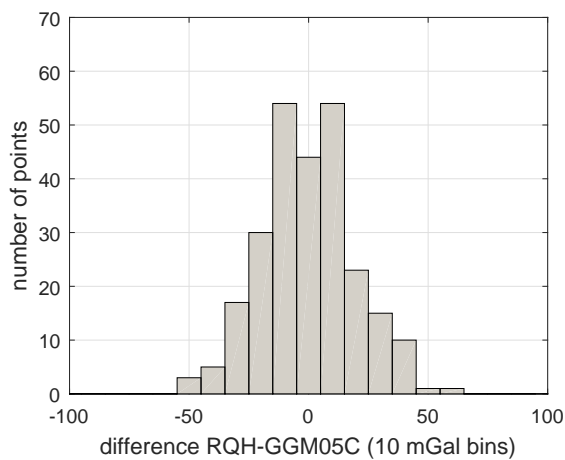


Figure 8.19: Mozambique: Histogram of grid point differences RQH-GGM05C for calibration method C_5 (black dots in Fig. 8.17).

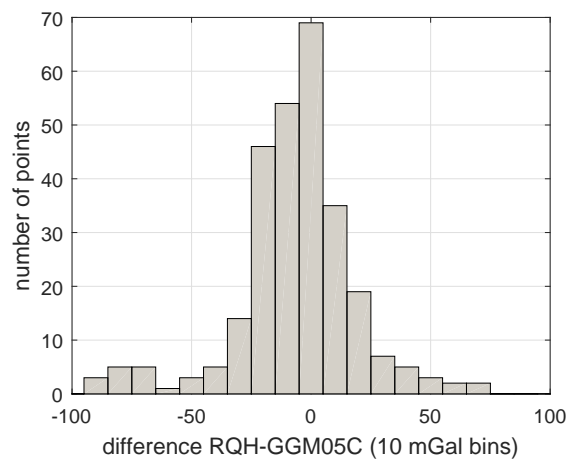


Figure 8.20: Malawi: Histogram of grid point differences RQH-GGM05C for calibration method C_5 (grey dots in Fig. 8.17).

8.4 PolarGap campaign, Antarctica (2015/2016)

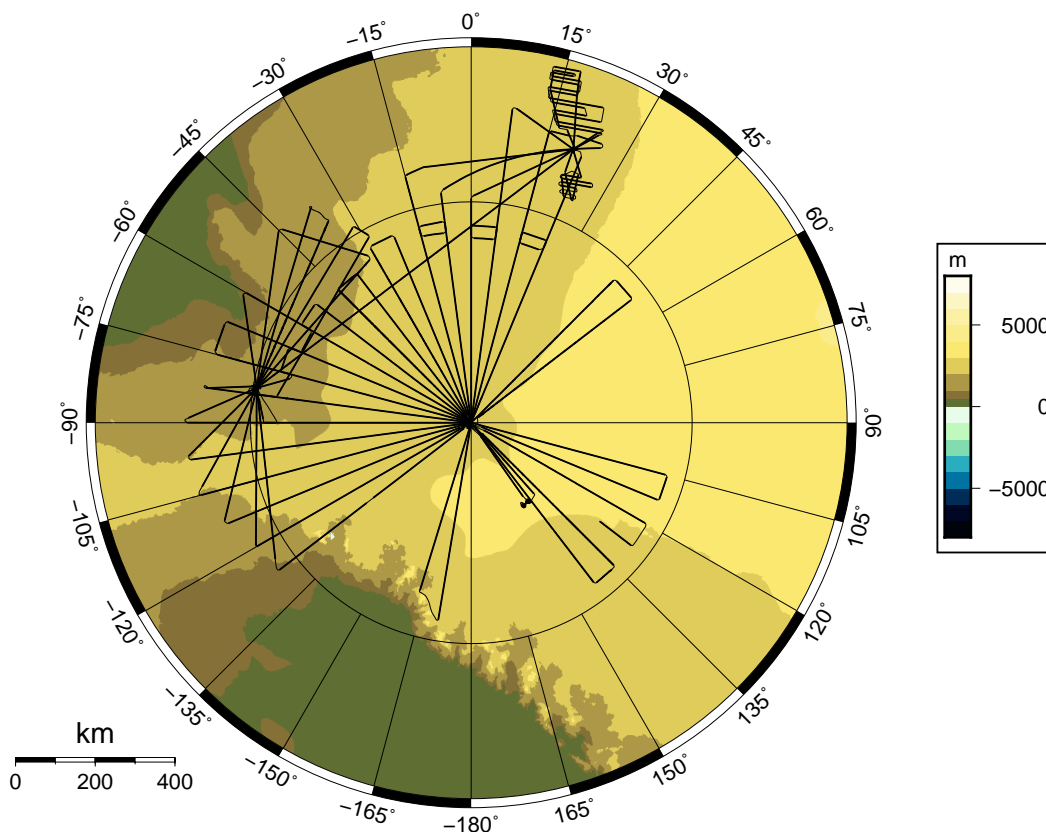


Figure 8.21: Overview of the PolarGap aerogravity campaign (2015/2016). The measurement lines are highlighted (bold lines). The inner circle represents the parallel at -85° .

The PolarGap campaign was carried out in Antarctica in December 2015 and January 2016. The main goal of this campaign was the gravity determination at very low altitudes ($\varphi < -85^\circ$), as this region is not covered by satellite gravity data. The iMAR RQH-1003 IMU was again flown side-by-side with a LaCoste & Romberg S-type gravity meter (LCR). Two GNSS receiver types were used for redundancy: a Javad Delta-3 receiver, and a Novatel OEM-V receiver. For both receivers, PPP solutions were computed using the software Waypoint GrafNav (*Novatel Inc.*, 2014). It is just noted here, that the choice of the GNSS receiver among the two available data sets did not significantly affect the quality of the strapdown gravity determination.

For the strapdown gravity processing, the PolarGap data set is a particularly challenging one:

- Many of the flights start and end at the South Pole station. For the strapdown processing, this introduces difficulties with the alignment: Gyro-compassing is impossible at the poles. (A strategy to circumvent this problem is presented the following section.)
- Limited battery power prevented a sufficiently long IMU warm-up period on ground before the flights. As a result, very large internal sensor temperature ranges, starting from below -5°C , can be observed in the data (Fig. 8.22). The warm-up calibration C_1 is not applied to this data set, because the extrapolation from the range of 20°C to 43°C to temperatures below 0°C can not be expected to yield any useful results.
- The flights were operated manually by the pilots. An autopilot was not available. As a result, relatively strong correction manoeuvres can be observed on the measurement

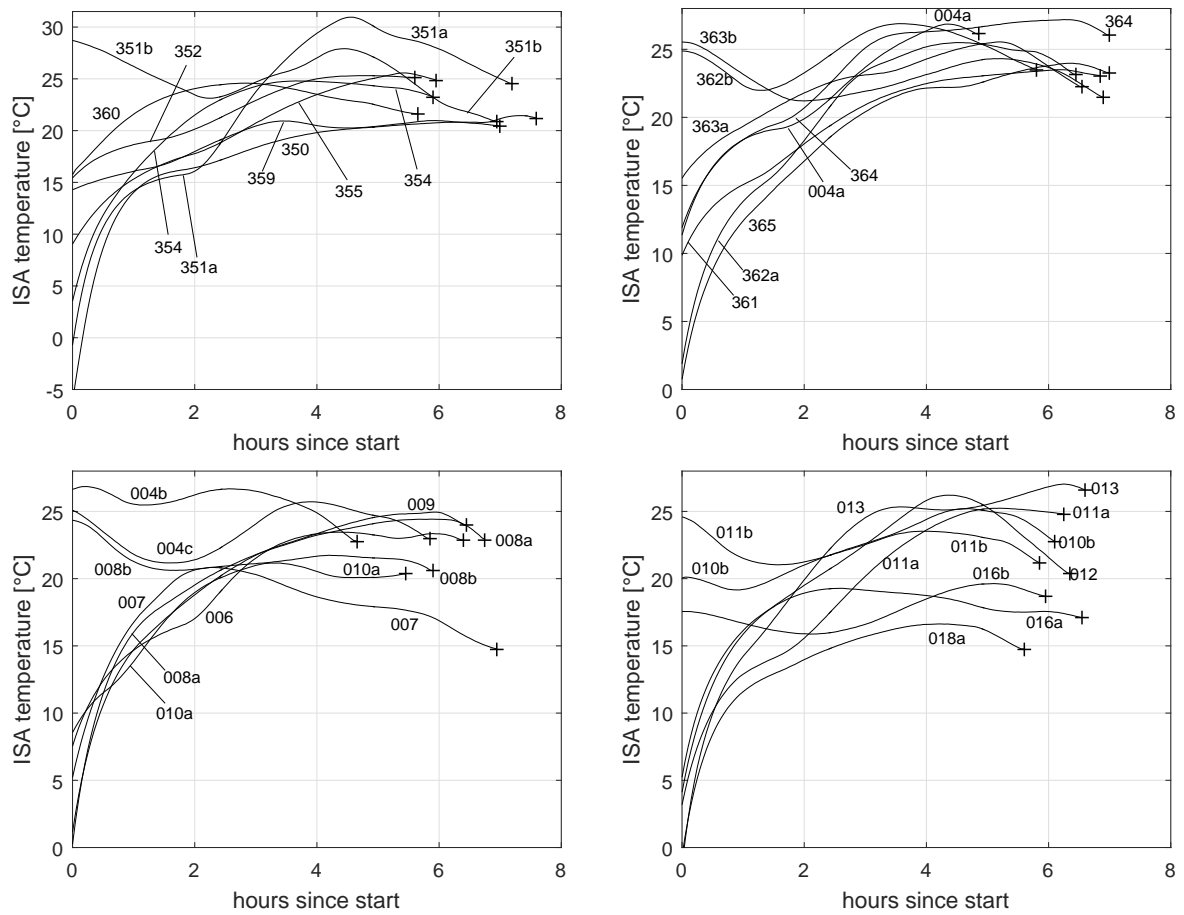


Figure 8.22: Sensor temperatures for the PolarGap Antarctica campaign.

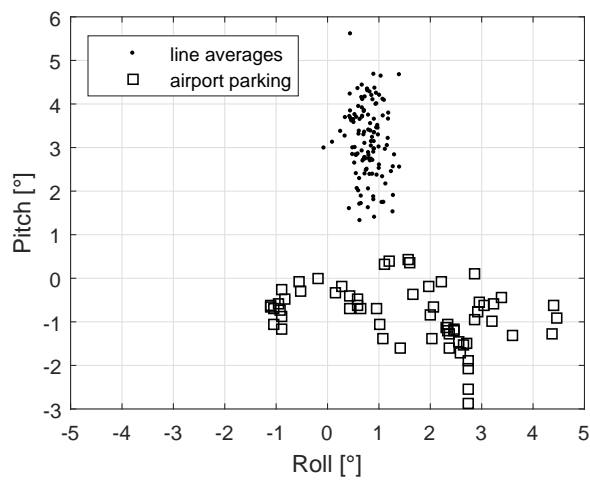


Figure 8.23: PolarGap campaign: Average roll- and pitch angles on the measurement lines, and on the airport parking positions.

lines, to maintain a constant speed, course, and flight altitude. This can clearly be seen by the wider range of observed roll and pitch angles on the measurement lines, compared to the other campaigns, see Fig. A.1 and App. A.1.

- The weather conditions have led to strong turbulence for most of the measurement lines, see App. A.2.
- Due to data acquisition errors of both the iMAR RQH-1003 strapdown IMU and the GNSS receivers, the flights 360, 010a, and 011a could not be processed from start to end, preventing the removal of a linear drift based on the terrestrial gravity ties.
- The average GNSS satellite elevation angles at the poles are relatively low. This introduces a larger uncertainty in the vertical GNSS coordinate.
- The average roll- and pitch angles at the aircraft parking positions have a significantly wider spread compared to the campaigns shown in the previous sections, see Fig. 8.23. (The aircraft was parked on ice.) Uncalibrated roll- and pitch-dependent accelerometer errors may significantly propagate into the gravity estimates.

For the region covered by the PolarGap campaign data set, no reliable *high-resolution* bedrock and ice thickness data is available. As could be seen in the previous sections, only the high-resolution topographic effect showed a significant benefit for the gravity determination, for along-track wavelengths of approximately 100 s and less, equivalent to a half-wavelength spatial resolution of approximately 3 km to 5 km. The BEDMAP2 data set contains bedrock and ice thickness information for Antarctica, however the data basis in the region covered by the PolarGap campaign is rather sparse, as can be seen in *Fretwell et al. (2013)*.

Further, the satellite-based global gravity models do not provide reliable information for the polar regions. Therefore, *no* gravity reductions were applied for the processing (R_0 only).

8.4.1 Heading initialisation without gyro-compassing

The north-finding procedure is based on the fundamental assumption, that the Earth's rotation rate can only be sensed around the North- and Down-axes. Thus, for a static alignment, $\omega_{ib}^E = 0$. At the poles, the Earth's rotation can however *only* be sensed around the Down-axis, while $\omega_{ib}^N = 0$, preventing the initial heading angle determination by gyro-compassing. Also, when initialising at high latitudes ($|\varphi| > 70^\circ$), the gyro-compassing is subject to larger uncertainties, because the North-component of the Earth rotation vector, $\omega_e \cdot \cos(\varphi)$, is relatively weak.

To cope with this issue, the Kalamn filter processing is done for this data set using an iterative *two-pass* approach. For each of the individual flights, the following steps are performed:

1. The heading angle is initialised with a large heading uncertainty (90° at the South Pole station, and 15° for the other base stations at $\varphi \approx -83^\circ$ and $\varphi \approx -85^\circ$).
2. All flights are processed in forward and backward direction. Along the flight tracks, the attitude converges to the true value, mainly due to manoeuvres with accelerations, cf. Sect. 4.2. At the end of the flight tracks, the attitude estimates can then be expected close to the true value (typically better than one arc minute for the heading).
3. For the second pass, the filter is initialised with the attitude estimates, and also attitude accuracy estimates, *taken from the first pass*: For the forward processing, the initial heading is taken from the last epoch of the backward-processed estimates, and vice versa.

4. Reliable gravity estimates are then provided by the second pass. (For the first pass, in particular for the South Pole flights, the attitude errors significantly propagate into the gravity estimates.)

8.4.2 Cross-over analysis

The non-adjusted cross-over residual statistics are shown in Tab. 8.20. All flights are included in the statistics, however there is a significant number of measurement lines which are not adjacent to any cross-over point (cf. App. A.2). The shown statistics are still expected to provide meaningful quality estimates, however it should be noted, that the shown RMS values only represent $\approx 50\%$ of the flight lines (cf. Fig. 8.21). The warm-up calibration C_1 was not applied, as mentioned above. The BSC and BSSC calibrations (C_3 and C_4) were implemented for ambient temperatures in the range from $10\text{ }^\circ\text{C}$ to $40\text{ }^\circ\text{C}$ (with internal sensor temperatures starting at $22\text{ }^\circ\text{C}$). Thus, relevant extrapolation errors have to be expected also when applying these calibrations, evident in Tab. 8.20 from the very poor cross-over precision.

The estimated precision of 1.9 mGal is significantly worse compared to all other campaigns evaluated in the scope of this thesis (a factor of ≈ 2), presumably coming from the particular difficulties for this data set as discussed in the previous section. The best results are provided by the temperature-chamber calibration C_2 , and the sample-based approaches C_5 and C_6 .

A deeper analysis, e.g. comparisons against terrain effects and global gravity models, can not be carried out due to the lack of reliable reference data sets. It is just noted here, that a combined solution with the LCR gravity data may yield an optimised gravity data set, circumventing the strapdown long-term instability, which is presumably coming from thermal effects.

	Cross-over residuals: RMS [mGal] (RMSE [mGal])						
	C_0	C_1	C_2	C_3	C_4	C_5	C_6
R_0	4.0 (2.8)	–	2.6 (1.9)	(5.9 (4.2))	(5.4 (3.8))	2.8 (2.0)	2.8 (2.0)

Table 8.20: PolarGap campaign: Cross-over residual statistics. No cross-over adjustment was applied. The analysis is limited to cross-over points with a height difference of $\Delta h < 100\text{ m}$ (42 points). The results for C_3 and C_4 presumably suffer from strong extrapolation errors. The best result is highlighted.

8.5 Effect of turbulence

The effect of turbulence shall be quantified here using the results from the cross-over analyses. The Malaysia and Mozambique/Malawi data sets are chosen, because they contain a sufficient amount of cross-over points to allow the deduction of a general statement for the strapdown gravimetry system.

RMS-g values are computed for all measurement lines of both data sets, using a time-window of 10s, cf. Sect. 7.3. The results are shown in Fig. 8.24. Apparently, there is *no* recognisable relation between turbulence, and the quality of the strapdown airborne gravity data. This is an important result in practice. It indicates, that strapdown gravimetry is capable of providing reliable gravity estimates during flight segments containing strong turbulence.

Conversely, mechanical spring-gravimeters (as the LaCoste & Romberg S-type gravimeter) are known to be rather sensitive to strong turbulence.

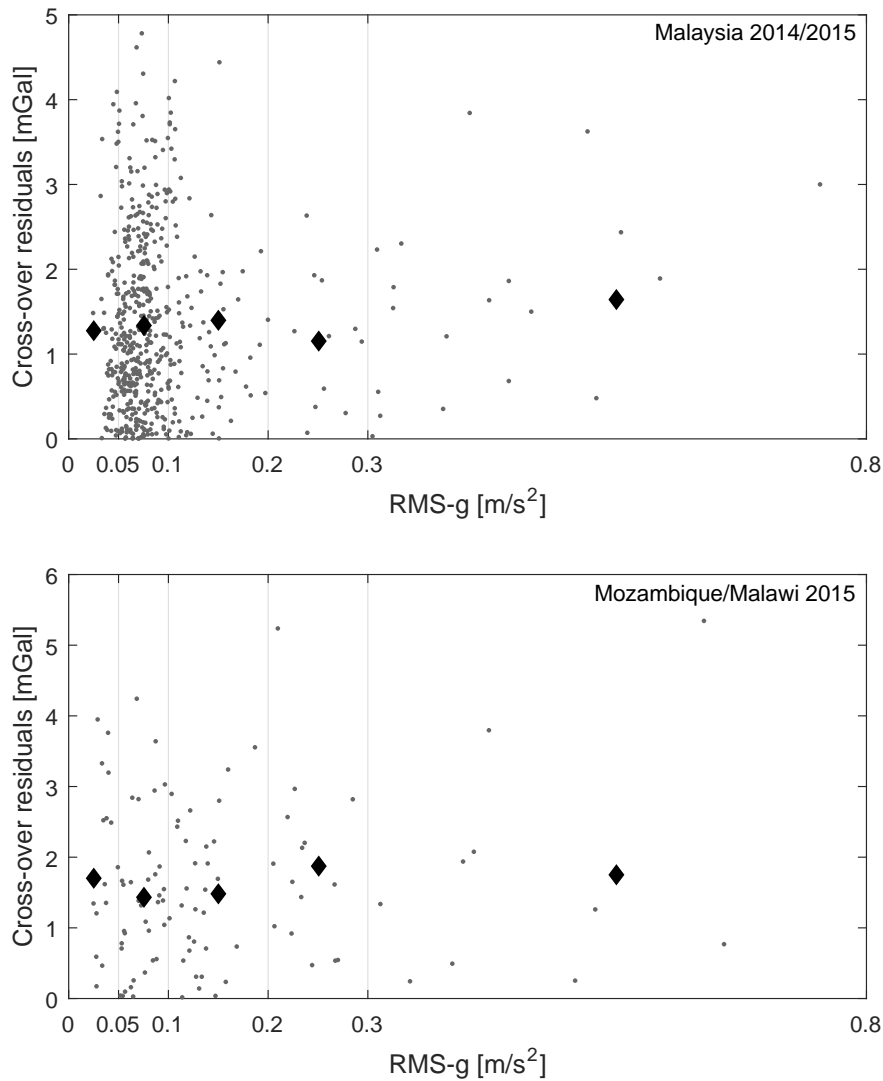


Figure 8.24: Cross-over residuals for cross over points with $\Delta h < 100$ m, plotted against the actual RMS-g values. *Top:* Malaysia 2014/2015 (combined, 403 points). *Bottom:* Mozambique/Malawi 2015 (122 points).

The *maximum* RMS-g value of the two intersecting measurement lines is used for each point. Five bins are defined. The bin intervals are depicted by the vertical grid lines. The average cross-over residual for each bin is shown as a diamond-shaped marker.

8.6 Summary

The results of the four aerogravity campaigns are summarised in Tabs. 8.21 and 8.22. For those data sets, that were processed using different gravity reduction types R_0 to R_3 , the best result is presented.

	Cross-over residuals: RMSE [mGal]						
	C_0	C_1	C_2	C_3	C_4	C_5	C_6
Chile	3.3	0.9	2.0	1.3	1.2	1.2	1.3
Malaysia 2014	1.5	1.0	1.1	1.0	1.0	0.9	0.8
Malaysia 2015	2.1	1.0	1.6	1.2	1.2	1.3	1.3
Mozambique/Malawi	2.9	1.0	1.1	1.0	0.9	0.9	0.9
Antarctica PolarGap	2.8	–	1.9	(4.2)	(3.8)	2.0	2.0
average (w/o Antarctica)	2.45	0.98	1.45	1.13	1.08	1.08	1.08

Table 8.21: Non-adjusted cross-over residuals. Best results are highlighted, and results of equal quality (within 0.1 mGal). The averages are presented excluding the results from the Antarctica campaign in order to provide a meaningful average for C_1 .

	mean(RQH-GGM05C) [mGal]						
	C_0	C_1	C_2	C_3	C_4	C_5	C_6
Chile	7.9	-1.0	2.8	-0.1	0.1	-0.5	-0.7
Malaysia 2014/2015	2.9	1.1	2.0	1.8	1.8	0.3	0.0
Mozambique	6.4	1.3	3.0	2.6	2.4	-0.3	-0.6
Malawi	(3.0)	(-7.2)	(-2.5)	(-5.2)	(-5.1)	(-6.4)	(-6.6)

Table 8.22: Biases against GGM05C. Absolute bias offsets of ≤ 1 mGal are highlighted. For the Malawi data set, the reader is referred to the discussion of Sect. 8.3.2.

Chapter 9

Conclusions

The main conclusion of the methods and results presented in this thesis is, that strapdown airborne gravimetry using an off-the-shelf navigation-grade IMU can reliably provide *non-adjusted* gravity estimates at an accuracy level of 1 mGal to 1.5 mGal, if suitable accelerometer corrections are applied. It is pointed out again, that the evaluated aerogravity campaigns were production-oriented. Except for the Antarctica campaign, the accuracy of 1 mGal could be consistently verified

- for aircraft velocities of up to 100 m/s,
- for different types of terrain (ocean, flat/coastal, high-mountain),
- for different types of aircraft,
- for different temperature ranges, and
- for flight segments with strong turbulence.

It was shown in theory, and confirmed by real data examples, that the estimation of accelerometer errors *only* using the recorded flight data itself can *not* provide gravity estimates at such quality, because the in-flight accelerometer drifts can not (or only weakly) be separated from changes of the gravity signal, which is to be determined. This is in particular relevant for flight segments of almost non-accelerated motion, as it is typically the case along the measurement lines. In theory, when using an error-free system, the introduction of *calibration manoeuvres*, including significant accelerations and attitude changes, may improve the gravity estimates, because such manoeuvres may enable the separation of attitude errors, accelerometer biases, and gravity (cf. Chap. 4). However in practice, the drawbacks of such manoeuvres, as the stronger error propagation of inertial sensor cross-couplings, lever-arm errors, or gyroscope biases, can be expected to compensate or even overcompensate the benefits of such manoeuvres for the gravity determination (cf. Chap. 5).

As a consequence, the requirement of using *off-line* calibration methods, for example in a laboratory set-up, is evident. This contradicts the well-established approach of *only* estimating accelerometer bias changes *on-line*, i.e. on the recorded data itself, by modelling the biases as random walk or Gauss-Markov process in the Kalman filter.

In general, it can be expected that the inertial sensors of a navigation-grade IMU regularly undergo a manufacturer laboratory calibration. In particular, a thermal calibration is carried out by the manufacturer for the QA-2000 accelerometers (*Honeywell International*, 2016b). It is further expected, that these manufacturer calibration methods can compensate the majority of the sensor errors. However, this thesis could clearly show, that the residual errors are still relevant for gravimetry applications. In particular, the observed residual thermal accelerometer drifts of 1 mGal/°C to 2 mGal/°C emphasise the importance of additional

calibrations. As an alternative to thermal calibrations, a thermal stabilisation system can be expected significantly improve the accelerometer stability.

The main emphasis of this thesis is put on the use of strapdown gravimetry for *geodetic* applications, as the determination of local geoid models. For this application, an adjustment of the gravity data is commonly not suggested, because systematic errors may propagate into the gravity estimates, and eventually into the estimated geoid model. For example, removing linear drifts from the strapdown gravity data set based on cross-over residuals may introduce a vertical offset, and potentially also a tilt of the gravity data set.

Similarly, it was shown for the Malawi data set, that satellite-based global gravity models have to be used with caution for the adjustment of gravity data. It could be seen in this data set, that the average GGM value along a measurement line can be off by several mGal. This is in particular the case, if local structures in the true gravity field, spatially correlate with the ground tracks of the measurement lines. The lower resolution of the GGM can then yield a systematic offset of the GGM along the measurement line with respect to the true gravity field. Such systematic, local effects may then prevent the use of satellite-based gravity data as a suitable reference, even if only the mean GGM gravity value along a measurement line is being used for the adjustment.

The calibration methods introduced in Chap. 6 are mainly designed for geodetic applications, aiming to correct *long-term* accelerometer drifts:

- Thermal effects of the accelerometers, which were shown to yield drifts of the order of tens of mGal within several hours, propagate into the relevant long-wavelength components of the gravity estimates, and
- long-term variations of the average attitude, e.g. coming from weather-dependent changes of the roll and pitch angles on the flight lines, can also generate long-term drifts in the gravity estimates. It was shown for the iMAR RQH-1003 unit, that the accelerometer errors indeed show a roll- and pitch-angle dependency (Sect. 6.6.1).

Each of the six accelerometer calibration methods evaluated in the scope of this thesis (C_1 – C_6) could be shown to significantly improve the non-adjusted gravity results,

- for the internal *precision* of the data set, as indicated by the cross-over residuals, and
- for the *absolute* level of the data set as well, indicated by the agreement with satellite gravity data for gridded data points, and by the inter-system agreement with LCR.

Combining these two quality measures, an *accuracy* of approximately 1 mGal to 1.5 mGal can be derived for the Chile, Malaysia, and Mozambique/Malawi data sets, while the gravity accuracy of the uncorrected data sets (C_0) is only of the order of 3 mGal to 6 mGal. (For the Antarctica data set, a comparison against satellite-data was not possible. The overall accuracy can be expected to be worse by a factor of 2 compared to the other data sets, presumably due to the particular challenges of this data set as discussed in Sect. 8.4).

No particular accelerometer calibration method could be found to be clearly superior with respect to the other methods, which is evident from the summary tables shown in Sect. 8.6. However, the sample-based TRP calibration methods (C_5 and C_6) show the best combined results in terms of precision (cross over residuals) and absolute gravity level (comparison against GGM05C). The simple Z-accelerometer warm-up calibration (C_1) also yields very precise results at the 1 mGal level, while the absolute gravity level was off by approximately 1 mGal for the different campaigns. Presumably, this comes from the fact, that the systematic differences between the average roll and pitch angles at the airport parking positions, and on the measurement lines, are not taken into account for this kind of calibration. Note, that the strapdown gravity data is tied to the terrestrial measurements at the airport parking

positions. Indeed, the sample-based TRP calibration, which *explicitly* models such a roll and pitch angle dependency, shows consistently better results, with biases well below 1 mGal (cf. Sect. 8.6).

Geophysical applications are mainly concerned with local structures of the gravity field, enabling the discovery of geological sub-surface features by using inversion techniques. This includes the application of mineral exploration. For such applications, an adjustment of the gravity data appears reasonable, because the local structure of the gravity field is the main interest, while an absolute stability of the gravity data over longer distances (several hundreds of km) at 1 mGal accuracy is commonly not a primary requirement. It was shown for the Malaysia data sets, that the cross-over adjusted precision of strapdown airborne gravimetry can reach a precision level of 0.5 mGal (RMSE), which is a remarkable result for an off-the-shelf navigation-grade IMU, that was actually not designed for this kind of application. When applying a cross-over adjustment, the accelerometer corrections could be shown to be less important, compared to the non-adjusted case.

The low sensitivity to turbulence underlines the practical benefits of strapdown gravimetry. In fact, being able to determine gravity during even strong turbulence can be cost-saving in practice, because less measurement lines may have to be re-flown due to perturbed gravity data. This is a particularly notable result, because the more established, platform-stabilised spring gravimeters are known to be rather sensitive to strong turbulence.

Chapter 10

Outlook

The real-data evaluation results do not clearly indicate a particular accelerometer calibration method, which outperforms the other methods for all combinations of data sets and quality measures. The significant difference between the C_1 and C_2 corrections already indicate, that the accelerometer errors are *not* only dependent on the internal temperature reading (as provided by the ISA), but also on the temperature gradient (warming-up periods versus periods of almost constant temperature). This indicates a potential of further extensions of the presented methods:

- The thermal correction might be repeated not only for different ambient temperatures, but also for different temperature gradients (yielding a two-dimensional state space). Still, a significant uncertainty may be introduced by the fact, that the provided ISA temperature does not exactly reflect the core sensor temperatures. The inhomogeneous temperature distribution inside of the ISA clearly indicates the limitations of such methods.
- The different calibration results may be combined to new, hybrid error models. For example, a combination of the warm-up calibration and the TRP calibration appears reasonable: The *absolute* level of the correction is taken from the warm-up calibration, while only the roll and pitch angle dependent error components are taken from the TRP calibration results.
- Another hybrid model could be a *temporal* concatenation of the warm-up correction, only used for the actual warm-up phase of the sensor, and one of the other calibration methods afterwards (assuming smaller temperature gradients). For such a hybrid model, it is important to implement the concatenation in a way, that the applied corrections do not contain jumps, as such jumps would directly propagate into the gravity estimates.

For the future development of strapdown gravimetry systems, the findings of this thesis support two general strategies:

1. When doing fixed-wing airborne gravimetry, there is typically sufficient space and power available in order to complement the IMU by a thermal stabilisation system. Depending on the technical specifications of a system, upgrading an existing strapdown IMU with an *internal* thermal stabilisation system may be feasible. If this is not possible, due to technical properties, or due to policy issues (manufacturer warranty), a thermally insulated housing for the IMU may be designed, with a temperature feedback loop controlling the inside air temperature of the housing.

It was shown in Sect. 6.2, that a sufficiently stable ambient temperature can yield a remarkable stability of the QA-2000 accelerometer, better than 0.1 mGal when averaging

over one hour. This emphasises the immense potential of using a thermally stabilised quartz accelerometer (as the QA-2000) for gravimetry.

It is noted, that also a thermally stabilised system should be complemented by extended laboratory calibrations, e.g. modelling attitude dependent errors.

2. The main advantages of a strapdown IMU are the low space and power consumption compared to platform-stabilised gravimeters. This enables the use of much smaller platforms, as miniature unmanned aerial vehicles (UAV). A UAV-based strapdown gravimetry system has an enormous potential in terms of operational flexibility, and cost savings. Modern miniature drones with combustion engines already provide a sufficient flight altitude and reach. For example, the Penguin-B drone (wingspan 3.3 m) enables
 - a maximum payload of 10 kg,
 - a maximum flight altitude of 4500 m,
 - a maximum endurance of up to 20 hours,
 - at a cruise speed of approximately 20 m/s, and thereby
 - a maximum reach of more than 1400 km.

The flight conditions of such a UAV-based strapdown gravimetry system can be expected to comprise

- strong temperature variations, as there is no heating or air-conditioning system available,
- considerable turbulence (because the aircraft is relatively small), and
- significant roll and pitch angle variations along the measurement lines due to changes of the wind speed and direction.

These characteristics emphasise the importance of off-line calibration methods as discussed in the scope of this thesis.

References

- Aggarwal, P., Z. Syed, and N. El-Sheimy, Thermal calibration of low cost mems sensors for land vehicle navigation system, in *Vehicular Technology Conference, 2008. VTC Spring 2008. IEEE*, pp. 2859–2863, IEEE, 2008a.
- Aggarwal, P., Z. Syed, X. Niu, and N. El-Sheimy, A standard testing and calibration procedure for low cost mems inertial sensors and units, *Journal of navigation*, 61(02), 323–336, 2008b.
- Allan, D. W., Statistics of atomic frequency standards, *Proceedings of the IEEE*, 54(2), 221–230, 1966.
- Altamimi, Z., X. Collilieux, and L. Métivier, Itrf2008: an improved solution of the international terrestrial reference frame, *Journal of Geodesy*, 85(8), 457–473, 2011.
- Amante, C., and B. W. Eakins, ETOPO1 Global Relief Model converted to PanMap layer format, doi:10.1594/PANGAEA.769615, 2009.
- Ayres-Sampaio, D., R. Deurloo, M. Bos, A. Magalhães, and L. Bastos, A comparison between three imus for strapdown airborne gravimetry, *Surveys in Geophysics*, 36(4), 571–586, 2015.
- Baram, Y., and T. Kailath, Estimability and regulability of linear systems, in *Decision and Control, 1987. 26th IEEE Conference on*, vol. 26, pp. 1706–1713, IEEE, 1987.
- Barthelmes, F., and C. Förste, The icgem-format, *Potsdam: GFZ German Research Centre for Geosciences, Department*, 1, 2011.
- Bastos, L., S. Cunha, R. Forsberg, A. Olesen, A. Gidskehaug, U. Meyer, T. Boebel, L. Timmen, G. Xu, M. Nesemann, et al., An airborne geoid mapping system for regional sea-surface topography: application to the skagerrak and azores areas, in *Geodesy on the Move*, pp. 30–36, Springer, 1998.
- Batista, P., C. Silvestre, P. Oliveira, and B. Cardeira, Accelerometer calibration and dynamic bias and gravity estimation: Analysis, design, and experimental evaluation, *Control Systems Technology, IEEE Transactions on*, 19(5), 1128–1137, 2011.
- Becker, D., and M. Becker, A study of non-stochastic imu errors in strapdown airborne gravimetry, in *Inertial Sensors and Systems Symposium (ISS), 2015 DGON*, pp. 1–18, IEEE, 2015.
- Becker, D., M. Becker, S. Leinen, and Y. Zhao, *Estimability in Strapdown Airborne Vector Gravimetry*, pp. 1–5, Springer Berlin Heidelberg, Berlin, Heidelberg, doi:10.1007/1345_2015_209, 2015a.
- Becker, D., J. E. Nielsen, D. Ayres-Sampaio, R. Forsberg, M. Becker, and L. Bastos, Drift reduction in strapdown airborne gravimetry using a simple thermal correction, *Journal of Geodesy*, 89(11), 1133–1144, 2015b.

- Becker, D., M. Becker, A. V. Olesen, J. E. Nielsen, and R. Forsberg, Latest results in strap-down airborne gravimetry using an iMAR RQH unit, in *Terrestrial Gravimetry: Static and Mobile Measurements (TG-SMM), 2016*, International Association of Geodesy (IAG), 2016.
- Becker, J. J., D. T. Sandwell, W. H. F. Smith, J. Braud, B. Binder, J. Depner, D. Fabre, J. Factor, S. Ingalls, S. H. Kim, R. Ladner, K. Marks, S. Nelson, A. Pharaoh, R. Trimmer, J. Von Rosenberg, G. Wallace, and P. Weatherall, Global Bathymetry and Elevation Data at 30 Arc Seconds Resolution: SRTM30 PLUS, *Marine Geodesy*, 32, 2009.
- Bhatt, D., P. Aggarwal, P. Bhattacharya, and V. Devabhaktuni, An enhanced mems error modeling approach based on nu-support vector regression, *Sensors*, 12(7), 9448–9466, 2012.
- Bidel, Y., O. Carraz, R. Charrière, M. Cadoret, N. Zahzam, and A. Bresson, Compact cold atom gravimeter for field applications, *Applied Physics Letters*, 102(14), 144,107, 2013.
- Bos, M., R. Deurloo, M. Bastos, and A. Magalhães, A new local geoid for madeira using airborne gravimetry, in *AGU fall meeting abstracts*, vol. 1, p. 0880, 2011.
- Boulanger, O., and M. Chouteau, Constraints in 3d gravity inversion, *Geophysical Prospecting*, 49(2), 265–280, 2001.
- Britting, K. R., *Inertial navigation systems analysis*, 1971.
- Brozena, J., The greenland aerogeophysics project: Airborne gravity, topographic and magnetic mapping of an entire continent, in *From Mars to Greenland: Charting Gravity With Space and Airborne Instruments*, pp. 203–214, Springer, 1992.
- Brozena, J., M. Peters, and R. Salman, Arctic airborne gravity measurement program, in *Gravity, Geoid and Marine Geodesy*, pp. 131–138, Springer, 1997.
- Bruton, A., Y. Hammada, S. Ferguson, K. Schwarz, M. Wei, and J. Halpenny, A comparison of inertial platform, damped 2-axis platform and strapdown airborne gravimetry, in *Proceedings of the international symposium on kinematic systems in geodesy, geomatics and navigation, Banff, Canada*, pp. 542–550, 2001.
- Bruton, A., K. Schwarz, S. Ferguson, M. Kern, and M. Wei, Deriving acceleration from dgps: toward higher resolution applications of airborne gravimetry, *GPS Solutions*, 5(3), 1–14, 2002.
- Bruton, A. M., *Improving the accuracy and resolution of SINS/DGPS airborne gravimetry*, National Library of Canada= Bibliothèque nationale du Canada, 2002.
- Cohen, C. E., B. W. Parkinson, and B. D. McNally, Flight tests of attitude determination using gps compared against an inertial navigation unit, *Navigation*, 41(1), 83–97, 1994.
- Commault, C., J.-M. Dion, and D. H. Trinh, Observability recovering by additional sensor implementation in linear structured systems, in *Decision and Control, 2005 and 2005 European Control Conference. CDC-ECC'05. 44th IEEE Conference on*, pp. 7193–7197, IEEE, 2005.
- Deurloo, R., W. Yan, M. Bos, D. Ayres-Sampaio, A. Magalhães, M. Becker, D. Becker, and L. Bastos, A comparison of the performance of medium-and high-quality inertial systems grades for strapdown airborne gravimetry, 2015.
- Deurloo, R. A., Development of a kalman filter integrating system and measurement models for a low-cost strapdown airborne gravimetry system, Ph.D. thesis, Faculty of Sciences, University of Porto, Porto, Portugal, 2011.

- Dion, J.-M., C. Commault, and J. Van Der Woude, Generic properties and control of linear structured systems: a survey, *Automatica*, 39(7), 1125–1144, 2003.
- El-Diasty, M., and S. Pagiatakis, Calibration and stochastic modelling of inertial navigation sensor errors, *Journal of Global Positioning Systems*, 7(2), 170–182, 2008.
- El-Sheimy, N., H. Hou, and X. Niu, Analysis and modeling of inertial sensors using allan variance, *Instrumentation and Measurement, IEEE Transactions on*, 57(1), 140–149, 2008.
- Forsberg, R., A study of terrain reductions, density anomalies and geophysical inversion methods in gravity field modelling, *Tech. rep.*, DTIC Document, 1984.
- Forsberg, R., and A. V. Olesen, Airborne gravity field determination, in *Sciences of Geodesy-I*, pp. 83–104, Springer, 2010.
- Forsberg, R., and C. Tscherning, The use of height data in gravity field approximation by collocation, *J. geophys. Res.*, 86(B9), 7843–7854, 1981.
- Forsberg, R., A. Vassiliou, K. Schwarz, and R. Wong, Inertial gravimetry: a comparison of kalman filtering-smoothing and post-mission adjustment techniques, *Bulletin géodésique*, 60(2), 129–142, 1986.
- Forsberg, R., A. Olesen, K. Keller, M. Møller, A. Gidskehaug, and D. Solheim, Airborne gravity and geoid surveys in the arctic and baltic seas, in *Proceedings of international symposium on kinematic systems in geodesy, geomatics and navigation (KIS-2001), Banff*, pp. 586–593, 2001.
- Fretwell, P., H. D. Pritchard, D. G. Vaughan, J. Bamber, N. Barrand, R. Bell, C. Bianchi, R. Bingham, D. Blankenship, G. Casassa, et al., Bedmap2: improved ice bed, surface and thickness datasets for antarctica, *The Cryosphere*, 7(1), 2013.
- Gelb, A., *Applied optimal estimation*, MIT press, 1974.
- Glennie, C., and K. Schwarz, A comparison and analysis of airborne gravimetry results from two strapdown inertial/dgps systems, *Journal of Geodesy*, 73(6), 311–321, 1999.
- Glennie, C., K. Schwarz, A. Bruton, R. Forsberg, A. V. Olesen, and K. Keller, A comparison of stable platform and strapdown airborne gravity, *Journal of Geodesy*, 74(5), 383–389, 2000.
- Groves, P. D., *Principles of GNSS, inertial, and multisensor integrated navigation systems*, Artech house, 2013.
- Heck, B., and K. Seitz, A comparison of the tesseroïd, prism and point-mass approaches for mass reductions in gravity field modelling, *Journal of Geodesy*, 81(2), 121–136, 2007.
- Hofmann-Wellenhof, B., and H. Moritz, *Physical geodesy*, Springer Science & Business Media, 2006.
- Hofmann-Wellenhof, B., H. Lichtenegger, and J. Collins, *Global positioning system: theory and practice*, Springer Science & Business Media, 2012.
- Honeywell International, I., GG1320AN Digital Laser Gyro specification sheet, <https://aerospace.honeywell.com/~media/aerospace/files/brochures/gg1320andigitalallasergyro-bro.pdf>, accessed: 2016-05-09, 2016a.

- Honeywell International, I., Q-Flex QA-2000 Accelerometer specification sheet, https://aerospace.honeywell.com/~media/aerospace/files/brochures/accelerometers/q-flexqa-2000accelerometer_bro.pdf, accessed: 2016-05-09, 2016b.
- Hong, S., M. H. Lee, H.-H. Chun, S.-H. Kwon, and J. L. Speyer, Observability of error states in gps/ins integration, *Vehicular Technology, IEEE Transactions on*, 54(2), 731–743, 2005.
- Hunzinger, J. F., carrier-phase differential gps, Ph.D. thesis, Department of Electrical Engineering, McGill University, Montreal, 1997.
- Hwang, C., Y.-S. Hsiao, and H.-C. Shih, Data reduction in scalar airborne gravimetry: Theory, software and case study in taiwan, *Computers & geosciences*, 32(10), 1573–1584, 2006.
- Jekeli, C., Balloon gravimetry using gps and ins, in *Position Location and Navigation Symposium, 1992. Record. 500 Years After Columbus-Navigation Challenges of Tomorrow. IEEE PLANS'92.*, IEEE, pp. 481–487, IEEE, 1992.
- Jekeli, C., Airborne vector gravimetry using precise, position-aided inertial measurement units, *Bulletin Géodésique*, 69(1), 1–11, 1994.
- Jekeli, C., *Inertial navigation systems with geodetic applications*, Walter de Gruyter, 2001.
- Jekeli, C., and R. Garcia, Gps phase accelerations for moving-base vector gravimetry, *Journal of Geodesy*, 71(10), 630–639, 1997.
- Kouba, J., and P. Héroux, Precise point positioning using igs orbit and clock products, *GPS solutions*, 5(2), 12–28, 2001.
- Kreye, C., and G. W. Hein, Gns based kinematic acceleration determination for airborne vector gravimetry-methods and results, in *Proceedings of the ION GPS/GNSS 2003 Meeting, Portland, Oregon*, 2003.
- Kwon, J. H., and C. Jekeli, A new approach for airborne vector gravimetry using gps/ins, *Journal of Geodesy*, 74(10), 690–700, 2001.
- LaCoste, L., The zero-length spring gravity meter, *The Leading Edge*, 7(7), 20–21, 1988.
- LaCoste, L. J., Measurement of gravity at sea and in the air, *Reviews of Geophysics*, 5(4), 477–526, 1967.
- Lee, M. H., W. C. Park, K. S. Lee, S. Hong, H. G. Park, H. H. Chun, and F. Harashima, Observability analysis techniques on inertial navigation systems, *Journal of System Design and Dynamics*, 6(1), 28–44, 2012.
- Lelièvre, P. G., C. G. Farquharson, and C. A. Hurich, Joint inversion of seismic traveltimes and gravity data on unstructured grids with application to mineral exploration, *Geophysics*, 77(1), K1–K15, 2012.
- Li, Y., and D. W. Oldenburg, 3-d inversion of gravity data, *Geophysics*, 63(1), 109–119, 1998.
- MacCready, P. B., The inertial subrange of atmospheric turbulence, *Journal of Geophysical Research*, 67(3), 1051–1059, 1962.
- McRuer, D. T., D. Graham, and I. Ashkenas, *Aircraft dynamics and automatic control*, Princeton University Press, 2014.
- Moon, J. H., S. Hong, H.-H. Chun, and M. H. Lee, Estimability measures and their application to gps/ins, *Journal of Mechanical Science and Technology*, 22(5), 905–913, 2008.

- Moritz, H., Geodetic reference system 1980, *Journal of Geodesy*, 54(3), 395–405, 1980.
- Nettleton, L. L., L. LaCoste, and J. C. Harrison, Tests of an airborne gravity meter, *Geophysics*, 25(1), 181–202, 1960.
- Novatel Inc., Waypoint grafnav, 2014.
- Oldenburg, D. W., The inversion and interpretation of gravity anomalies, *Geophysics*, 39(4), 526–536, 1974.
- Olesen, A. V., Improved airborne scalar gravimetry for regional gravity field mapping and geoid determination, Ph.D. thesis, Faculty of Science, University of Copenhagen, 2002.
- Pavlis, N. K., S. A. Holmes, S. C. Kenyon, and J. K. Factor, An earth gravitational model to degree 2160: Egm2008, *EGU General Assembly*, pp. 13–18, 2008.
- Rauch, H. E., C. Striebel, and F. Tung, Maximum likelihood estimates of linear dynamic systems, *AIAA journal*, 3(8), 1445–1450, 1965.
- Ries, J., S. Bettadpur, R. Eanes, Z. Kang, U. Ko, C. McCullough, P. Nagel, N. Pie, S. Poole, T. Richter, H. Save, and B. Tapley, The Combined Gravity Model GGM05C, 2016.
- Rothman, Y., I. Klein, and S. Filin, Analytical observability analysis of ins with vehicle constraints, *Navigation*, 61(3), 227–236, 2014.
- Schwarz, K., Inertial surveying and geodesy, *Reviews of Geophysics*, 21(4), 878–890, 1983.
- Schwarz, K., and M. Wei, A framework for modelling kinematic measurements in gravity field applications, *Bulletin géodésique*, 64(4), 331–346, 1990.
- Schwarz, K., and M. Wei, Some unsolved problems in airborne gravimetry, in *Gravity and Geoid*, pp. 131–150, Springer, 1995.
- Schwarz, K., O. Colombo, G. Hein, and E. Knickmeyer, Requirements for airborne vector gravimetry, in *From Mars to Greenland: Charting Gravity With Space and Airborne Instruments*, pp. 273–283, Springer, 1992.
- Shin, E.-H., and N. El-Sheimy, A new calibration method for strapdown inertial navigation systems, *Zeitschrift für Vermessungswesen.–2002.–Zfv*, 127(1), 41–50, 2002.
- Skaloud, J., I. Colomina, M. Parés, M. Blázquez, J. Silva, and M. Cherisch, Progress in airborne gravimetry by combining strapdown inertial and new satellite observations via dynamic networks, in *26th IUGG General Assembly, IAG Symposia*, EPFL-TALK-217065, 2015.
- Skog, I., and P. Händel, Calibration of a mems inertial measurement unit, in *XVII IMEKO World Congress*, pp. 1–6, Citeseer, 2006.
- Studinger, M., R. Bell, and N. Frearson, Comparison of AIRGrav and GT-1A airborne gravimeters for research applications, *Geophysics*, 73(6), I51–I61, 2008.
- Syed, Z., P. Aggarwal, C. Goodall, X. Niu, and N. El-Sheimy, A new multi-position calibration method for mems inertial navigation systems, *Measurement Science and Technology*, 18(7), 1897, 2007.
- Titterton, D., and J. L. Weston, *Strapdown inertial navigation technology*, vol. 17, The Institution of Engineering and Technology, 2004.

- Tomé, P., Integration of inertial and satellite navigation systems for aircraft attitude determination, Ph.D. thesis, Faculty of Sciences, University of Porto, Porto, Portugal, 2002.
- Torge, W., Gravimetry walter de gruyter, *Berlin–New York*, 1989.
- Torge, W., and J. Müller, *Geodesy*, Walter de Gruyter, 2012.
- Tscherning, C., R. Forsberg, P. Knudsen, and K. og Matrikelstyrelsen, Gravsoft-a system for geodetic gravity field modelling, in *Proc. 1. Continental Workshop on the Geoid in Europe, Research Institute of Geodesy, Topography and Cartography, Prague*, pp. 327–334, 1992.
- Vander Kuylen, L., P. Nemry, F. Boon, and A. Simsky, Comparison of attitude performance for multi-antenna receivers, *European Journal of Navigation*, 4(2), 1–9, 2006.
- Wei, M., and K. Schwarz, Flight test results from a strapdown airborne gravity system, *Journal of Geodesy*, 72(6), 323–332, 1998.
- Wendel, J., *Integrierte Navigationssysteme: Sensordatenfusion, GPS und Inertiale Navigation*, Walter de Gruyter, 2011.
- Yang, J., W. Wu, Y. Wu, and J. Lian, Thermal calibration for the accelerometer triad based on the sequential multiposition observation, *Instrumentation and Measurement, IEEE Transactions on*, 62(2), 467–482, 2013.
- Zahzam, N., A. Bonnin, F. Theron, M. Cadoret, Y. Bidel, and A. Bresson, New advances in the field of cold atom interferometers for onboard gravimetry, in *Terrestrial Gravimetry: Static and Mobile Measurements (TG-SMM), 2016*, International Association of Geodesy (IAG), 2016.

List of Acronyms

BSC	Bias – Scale factor – Cross coupling calibration (Sect. 6.5.1)
BSSC	Bias – double Scale factor – Cross coupling calibration (Sect. 6.5.2)
DCM	Direction-Cosine-Matrix
DoV	Deflection of the vertical (of the gravity vector)
DTM	Digital Terrain Model
EKF	Extended Kalman Filter
GNSS	Global Navigation Satellite System
GGM	Global Gravity Model
GPS	The Global Positioning System
IMU	Inertial Measurement Unit
ISA	Inertial Sensor Assembly (cf. Sect. 6.1)
KF	Kalman Filter
LCR	LaCoste & Romberg S-type spring gravimeter
NMEA	National Marine Electronics Association (navigation data streaming format)
PD-GNSS	Carrier Phase-Differential GNSS
PPP	Precise Point Positioning
PPS	Pulse Per Second
RMS	Root-Mean-Square
RMS-g	RMS of vertical accelerations (used as turbulence metric, cf. Sect. 7.3)
RMSE	Root-Mean-Square Error (= $\text{RMS}/\sqrt{2}$)
SAG	Strapdown Airborne Gravimetry
TRP	Temperature-Roll-Pitch (cf. Sect. 6.6)
UAV	Unmanned Aerial Vehicle
UTM	Universal Transverse Mercator (a map projection)



Appendix A

Detailed campaign information

A.1 Attitude characteristics

For each of the campaigns, the attitude characteristics on the lines differ significantly, coming from different aircraft speed, weather conditions, auto pilot characteristics, and aircraft model. 2-D histograms of the combinations of roll and pitch angle are depicted in Fig. A.1.

A.2 Measurement lines

For each of the aerogravity campaigns evaluated in the scope of this thesis, detailed information is provided for each of the measurement lines. For each campaign, a line overview map is provided, followed by a table with numerical properties. For the tables, the following abbreviations are being used:

- F : Flight ID
- FL : Measurement Line ID
- $topo$: topography (or bathymetry) height
- N_χ : Number of adjacent cross-over points.

Again, μ and σ denote the average, and the standard deviation, respectively.

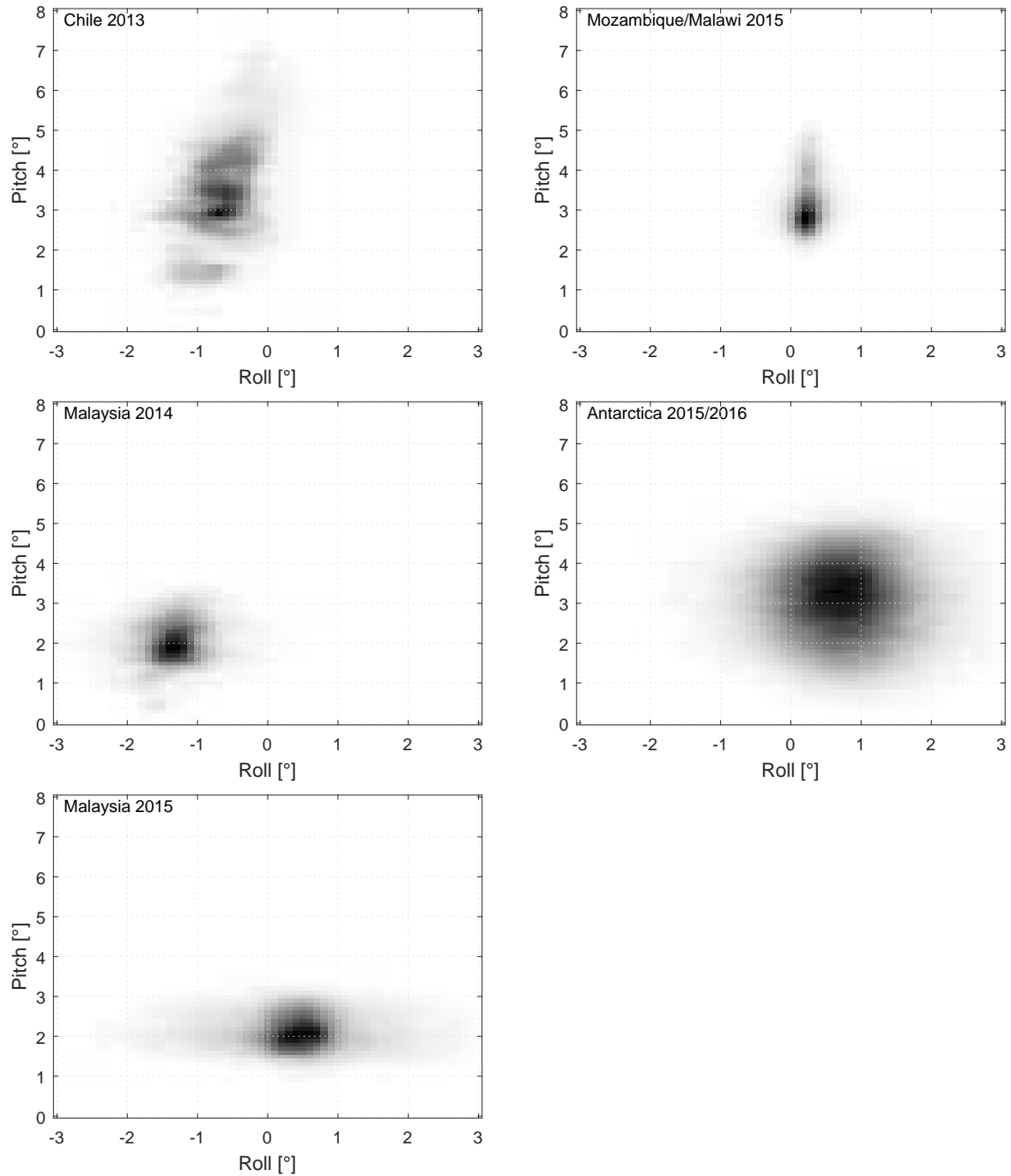


Figure A.1: Histograms of roll- and pitch angles on the measurement lines. Darker dots indicate a higher frequency of occurrence of the respective attitude.

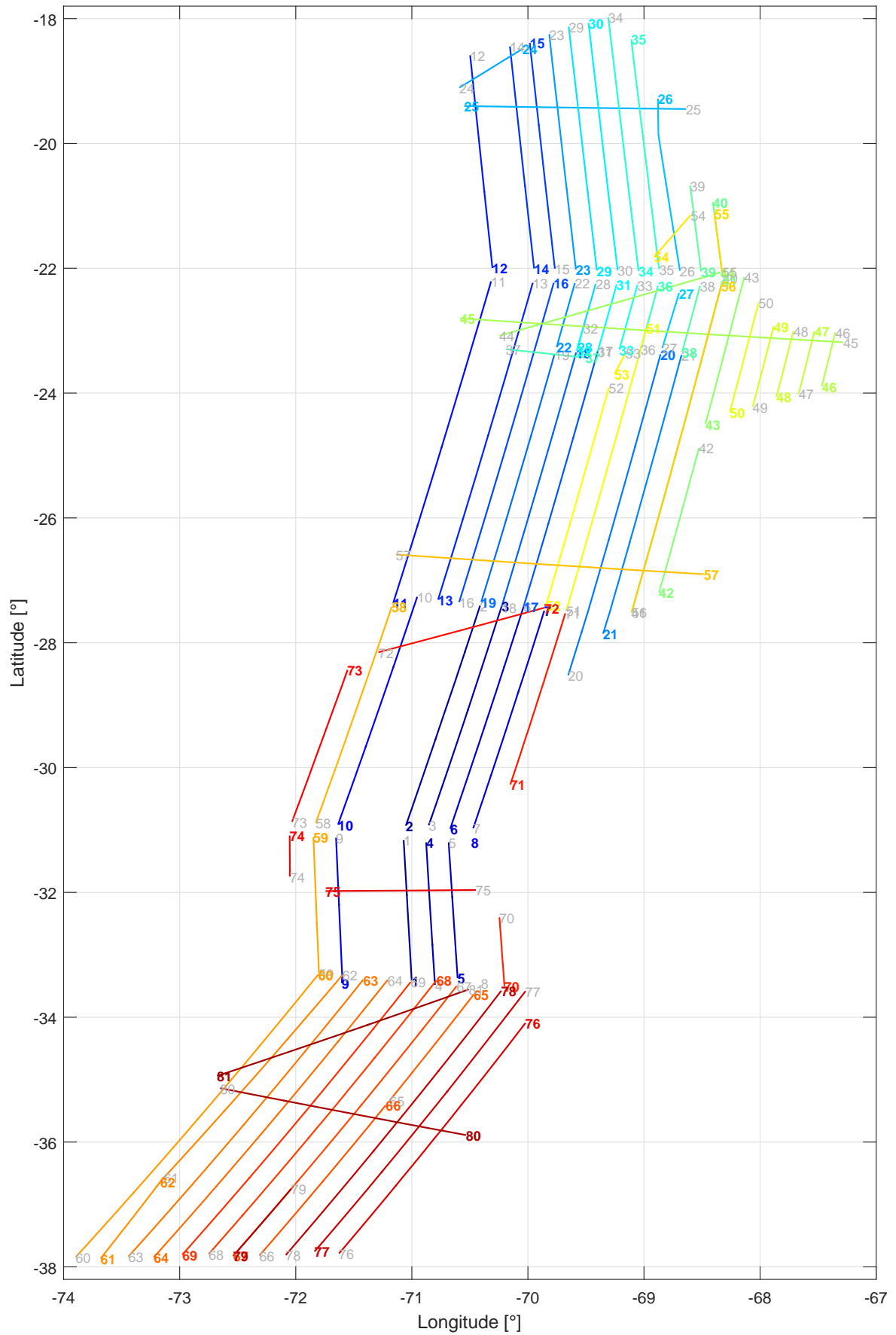


Figure A.2: Chile 2013 measurement lines. (The Scaling is considerably widened for clarity.)

Table A.1: Chile 2013: detailed line information

FL	F	dur. [h:mm]	dist. [km]	vel.	altitude	topo.	RMS-g	dg^{Down}	N_{χ}
				[m/s]	[m]	[m]	[mm/s ²]	[mGal]	
				μ/σ	μ/σ	$\mu/\text{max.}$	$\mu/\text{max.}$	$\mu/\sigma/\text{min}/\text{max}$	
1	285	0:39	250	104/1	3804/6	1135/2237	47/67	105/32/49/182	2
2	285	1:02	397	106/1	3824/4	1065/2194	63/214	77/36/15/139	2
3	285	0:50	395	129/2	4777/4	1770/3365	142/382	98/46/20/198	2
4	285	0:33	254	125/1	4759/6	1262/3225	55/148	93/50/15/230	2
5	288	0:40	242	99/2	5733/6	1971/4022	42/84	108/61/12/245	1
6	288	1:07	401	99/2	5761/10	2413/4603	186/553	117/51/46/262	2
7	288	1:05	392	100/2	6715/8	3215/5080	135/297	141/51/44/247	1
8	288	0:42	251	99/3	6693/6	2982/4268	57/157	133/39/45/195	1
9	289	0:45	259	95/4	4459/4	-149/546	42/93	49/15/32/82	2
10	289	1:11	410	96/1	4485/6	142/1022	41/191	72/27/21/128	1
11	290a	1:41	579	95/1	4500/12	-978/221	34/125	27/36/-26/95	2
12	290a	1:06	379	95/2	4532/5	-635/-37	30/63	19/29/-21/56	2
13	291	1:34	569	100/1	4517/4	998/2181	44/257	136/57/48/248	4
14	291	1:05	396	100/2	4534/4	963/1737	47/112	112/35/18/203	2
15	291	1:06	402	100/1	5511/7	1215/1835	38/126	100/28/30/143	1
16	291	1:35	574	99/3	5494/7	1283/2912	51/160	122/48/32/240	4
17	292	1:15	460	101/3	5816/10	1750/2656	30/110	51/35/-23/104	3
18	292	1:16	457	99/1	5493/9	1434/2377	31/62	66/37/-13/129	4
19	292	1:14	444	100/1	5165/7	1250/2310	37/109	84/46/-4/187	3
20	294	1:26	577	110/4	7409/33	3484/5681	58/312	108/43/21/230	1
21	294	1:15	501	111/4	8387/31	3734/5297	57/268	100/38/43/174	1
22	295	0:19	116	97/1	5813/3	1390/1620	28/38	95/16/56/116	2
23	295	1:11	419	98/3	5832/7	1305/3174	29/94	76/25/23/133	1
24	295	0:09	91	151/1	6817/3	56/1211	106/135	22/28/-34/54	2
25	295	0:32	202	103/3	6822/7	2088/4815	37/106	101/42/-3/169	9
26	295	0:48	307	104/1	6826/4	4050/4902	34/81	143/20/103/183	2
27	295	0:16	99	101/1	6807/4	2833/3279	32/60	92/24/50/128	1
28	296	0:19	114	96/2	5810/4	1439/1631	46/90	56/9/41/70	2
29	296	1:13	434	98/2	5836/10	1709/3581	57/166	63/57/-15/168	1
30	296	1:13	441	100/2	6171/7	2468/5233	57/573	80/79/-28/218	1
31	296	0:19	121	101/1	6149/4	1667/2078	97/190	27/5/19/39	3
32	296	0:06	41	95/3	5818/2	1519/1628	62/111	52/5/38/61	2
33	297	0:20	117	97/3	6478/5	2221/2786	290/608	44/13/29/74	2
34	297	1:18	452	96/3	6498/6	3213/4834	141/645	110/49/20/190	1
35	297	1:00	410	113/4	7479/6	4049/5468	102/387	147/24/98/216	2
36	297	0:15	115	119/5	7457/4	2730/3177	101/220	71/16/43/102	2
37	297	0:12	73	98/1	4849/2	1332/1916	164/538	65/36/7/141	4
38	298	0:18	119	107/2	7133/5	2930/3756	61/115	98/24/56/142	1
39	298	0:24	153	105/2	7152/4	4022/5135	104/218	133/27/93/196	1
40	298	0:20	134	106/4	7480/4	4213/5878	47/114	130/21/92/178	2
41	298	1:34	596	104/5	7435/29	3527/4758	72/325	88/40/-2/154	3
42	298	0:43	260	100/6	7728/20	4497/5515	94/538	132/16/101/166	1
43	298	0:43	265	100/4	7783/9	3036/4641	43/100	46/48/-23/140	1
44	298	0:38	226	98/3	7135/7	1955/4125	43/137	73/39/19/141	10
45	299	0:55	342	102/2	7138/9	2343/5101	26/50	88/52/-11/164	21

Table A.2: Chile 2013: detailed line information

FL	F	dur. [h:mm]	dist. [km]	vel.	altitude	topo.	RMS-g	dg^{Down}	N_χ
				[m/s] μ/σ	[m] μ/σ	[m] $\mu/\text{max.}$	[mm/s ²] $\mu/\text{max.}$	[mGal] $\mu/\sigma/\text{min}/\text{max}$	
46	299	0:15	97	102/1	7153/3	4518/5064	34/56	121/7/108/135	1
47	299	0:18	113	102/5	7152/3	4676/5422	36/68	137/20/106/175	1
48	299	0:19	119	101/3	7151/4	4403/5225	28/41	132/18/107/163	1
49	299	0:23	145	104/1	7150/3	3416/6098	30/40	71/39/28/207	1
50	299	0:31	196	103/2	7151/6	2765/4437	30/55	26/41/-13/133	1
51	299	1:22	507	102/6	6160/11	2925/3937	84/516	88/37/20/168	2
52	299	1:04	391	100/2	5831/8	2267/3021	120/478	60/35/-17/119	2
53	299	0:06	39	101/1	5843/1	2105/2447	61/92	-10/15/-25/25	0
54	301a	0:08	83	150/2	7481/3	3950/5013	109/150	144/12/127/163	3
55	301a	0:16	104	102/2	7806/1	4227/5939	55/140	123/20/91/169	1
56	301a	1:33	584	104/3	7772/19	3538/4777	45/134	87/39/-2/151	2
57	301a	0:43	267	103/2	7742/6	2155/4976	53/112	91/40/-51/145	13
58	301b	1:01	389	105/1	4327/13	-726/203	57/171	29/30/-24/84	1
59	301b	0:37	242	106/2	4274/11	-1267/-134	61/143	-16/28/-55/44	1
60	302	1:36	538	93/1	4233/16	-256/373	64/282	47/29/-33/104	3
61	302	0:27	153	93/1	4526/5	4/252	29/41	83/6/66/92	1
62	302	1:10	395	93/1	4573/16	-112/229	38/106	77/15/37/99	4
63	302	1:33	526	93/1	4881/23	280/718	29/65	95/12/70/125	2
64	302	1:34	527	92/1	5192/20	253/1166	30/90	70/20/43/137	2
65	303	0:32	201	102/3	4878/14	666/1870	251/605	13/17/-6/57	0
66	303	0:47	285	99/2	4203/13	329/718	65/535	8/5/-3/18	1
67	303	1:28	511	96/2	3904/26	297/1764	153/1006	13/18/-8/100	2
68	303	1:26	519	100/3	4224/30	275/1723	172/851	32/17/8/108	3
69	303	1:29	517	96/5	3897/23	234/1162	75/481	48/18/26/131	3
70	304	0:19	123	105/3	7536/8	3539/5279	84/149	160/31/96/231	0
71	304	0:48	309	106/5	7627/26	3667/5239	108/418	145/32/71/200	0
72	304	0:25	163	104/2	7655/12	757/2225	31/47	57/18/26/90	7
73	304	0:45	275	100/2	5372/19	-2361/-1218	40/102	-30/32/-67/24	0
74	304	0:11	73	102/3	5325/5	-2881/-2412	233/622	-76/14/-96/-56	0
75	304	0:18	123	112/4	7543/13	1019/3005	86/204	85/29/8/128	5
76	305a	1:10	435	103/4	6567/6	2254/4479	77/234	109/29/60/192	1
77	305a	1:21	492	101/3	6261/6	1972/4079	75/288	91/34/7/180	1
78	305b	1:21	500	102/3	5963/4	1230/3523	61/161	42/32/-8/156	1
79	305b	0:21	128	100/1	4405/1	158/214	50/103	-1/7/-10/10	0
80	305b	0:33	210	105/3	5654/2	597/2757	117/388	34/29/-14/97	11
81	305b	0:40	253	104/2	5653/5	150/1954	113/345	39/33/-23/93	7

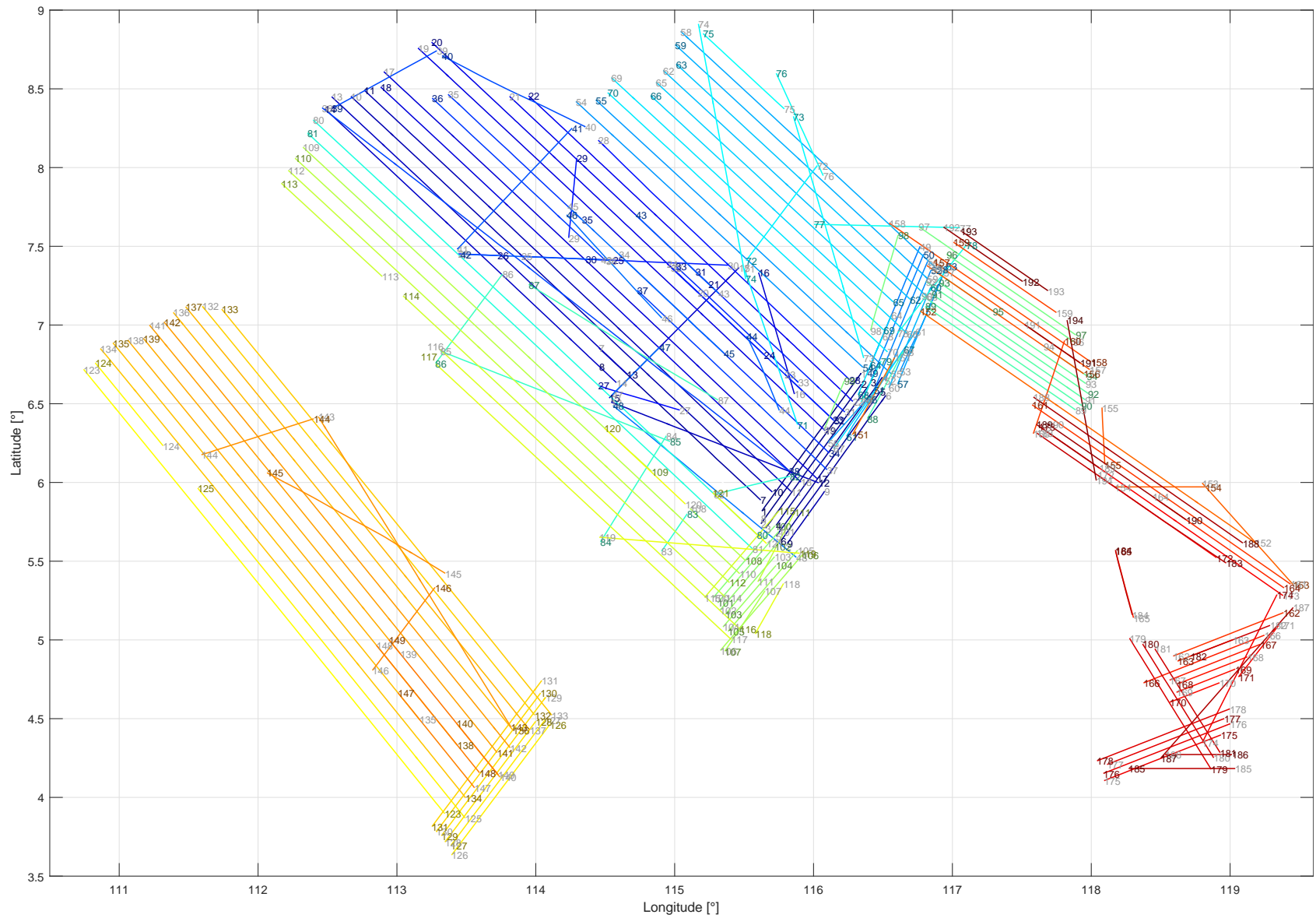


Figure A.3: Malaysia 2014/2015 measurement lines

Table A.3: Malaysia 2014/2015: detailed line information

FL	F	dur. [h:mm]	dist. [km]	vel.	altitude	topo.	RMS-g	dg^{Down}	N_{χ}
				[m/s] μ/σ	[m] μ/σ	[m] $\mu/\text{max.}$	[mm/s ²] $\mu/\text{max.}$	[mGal] $\mu/\sigma/\text{min}/\text{max}$	
1	232	0:24	126	86/1	1027/2	-40/-11	74/141	38/6/28/50	13
2	232	0:24	127	86/1	1024/2	-37/-5	76/124	37/7/23/47	8
3	233	0:25	133	87/2	1031/2	-33/41	88/231	41/9/22/54	8
4	233	0:25	135	88/1	1029/2	-35/-23	71/154	46/10/17/58	5
5	233	0:25	131	87/1	1985/3	-14/213	65/113	46/10/19/55	3
6	233	0:25	132	88/2	1983/2	2/142	84/160	48/8/22/60	0
7	234	0:31	168	88/1	1983/4	-1183/-3	68/241	24/38/-41/76	5
8	234	0:31	167	89/2	1981/3	-1065/-21	58/90	30/31/-36/76	6
9	234	0:08	48	88/3	1984/2	-8/25	103/192	40/5/26/45	0
10	235	1:22	436	88/1	1987/6	-1485/126	65/780	24/29/-43/75	10
11	235	1:22	442	89/1	1980/2	-1375/15	47/109	26/31/-47/90	12
12	236	0:33	176	87/1	1997/3	-676/-8	77/157	45/18/2/78	11
13	236	0:59	305	85/1	1987/4	-1839/29	50/233	23/28/-38/77	5
14	236	0:58	301	86/1	1985/2	-1919/-630	48/113	19/26/-36/55	6
15	236	0:26	138	87/1	1985/2	-2426/-1725	63/102	-21/12/-40/-5	21
16	236	0:17	90	87/1	1988/2	-525/-19	79/144	69/26/9/95	6
17	237	1:28	448	84/2	1998/7	-1263/135	67/315	34/34/-40/111	9
18	237	1:21	435	88/1	1997/6	-1312/4	60/345	31/34/-45/103	10
19	238	1:20	422	88/1	1986/7	-1343/3	97/586	42/32/-22/122	9
20	238	0:52	276	87/1	1981/4	-1694/3	131/949	36/35/-23/131	6
21	238	0:38	207	88/1	1982/3	-1811/31	151/713	24/36/-26/109	3
22	238	1:01	336	91/1	1978/3	-1326/-24	78/248	35/36/-28/97	9
23	239	0:09	50	88/2	2008/4	-48/-21	182/525	61/15/39/85	3
24	239	0:18	101	88/2	1999/3	-1731/-283	109/186	19/36/-24/85	3
25	239	0:14	73	85/4	1997/5	-1549/-808	281/789	34/7/25/48	7
26	239	0:06	32	83/1	1994/2	-1496/-1053	70/101	43/2/40/45	1
27	239	0:10	68	107/5	4214/3	-2080/-1459	81/283	5/17/-26/34	5
28	240	0:50	262	87/1	1974/7	-1338/8	54/119	30/41/-32/89	3
29	240	0:10	57	87/1	1963/1	-420/8	63/96	83/26/36/111	7
30	240	0:21	114	86/1	1961/2	-2536/-1612	54/114	-8/27/-33/43	11
31	240	0:29	155	87/1	1962/3	-805/-7	46/84	44/38/-33/91	6
32	240	0:32	170	86/1	1984/3	-987/-21	47/138	34/39/-32/85	7
33	240	0:24	127	87/1	1983/3	-1292/-62	40/74	33/45/-31/89	3
34	241	0:42	218	86/1	1981/6	-1271/-9	90/192	24/37/-31/78	8
35	241	0:26	138	88/1	1965/5	-948/24	74/337	53/27/14/113	3
36	241	0:33	180	90/1	1960/4	-1183/-5	81/355	47/24/16/108	4
37	241	0:37	197	87/2	1972/13	-1052/-6	120/1160	23/38/-40/75	6
38	243a	1:27	451	85/1	1998/8	-1533/-3	66/242	25/29/-43/75	9
39	243a	0:17	93	88/1	1988/2	-2050/-1611	78/130	25/5/20/38	5
40	243a	0:24	124	86/1	1992/2	-1653/-1211	97/243	39/9/22/57	2
41	243a	0:24	125	86/1	1990/2	-1126/18	88/172	41/9/26/67	13
42	243a	0:21	113	88/1	1993/1	-1334/-222	70/127	38/8/26/51	8
43	243a	0:16	86	87/1	1991/1	-2651/-1866	65/184	-12/13/-26/18	2
44	243a	0:10	59	92/1	1995/3	-226/-63	110/280	75/8/57/82	4
45	243b	0:29	162	92/8	1980/2	-1964/-3	77/270	15/42/-31/113	4

Table A.4: Malaysia 2014/2015: detailed line information

FL	F	dur.	dist.	vel.	altitude	topo.	RMS-g	dg^{Down}	N_{χ}	
		[h:mm]	[km]	[m/s]	[m]	[m]	[mm/s ²]	[mGal]		
				μ/σ	μ/σ	$\mu/\text{max.}$	$\mu/\text{max.}$	$\mu/\sigma/\text{min}/\text{max}$		
46	243b	0:15	106	110/4	1975/2	-2038/-6	83/202	13/43/-43/108	3	
47	243b	0:09	51	86/0	1981/1	-2634/-2382	63/101	-32/10/-42/-13	8	
48	243b	0:34	182	87/1	1994/5	-560/12	63/158	39/18/4/75	10	
49	140a	0:18	99	87/1	2000/2	-65/-20	47/101	36/5/24/44	7	
50	140a	0:21	112	87/1	1996/2	-55/-19	48/104	39/3/30/48	9	
51	140a	0:19	101	87/1	1997/2	-50/-19	53/98	43/2/37/47	5	
52	140a	0:16	86	87/1	1993/2	-43/7	89/217	46/3/42/50	8	
53	140a	0:15	83	88/1	2639/2	12/131	101/172	52/4/43/56	11	
54	140b	0:56	295	87/1	1997/6	-1392/47	50/106	36/39/-21/118	2	
55	140b	0:57	304	87/1	1999/7	-1324/66	59/121	32/32/-20/103	13	
56	140b	0:08	44	81/1	2003/1	-34/-28	51/87	48/4/41/53	0	
57	141a	0:16	87	87/1	2016/2	29/400	129/462	58/5/47/71	10	
58	141a	0:50	264	87/1	2005/5	-1780/-44	48/89	11/19/-26/54	6	
59	141a	0:49	259	87/1	1999/2	-1674/23	50/262	11/23/-24/64	8	
60	141a	0:14	78	87/1	1997/2	-10/59	60/108	51/3/45/56	4	
61	141b	0:17	92	89/1	2005/3	-17/74	57/85	50/3/45/58	5	
62	141b	0:48	254	87/1	1998/4	-1592/-29	66/202	19/29/-22/106	7	
63	141b	0:49	258	87/1	2001/5	-1496/35	58/105	16/25/-24/68	10	
64	142	0:07	40	87/1	2011/1	-56/-25	57/111	44/3/41/48	3	
65	142	0:46	244	87/1	2005/5	-1653/-54	67/155	25/24/-12/82	4	
66	142	0:50	264	87/1	2003/2	-1400/216	58/146	27/19/-10/54	10	
67	142	0:16	89	89/1	1999/7	-26/20	84/193	51/2/47/57	4	
68	143a	0:08	46	87/1	1990/1	-40/-19	54/92	44/2/40/48	2	
69	143a	0:53	280	87/1	1986/3	-1495/-14	66/149	28/19/-10/64	4	
70	143a	0:55	288	87/1	1984/4	-1436/-20	59/118	28/22/-14/65	7	
71	143b	0:22	118	87/1	1982/3	-517/-10	40/64	63/27/-1/95	7	
72	143b	0:16	88	87/0	1978/2	-2594/-1899	44/83	-9/7/-20/2	10	
73	143b	0:34	179	87/1	1981/2	-1396/-14	53/116	19/28/-20/59	11	
74	144	0:34	183	87/1	1998/2	-1942/269	78/198	17/28/-22/83	10	
75	144	0:15	84	87/1	2637/3	-2122/-1534	160/524	22/12/-5/43	0	
76	144	0:15	82	87/1	2635/2	-2625/-1328	95/265	0/18/-25/41	1	
77	144	0:22	117	87/1	1994/2	-684/-52	78/164	12/11/-2/46	6	
78	144	0:15	83	87/1	1996/2	-30/35	68/105	51/5/42/58	15	
79	144	0:06	33	88/0	1995/1	-42/-31	50/76	42/4/38/51	3	
80	145a	1:27	459	87/1	1977/8	-1539/20	57/183	30/26/-30/82	8	
81	145a	1:28	460	87/1	1968/3	-1552/2	65/216	29/26/-33/79	4	
82	145b	0:11	63	87/1	1987/2	-43/-18	50/71	38/4/31/46	8	
83	145b	0:06	34	87/2	1983/2	-17/-5	44/61	56/1/55/59	4	
84	145b	0:17	91	87/1	1981/1	-617/-80	40/75	67/10/50/83	12	
85	145b	0:36	194	89/2	1973/4	-2183/-991	81/441	6/29/-40/55	10	
86	145b	0:15	83	87/1	1973/2	-1676/-1191	50/87	36/6/27/55	9	
87	145b	0:32	172	87/1	1980/4	-2156/-747	54/115	-3/32/-47/53	7	
88	147a	0:10	56	89/1	1986/3	-12/11	78/130	51/2/47/55	0	
89	147a	0:26	140	87/1	1983/2	-5/69	131/623	71/19/37/98	3	
90	147a	0:28	149	87/1	1980/3	-16/27	115/609	71/21/35/104	5	

Table A.5: Malaysia 2014/2015: detailed line information

FL	F	dur. [h:mm]	dist. [km]	vel. [m/s] μ/σ	altitude [m] μ/σ	topo. [m] $\mu/\max.$	RMS-g [mm/s ²] $\mu/\max.$	dg^{Down} [mGal] $\mu/\sigma/\min/\max$	N_χ
91	147a	0:27	143	87/1	1975/2	-18/15	78/232	72/21/35/106	4
92	147a	0:28	152	87/1	1970/3	-20/49	61/112	69/21/34/105	6
93	147a	0:26	137	87/1	1964/2	-14/102	60/204	69/22/32/104	4
94	147b	0:07	41	87/1	1990/1	-33/-24	45/67	47/9/34/63	2
95	147b	0:10	57	88/1	1987/3	-5/104	112/227	83/21/52/106	3
96	147b	0:22	118	87/1	1986/2	-16/159	91/267	75/17/39/102	2
97	147b	0:27	147	87/1	1987/2	-42/35	63/105	63/25/20/95	2
98	147b	0:13	71	85/1	1984/2	-76/-32	55/89	34/4/25/43	6
99	147b	0:07	39	84/1	1987/1	-39/-18	55/79	43/3/39/52	6
100	148a	0:13	71	86/1	1982/1	7/59	39/60	24/4/17/28	7
101	148a	0:13	70	88/1	1987/2	-0/22	46/90	25/3/19/28	3
102	148a	0:11	63	86/0	1985/1	3/18	36/63	22/2/18/25	1
103	148a	0:10	57	88/1	1987/2	5/22	44/81	24/3/20/29	1
104	148a	0:11	61	88/1	1983/1	-1/28	33/51	26/3/20/30	1
105	148a	0:15	81	88/1	1986/2	5/36	51/82	33/4/25/41	3
106	148a	0:17	94	87/1	1984/1	16/221	36/63	35/3/30/43	3
107	148a	0:09	53	89/2	1986/2	-6/33	36/79	33/3/24/39	1
108	148b	0:10	58	88/1	1991/2	-22/29	34/66	38/10/26/59	3
109	148b	1:08	359	87/1	1971/7	-1943/-713	54/153	26/26/-33/63	3
110	148b	1:27	459	87/1	1967/5	-1502/45	55/380	30/27/-38/79	7
111	149	0:10	57	88/2	1992/2	-12/18	57/108	19/7/10/39	3
112	149	1:26	456	88/1	1979/6	-1460/52	50/143	31/29/-38/82	7
113	149	0:19	104	88/1	1970/1	-1854/-952	42/71	25/13/8/63	0
114	149	1:03	334	88/1	1977/4	-1359/52	48/170	27/34/-73/79	8
115	150a	0:16	85	87/1	1985/2	-11/34	44/74	25/3/21/30	10
116	150a	0:59	310	87/1	1979/5	-1210/33	61/373	23/37/-47/82	10
117	150a	0:58	306	87/1	1980/5	-1141/19	75/319	24/36/-44/82	5
118	150a	0:07	42	90/4	1988/2	113/354	138/406	41/1/38/43	0
119	150b	0:30	161	87/1	1979/3	-36/40	69/143	47/21/17/82	15
120	150b	0:16	85	88/1	1972/2	-976/-61	48/74	60/14/29/81	1
121	150b	0:10	56	87/1	1975/2	-29/-5	56/100	33/9/18/47	3
122	150b	0:12	71	94/1	1972/2	-2/74	64/113	32/6/25/44	3
123	151	1:21	426	87/1	1952/7	-619/-23	51/119	32/13/11/59	1
124	151	0:15	80	88/1	1939/1	-1611/-1560	63/143	18/7/11/36	0
125	151	1:00	315	87/1	1941/1	-273/-12	54/120	35/13/10/58	4
126	152	0:23	121	87/1	2002/2	6/24	56/97	43/8/26/60	0
127	152	0:22	117	87/1	2003/2	-5/15	54/90	40/6/30/55	0
128	152	0:21	112	87/1	2006/2	-12/6	71/249	37/3/29/45	4
129	152	0:24	128	87/1	2004/2	-17/6	96/481	31/4/25/38	7
130	152	0:24	129	88/1	2004/2	-24/2	64/115	27/4/20/34	11
131	152	0:25	135	87/1	2001/2	-28/-2	69/111	27/4/20/33	14
132	154	1:14	391	87/1	1950/6	-1234/5	53/108	26/21/-18/68	7
133	154	1:13	388	88/1	1948/5	-1294/17	71/865	25/22/-19/67	6
134	155a	1:21	430	87/1	2002/5	-672/-2	58/395	32/16/11/61	2
135	155a	1:08	361	87/1	1998/3	-834/1	53/122	31/18/8/62	2

Table A.6: Malaysia 2014/2015: detailed line information

FL	F	dur. [h:mm]	dist. [km]	vel. [m/s] μ/σ	altitude [m] μ/σ	topo. [m] $\mu/\max.$	RMS-g [mm/s ²] $\mu/\max.$	dg^{Down} [mGal] $\mu/\sigma/\min/\max$	N_x
136	155b	1:16	400	87/1	1947/6	-1088/21	64/149	26/18/-15/70	5
137	155b	1:17	405	87/1	1937/2	-1135/15	70/187	24/20/-15/62	8
138	156a	1:13	388	87/1	2637/5	-802/-16	101/717	34/17/9/66	2
139	156a	0:57	302	87/1	2633/3	-990/3	72/131	34/17/10/63	2
140	156a	0:09	51	87/1	2640/2	-42/-12	102/175	32/2/30/37	4
141	156b	1:17	409	87/1	2624/7	-801/31	88/924	34/14/8/61	5
142	156b	1:17	407	87/1	2615/3	-948/22	92/401	29/14/2/66	6
143	157	0:50	267	87/1	1998/4	-1025/-37	60/109	29/24/-16/63	6
144	157	0:17	94	87/1	1986/3	-1498/-1063	109/544	31/12/12/49	9
145	157	0:30	159	87/1	1984/2	-1475/19	68/180	17/29/-17/75	7
146	157	0:14	77	88/1	1984/2	-626/-31	63/100	33/17/2/55	11
147	157	0:17	91	87/1	1987/2	-58/-18	50/67	30/4/22/34	2
148	157	0:23	122	87/1	1987/2	-74/-24	55/150	35/4/27/44	2
149	157	0:24	130	87/1	1990/2	-70/-14	56/90	37/6/27/48	5
150	158	0:11	82	117/1	4873/2	-14/24	66/97	37/6/27/46	3
151	159	0:12	64	87/1	1988/2	-21/41	64/101	51/2/48/54	5
152	159	0:59	313	87/0	1990/1	-40/87	52/94	69/17/38/99	7
153	159	0:19	102	87/1	1990/2	-146/-14	57/88	79/15/45/98	0
154	159	0:13	72	87/1	1986/2	-64/-7	47/78	61/7/38/75	5
155	160a	0:07	41	86/1	2009/3	-30/-10	60/98	40/2/37/44	4
156	160a	0:27	146	87/1	2010/2	-19/102	72/138	73/21/37/109	5
157	160a	0:27	146	87/1	2008/2	-15/177	112/754	74/21/40/113	4
158	160a	0:35	188	87/1	2006/4	-46/136	93/212	61/26/20/106	4
159	160a	0:18	96	87/1	2003/2	-30/-4	117/214	77/16/40/96	1
160	160a	0:13	70	87/1	2003/2	-11/21	85/180	53/3/48/59	14
161	160b	0:46	242	87/1	1989/2	-49/18	54/95	60/19/25/93	4
162	160b	0:17	93	87/2	1988/3	-42/9	193/634	80/21/60/128	1
163	160b	0:08	47	87/1	1983/3	-62/-43	111/379	104/16/77/129	0
164	160b	0:23	124	87/1	1981/2	-59/-19	118/239	70/12/40/85	0
165	162	0:09	50	87/0	2321/1	30/118	92/158	15/15/0/51	1
166	162	0:19	103	87/0	1999/2	-89/-34	42/114	122/10/106/137	4
167	162	0:14	77	88/1	1997/2	-123/-74	46/73	136/7/123/146	2
168	162	0:11	60	87/0	1995/1	-138/-47	39/62	140/10/123/153	2
169	162	0:09	50	87/1	1995/2	-122/-10	57/80	129/9/114/143	1
170	162	0:08	43	87/1	1990/2	-83/21	77/132	115/7/106/126	2
171	162	0:09	49	88/1	1987/1	-224/-23	53/74	128/11/100/139	0
172	162	0:21	112	87/1	1982/2	-8/-2	51/84	58/16/23/76	0
173	163a	0:43	229	87/1	2002/3	-19/28	76/722	59/19/21/86	2
174	163a	0:22	120	87/1	2008/1	-112/-7	51/109	104/28/50/149	12
175	163a	0:18	100	87/1	2004/2	-81/6	55/87	99/16/78/122	6
176	163a	0:20	108	87/1	2001/1	-29/1	59/85	102/10/80/116	5
177	163a	0:18	100	87/1	2002/2	-18/137	55/81	101/8/82/114	5
178	163a	0:21	113	87/1	1999/1	-10/53	77/180	97/8/81/110	5
179	163b	0:21	114	87/1	1982/2	-18/175	81/213	112/11/88/128	8
180	163b	0:18	98	87/1	1980/1	-36/59	60/84	112/11/93/132	9

Table A.7: Malaysia 2014/2015: detailed line information

FL	F	dur. [h:mm]	dist. [km]	vel. [m/s] μ/σ	altitude [m] μ/σ	topo. [m] $\mu/\max.$	RMS-g [mm/s ²] $\mu/\max.$	dg^{Down} [mGal] $\mu/\sigma/\min/\max$	N_{χ}
181	163b	0:17	91	87/1	1978/1	-74/14	66/125	110/11/92/126	11
182	163b	0:12	68	87/1	1978/1	-64/-35	67/101	88/13/75/115	1
183	163b	0:33	177	87/1	2641/2	-5/40	55/120	49/20/14/76	1
184	164a	0:08	48	98/0	2324/2	28/68	44/84	13/13/-0/46	1
185	164a	0:16	86	87/1	2007/2	-395/26	75/155	98/25/61/135	2
186	164a	0:10	54	87/1	2008/2	-141/14	65/96	119/13/76/136	3
187	164a	0:28	150	87/1	2008/2	-145/12	62/143	115/19/69/147	7
188	164a	0:37	197	87/1	2005/3	-41/2	52/96	61/18/32/94	4
189	164a	0:11	59	87/1	1997/1	0/28	61/128	34/12/19/58	2
190	164b	0:24	130	87/1	1990/3	-23/15	51/85	48/16/23/73	3
191	164b	0:09	52	87/1	1983/1	-33/-5	47/71	55/11/36/73	2
192	164b	0:13	74	87/1	1979/3	-47/-2	76/107	70/25/21/96	0
193	164b	0:15	82	87/1	1975/2	-33/1	62/113	78/15/46/97	0
194	164b	0:21	115	87/1	1975/2	-26/9	46/79	33/8/20/49	17

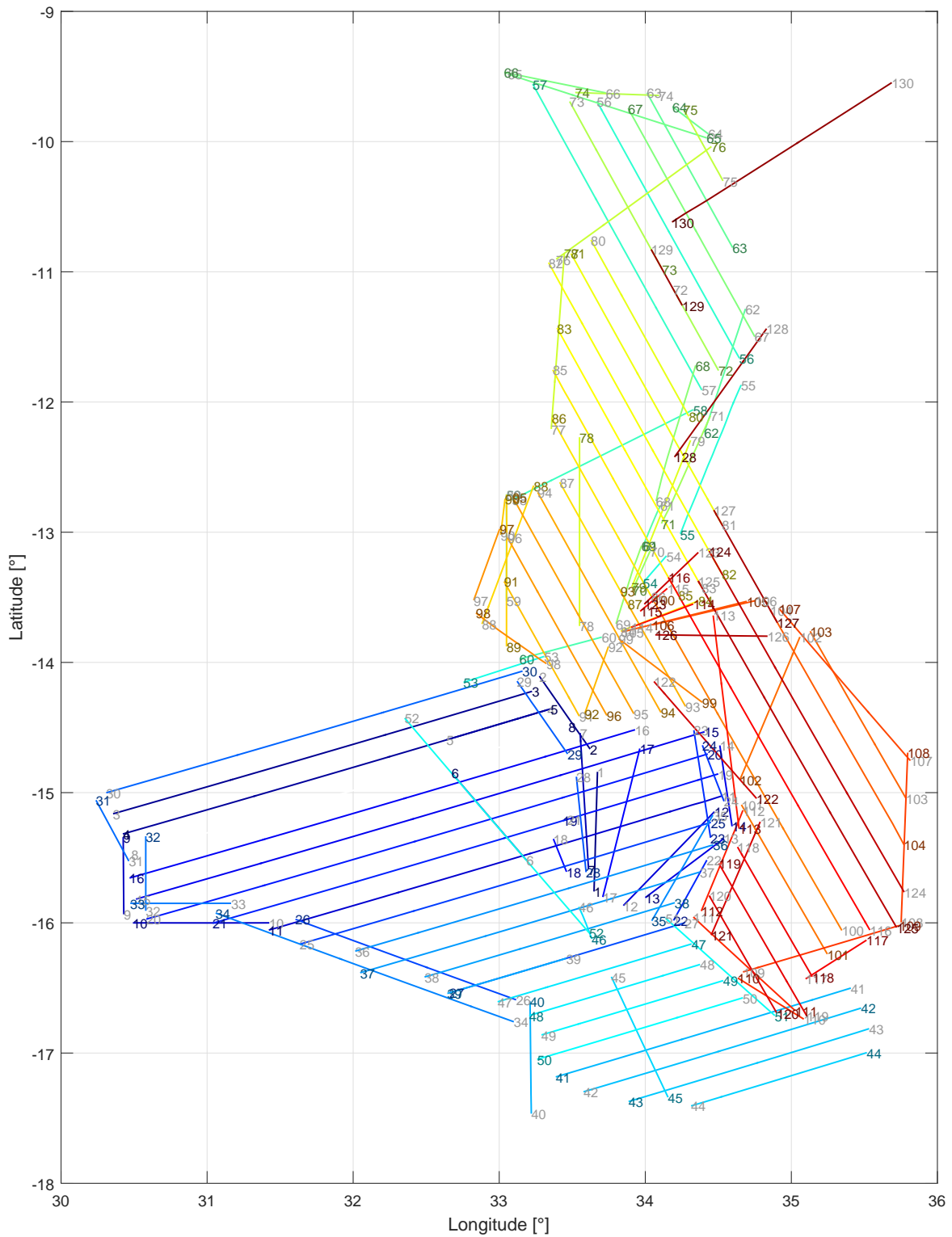


Figure A.4: Mozambique/Malawi 2015 measurement lines

Table A.8: Mozambique/Malawi 2015: detailed line information

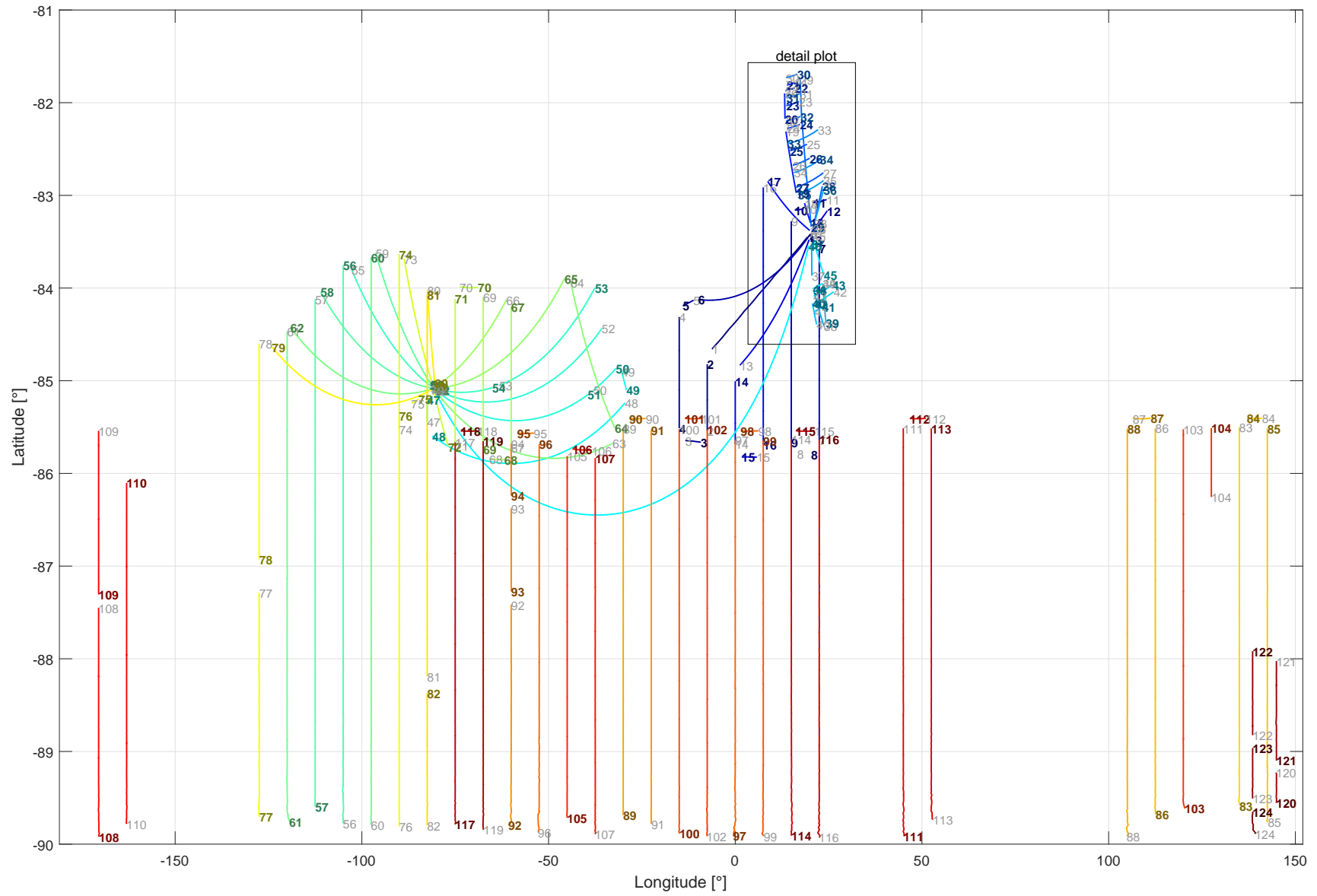
FL	F	dur. [h:mm]	dist. [km]	vel.	altitude	topo.	RMS-g	dg^{Down}	N_χ
				[m/s] μ/σ	[m] μ/σ	[m] $\mu/\text{max.}$	[mm/s ²] $\mu/\text{max.}$	[mGal] $\mu/\sigma/\text{min}/\text{max}$	
1	278	0:23	102	73/1	2435/1	795/1294	154/377	-0/31/-50/44	5
2	278	0:15	73	78/2	2431/1	1361/1538	76/154	9/9/-11/22	2
3	278	1:08	327	79/2	2436/3	890/1234	80/335	-10/24/-75/27	2
4	278	1:19	331	69/3	2765/2	865/1473	240/1099	-7/18/-58/23	2
5	278	0:16	82	81/2	3884/1	885/1537	121/291	-24/8/-36/-6	1
6	278	0:20	93	74/1	3826/5	492/723	76/214	-41/12/-55/-20	5
7	279	0:25	117	75/3	2749/2	921/1560	73/197	8/24/-51/40	7
8	279	1:12	340	78/2	2751/4	782/1268	139/491	-15/14/-60/10	3
9	279	0:14	66	78/1	2761/1	406/625	72/175	-69/8/-82/-53	1
10	279	0:22	101	73/1	3403/1	381/468	102/221	-99/7/-107/-81	2
11	279	1:23	352	70/3	4046/2	595/1462	99/1029	-28/28/-88/36	9
12	279	0:21	104	81/1	4205/1	741/1517	77/243	-19/24/-55/28	4
13	280	0:17	77	73/2	2753/0	732/1242	126/439	-15/28/-61/25	2
14	280	0:14	70	77/2	3075/1	1470/1696	398/609	59/9/44/71	1
15	280	1:34	442	78/2	3563/5	717/1438	81/315	-17/31/-81/72	7
16	280	1:30	393	72/1	4052/3	748/1415	36/106	-25/23/-68/26	6
17	280	0:27	130	78/2	4049/1	755/1497	60/127	-16/13/-43/12	6
18	281	0:06	30	75/0	2744/0	414/493	213/302	-45/5/-50/-37	2
19	281	0:27	121	73/1	2745/1	984/1392	136/229	10/26/-25/69	6
20	281	1:34	437	77/2	3393/4	602/1404	124/357	-24/34/-100/58	9
21	281	1:00	275	76/2	3719/2	405/888	51/157	-42/25/-105/-5	4
22	282	0:12	57	73/2	2742/1	587/1017	76/140	-11/15/-36/18	0
23	282	0:20	93	75/1	2739/1	1280/1563	49/168	39/17/14/77	7
24	282	0:10	51	76/2	3062/1	1342/1538	60/110	55/7/40/65	2
25	282	1:07	320	79/1	3071/4	536/1463	85/420	-31/23/-75/35	10
26	282	0:40	176	72/1	3082/3	479/726	69/250	-37/25/-85/-4	8
27	282	0:45	183	66/2	3564/1	325/511	170/358	-15/20/-48/21	2
28	283	0:18	82	75/2	2741/1	695/1205	91/301	-4/28/-53/37	4
29	283	0:15	73	78/1	2739/2	1054/1356	347/641	-8/14/-30/15	5
30	283	1:11	325	75/1	3063/4	923/1257	59/643	-12/18/-43/19	0
31	283	0:13	57	71/1	3075/1	373/453	54/170	-65/6/-76/-54	1
32	283	0:13	64	77/1	3077/1	404/609	54/109	-60/18/-97/-26	4
33	283	0:17	74	68/1	3078/1	381/455	41/106	-76/6/-89/-70	2
34	283	0:57	238	69/2	3078/1	490/717	110/417	-46/36/-99/-1	3
35	285	0:22	101	74/1	2427/1	768/1528	82/207	-14/26/-67/30	6
36	285	0:59	278	78/1	2750/3	535/1068	73/190	-24/21/-52/45	6
37	285	1:06	264	66/1	3083/1	424/814	42/171	-27/17/-60/7	7
38	285	0:38	194	83/1	3081/1	328/622	43/115	-22/15/-50/6	4
39	285	0:23	92	66/1	3083/1	352/507	49/100	-29/14/-52/-6	1
40	287	0:21	96	75/1	2418/2	473/887	53/131	-27/11/-49/-14	1
41	287	0:56	229	67/1	2424/1	256/643	71/231	-8/14/-41/9	6
42	287	0:47	215	75/1	2426/1	272/601	56/212	-4/12/-32/11	1
43	287	0:45	187	68/2	2428/2	219/862	77/489	-14/11/-38/17	1
44	287	0:29	136	77/1	3391/1	158/472	93/193	-10/15/-39/14	0
45	287	0:23	111	77/2	3389/2	290/464	110/351	-15/13/-36/2	6

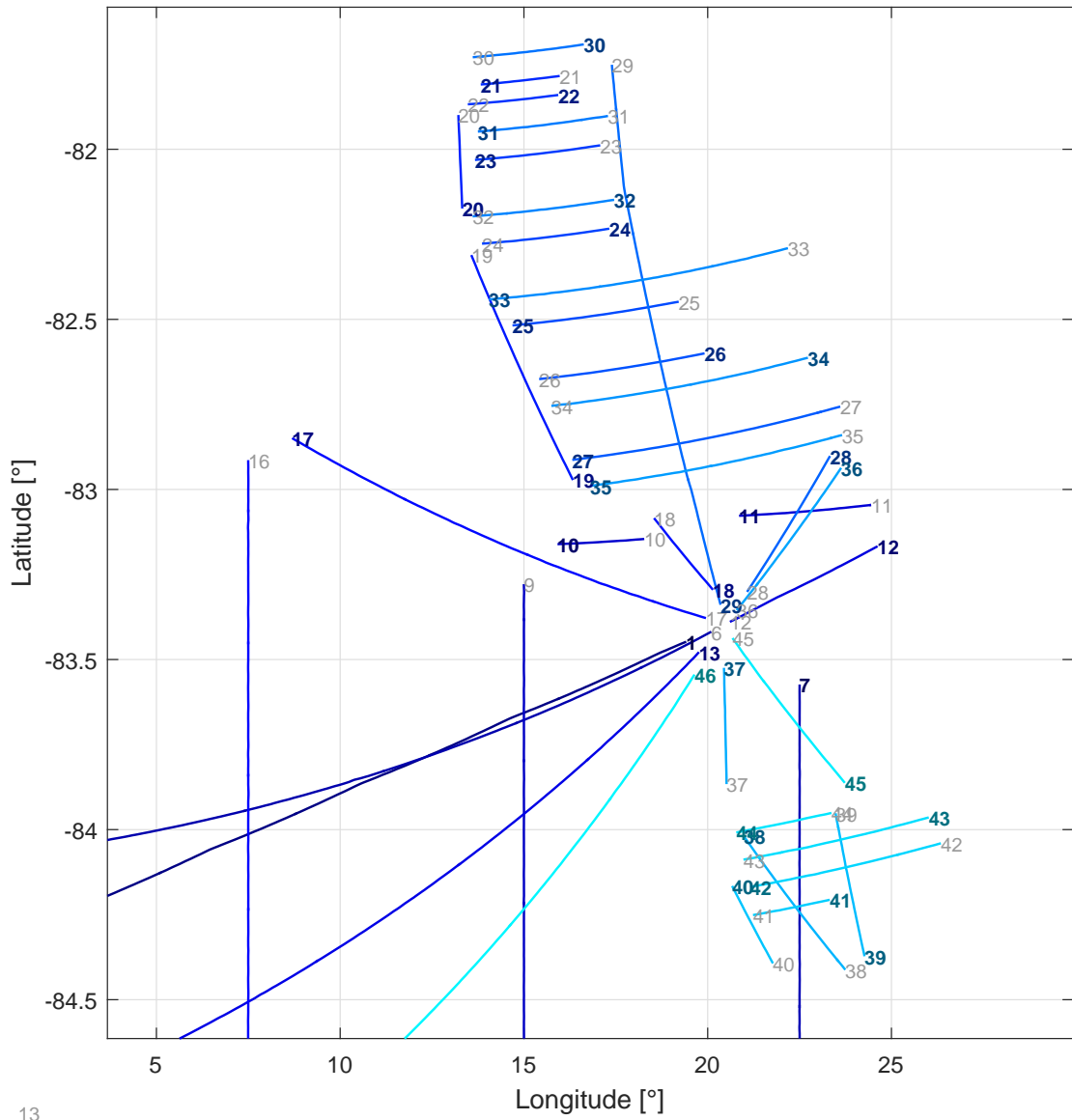
Table A.9: Mozambique/Malawi 2015: detailed line information

FL	F	dur. [h:mm]	dist. [km]	vel.	altitude	topo.	RMS-g	dg^{Down}	N_x
				[m/s]	[m]	[m]	[mm/s ²]	[mGal]	
				μ/σ	μ/σ	$\mu/\text{max.}$	$\mu/\text{max.}$	$\mu/\sigma/\text{min/max}$	
46	287	0:05	29	78/1	3385/1	302/551	336/552	-10/8/-31/-3	2
47	288	0:32	150	77/1	2400/1	266/561	41/192	-14/18/-39/20	1
48	288	0:31	133	71/1	2404/1	259/395	69/252	-19/13/-45/0	2
49	288	0:30	141	77/1	2730/1	313/557	50/159	-15/11/-38/1	1
50	288	0:35	159	74/1	2732/1	316/530	49/196	-7/7/-22/7	1
51	288	0:24	115	77/1	2730/1	305/425	45/151	0/9/-14/14	2
52	289	0:49	228	76/2	2394/1	487/925	66/224	-35/14/-57/-5	12
53	289	0:14	64	71/1	3043/1	1018/1161	139/252	-27/14/-44/9	1
54	290	0:06	30	76/2	3365/1	971/1628	328/495	3/26/-32/51	2
55	290	0:27	135	81/2	3361/3	479/539	143/342	-89/26/-127/-56	2
56	290	0:50	244	79/4	3360/4	742/1722	102/288	-54/63/-168/40	3
57	290	1:09	289	70/6	3375/2	1310/2287	175/709	37/66/-125/148	2
58	290	0:30	155	83/2	3374/3	1017/1539	80/183	-15/55/-131/48	10
59	290	0:22	91	68/2	3380/2	1084/1156	116/638	-1/10/-14/19	2
60	290	0:14	64	75/1	4189/1	1137/1188	205/458	19/17/-19/39	4
61	292	0:07	37	79/1	3694/1	852/1090	107/233	-8/8/-19/7	2
62	292	0:22	110	80/2	3690/1	476/476	105/461	-91/19/-122/-71	4
63	292	0:31	147	77/5	3692/2	476/476	85/424	-124/13/-148/-88	4
64	292	0:07	36	79/1	3699/1	476/476	177/386	-127/12/-137/-94	1
65	292	0:35	160	74/2	3704/3	899/1775	55/163	-40/65/-141/40	4
66	292	0:15	79	84/1	3707/1	1152/1591	49/95	15/28/-51/40	0
67	292	0:46	216	77/4	3700/2	483/593	90/275	-105/33/-156/-66	4
68	292	0:25	120	77/1	4017/2	513/860	98/223	-91/29/-127/-20	5
69	292	0:14	70	79/1	4027/1	1290/1542	141/292	35/15/5/51	3
70	293	0:07	36	74/3	3051/1	1188/1617	168/503	29/23/-6/63	1
71	293	0:22	99	72/3	3047/2	501/647	290/770	-86/35/-128/-29	4
72	293	0:16	78	80/1	3688/2	494/994	310/918	-98/27/-125/-17	0
73	293	0:34	159	77/2	3760/2	1551/2482	106/357	70/44/16/151	1
74	293	0:12	63	85/1	4020/1	664/1348	51/84	-61/46/-135/24	1
75	293	0:13	68	82/1	4017/1	476/476	57/159	-138/9/-150/-118	3
76	293	0:34	151	72/1	4022/3	1280/2371	54/160	19/103/-152/154	6
77	293	0:32	150	76/2	4025/1	1160/1239	102/342	19/5/13/36	4
78	293	0:36	161	73/2	4345/1	1150/1470	83/261	20/14/0/55	5
79	294	0:27	132	79/1	3362/2	744/1474	107/222	-32/48/-118/57	5
80	294	0:35	167	79/1	3365/3	979/1807	208/635	3/64/-123/102	2
81	294	0:54	257	79/1	3690/3	878/1689	79/298	-24/68/-115/77	6
82	294	1:01	295	80/2	3692/2	937/1821	75/346	-9/53/-76/79	7
83	294	0:52	246	77/2	4011/2	1003/1693	54/533	-4/36/-56/48	6
84	294	0:13	63	78/1	4009/2	928/1457	31/105	7/35/-49/48	3
85	295	0:45	213	78/2	3038/2	1092/1644	207/480	16/28/-30/82	6
86	295	0:35	169	78/1	3365/1	1177/1466	148/294	32/14/10/65	7
87	295	0:25	115	76/1	3688/1	1147/1424	35/65	29/16/7/63	2
88	295	0:27	124	74/1	3692/2	1099/1601	38/91	12/13/-4/36	6
89	295	0:26	129	82/1	3693/1	1091/1159	33/61	10/11/-6/30	3
90	295	0:06	32	77/1	3692/1	1116/1150	40/64	-3/3/-9/5	0

Table A.10: Mozambique/Malawi 2015: detailed line information

FL	F	dur.	dist.	vel.	altitude	topo.	RMS-g	dg^{Down}	N_{χ}	
		[h:mm]	[km]	[m/s]	[m]	[m]	[mm/s ²]	[mGal]		
				μ/σ	μ/σ	$\mu/\text{max.}$	$\mu/\text{max.}$	$\mu/\sigma/\text{min/max}$		
91	295	0:28	127	75/2	4174/2	1144/1523	86/316	8/9/-9/20	3	
92	295	0:11	60	84/1	4334/1	1124/1245	108/190	20/15/-4/40	2	
93	296	0:23	109	79/1	3053/2	1282/1901	192/410	57/15/35/90	5	
94	296	0:43	209	79/1	3378/1	1139/1409	192/391	40/20/3/67	2	
95	296	0:44	206	77/1	3703/2	1108/1234	194/404	29/18/-1/53	5	
96	296	0:34	168	80/1	4024/1	1120/1237	93/273	22/11/-4/40	3	
97	296	0:13	64	77/1	4024/1	1079/1181	43/94	11/14/-5/32	0	
98	296	0:13	68	82/0	4023/1	1135/1236	105/400	11/10/2/35	4	
99	296	0:16	83	80/1	4660/1	1255/1668	27/52	55/13/36/74	2	
100	297	1:11	314	73/2	3051/4	891/1657	64/284	23/29/-32/79	8	
101	297	0:29	142	81/1	3060/1	818/1426	48/211	28/40/-37/86	2	
102	297	0:27	130	79/1	3059/1	647/1170	105/510	-16/28/-44/42	6	
103	297	0:35	159	73/1	3063/1	906/1658	88/266	8/13/-15/34	1	
104	297	0:46	223	79/1	3063/2	542/709	56/141	-31/18/-61/7	1	
105	297	0:20	97	80/1	3061/2	760/1348	85/171	-17/42/-79/43	5	
106	299	0:18	79	70/1	2730/1	607/1193	39/75	-60/31/-110/13	4	
107	299	0:35	162	77/1	2734/3	782/1188	159/555	-25/23/-64/3	2	
108	299	0:31	145	76/1	3384/2	681/1519	50/117	-6/18/-25/49	2	
109	299	0:26	122	76/3	3391/1	460/1415	83/249	-5/37/-68/46	6	
110	299	0:13	60	73/1	3394/0	234/356	38/64	-18/7/-33/-10	2	
111	299	0:22	109	80/2	3394/0	227/379	60/178	-39/6/-46/-27	4	
112	299	0:18	91	82/1	3394/0	910/1504	34/61	-1/21/-48/33	2	
113	299	0:35	183	85/0	4035/2	918/1719	29/57	1/38/-49/57	5	
114	299	0:10	51	77/1	4032/2	915/1433	42/103	3/32/-46/47	3	
115	300	0:06	28	68/0	2728/0	949/1311	36/55	12/21/-19/42	1	
116	300	1:16	335	73/2	2735/3	622/1133	112/303	-7/32/-41/60	8	
117	300	0:11	56	77/1	2738/0	405/630	56/115	11/21/-40/34	1	
118	300	0:25	124	79/1	3063/1	401/905	88/368	-3/14/-28/24	3	
119	300	0:31	146	77/1	3065/1	216/792	68/232	-34/15/-60/1	4	
120	300	0:24	112	76/1	3387/1	269/572	48/103	-26/19/-54/8	5	
121	300	0:21	104	79/1	3388/0	523/886	38/62	-23/9/-49/-12	5	
122	300	0:26	126	78/1	3390/1	1288/1506	109/466	56/21/-10/78	4	
123	301	0:13	60	73/1	2707/1	705/1484	64/176	-25/31/-68/45	3	
124	301	1:09	324	77/2	2708/1	572/1336	60/295	-36/29/-83/18	6	
125	301	1:14	329	73/1	3037/2	728/2413	46/186	-13/46/-66/143	5	
126	302	0:20	84	69/2	2382/1	593/1077	36/105	-37/32/-77/31	5	
127	302	0:25	107	70/1	2384/1	480/524	97/184	-97/22/-124/-44	0	
128	302	0:32	129	66/1	2384/1	476/476	95/278	-94/25/-130/-53	2	
129	302	0:11	53	75/1	3348/2	1154/1825	170/249	23/51/-80/71	0	
130	302	0:42	204	79/2	3671/2	999/1713	137/330	-13/65/-144/60	2	
131	302	0:50	248	81/1	4147/1	283/1337	98/250	-16/28/-47/72	0	





13

Figure A.6: Antarctica 2015/2016 measurement lines (detail)

Table A.11: Antarctica 2015/2016: detailed line information

FL	F	dur.	dist.	vel.	altitude	topo.	RMS-g	dg^{Down}	N_χ	
		[h:mm]	[km]	[m/s]	[m]	[m]	[mm/s ²]	[mGal]		
				μ/σ	μ/σ	$\mu/\text{max.}$	$\mu/\text{max.}$	$\mu/\sigma/\text{min/max}$		
1	350	1:26	326	63/1	2798/5	- / -	66/144	-18/22/-64/9	3	
2	350	0:22	80	59/1	2732/4	- / -	81/145	-3/5/-11/7	0	
3	350	0:09	35	63/1	2721/3	- / -	69/107	13/2/6/17	0	
4	350	0:35	134	64/1	2636/2	- / -	54/109	-5/11/-23/14	0	
5	350	0:09	34	62/0	2785/4	- / -	69/111	1/6/-6/12	0	
6	350	1:39	368	61/1	2794/15	- / -	79/151	-20/23/-64/13	3	
7	351a	0:54	231	71/2	2932/4	- / -	107/209	-50/18/-80/-9	7	
8	351a	0:08	31	63/1	2928/4	- / -	110/140	-37/15/-54/-7	0	
9	351a	1:15	267	59/4	2905/6	- / -	115/239	-26/29/-64/19	5	
10	351a	0:07	32	66/1	2892/3	- / -	94/145	-51/3/-56/-45	0	
11	351a	0:12	49	67/1	2902/5	- / -	117/169	-36/8/-43/-10	2	
12	351a	0:12	58	76/1	2905/5	- / -	126/181	-39/23/-75/3	0	
13	351b	1:00	258	71/1	2803/9	- / -	99/270	-29/25/-64/7	2	
14	351b	0:18	76	70/1	2826/3	- / -	63/121	4/4/-3/11	2	
15	351b	0:08	33	62/1	2860/4	- / -	89/140	12/3/6/18	0	
16	351b	1:29	310	58/1	2858/8	- / -	83/174	-15/21/-71/15	4	
17	351b	0:42	162	64/1	2826/7	- / -	104/189	-25/15/-62/6	0	
18	352	0:08	32	65/1	2869/4	- / -	109/145	-67/2/-71/-64	0	
19	352	0:21	84	64/0	2868/5	- / -	93/158	-36/11/-56/-18	1	
20	352	0:08	31	62/0	2872/3	- / -	85/127	-25/2/-30/-23	0	
21	352	0:08	35	69/0	2875/3	- / -	92/139	-19/8/-31/-5	0	
22	352	0:09	40	66/1	2876/4	- / -	102/145	-31/6/-38/-20	0	
23	352	0:12	53	68/1	2882/3	- / -	98/160	-48/6/-56/-31	0	
24	352	0:12	53	68/1	2877/3	- / -	94/136	-47/6/-57/-32	0	
25	352	0:16	67	66/1	2876/4	- / -	111/159	-56/11/-70/-38	1	
26	352	0:15	65	72/1	2875/4	- / -	117/156	-69/10/-79/-38	1	
27	352	0:26	104	65/1	2878/6	- / -	112/174	-63/9/-79/-46	1	
28	352	0:11	54	77/1	2876/4	- / -	118/149	-49/7/-64/-38	1	
29	354	0:53	183	56/1	2882/4	- / -	63/131	-53/22/-72/28	6	
30	354	0:13	49	61/1	2886/3	- / -	72/109	-9/7/-22/6	0	
31	354	0:15	56	61/1	2888/6	- / -	85/175	-42/7/-53/-26	0	
32	354	0:15	59	61/0	2889/3	- / -	78/108	-36/11/-51/-19	0	
33	354	0:33	122	61/1	2889/4	- / -	79/137	-40/13/-56/-13	2	
34	354	0:26	101	63/1	2889/5	- / -	87/157	-60/9/-76/-45	1	
35	354	0:25	96	62/1	2890/5	- / -	94/162	-57/10/-74/-43	1	
36	354	0:14	60	67/1	2895/6	- / -	79/126	-44/14/-71/-17	1	
37	355	0:08	38	71/0	2892/4	- / -	82/129	-71/6/-80/-58	0	
38	355	0:13	54	69/0	2893/3	- / -	67/93	-68/3/-74/-61	4	
39	355	0:13	48	59/1	2895/2	- / -	73/105	-36/6/-48/-20	2	
40	355	0:06	28	69/0	2895/2	- / -	63/82	-71/4/-76/-62	0	
41	355	0:06	24	65/0	2899/3	- / -	84/141	-69/7/-75/-48	2	
42	355	0:15	61	65/1	2905/4	- / -	80/122	-31/35/-70/26	3	
43	355	0:15	61	66/1	2901/5	- / -	100/165	-36/30/-74/13	3	
44	355	0:07	31	65/0	2904/3	- / -	73/104	-53/10/-63/-22	1	
45	355	0:17	61	59/1	2906/4	- / -	93/141	-50/31/-81/-2	1	

Table A.12: Antarctica 2015/2016: detailed line information

FL	F	dur. [h:mm]	dist. [km]	vel.	altitude	topo.	RMS-g	dg^{Down}	N_x
				[m/s] μ/σ	[m] μ/σ	[m] $\mu/\text{max.}$	[mm/s ²] $\mu/\text{max.}$	[mGal] $\mu/\sigma/\text{min}/\text{max}$	
46	359	4:11	983	65/3	2927/11	- / -	179/494	-27/41/-99/63	14
47	360	0:06	27	64/2	2220/6	- / -	90/134	-99/11/-111/-74	0
48	360	2:00	447	62/3	2241/5	- / -	123/363	-18/49/-122/71	8
49	360	0:06	26	62/1	2265/3	- / -	103/154	56/5/44/62	0
50	360	0:16	64	64/1	2180/4	- / -	100/146	45/16/6/67	1
51	360	1:43	388	63/2	2178/4	- / -	134/451	-31/39/-124/36	5
52	361	2:23	446	52/3	2191/11	- / -	130/282	-17/47/-96/79	4
53	361	1:09	295	70/2	1954/15	- / -	141/273	-16/40/-95/58	2
54	361	0:34	154	74/1	1951/7	- / -	126/219	-43/41/-94/63	4
55	362a	1:01	265	71/3	2468/4	- / -	101/266	-9/27/-93/39	3
56	362a	2:51	673	65/3	2899/5	- / -	140/323	-7/32/-85/86	3
57	362b	2:28	612	69/3	3137/10	- / -	136/459	-9/34/-64/80	2
58	362b	1:18	329	70/1	2466/11	- / -	174/353	-10/41/-89/135	4
59	363a	1:03	227	60/2	2286/9	- / -	68/174	-8/36/-102/65	2
60	363a	2:57	684	64/2	2875/12	- / -	183/451	-5/35/-66/128	4
61	363b	2:38	591	62/4	3191/5	- / -	129/429	-16/26/-73/39	1
62	363b	1:37	395	68/2	3194/4	- / -	113/281	-10/38/-79/122	7
63	364	1:48	418	64/2	2144/5	- / -	75/239	-34/49/-130/66	7
64	364	0:56	212	63/1	2153/4	- / -	66/111	36/16/11/61	4
65	364	1:45	387	61/2	2198/5	- / -	109/264	-30/46/-88/151	3
66	365	1:02	225	60/1	1631/4	- / -	87/162	-45/30/-149/-3	2
67	365	0:41	170	68/2	1960/5	- / -	84/164	-37/55/-129/59	4
68	365	0:07	32	69/1	1960/3	- / -	145/189	63/11/45/81	0
69	365	0:52	183	58/2	1991/7	- / -	118/238	-21/61/-165/74	7
70	365	0:18	58	53/1	1564/6	- / -	153/233	17/9/6/33	0
71	365	0:51	178	58/2	1567/10	- / -	118/280	-57/40/-129/37	7
72	365	0:20	76	63/1	1582/6	- / -	95/138	-75/22/-106/-42	1
73	004a	0:40	175	72/2	1959/10	- / -	123/203	-16/33/-74/70	1
74	004a	1:10	212	50/3	2857/12	- / -	153/544	10/38/-85/72	5
75	004b	0:06	19	50/1	2825/25	- / -	84/129	-54/6/-61/-40	0
76	004b	2:23	496	57/4	2857/10	- / -	123/287	-21/30/-68/68	0
77	004c	1:02	270	72/1	3320/8	- / -	94/219	-19/23/-47/24	0
78	004c	1:04	260	67/1	4310/7	- / -	83/179	-27/60/-98/184	0
79	004c	1:34	418	73/2	2595/9	- / -	159/502	2/45/-67/98	6
80	006	0:26	114	71/3	1684/11	- / -	100/173	-32/22/-69/13	0
81	006	2:16	460	56/6	2680/9	- / -	108/261	-33/22/-100/13	6
82	006	0:40	160	66/1	2921/9	- / -	119/218	-34/9/-49/-12	0
83	007	2:02	456	62/1	3389/4	- / -	92/301	-32/14/-69/-7	0
84	007	0:09	36	63/1	3306/6	- / -	80/116	-28/3/-34/-23	0
85	007	1:55	475	68/3	3298/6	- / -	129/361	-36/10/-56/-14	0
86	008a	2:00	466	64/2	3299/4	- / -	108/380	-43/9/-66/-27	0
87	008a	0:11	43	65/1	3443/2	- / -	85/123	-26/7/-36/-16	0
88	008a	2:05	492	65/2	3436/5	- / -	93/171	-40/8/-58/-21	0
89	008b	2:10	466	60/2	3070/8	- / -	126/399	-46/29/-102/42	1
90	008b	0:10	40	64/1	2871/4	- / -	73/123	41/19/10/70	0

Table A.13: Antarctica 2015/2016: detailed line information

FL	F	dur.	dist.	vel.	altitude	topo.	RMS-g	dg^{Down}	N_{χ}	
		[h:mm]	[km]	[m/s]	[m]	[m]	[mm/s ²]	[mGal]		
				μ/σ	μ/σ	$\mu/\text{max.}$	$\mu/\text{max.}$	$\mu/\sigma/\text{min}/\text{max}$		
91	008b	1:50	475	72/1	2870/9	- / -	164/537	-46/32/-100/50	1	
92	009	1:09	266	64/3	3121/8	- / -	124/313	-18/16/-37/28	0	
93	009	0:26	100	64/1	3122/5	- / -	109/310	30/15/-8/46	0	
94	009	0:16	63	62/1	3125/3	- / -	84/147	13/22/-18/52	3	
95	009	0:11	39	55/1	2927/3	- / -	89/167	-1/20/-21/36	0	
96	009	2:11	469	59/1	2928/6	- / -	160/464	-21/18/-43/25	3	
97	010a	2:12	478	60/1	3205/7	- / -	102/377	-39/29/-91/11	1	
98	010a	0:10	41	62/0	3206/3	- / -	67/92	4/3/-3/8	0	
99	010a	2:00	477	66/1	3213/9	- / -	175/506	-34/30/-96/14	0	
100	010b	2:12	488	61/1	3215/21	- / -	133/473	-44/33/-110/23	1	
101	010b	0:10	40	60/1	3228/4	- / -	80/172	6/2/3/9	0	
102	010b	1:54	491	72/2	3233/10	- / -	174/521	-37/31/-100/22	1	
103	011a	2:05	457	61/2	3370/4	- / -	98/194	-43/12/-63/-19	0	
104	011a	0:20	83	66/1	3248/3	- / -	91/144	-44/7/-55/-33	0	
105	011b	1:58	436	61/3	3124/12	- / -	100/215	-61/14/-87/-35	2	
106	011b	0:12	43	57/1	2941/8	- / -	106/151	-97/20/-122/-61	0	
107	011b	1:48	454	70/2	2940/12	- / -	204/643	-57/18/-112/-28	1	
108	012	1:10	277	65/2	3426/11	- / -	182/412	2/20/-37/47	0	
109	012	0:54	198	60/2	3419/6	- / -	100/206	21/15/-3/51	0	
110	012	1:37	412	70/2	3438/12	- / -	161/416	-5/30/-100/45	0	
111	013	2:11	492	62/3	3405/5	- / -	95/191	-17/28/-63/28	0	
112	013	0:08	39	72/1	3404/5	- / -	146/239	-22/5/-38/-8	0	
113	013	2:09	472	61/3	3397/6	- / -	117/213	-14/27/-64/24	0	
114	016a	2:03	478	64/3	3199/5	- / -	90/253	-33/37/-96/19	1	
115	016a	0:11	43	61/0	3202/3	- / -	77/120	-32/21/-49/17	0	
116	016a	2:11	480	61/2	3199/6	- / -	126/412	-35/27/-93/6	1	
117	016b	1:43	461	74/2	3122/10	- / -	116/299	-15/22/-51/27	1	
118	016b	0:11	39	58/1	3123/4	- / -	118/204	-3/29/-57/30	1	
119	016b	2:06	469	62/2	2927/9	- / -	143/316	4/32/-42/66	3	
120	018a	0:10	37	61/1	3309/18	- / -	105/136	-35/2/-40/-31	0	
121	018a	0:32	121	62/1	3456/36	- / -	102/215	-33/9/-44/-14	0	
122	018a	0:27	102	62/2	3475/14	- / -	83/152	-26/6/-36/-17	0	
123	018a	0:15	61	66/1	3398/37	- / -	99/216	-40/7/-46/-23	0	
124	018a	0:06	27	66/1	3283/19	- / -	101/144	-44/3/-48/-39	0	